UNIVERSITY OF SYDNEY

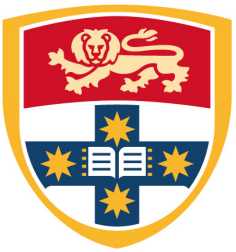

A Fundamental and Systematic Investigation into the Solid State Chemistry of Some Ternary Uranium Oxides

by

Gabriel L. Murphy

A thesis submitted in fulfilment of the requirements for the degree of
Doctor of Philosophy

in the
Faculty of Science
School of Chemistry

April 2019

Declaration of Authorship

I, Gabriel L. Murphy, declare that this thesis titled, 'A Fundamental and Systematic Investigation into the Solid State Chemistry of Some Ternary Uranium Oxides' and the work presented in it are my own except where otherwise acknowledged.

Gabriel L. Murphy

April 2019

"The visions we offer our children shape the future. It matters what those visions are. Often they become self-fulfilling prophecies. Dreams are maps... Where are the cartographers of human purpose?"

C. Sagan.

Abstract

The research presented in this Ph.D. dissertation explores the solid state chemistry of the $A\mathrm{UO}_4$ family of oxides (A = divalent or trivalent cation), addressing the role uranyl bonding and $5f$ electron chemistry play in influencing their physicochemical properties. This involved the systematic synthesis of targeted oxides combined with high resolution diffraction and spectroscopy coupled with theoretical modelling.

The dissertation begins with the investigation of the irreversible phase transformation that occurs between the rhombohedral (α) and orthorhombic (β) variants of SrUO_4. It is demonstrated that the transformation is first order and reconstructive. Crucial to the transformation is the generation of oxygen vacancies in the α variant as it is heated in air towards 600 ^{o}C involving the generation of reduced uranium valence states. Thereafter, a source of oxygen is required to re-oxidise the sub-stoichiometric structure to allow the transformation to the β variant to proceed, as without a source of oxygen, the β variant cannot form and the α phase persists at high temperature. *Ab initio* calculations indicate the origin of this oxygen transfer phenomena lies in the thermodynamic instability of the β orthorhombic structure to retain vacancies relative to the α rhombohedral structure which can retain them over a wide range of sub-stoichiometries at high temperature.

The interest in oxygen vacancy formation is continued by examining the isostructural oxides α-SrUO_4, CaUO_4 and members of the series α-$\mathrm{Sr_xCa_{1-x}UO_4}$. It is demonstrated that an approximately linear relationship exists between the number of oxygen vacancies that can form under oxidising conditions and the increasing size of the A site cation. This trend is attributed to variable defect-defect interactions which are modulated by the size of A site cation. When a critical number of oxygen vacancies are generated in α-SrUO_4, α-$\mathrm{Sr_{0.4}Ca_{0.6}UO_4}$, and CaUO_4, heating these results in reversible first order symmetry lowering phase transformations forming novel phases denoted δ. Pertinent to δ phase formation is the ordering of previously disordered oxygen vacancies with heating which does not involve any chemical change and is purely thermodynamic in origin. A proposed thermodynamic explanation to the observed phenomena is provided by *ab initio* calculations which suggests decreasing entropy, associated with the ordering of the vacancies, is counterbalanced by an increase in electronic entropy caused by mixed uranium valence states. Although this is a tentative conclusion based on theoretical predication it would be the first demonstration of the significance of electronic entropy in influencing phase diagrams.

The later sections of this dissertation focus on the broader family of AUO_4 oxides, in particular establishing a structural hierarchy that can be used to predict the structures formed for specific A and U cations. This involved establishing precise structural models using high resolution synchrotron and neutron diffraction methods of several of the AUO_4 oxides that had either been poorly or incorrectly described. The $NiUO_4$ polymorphs, first identified in the 1960's but questioned in more recent work were investigated. Using high temperature and high pressure synthesis methods the orthorhombic $NiUO_4$ polymorphs in space group *Pbcn* (α) and *Ibmm* (β) were prepared and structures established with high precision. *Ex situ* experimentation indicate that the β phase is the preferred phase at higher temperature and pressure where the α transforms to it irreversibly. Perovskite like tilting of the NiO_6 polyhedra was identified in β-$NiUO_4$, which was also observed in other isostructural AUO_4 oxides. The size of the A site cation is shown to modulate the tilt. Prior to this work phase transformations between the various AUO_4 oxides structures were known with various degrees of precision, except for a transition between the orthorhombic *Pbcn* and *Ibmm* variants. The $NiUO_4$ polymorphs provide this "missing link". Furthermore this work provides the first complete structure solution of NiU_3O_{10} enabling a comprehensive description of the Ni-U-O system. With the $NiUO_4$ polymorphs, and other precise models developed in this dissertation, the specific structure type formed of AUO_4 oxide can be understood on the basis of the ratio of the A to U cation sizes. This can potentially be used to understand structure formation within spent fuel and waste form systems.

The final section of this dissertation examined the response of the uranyl group to high pressure. This involved neutron diffraction of α-$SrUO_4$ and β-$SrUO_4$ subjected to pressures of up to 5.7 and 6.15 GPa respectively. It was demonstrated that the application of pressure results in electron delocalisation causing lengthening of uranium-oxygen bonds most pronounced in the uranyl bonds. This indicates a departure of Badger's rule predicted to occur for uranium oxides in recent computational studies. It is argued that this bond lengthening contributes to the exceptional hardness of these two polymorphs identified in this work; measurements indicate that α-$SrUO_4$ has a bulk modulus comparable to that of diamond.

Acknowledgements

This dissertation and research outcomes would not be possible without the support and encouragement of so many people. Of special mention are Prof. Brendan Kennedy, Dr. Zhaoming Zhang and Dr. Chris Griffith:

Brendan - I am eternally grateful for the advice, assistance, training and support you have given me throughout my Ph.D. I am aware I am likely one of the more demanding students you have had when it came to me pushing research excellence often through unconventional scientific avenues. Be it my initial wish/demand to do uranium chemistry, insisting on technically challenging experiments or my want to tackle more 'exotic' actinides, throughout, you have continually supported and encouraged me in the pursuit of scientifici excellence and all areas of science important to me. A Ph.D. is one of the rare moments of a scientific career that you are able to conduct research of a professional standing that is of your free choosing, through your guidance and support you have allowed me to do this, let me follow my passion in nuclear science and direct me towards the career I am now pursuing with it, thank you for everything.

Zhaoming - I think we have had one of the more colourful working relationships that can occur between supervisor and student. You have been one of the biggest positive influences on my scientific training, constantly pushing me to improve in all areas of development. The scientist I have become is a consequence of your guidance and support. I often look back to our often heated scientific debates over topics ranging from the significance of U^{5+} chemistry, grey phase material formation to the 2^{nd} law of thermodynamics with such fondness. Your alacrity towards me pursuing often such complicated and paperwork heavy experiments whilst pushing and advancing my research publications is truly appreciated and I hope you're as proud of the strides we've made at ANSTO as I am. However, what I am most grateful for though is your willingness to always be there for me, defend me and be on my side when things, as so often it seemed, went dire, for that I am truly thankful. My Ph.D. has been an interesting journey, I hope you enjoyed it as much as I have working with you, thank you for everything.

Chris - It has been a great honour to have originally worked for you when I was an intern at ANSTO Minerals and be supported by you during my Ph.D. Then and still, your dedication, professionalism and tenacity towards all avenues of science constantly impressed me to the extent you're one of the prominent reasons I was inspired to undertake my Ph.D. I am further incredibly thankful for you letting me conduct my research in Minerals when it

became untenable in other parts of ANSTO whilst continually supporting and encouraging me throughout. The advice you have given over the year's I hold very dear and I consider you a role model scientist to whom I aspire to be. The successes of my Ph.D., research and the early career scientist stage I enter, in many ways I attribute to your support and inspiration, thank you for everything.

ANSTO Minerals - To everyone at ANSTO Minerals it has been a privilege and honour to have been in your presence over the years from the early beginnings as an intern to now. Of the places/divisions I've worked in through my research no other has come close to the hospitality you have given me. I strongly believe my dissertation and research outcomes would not be possible without you. Particularly thank you to Dr. Mellodee Anvia, for being an amazing friend and for being there for me during trying times. (Soon to be Dr.) John Demol, for being such a great friend over the years, the pointless scientific debates and endless enjoyable conversations. Dr. Adam Roper, for being a great friend and office companion, also for putting up with the fruit fly infestation of the office caused by my forgotten fruit (oops). To Dr. Rob Gee and Hamilton Wearing for consistently supporting me and my research I am eternally grateful.

University of Sydney Solid State Research - Thank you to everyone in the University of Sydney Solid State Research group past and present. Sean, Pierre, Dr. Adriano, Dr. Sam, Dr. Julia Wind, Julia Polt, Jitu, Qingbo, Dr. Emily, Dr. Tom, Dr. Morgan, Lucie, Dr. Paula, Dr. Chun-Hai, Felipe, A/Prof. Chris Ling and A/Prof. Sigi Schmid among many others. Although I wasn't there as much as I probably should have been, the bbq's, office banter, Friday night drinks and wild times on boat cruises were awesome thank you for the great memories.

Forschungszentrum Juelich - To everyone at IEK-6 Forshungszentrum Juelich thank you for having me during my guest research visits, the science, the beers and the parties were nature worthy. Special thank you to Prof. Evgeny Alekseev and Dr. Philip Kegler for hosting me and working with me, I learnt an incredible amount from both of you and I am delighted to call you both my good friends. Also thank you to James, Yucheng, Eike and other members of the actinide solid state chemistry research group, you're an amazing bunch whom contributed so much to the amazing time I had in Germany. Thank you to Dr. Piotr Kowalski and Dr. George Beridze for all the support with the brilliant collaboration we have entered and the successful science we have built.

NFC - Thank you to everyone in Nuclear Fuel Cycle Research and Actinide Immobilisation ANSTO who have helped encourage and contributed to my research. Particularly thank you to Dr. Yingjie Zhang for all the support in single crystal diffraction work, advice and the continual support of my research and career, Dr. Dan Gregg and

Dr. Lou Vance for support and encouragement, Dr. Greg Lumpkin for encouraging me and assisting me in being able to work with the CEA and to Prof. Mihail Ionescu for the encouragement and support particularly during the difficult periods of my research.

Australian Centre for Neutron Scattering (ACNS) - to everyone at the ACNS involved in my neutron scattering experiments thank you for support and willingness to undertake often such challenging experiments with nuclear materials. Particularly thank you to Dr. Helen Maynard-Caseley and Dr. Max Avdeev, your willingness to conduct and advance experiments and research is truly appreciated and it was a pleasure to work with you both.

Australian Synchrotron (AS) - To everyone at the AS involved in my synchrotron X-ray scattering work thank you for support and willingness to undertake often such difficult experiments with nuclear materials often under challenging experimental conditions. From powder diffraction Dr. Justin Kimpton, Dr. Helen Brand and Dr. Qinfen Gu, your assistance and support is truly appreciated. From X-ray absorption spectroscopy Dr. Bernt Johansson for the assistance with running quite difficult variable temperature experiments. From X-ray fluorescence microscopy Dr Martin de Jonge for your fantastic help in coordinating, assisting and helping us analyse the XFM data from a very challenging experiment. Particularly thank you to Dr Katie Sizeland for always being such a great, patient and supportive friend to me, I am sure one day we will find a mutual ground to combine our research interests.

French Alternative Energies and Atomic Energy Commission, Paris-Saclay (CEA) - To Dr. David Simone, Dr. Laurence Luneville, Dr. Vassilis Pontikis and everyone else at CEA Paris-Saclay, thank you for having me during my stay with you I learnt an incredible amount of both the French nuclear sector and also fundamental nuclear physics. David's decorum over lunch and dinner events will be missed. Particular thank you to Dr. Gianguido Baldinozzi for hosting me at CEA and CS, I had a wonderful time working for you and learnt so much than I could of ever imagined, I look forward to working with you again in the future.

Funding - I am incredibly grateful to the funding support and scholarships I have been given during my Ph.D. To AINSE, my PGRA scholarship, the SAAFE scholarship, my travel bursary award and also the support you have given me to help the ANSTO Young Researcher Group expand has been immense and I am very thankful for all this and how it is has enhanced my training and career progression. The proceeds of the Joan R. Clarke Scholarship and the United Uranium Trust Fund are greatly appreciated for allowing me to work with Forschungszentrum Juelich which has helped contribute to my employment with them. The Maslen scholarships courtesy of the

Society for Crystallography Australia and New Zealand (SCANZ) are also greatly appreciated for allowing me to attend Crystal31 conference in Perth 2017 and IUCr conference in Hyderabad India 2017. The awards and funding support I have been given by ANSTO are also greatly appreciated.

And lastly to my parents, Anne-Marie and Rita, I would have nothing without the everlasting love and support you have given me throughout my life, thank you for everything.

List of Publications

A number of publications have resulted or are in the process of being prepared from the research performed during the course of this dissertation. These are included below, ones that are included in this dissertation are labelled with an asterisk.

- *__Murphy, G. L.;__ Maynard-Casely, H. E.; Zhang, Z.; Voigt, T.; Kennedy, B. J. High Pressure Neutron Diffraction Studies of $SrUO_4$: A Departure in Badger's Rule and Bond Lengthening with Pressure. In Preparation. **2019**.

- *__Murphy, G. L.;__ Zhang, Z.; Kegler, P.; Alekseev, E.; Avdeev, M.; Gregg, D. J.; Kennedy, B. J. Structural and Spectroscopic Studies of Orthorhombic $M$$UO_4$ Oxides (M = Cd, Co, Mn, Mg, Cr, $Cr_{0.75}Al_{0.25}$ and $Cr_{0.5}Fe_{0.5}$). In Preparation. **2019**.

- *__Murphy, G. L.;__ Wang, C. H.; Zhang, Z.; Kowalski, P. M.; M.; Beridze, G.; Avdeev, M.; Muransky, O.; Brand, H.; Gu, Q. F.; Kennedy, B. J. Controlling Oxygen Defect Formation and its Effect on Reversible Symmetry Lowering and Disorder-to-Order Phase Transformations in Non-Stoichiometric Ternary Uranium Oxides. Accepted. Inorg. Chem. **2019**.

- *__Murphy, G. L.;__ Zhang, Z.; Kennedy, B. J. The Solid State Chemistry of $A$$UO_4$ Ternary Uranium Oxides, A Review. Published in the book "Complex Oxides: An Introduction". **2019**.

- Simeone, D.; Thorogood. G. J.; **Murphy, G. L.;** Luneville. L. Evidence of a Unique Length Scale in Rationalizing Radiation-Induced Patterns. J. Appl. Phys. **2019**, 125, 065103.

- *__Murphy, G. L.;__ Kegler, P.; Zhang, Y.; Alekseev, E.; Zhang, Z.; De Jong, M.; Kennedy, B. J. High-Pressure Synthesis, Structural and Spectroscopic Studies of the Ni-U-O System. Inorg. Chem. **2018**, 57, 21, 13847-13858.

- *__Murphy, G. L.;__ Wang, C. H.; Beridze, G.; Avdeev, M.; Zhang, Z. M.; Brand, H.; Kowalski, P. M.; Kennedy, B. J. Unexpected Crystallographic Phase Transformation in Nonstoichiometric $SrUO_{4-x}$: Oxygen Defect Ordering and Symmetry Lowering with Increasing Temperature. Inorg. Chem. **2018**, 57, 10, 5948-5958.

- Maynard-Casely, H. E.; Lee, S.; Booth, N.; Studer, A.; Peterson, V.; Duyker, S.; Komatsu, K.; Yamane, R.; **Murphy, G. L.;** Vogt, T. Putting Pressure on WOMBAT - Outcomes and Unique Capabilities. Acta Crystallogr. Sect. A **2017**. 73 (a2), C868.

- **Murphy, G. L.;** Zhang, Z.; Avdeev, M.; Wang, C. H.; Beridze, G.; Kowalski, P.; Gu, Q.; Kimpton, J.A; Johannessen, B.; Kennedy, B. J. Ion-Transport Phenomena and Anomalous Transformations in Strontium Uranium Oxides. Acta Crystallogr. Sect. A **2017**, 73 (a2), C1428.

- **Murphy, G. L.;** Kennedy, B. J.; Zhang, Z.; Avdeev, M.; Brand, H. E. A.; Kegler, P.; Alekseev, E. V. Structure and Phase Transition in $BaThO_3$: A Combined Neutron and Synchrotron X-ray Diffraction Study. J. Alloy. Compd. **2017**, 727, 1044-1049.

- Hao, Y.; **Murphy, G. L.;** Bosbach, D.; Modolo, G.; Albrecht-Schmitt, T. E.; Alekseev, E. V. Porous Uranyl Borophosphates with Unique Three-Dimensional Open-Framework Structures. Inorg. Chem. **2017**, 56 (15), 9311-9320.

- *__Murphy, G. L.;__ Kennedy, B. J.; Kimpton, J. A.; Gu, Q. F.; Johannessen, B.; Beridze, G.; Kowalski, P. M.; Bosbach, D.; Avdeev, M.; Zhang, Z. M. Nonstoichiometry in Strontium Uranium Oxide: Understanding the Rhombohedral-Orthorhombic Transition in $SrUO_4$. Inorg. Chem. **2016**, 55. 18, 9329-9334

- Hao, Y. C.; Klepov, V. V.; **Murphy, G. L.;** Modolo, G.; Bosbach, D.; Albrecht-Schmitt, T. E.; Kennedy, B. J.; Wang, S.; Alekseev, E. V. Influence of Synthetic Conditions on Chemistry and Structural Properties of Alkaline Earth Uranyl Borates. Cryst. Growth Des. **2016**, 16 (10), 5923-5931.

- **Murphy, G.;** Kennedy, B. J.; Johannessen, B.; Kimpton, J. A.; Avdeev, M.; Griffith, C. S.; Thorogood, G. J.; Zhang, Z. M. Structural Studies of the Rhombohedral and Orthorhombic Monouranates: $CaUO_4$, α-$SrUO_4$, β-$SrUO_4$ and $BaUO_4$. J. Solid State Chem. **2016**, 237, 86-92.

- Kennedy, B. J.; **Murphy, G.;** Reynolds, E.; Avdeev, M.; Brand, H. E. R.; Kolodiazhnyi, T. Studies of the Antiferrodistortive Transition in $EuTiO_3$. J. Phys.-Condes. Matter. **2014**, 26 (49), 495901.

Contents

List of Figures

List of Tables

Chapter 1

Introduction

This chapter is adapted from a manuscript titled "The Solid State Chemistry of $A\mathrm{UO}_4$ Ternary Uranium Oxides, A Review" by G. L. Murphy *et al.* that has been published as a chapter apart of the book "Complex Oxides: An Introduction".

1.1 Introduction

Uranium, though relatively scarce with terrestrial abundance of 2.7 ppm[1], is societally important in many applications including radiometric dating[2], military ordinance[3,4] catalysis[5,6] and pertinently forms the keystone to the nuclear fuel cycle and the current geopolitical climate resulting from the nuclear age[7–9]. Uranium is most commonly encountered as U(IV)O_2, which is the most widely utilised composition in nuclear fuels and is also the form most commonly encountered in nature, where it exists as the mineral uraninite[10–12]. The interaction of uraninite, and its partially oxidised forms, with other elements precipitates a myriad of minerals with various physical properties and exhibiting a range of uranium coordination environments and oxidation states[13,14]. When subjected to prolonged nuclear fission in nuclear reactors, UO_2 nuclear fuels spawn a plethora of fission daughters which are able to recombine with the fuel matrix forming a number of fuel derived secondary phases[15–18]. These display a range of chemistries, which can be further convoluted as the fuel is partitioned during fuel reprocessing. During reprocessing the spent fuel can become oxidised, leading to the presence of additional uranium oxidation states and the formation of new phases. Understanding the physico-chemical properties of these environmentally hazardous and physiologically dangerous phases is considered pertinent. As a part of international plans for the disposal of spent nuclear fuels, they would ultimately be subjected to deep geological disposal, it is imperative that these phases are properly identified, to ensure they are immobilised within appropriate waste forms so as to prevent their migration into the environment[12,15,19,20].

Surprisingly, despite the awareness of uranium compounds extending back to its discovery in 1789 by Martin Heinrich Klaproth and the subsequent development of the nuclear industry, a paucity of information remains regarding the structure and properties of even some of the most simple uranium oxides. This can be attributed to the challenges in both handling radioactive materials and in their analyses. In structural elucidation studies using X-rays, the absorption of X-rays by uranium and its strong X-ray scattering power can lead to relatively poor precision regarding the structure of these materials, particularly regarding the lighter elements such as oxygen[21]. Consequently the precise coordination environment of uranium in many complex oxides is relatively poorly defined.

Attempts to theoretically model materials containing uranium (and other actinides) are extremely challenging and their study can still be considered something of a developing science. This is a consequence of the large number of electrons in uranium cations, which requires the use of effective core

potentials, the need to take relativistic effects into account and the impact of correlation effects arising from the diffusivity of the valence orbitals that are often mixed between the s, p, d and f orbitals. Traditional calculation methods require significant alterations to correctly account for these factors. These complexities place limitations upon the validity of calculations of nuclear fuels or waste forms containing uranium. The continuously improving performance of neutron and synchrotron X-ray scattering facilities has led to a number of precise structural models of uranium and other actinide containing systems becoming available[22,23]. These provide a means to verify the accuracy of theoretical studies and enable the physicochemical behaviours of new phases to be more correctly predicted. The powerful combination of precise structural determination and theoretical modelling enables the solid state chemistry, which underpins the formation and properties of actinide-containing compounds (particularly those that arise from spent nuclear fuel), to be progressively unravelled, revealing a rich vein of chemistry and crystallography that is often unique to the actinides but with potential to guide further developments in inorganic and physical sciences.

The ternary uranium oxides of the form $A\mathrm{UO}_4$ are a class of materials relevant to spent nuclear fuel partitioning, waste forms and uranium oxide concentrates[24,25]. A number of examples occur naturally as minerals[26–28]. Colloquially known as the monouranates, the $A\mathrm{UO}_4$ oxides are distinct to the crystallographically similar tetragonal wulfenite, $A\mathrm{MoO}_4$, and scheelite, $A\mathrm{WO}_4$, structures. The $A\mathrm{WO}_4$ oxides, containing either pentavalent or hexavalent uranium cations with distorted tetragonal or hexagonal bipyramid coordination environments, often contain the covalent collinear oxo uranyl species. Knowledge of monouranate compounds is relatively sparse, with the structures described with varying degrees of accuracy and precision. This chapter will focus on examining the current literature of the monouranates in relation to their structure-property relationships.

1.2 Uranium Solid State and Structural Chemistry

The solid state chemistry of the monouranates is essentially defined by the chemistry of uranium. Thus it is pertinent to briefly discuss the core aspects of uranium oxide chemistry in relation to the monouranates. Uranium has the ground state electron configuration $[\mathrm{Rn}]5f^36d^17s^2$ and in the solid state it is regularly encountered in either the tetravalent ($[\mathrm{Rn}]5f^2$), pentavalent ($[\mathrm{Rn}]5f^1$) or hexavalent ($[\mathrm{Rn}]5f^0$) valence states. The uranyl group, $\mathrm{UO_2}^{2+}$, is synonymous with uranium oxides, and it is often found in other

transuranic compounds, consequently it is generally described as the actinyl group AnO_2^{2+} (An = actinide element). The uranyl group consists of a central uranium atom bonded to two oxygen atoms forming short, strong, covalent and collinear $[O{=}U{=}O]^{2+}$ bonds. Although similar functional groups are known in general inorganic materials, for instance the vanadyl group, the contrasting redox chemistry and the ability to access $5f$ electrons makes the uranyl/actinyl groups chemically distinct[29–33]. This is apparent in the literature with several examples of unique chemical phenomena and properties being uncovered in uranium materials, where the origin can be traced to the influence of the uranyl group[31,32,34–36]. The most significant orbital contributions in the uranyl linkage is the mixing of the uranium $6d$, $5f$, $6p$ and $6s$ orbitals with the oxygen $2p$ and $2s$ orbitals. A molecular-orbital energy level diagram for UO_2^{2+} is presented in Figure 1.1. The two uranium primary valence shells, $5f$ and $6d$, enable σ and π bonds primarily to oxygen $2p$ orbitals, forming $3\sigma_g$, $3\sigma_u$, $1\pi_g$ and $2\pi_u$ (the highest occupied molecular orbitals, HOMOs) and $4\sigma_u{}^*$, $3\pi_u{}^*$, $1\delta_u$ and $1\phi_u$ (the lowest unoccupied molecular orbitals, LUMOs). The uranium $6p$ and $6s$ shells must also be considered, because they have been shown to contribute to core electron behaviour and to spatially extend beyond the $5f$ shell[32,33,37]. Figure 1.1 omits the uranium $7s$ and $7p$ orbitals, however these have been shown to contribute to bonding in several cases[32,33,37]. References[32,33,35,37] present a more extensive discussion of the molecular orbitals and bonding of uranium. It should be apparent from this brief overview that understanding the bonding of uranium, both in uranyl and non-uranyl systems, is far from trivial.

The uranyl group is commonly encountered as the $U(VI)O_2^{2+}$ moiety, though it can exist as $U(V)O_2^{+}$. The latter is relatively unstable since it results in the addition of a single $5f$ electron into the $5f$ LUMO, which leads to the lengthening of the uranyl bond. The uranyl group is generally not expected to be encountered in U(IV) oxides. As a binary U(IV) oxide UO_2 adopts the regular fluorite structure[32]. UO_2 is far more ionic than UO_2^{2+}, where the introduction of two electrons into the $5f$ shell reduces the covalency and uranyl character[32,37]. It must be stressed that although the uranyl group has been assigned to many monouranate structures, precise chemical detail of its effects and interactions are not well understood. The current understanding of the uranyl group, its chemistry and related theoretical studies are largely derived from liquid, gas phase and organometallic uranium compound investigations. Such compounds are clearly distinct to the condensed matter oxide phases, although they provide a good foundation to the understanding of the observed structural and bonding properties found in the monouranates.

In the monouranates and other uranium oxides, the uranyl group is often surrounded by four to

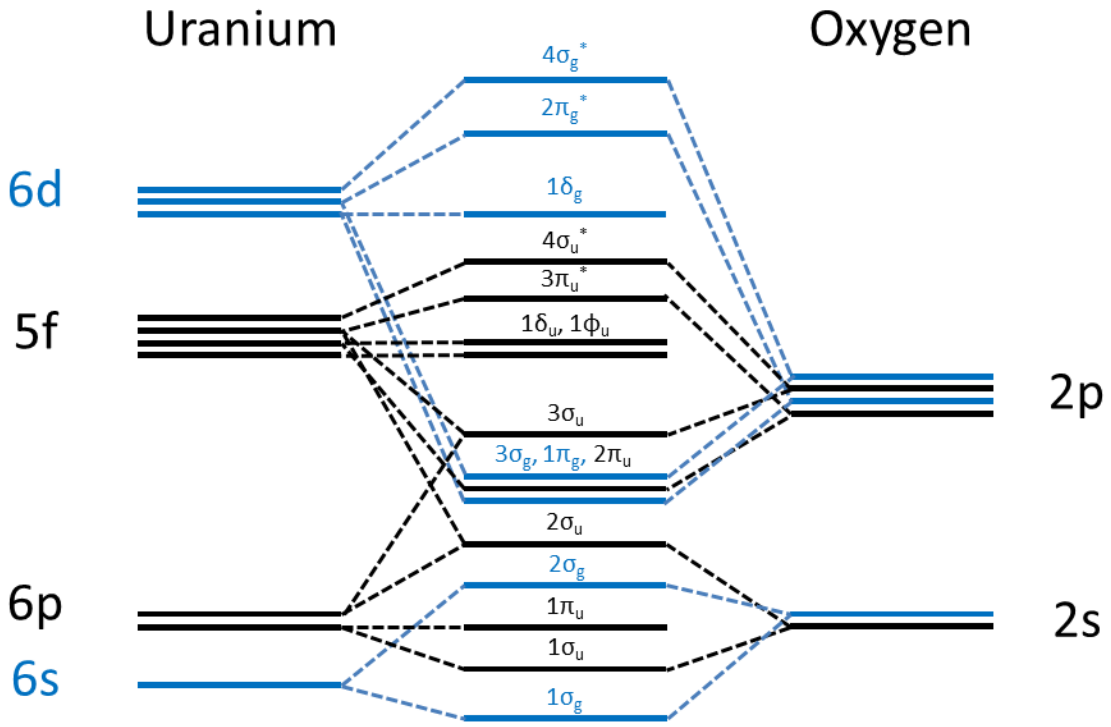

FIGURE 1.1: Molecular-orbital energy-level diagam for the uranyl bond (adapted from Figure 1 in reference [36]).

six additional oxygen atoms forming UO_6, UO_7 and UO_8 polyhedra with tetragonal, pentagonal and hexagonal bipyramidal coordination environment respectively. These motifs are illustrated in Figure 1.2. Of these three polyhedral arrangements, the UO_6 and UO_8 polyhedra are most frequently encountered in monouranates. UO_7 polyhedra are relatively uncommon but can be found in other complex oxides such as $Na_2[(UO_2)(MoO_4)_4]$[38]. The uranyl group is most often a terminal oxo ligand and it rarely bonds to other uranium centres. When such a rare bonding motif does occur, it is known as a cation-cation interaction (CCI)[39]. CCIs are observed much more frequently in $An(V)O_2^+$ than in $An(VI)O_2^{2+}$[39–41]. For example, they were seen in approximately 50% of Np oxides containing the NpO_2^+ group but only in around two percent of oxides containing the UO_2^{2+} group[40,42]. More CCIs are observed in UO_2^+ than in UO_2^{2+}, as it is more electrostatically favourable for a $[O{=}U{=}O]^+$-UO_2^+ interaction to occur than a $[O{=}U{=}O]^{2+}$-UO_2^{2+} interaction. Since hexavalent uranium is most commonly present in the monouranates, CCIs are

not regularly encountered in them or in other ternary uranium oxides. Considering the geometry of uranyl containing UO_n polyhedra (n = 6 - 8), most monouranates form either 1D chain or 2D layered structures where the terminal uranyl group is directed at the A-site cations between the 1D chain or 2D layers containing the uranium atoms. By extension, 3D dimensional framework structures generally constrain the presence of the uranyl group or if they do, they possess CCIs. Details of AUO_4 monouranate structural types will be discussed in the subsequent sections.

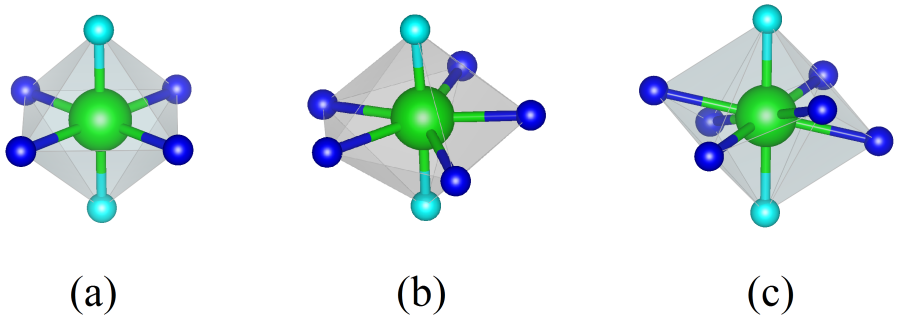

FIGURE 1.2: Uranium-oxygen coordination polyhedra motifs regularly encountered in the solid state: (a) UO_6 seen in β-$SrUO_4$ [43], (b) UO_7 seen in $Na_2[(UO_2)(MoO_4)_4]$ [38] and (c) UO_8 seen in $CaUO_4$ [44]. Uranium atoms are shown in green, uranyl oxygens in aqua and non-uranyl coordinating oxygens in blue.

1.3 $R\bar{3}m$ Rhombohedral and *Pbcm* and *Cmmm* Orthorhombic Monouranates

Knowledge of monouranates first emerged from the Manhattan project. In 1944 Zachariasen isolated single crystals of $CaUO_4$ and $SrUO_4$ from molten salts of $CaCl_2$ or $SrCl_2$ and U_3O_8 or UO_3 and his work was published in 1948 [45]. Due to the crystal quality, single crystal X-ray diffraction could not be performed rather the structures were investigated using powder X-ray diffraction methods. The two oxides were found to be isostructural, forming a rhombohedral structure in space group $R\bar{3}m$. As shown in Figure 1.3, the structure consists of edge sharing UO_8 polyhedra creating 2D layers with collinear axial oxygens, geometrically consistent with the uranyl group which are directed towards the Ca^{2+}/Sr^{2+} cations (which are also eight-fold coordinated to oxygens). Later studies [46–49] identified a second polymorph of $SrUO_4$

that was determined to be orthorhombic in space group *Pbcm* and denoted as β-$SrUO_4$, whereas the rhombohedral form was denoted as the α polymorph. The structure of β-$SrUO_4$ consists of edge sharing UO_6 polyhedra forming infinite 2D layers that are separated by Sr^{2+} cations (6 coordinated). Similar to α-$SrUO_4$, collinear axial oxo oxygens exist in β-$SrUO_4$, geometrically consistent with the uranyl group which are directed towards the Sr^{2+} cations. The structure of β-$SrUO_4$ is illustrated in Figure 1.4. The uranium coordination motifs for both polymorphs can be found in Figure 1.2.

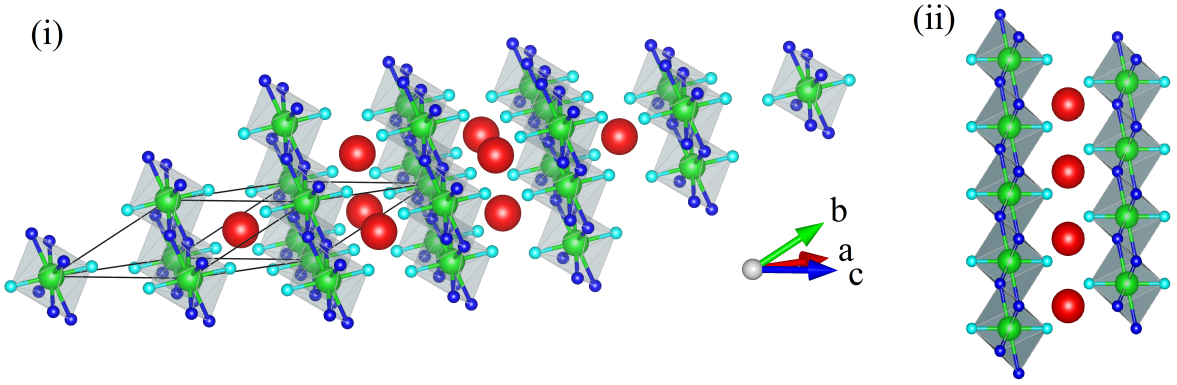

FIGURE 1.3: Structural representations of the rhombohedral structure in space group $R\bar{3}m$ for $CaUO_4$ [43] (isostructural to α-$SrUO_4$ and α-$CdUO_4$) . The red, green, blue and aqua spheres represent Ca, U, non-uranyl oxygen and uranyl oxygen atoms respectively. The inset (ii) highlights the terminal coordination of uranyl oxygens directed at the in-between layers with Ca^{2+} cations.

Neutron powder diffraction studies of $CaUO_4$ confirmed the original rhombohedral structural model [47,50,51]. However, the structural refinements for $CaUO_4$ and α-$SrUO_4$ produced relatively long uranyl bond lengths of above 1.95 Å. Such values are considered uncharacteristic of the uranyl bond [13,21,52]. Subsequent infrared and Raman spectroscopy studies by Liegeosi-Duyckaerts [53] confirmed the presence of the uranly group in $CaUO_4$ and in a solid solution of $Ca_{1-x}Sr_xUO_4$ with x up to 0.85. Recent computational, spectroscopic and structural investigations have further demonstrated the presence of the uranyl group in $CaUO_4$ [54–58] and α-$SrUO_4$ [59]. Some non-reproducibility in IR frequencies was noted in the investigation by Liegeosi-Duyckaerts [53], particularly at high Sr contents, suggestive of a miscibility gap in the solid solution. Pertinently this study suggested the ability for both $CaUO_4$ and α-$SrUO_4$ to support oxygen vacancy defects. Inspired by this, further studies exploring how many oxygen defects could be hosted in

$CaUO_4$ and α-$SrUO_4$ were initiated using either *ex situ* structural studies[49,60] or *in situ* thermogravimetric measurements[61–63]. The *ex situ* diffraction measurements provided evidence for phase separation in anion-deficient monouranates, particularly for $CaUO_4$[49]. Electron-microscopy investigations suggested that when $CaUO_4$ was treated under reducing conditions, it may contain both reduced and non-reduced regions[64,65]. Furthermore thermogravimetric measurements seemed to indicate that reduction and oxidation are not two completely equivalent processes[62,65]. Based on these experimental observations, Prodan and Boswell[65] postulated that microdomains, with variable oxygen contents, formed in reduced $CaUO_{4-x}$, and that the nature and number of these microdomains was influenced strongly by oxygen defect-defect interactions. These interactions were argued to lead to short-range order of the oxygen vacancies which influence the reactivity such that an oxidation thermal event would occur at a different stoichiometry from the corresponding reduction. *In situ* structural studies, using laboratory X-ray powder diffraction, by Pialoux and Touzelin[66,67] examined the reaction of $CaCO_3$ with UO_2 at high temperatures by varying the experimental condition from oxidising to neutral. They described a $CaUO_3$ perovskite-like monoclinic phase forming in heavily reduced samples, which existed from ambient temperature to 1500 ^{o}C, above which it was reported to undergo a phase transformation to an orthorhombic structure. However they did not solve or refine the two proposed $CaUO_3$ structures nor have there been any subsequent studies to corroborate their published work. Considering its low Goldschmidt tolerance factor (t) of 0.84 calculated using the equation (1.1), the existence of $CaUO_3$ as a perovskite is questionable[68–70]. In equation (1.1) r_A, r_U and r_O correspond to ionic radius of the A-site cation, uranium and oxygen respectively.

$$t = \frac{(r_A + r_O)}{(r_U + r_O)} \tag{1.1}$$

The structural phase transformation from rhombohedral α-$SrUO_4$ to orthorhombic β-$SrUO_4$ was originally examined by Rudorff and Pfitzer[48] who showed this occurs irreversibly above 600 ^{o}C. The transformation was also examined using thermogravimetric methods by Tagawa and Fujino[71,72] who found, interestingly, mass loss upon heating α-$SrUO_4$, consistent with the loss of oxygen, before mass gain as it formed stoichiometric β-$SrUO_4$. The two-step process associated with the transformation was also monitored with differential thermal analysis where the initial mass loss and subsequent gain steps were found to be endothermic and exothermic respectively. The mass loss was calculated to correspond to a stoichiometry of $SrUO_{3.7}$. Tagawa and Fujino further argued, based on estimates of the partial molar free

energies of oxygen for the two monouranates, that α-$SrUO_4$ is metastable and only exists on account of a high activation energy barrier that seemingly exists between itself and β-$SrUO_4$. Interestingly it was observed that whereas the rhombohedral polymorph can exist with a range of oxygen stoichiometries, orthorhombic β-$SrUO_4$ appears not to support oxygen vacancies. That Zachariasen[45] synthesized α-$SrUO_4$ at temperatures higher than the transformation temperature might be attributed to the use of the molten flux method which may limit the amount of oxygen present and thus inhibit the formation of orthorhombic β-$SrUO_4$. It is likely that the structure Zachariasen reported was sub-stoichiometric and is best described as α-$SrUO_{4-x}$. Flux growth methods have more recently become very topical, where the ability to generate crystals of suitable quality for single crystal X-ray diffraction studies has revealed several novel uranium and actinide phases[36,41,55,73–85]. A second phase transformation in $SrUO_4$ was reported to occur above 1200 ^{o}C where β-$SrUO_4$ loses oxygen, forming a rhombohedral structure described as γ-$SrUO_{4-x}$[71,86,87]. The authors argued that this transformation is the result of the inability of the β-$SrUO_4$ structure to accommodate oxygen vacancies above 1200 ^{o}C. From their description, however, this structural change might be better attributed to decomposition rather than a structural transformation.

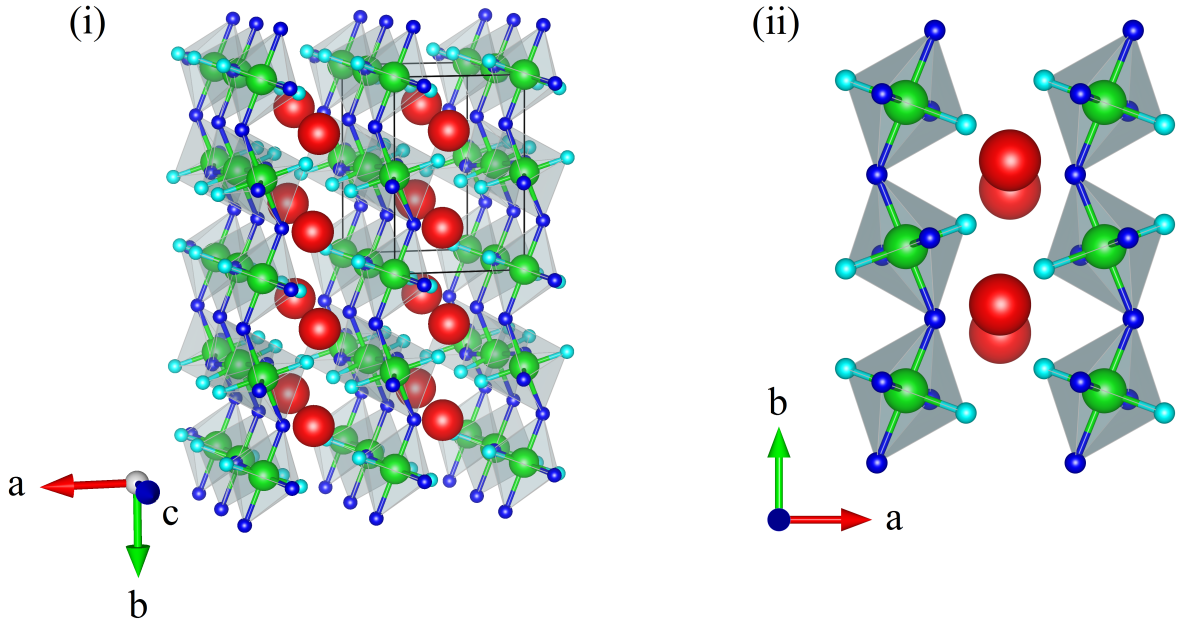

FIGURE 1.4: Structural representations of the orthorhombic structure in space group *Pbcm* for β-$SrUO_4$[43] (isostructural to $BaUO_4$). The red, green, blue and aqua spheres represent Sr, U, non-uranyl oxygen and uranyl oxygen atoms respectively. The inset (ii) highlights the coordination motif of the terminal uranyl oxygens directed at the Sr cations. Note the relative distortion compared to that observed in the rhombohedral motif of $CaUO_4$.

Tagawa and Fujinos investigations[71,72] revealed several unusual aspects in the α-β transformation in $SrUO_4$, however it remained unclear why orthorhombic β-$SrUO_4$ cannot support oxygen defects whereas rhombohedral α-$SrUO_4$ and $CaUO_4$ can. Further, Tagawa and Fujino speculated that the generation of a sub-stoichiometric structure requires uranium to be reduced to lower valence states. Takahashi *et al.*[49], from structural refinements against laboratory X-ray powder diffraction data, suggested that the formation of vacancies occurred preferentially on the equatorial O(2) site as opposed to the O(1) or uranyl oxygen site. Pialoux and Touzelin[88], using *in situ* high temperature laboratory X-ray powder diffraction, investigated the reaction between strontium oxide and uranium dioxide where they controlled the partial pressure of oxygen from highly oxidising to essentially inert. They identified both the rhombohedral and orthorhombic forms of $SrUO_4$ and determined the former exists with variable compositions in terms of oxygen content whereas the latter polymorph is stoichiometric. They further identified a perovskite like $SrUO_3$ phase which they concluded formed as a result of extensive reduction of $SrUO_4$. The Goldschmidt tolerance factor for $SrUO_3$ is quite low (0.88) similar to that for $CaUO_3$, suggesting that the formation of a perovskite structure is also unlikely to be favourable.

Ippolitova *et al.*[89] reported in 1961 that when oxides of cadmium and uranium were mixed together and heated at 570 ^{o}C, a rhombohedral structure formed which was seemingly isostructural to $CaUO_4$ and α-$SrUO_4$. Denoted as α-$CdUO_4$, they reported it to undergo a phase transformation above 720 ^{o}C to an orthorhombic phase denoted as β-$CdUO_4$ which transformed into an oxygen-deficient rhombohedral γ-$CdUO_{4-x}$ phase above 925 ^{o}C. β-$CdUO_4$ was originally described as orthorhombic, in space group *Pbam*, by Kovba *et al.*[46] in 1961, but a later study by Yamashita *et al.*[90] using laboratory X-ray powder diffraction with refinement methods was able to produce relatively precise models of both α-$CdUO_4$ and β-$CdUO_4$ structures. Yamashita *et al.* confirmed that α-$CdUO_4$ is isostructural to $CaUO_4$ and α-$SrUO_4$ in space group $R\bar{3}m$ (see Figure 1.3). Although β-$CdUO_4$ was found to be orthorhombic, it is not isostructural to β-$SrUO_4$, instead the structure is described as having a distorted rutile-like arrangement in space group *Cmmm*. This structure consists of edge sharing UO_6 polyhedra forming infinite chains along the [001] direction where the uranyl groups are directed at the six coordinated Cd^{2+} cations that form edge sharing chains also in the [001] direction, as displayed in Figure 1.5. Tagawa and Fujino[91] examined the α-$CdUO_4$ to β-$CdUO_4$ phase transformation and the transformation from β-$CdUO_4$ to the oxygen-deficient γ-$CdUO_{4-x}$ phase using thermogravimetric and differential thermal analysis measurements. They found, similar to the α-$SrUO_4$ to β-$SrUO_4$ transition, that as α-$CdUO_4$ is heated it loses mass, presumably

corresponding to the loss of oxygen, followed by a re-oxidation step before transforming to β-$CdUO_4$. The overall transition from α-$CdUO_4$ to β-$CdUO_4$ is irreversible whereas the β to γ transition is reversible under oxidising conditions. The reported β-$CdUO_4$ to γ-$CdUO_4$ transformation is similar to that described for the β-$SrUO_4$ to γ-$SrUO_{4-x}$ transition[71,86,87], involving a considerable oxygen loss from the β structure. It raises the same question whether the observed structural change was due to sample decomposition.

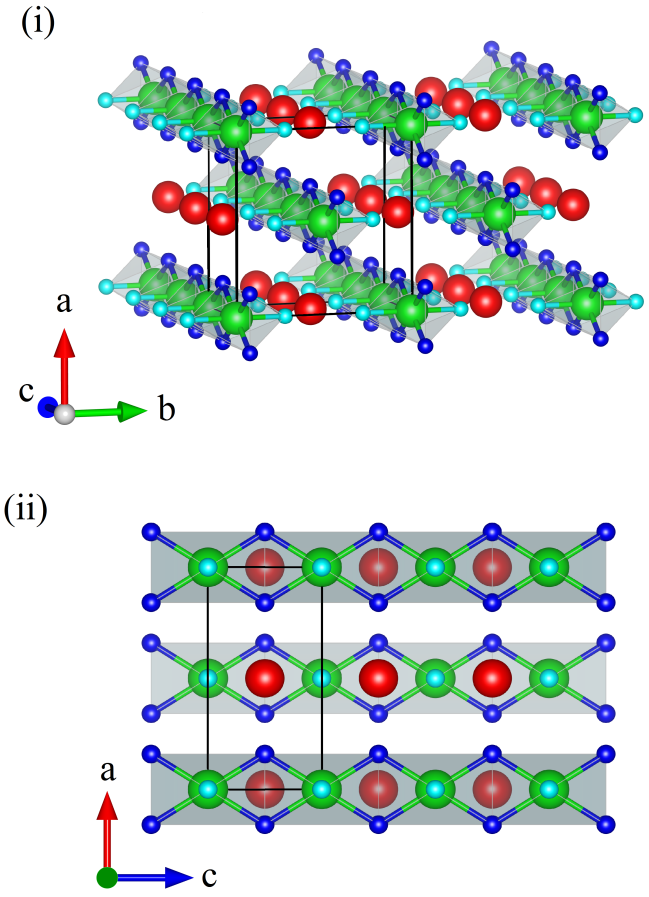

FIGURE 1.5: Structural representations of the orthorhombic structure in space group *Cmmm* for β-$CdUO_4$[90]. The red, green, blue and aqua spheres represent Cd, U, non-uranyl oxygen and uranyl oxygen atoms respectively. (ii) highlights the rutile-like chain configuration of the UO_6 and CdO_6 polyhedra in the [001] direction.

Matar and co-workers recently used *ab initio* methods, in the form of density functional theory, to examine $CaUO_4$[56] and β-$CdUO_4$[92] with a focus on their response to isotropic and anisotropic compression. Isotropic compression was found to amount to a bulk modulus comparable to other ternary metal

oxide compounds for both monouranates, but interestingly the anisotropic compression was found to be significantly larger, along the uranyl bond. This anisotropy has also been noted in other computational studies of uranium compounds[93], although there are few experimental *in situ* studies available that have studied such anisotropic compression in monouranates and other uranyl compounds.

$BaUO_4$ was first identified by Samson and Sillen[94] in 1948, who found it to be orthorhombic in space group *Pbcm* and isostructural to β-$SrUO_4$ (see Figure 1.4 for structural representation). The structure was later described by Loopstra and Rietveld in their neutron powder diffraction studies[50]. Further studies utilising vibrational spectroscopy have confirmed the presence of the uranyl group in both β-$SrUO_4$ and $BaUO_4$[58,95,96]. Reis *et al.*[97] re-determined the structure of $BaUO_4$ as orthorhombic in space group *Pbcm* using laboratory X-ray powder diffraction, solving the structure using a combination of Patterson, Fourier and least-squares techniques. A structural investigation by Jakes and Krivy[54], also using laboratory X-ray powder diffraction also supported the orthorhombic structural assignment for β-$SrUO_4$ and $BaUO_4$. Jakes and Krivy[54] confirmed the structural model developed Loopstra and Rietveld and highlighted the peculiarity of having a uranyl species with bond length above the typically encountered range of 1.75 - 1.82 Å. $BaUO_4$ has received relatively less attention than $CaUO_4$ and $SrUO_4$. It is not known to undergo any phase transformations below 1200 ^{o}C under oxidising conditions. Thermodynamic studies[98,99] have shown that it exhibits unexceptional thermal behaviour. In contrast to oxygen defect formation in $CaUO_4$ and α-$SrUO_4$, $BaUO_4$ is reported to transform directly to $Ba_2U_2O_7$ when heated under mildly reducing conditions, without forming oxygen vacancies[100–104]. $Ba_2U_2O_7$ has a weberite-type Na_2MgAlF_7 structure with the two crystallographically distinct uranium cations having different distorted octahedral geometries[100], but both are pentavalent[102,104]. When exposed to highly reducing conditions, $BaUO_4$ can be reduced to a perovskite, $BaUO_3$[105]. $BaUO_3$, $t = 0.92$, can also be prepared by reacting UO_2 and $BaCO_3$ at high temperatures.[106,107] The structure of $BaUO_3$ is still somewhat debated. Cordfunke *et al.*[108] and Barret *et al.*[109], both using neutron powder diffraction, described it as orthorhombic in space group *Pbnm* (or *Pnma* in an alternative setting). They both concluded that the structure is non-stoichiometric, containing an equivalent number of uranium and barium vacancies and is hyperstoichiometric with respect to oxygen and is best denoted as $BaUO_{3+x}$. However Hinatsu[105] argued that the near stoichiometric structure ($BaUO_{3.03}$) is cubic in space group $Pm\bar{3}m$ and that the excess oxygen leads to an orthorhombic distortion.

In 1958 Frondel and Barnes[110] used laboratory X-ray powder diffraction to identify $PbUO_4$ from

heating oxides of lead and uranium with an excess of lead sheet in water at 230 - 290 ^{o}C, finding it to be isostructural to β-$SrUO_4$ and $BaUO_4$ (see Figure 1.4 for its structural representation). A later single crystal X-ray diffraction study of $PbUO_4$ by Cremers *et al.*[111] provided a more accurate description of the structure confirming it to be orthorhombic in space group *Pbcm*. Popa *et al.*[112] investigated the thermal properties of $PbUO_4$ including thermal expansivity, thermal diffusivity and thermal conductivity from 272 to 627 ^{o}C. It was found that, despite being considered to be an insulator, $PbUO_4$ exhibited an electronic contribution to its conductivity, characteristic of a semi-conductor similar to that observed in $BaUO_4$[99]. Such behaviour is absent in β-$SrUO_4$[113]. Other than this $PbUO_4$ displayed unexceptional behaviour and is reported to volatilise above 800 ^{o}C with loss of Pb[112].

1.4 *Ibmm (Imma)* and *Pbcn* Orthorhombic Monouranates

$MgUO_4$, first identified by Zachariasen in 1954, forms a distinctly different structure to the other alkaline earth metal monouranates, adopting an orthorhombic structure in space group *Imma*[114]. In this structure, described hereafter in the alternative space group setting of *Ibmm* for ease of comparison with the *Cmmm* structure of β-$CdUO_4$, the UO_6 polyhedra edge share forming 1D chains along the [001] direction where oxo uranium oxygen bonds, consistent with the formation of the uranyl group, are directed at the Mg cations which are six-fold coordinated in a chain configuration along the [010] direction, as illustrated in Figure 1.6. X-ray absorption spectroscopic measurements by Guo *et al.*[115] showed the oxidation state of U in $MgUO_4$ to, unequivocally, be hexavalent.

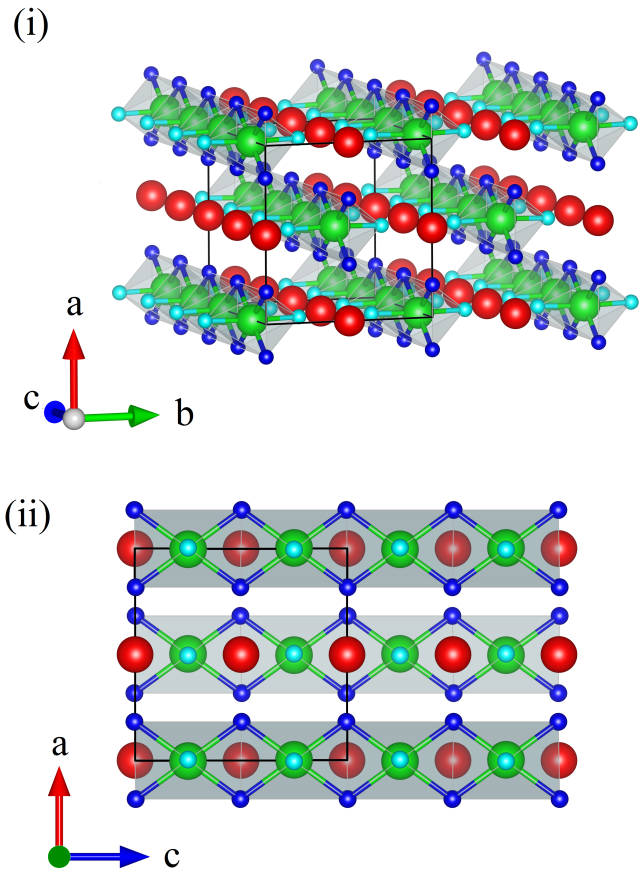

FIGURE 1.6: Structural representations of the orthorhombic structure in space group *Ibmm* for $MgUO_4$ [114] (isostructural to $CoUO_4$ and $MnUO_4$). The red, green, blue and aqua spheres represent Mg, U, non-uranyl oxygen and uranyl oxygen atoms respectively. (ii) Highlights the rutile-like chain configuration of the UO_6 and MgO_6 polyhedra in the [001] direction.

In comparison to the *Cmmm* structure, assigned to β-$CdUO_4$ by Yamashita *et al.*[90] as shown in Figure 1.5, the *Ibmm* structure has a less regular anionic sub-lattice resulting in a doubling of the *c*-axis[116]. The non-uranyl oxygen atoms edge share along the [001] direction in the (010) planes. Given that the subtle difference between the *Cmmm* and *Ibmm* structures lies in the oxygen sublattice and the study by Yamashita *et al.*[90] used laboratory X-ray powder diffraction which is not very sensitive to oxygens (especially in the presence of much heavier Cd and U cation), it is desirable to confirm the crystal structure of β-$CdUO_4$ using neutron diffraction.

Both $CoUO_4$ and $MnUO_4$, first studied by Bertaut *et al.*[117] using neutron diffraction measurements,

are isostructural to $MgUO_4$ with an orthorhombic structure in space group *Ibmm*. The magnetic structures of these two oxides were determined by Bacmann, Bertaut and others[117–120]. Below 11 K $CoUO_4$ adopts an antiferromagnetic structure. Bacmann and Bertaut[119] proposed a non collinear model for the magnetic structure of $CoUO_4$ based on a 2D irreducible representation with the wave vector k = $[\frac{1}{2}\ 0\ \frac{1}{2}]$ in magnetic space group (Shubnikov group) $P2_1'/m$. Anisotropic exchange coupling was attributed to the Co^{2+} cation, having a paramagnetic electron configuration $[Ar]d^7$, with no magnetic moment arising from the diamagnetic U^{6+} cation. The magnetic structure of $MnUO_4$ is different from that of $CoUO_4$. $MnUO_4$ undergoes a magnetic transition near 44 K forming an antiferromagnetic structure similar to that of pyrolusite (MnO_2)[121–123]. The magnetic structure consists of Mn^{2+} spins aligning antiferromagnetically along the [010] direction being described by the wave vector k = $[\frac{1}{2}\ 1\ \frac{1}{2}]$ with the same magnetic and nuclear unit cells. Magnetisation measurements by Guillot and Pauthene[124] revealed that $CoUO_4$ undergoes a metamagnetic transition to a ferromagnetic state that saturates above 130 kOe, whereas they did not observe saturation for $MnUO_4$.

The monouranates $CrUO_4$ and $FeUO_4$, first identified in the 1960s, adopt an orthorhombic structure in space group *Pbcn*[125–130]. This structure can be considered as approximately 2D layered, where UO_6 polyhedra corner share in the [100] direction forming a layered configuration and the CrO_6 or FeO_6 octahedra edge share, forming corrugated chains in the [001] direction in-between the UO_6 layers, as illustrated in Figure 1.7. From X-ray absorption spectroscopic measurements[115], supported by neutron diffraction[126,127] and magnetic measurements[118], the oxidation states of the uranium and transition metal cations were determined to be pentavalent and trivalent respectively. Guo *et al.*[115] argued, based on *ab initio* calculations, that the strong preference of iron and chromium to be trivalent drives the reduction of uranium even when the materials are prepared under oxidising conditions. Single crystal X-ray diffraction studies of $FeUO_4$ by Read *et al.*[128] highlighted the peculiarity of the UO_6 polyhedra, in which the uranyl group is not observed as there are no apparent trans oxo groups, rather all the U-O bonds are of a similar length.

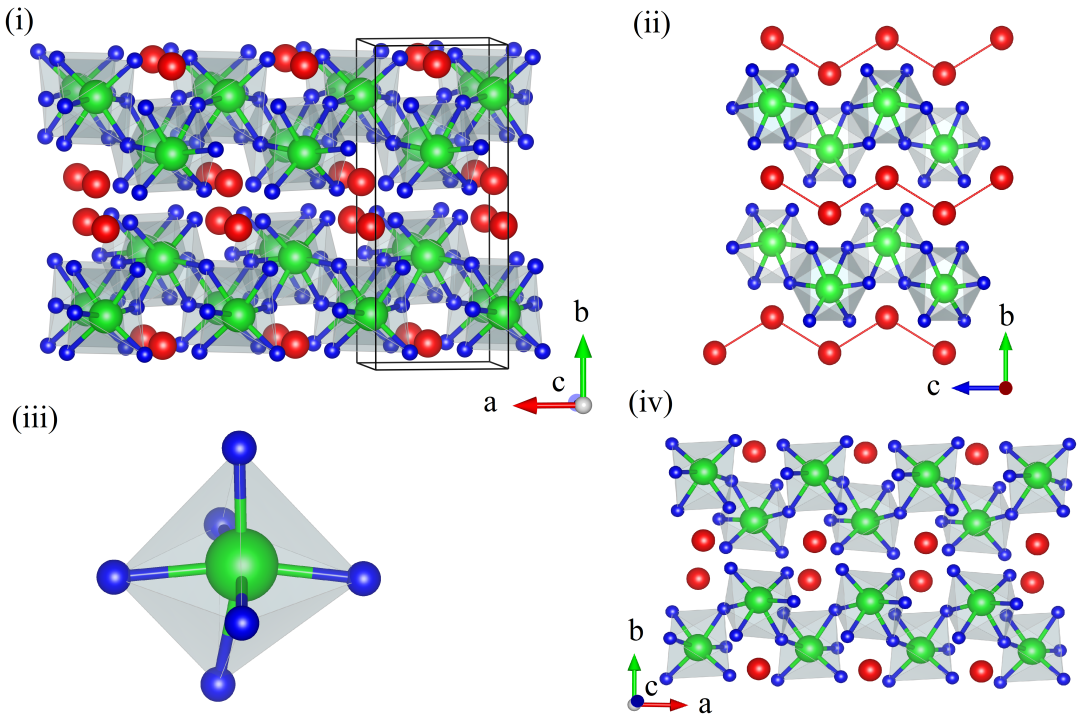

FIGURE 1.7: Structural representations of the orthorhombic structure in space group *Pbcn* for $FeUO_4$ [128] (isostructural to CrUO4). The red, green and blue spheres represent Fe, U and non-uranyl oxygen atoms respectively. The inset (ii) highlights the chain configuration in the [001] the c-axis of UO_6 and FeO_6 polyhedra (red line illustrates the zig-zag connectivity of Fe) , (iii) the coordination environment of the UO_6 polyhedra particularly the non linear trans oxo O-U-O configuration of U-O bonds, suggestive of the absence of uranyl and (iv) the corner sharing motif of the UO_6 polyhedra in the [100] direction.

$CrUO_4$ is antiferromagnetic below 44.5K and its magnetic structure was established using neutron diffraction [127,131]. The structure contains two magnetic sublattices from the ordered magnetic Cr^{3+} and U^{5+} cations respectively, and was described in the magnetic space group *Pbcn*'. $CrUO_4$ and $NdCrTiO_5$ were the early examples of magnetoelectric materials having two magnetic sublattices [131]. $FeUO_4$ undergoes an antiferromagnetic transition below 55 K forming an antiferromagnetic structure that can be described using a non collinear model [125]. The overall magnetic moment is determined by the antiferromagnetically aligned $3d^5$ Fe^{3+} cations (4 μ_B) as well as the antiferromagnetically aligned $5f^1$ U^{5+} cation (2 μ_B) [125,126,129,130]. This non collinear structure can be described using the magnetic space group *Pbcn*. Below 42 K $FeUO_4$ undergoes a second magnetic ordering transition, forming a ferromagnetic structure with a magnetic moment of 2 μ_B from the ferromagnetically aligned Fe^{3+} cations whereas the spins of the U^{5+} remains antiferromagnetically coupled. The resulting collinear magnetic structure can be refined in the magnetic space group *Pbcn*. $FeUO_4$ is a rare example of a ferromagnetic insulator [132].

The structures of $NiUO_4$ and $ZnUO_4$ have both been reported by Young and Hoekstra *et al.*[133,134] although the synthesis of these required the use of high pressure-high temperature methods. Two polymorphs of $NiUO_4$ have been described; the first was reported to be isostructural with $MgUO_4$ and the other with $CrUO_4$, based on indexing their laboratory powder X-ray diffraction patterns without refining the structures. $ZnUO_4$, also prepared using high pressure-high temperature methods by Hoekstra *et al.*[134], was reported to be isostructural to $CrUO_4$. Hoekstra *et al.* could not discern which of the $NiUO_4$ polymorphs formed at the higher pressure and no further investigations of these have been reported, prompting some authors to question their existence[128].

1.5 Monoclinic $CuUO_4$ Monouranate

Brisi[135] reported the synthesis of $CuUO_4$ in 1963 and its structure was solved by Siegel and Hoekstra[136] using single crystal X-ray diffraction in 1968. $CuUO_4$ forms a distinctly different structure from the other orthorhombic transition metal monouranates described above[136]. $CuUO_4$ has a monoclinic structure in space group $P2_1/n$, see in Figure 1.8. In this structure the UO_6 polyhedra, containing the uranyl group, corner share forming 2D sheets running along the b axis. That the structure differs from the other transition metal type monouranate structures is due to the presence of the Jahn-Teller active (d^9) Cu^{2+} cation. The Jahn-Teller effect lifts the degeneracy of the e_g orbitals leading to a distortion of the CuO_6 from octahedral to tetragonal (see Figure 1.9), with two of the Cu-O bonds significantly lengthened whereas the other four are shortened. In both the *Ibmm* and *Pbcn* transition metal monouranate structures, the transition metal coordination environments have four long and two short A-O bonds[120,127,128,130,137].

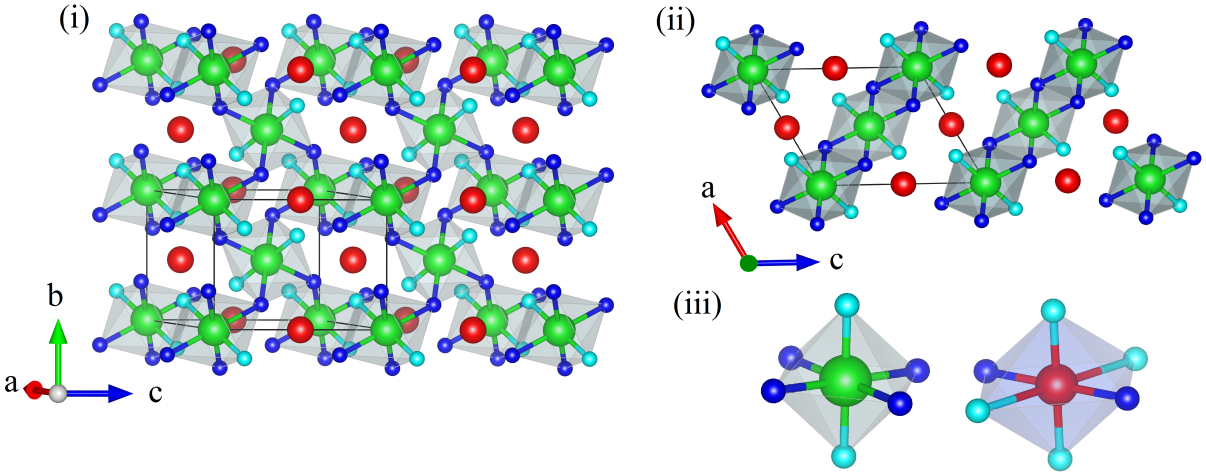

FIGURE 1.8: Structural representations of the monoclinic structure in space group $P2_1/n$ for $CuUO_4$ [136]. The red, green, aqua and blue spheres represent Cu, U, uranyl oxygen and non-uranyl oxygen atoms respectively. The inset (ii) highlights the layered configuration of UO_6 and CuO_6 polyhedra in the [010] direction] and (iii) highlights the distorted UO_6 polyhedra environment and also the apparently Jahn-Teller distorted CuO_6 coordination environment.

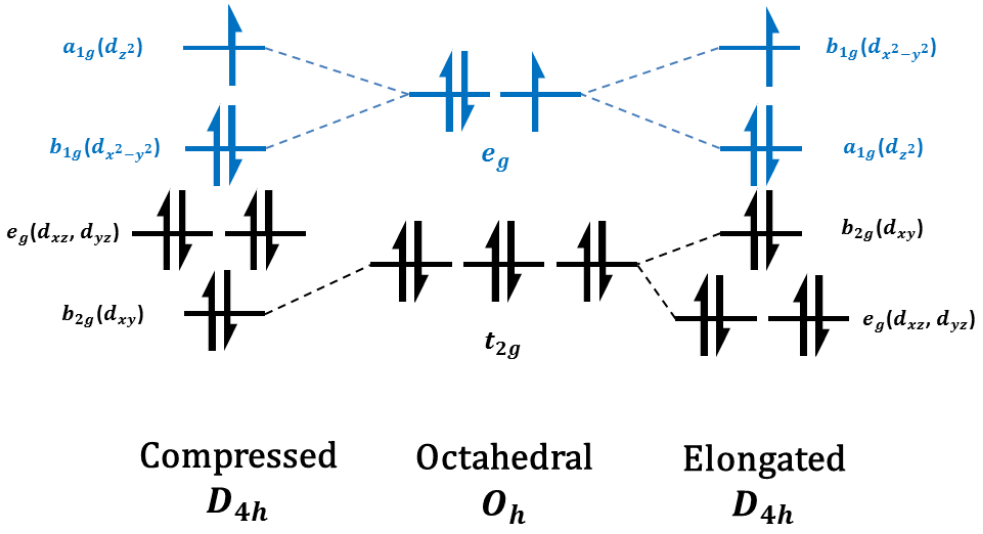

FIGURE 1.9: The prototypical Jahn-Teller distortions experienced by Cu^{2+} in an octahedral coordination environment. For $CuUO_4$, it is crystallographically consistent with a 2L + 4S distortion (adapted from reference [138].

1.6 Anomalous Monouranates

UO_2 forms a cubic fluorite structure where the tetravalent uranium atoms are coordinated by eight oxygen anions[22,23,139,140]. UO_2 can form fluorite structured solid solutions with lanthanide, $U_{1-x}Ln_xO_{2-\delta}$,and actinide cations, $U_{1-x}An_xO_{2\pm\delta}$[141–145]. Here uranium is encountered predominantly in its tetravalent state, with the *Ln* or *An* doping only resulting in a slight deviation from U^{4+}. However there are exceptions, e.g., Popa *et al.*[146] recently showed that when stoichiometric quantities of UO_2 and Bi_2O_3 are mixed and heated under an argon atmosphere they form a fluorite structure in space group $Fm\bar{3}m$ with the composition $Bi_{0.5}U_{0.5}O_2$ or $BiUO_4$, based on Rietveld refinement analysis against their X-ray powder diffraction data. They also determined, using X-ray absorption spectroscopic measurements coupled with Raman spectroscopy, that the uranium cation retains a pentavalent valence state (ionic radius 0.84 Å[147] whilst the bismuth cation is trivalent (ionic radius 1.17 Å[147]). The structure of $BiUO_4$ is presented in Figure 1.10 with the fluorite UO_2 for comparison. Both the uranium and bismuth cations are disordered on the fluorite $4a$ site and have eight fold coordination environments to oxygen. Popa *et al.*[146] described the trivalent Bi as being poorly bonded to oxygen compared to the smaller pentavalent uranium cation. The refined atomic displacement parameter of the oxygen atoms is unusually large indicating considerable disorder, which was supported by Raman spectroscopic measurements. The pentavalent uranium oxidation state in $BiUO_4$ has been supported by magnetic studies by Miyake *et al.*[148,149] who also examined $ScUO_4$ and YUO_4. Based on magnetic measurements, they argued for the presence of pentavalent uranium which is consistent with trivalent Sc^{3+} ($[Ar]d^0$) and Y^{3+} ($[Kr]d^0$). No further studies of these oxides appear to have been conducted.

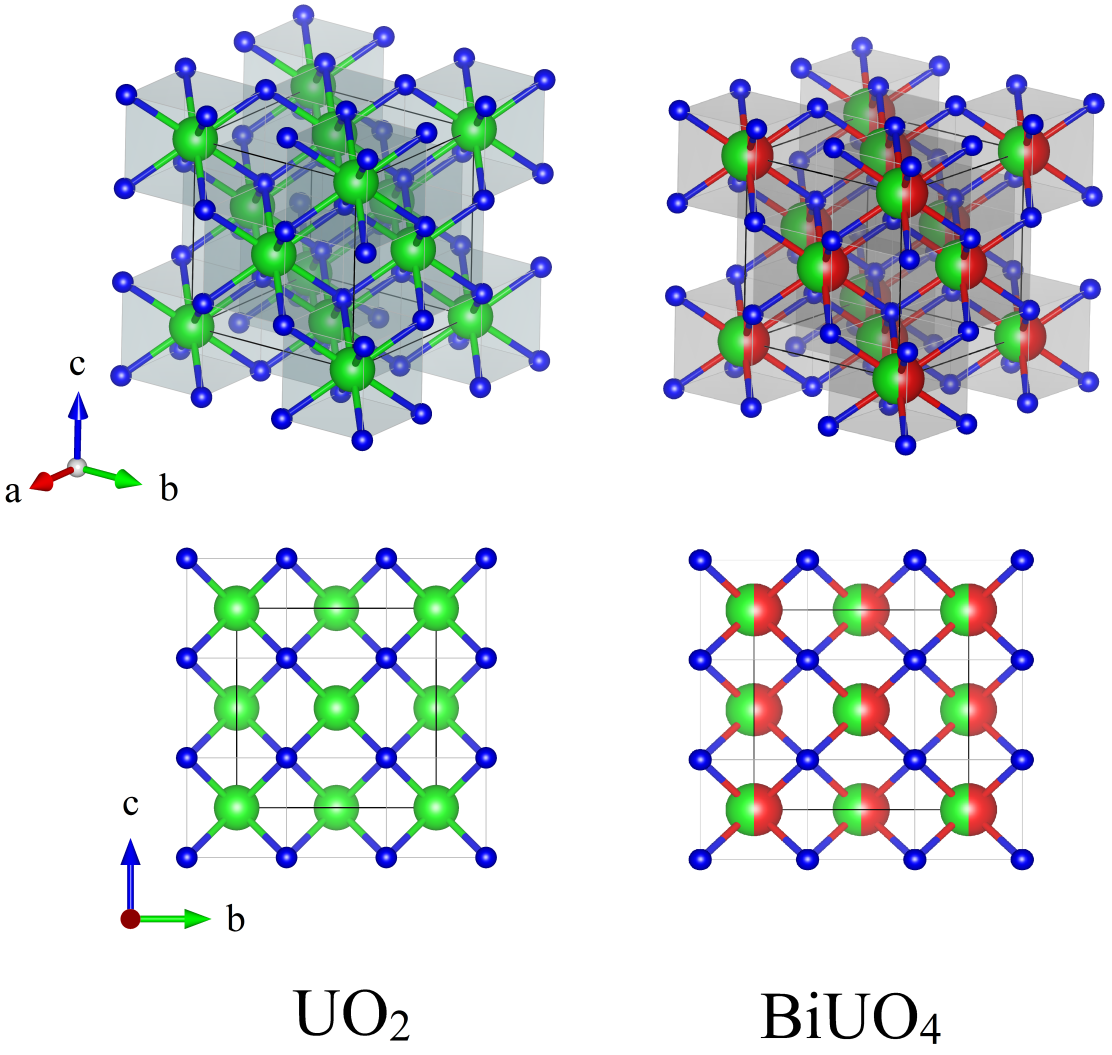

FIGURE 1.10: Structural representations of the cubic fluorite structure in space group $Fm\bar{3}m$: (left) UO_2 [150] and (right) $BiUO_4$ [146]. The red, green and blue spheres represent Bi, U and oxygen atoms respectively.

Vorlanite is a naturally occurring mineral with the formula $CaUO_4$. It has a fluorite structure in space group $Fm\bar{3}m$ and is isostructural with uraninite (UO_2), but contains hexavalent rather than tetravalent uranium [26–28,151,152]. Vorlanite is postulated to be a pseudomorphic replacement of rhombohedral $CaUO_4$ (protovorlanite) in space group $R\bar{3}m$, as a consequence of radiation damage caused by decay of uranium [26]. Although no radiation damage studies have been conducted on rhombohedral $CaUO_4$, this behaviour is consistent with irradiation studies of pyrochlore materials [153–156].

1.7 Recent Progress in Monouranate Solid State Chemistry and Crystallography

Understanding structure-property relationships is salient towards the design and manufacture of novel materials which possess advanced functional properties. As a strategy this has been shown to be highly successful, particularly in the case of energy storage area, utilising for example perovskite, pyrochlore and brownmillerite structured materials[157–164]. In the case of candidate nuclear waste form materials, understanding such relationships is pertinent as it may guide their storage conditions or disposal method. It is apparent from the above discussion of the $A\mathrm{UO}_4$ monouranates that the majority of investigations have focussed on uncovering new compositions and structural types rather than attempting to systematically understand why certain structures form and the consequence for their resulting chemistries. However, recent investigations by Read *et al.*[128], Guo *et al.*[115] and the published work of the BSc(Adv)(Hons) thesis of the author[43] have shed some light on the structure-property relationships of the monouranates and unravelled some of the more remarkable properties that they may exhibit. These investigations will be discussed below.

Read *et al.*[128] examined MnUO_4 and FeUO_4 (and, but not discussed here, $\mathrm{NiU_2O_6}$) produced from flux growth methods and studied using single crystal X-ray diffraction. They compared their structural solutions against existing literature of other monouranates, proposing that the structural preference for each monouranate, e.g *Ibmm* orthorhombic, *Pbcn* orthorhombic, $R\bar{3}m$ rhombohedral, etc. is dictated by the size of the A site cation. The rhombohedral $R\bar{3}m$ structure of CaUO_4 and others, is preferred for the larger A site cations, but as the size is reduced towards Cd (6-coordinate ionic radius = 0.95 Å) Mn (0.83 Å), Co (0.745 Å) and Mg (0.72 Å) the structure reverts to a rutile-like structure in orthorhombic (*Ibmm* or *Cmmm*) space groups. They argued that iron and chromium are too small for such lattices, resulting in the formation of the orthorhombic *Pbcn* structure. They discounted the formation of NiUO_4, suggesting that the Ni^{2+} cation is too small for any of the known monouranate structures. This variation in structure is more dramatic than the changes induced by modulating the size of the A site cation in $AB\mathrm{O}_3$ perovskites[165,166].

Guo *et al.*[115] used a combined experimental and theoretical approach to examine the ability for pentavalent uranium to form within CrUO_4 and FeUO_4, but not in MgUO_4, using X-ray powder diffraction,

X-ray absorption spectroscopy and *ab initio* calculation methods. They argued that the thermodynamic penalty for forming the less stable pentavalent (relative to hexavalent) uranium cation is benign compared to the preferred formation of trivalent chromium and iron. When the enthalpies of formation of these oxides were examined and compared with literature values, both experimental and theoretical, they concluded that $CrUO_4$ and $FeUO_4$ have the least negative enthalpy of formation whereas the alkaline-earth containing monouranates $BaUO_4$ and β-$SrUO_4$ have the most negative values. Based on the data available for AUO_4 monourantes with A = Cr, Fe, Mg, Ca, Sr and Ba, a negative linear relationship was proposed between the thermodynamic stability of AUO_4 and the ionic radius of the A site cation. This trend is consistent with the uranyl group contributing substantially to the structural integrity. That the uranyl moiety is absent in $CrUO_4$ and $FeUO_4$ would likely contribute to their least negative enthalpy of formation. $BaUO_4$ and β-$SrUO_4$, which have the shortest uranyl bond length of the monouranates, are expected to be more stable. However, this does not explicitly explain the ability for some monouranates to retain oxygen vacancies while others do not.

Murphy *et al.*[43] used neutron and synchrotron X-ray powder diffraction in conjunction with X-ray absorption spectroscopy to further understand the structural trends and relationships between $CaUO_4$, α-$SrUO_4$, β-$SrUO_4$ and $BaUO_4$. This investigation suggested that both the relative size of the A site cations and their bonding requirements play a significant role in determining which structural type, rhombohedral or orthorhombic forms and whether they can support oxygen vacancies. In the rhombohedral variants of $CaUO_4$ and α-$SrUO_4$ the A site cation is inherently over bonded from bond valence sums (BVS) calculations, when the materials are stoichiometric (i.e, containing no oxygen vacancies). The formation of oxygen vacancies would reduce the BVS of both cations, leading to the formation of reduced uranium cations. The tendency for oxygen defects to form in these rhombohedral variants has been noted in several previous studies[53,71,72,88]. This over bonding is more pronounced in α-$SrUO_4$where the A site cation has a calculated BVS of 2.55 compared to 2.25 in $CaUO_4$, see Table 1.1 for details. This would imply that α-$SrUO_4$ is more inclined to support oxygen vacancies than CaUO4 under ambient conditions, as experimentally observed[43]. In contrast, no oxygen vacancies were observed in orthorhombic β-$SrUO_4$ and $BaUO_4$[71,100,108], which is consistent with their BVS values of 1.92 and 2.11 for the Sr and Ba cations respectively.

A solid solution of $Sr_{1-x}Ca_xUO_4$ was prepared under oxidising conditions. It was found to be single

phase with an orthorhombic structure for $x = 0$ and 0.1, and single phase with a rhombohedral structure from $x = 0.7$ to 1.0[43]. In the rhombohedral phase region (*i.e.*, Ca-rich end) it was found that the replacement of the smaller Ca^{2+} cation by the larger Sr^{2+} cation reduces the effective overbonding at both the Ca^{2+} and Sr^{2+} sites, stabilising the bonding requirements of the *A* site, see Table 1.2 for details. Conversely, the substitution of 0.1 f.u. of Ca^{2+} cations for Sr^{2+} in the orthorhombic structured β-$SrUO_4$ causes the Sr^{2+} to become over bonded with the BVS increasing from 1.93 to 2.36. Under these conditions, the formation of oxygen vacancies would not be favourable, although it may stabilise the *A* site, it would further compromise the stability of the uranium site. This investigation strongly suggests that the ability of the rhombohedral monouranates to host oxygen vacancies (and potentially for the material to function as an oxygen ion conductor) is a consequence of the balance between reducing the *A* site cations overbonding and the uranium cations ability to accommodate this through reduction. Consistent with previous studies[71,72,88], the oxygen loss and gain phenomena were also apparent in this study[43] of the transformation from the rhombohedral α-$SrUO_4$ to the β orthorhombic polymorph. Using thermogravimetric analysis with variable heating rates it was further shown that the transformation has a considerable kinetic component.

Table 1.1: Bond valence sums (BVS) obtained from neutron and synchrotron X-ray powder diffraction data sets refined jointly using the Rietveld method[43].

Composition	$CaUO_4$	α-$SrUO_4$	β-$SrUO_4$	$BaUO_4$
Space group	$R\bar{3}m$	$R\bar{3}m$	*Pbcm*	*Pbcm*
U site BVS	6.15	6.00	5.81	5.71
A site BVS	2.25	2.55	1.93	2.11
Vol ($Å^3$)	75.9496(16)	80.499(8)	355.984(3)	385.441(14)

Table 1.2: Bond valence sums (BVS) in AUO_4 obtained from analysing the synchrotron X-ray powder diffraction data using the Rietveld method for the series $Sr_{1-x}Ca_xUO_4$ synthesized in air with $x = 1$, 0.9, 0.8, 0.7, 0.1 and 0 (the single phase regions)[43].

Composition	$CaUO_4$	β-$Sr_{0.1}Ca_{0.9}UO_4$	β-$Sr_{0.2}Ca_{0.8}UO_4$	β-$Sr_{0.3}Ca_{0.7}UO_4$	β-$Sr_{0.9}Ca_{0.1}UO_4$	β-$SrUO_4$
Space group	$R\bar{3}m$	$R\bar{3}m$	$R\bar{3}m$	$R\bar{3}m$	*Pbcm*	*Pbcm*
Ca BVS	2.24	2.14	2.09	2.04	1.57	1.15
Sr BVS	3.36	3.21	3.14	3.07	2.36	1.93
Vol ($Å^3$)	75.9496(16)	76.77(2)	77.48(2)	77.97(2)	354.940(6)	355.984(3)

1.8 Overview and Project Objectives

The above discussion hints at the rich chemical and structural complexity of the $A\mathrm{UO}_4$ monouranates, whose history transcends that of the nuclear age. However, the majority of published studies have traditionally applied an approach of *ex situ* structural examination via medium to low resolution measurement, using somewhat serendipitous synthesis methodologies that present little in systematics. This results in little progress regarding the understanding of the solid state chemistry and structural relationships that exist between different $A\mathrm{UO}_4$ oxides. Systematic approaches are pertinent in this aspect as they can enable a near phenomenological understanding of the solid state chemistry and physics of materials and compounds to be obtained. This may guide further advances in general inorganic actinide sciences and further, can potentially be applied to the understanding of other uranium materials, such as naturally occurring systems and those resulting directly from spent nuclear fuel or from reprocessed nuclear waste. The recent studies by Read *et al.*[128], Guo *et al.*[115], and the published work of the present authors BSc(Adv)(Hon) thesis[42] demonstrate this in slowly unravelling some components of the fundamental actinide chemistry that underpins some of the $A\mathrm{UO}_4$ oxides. However a complete systematic understanding of the solid state chemistry of the $A\mathrm{UO}_4$ monouranates remains elusive.

The present dissertation is intended to near create this understanding, through systematic synthesis methods coupled with high resolution measurement and theoretical modelling. The dissertation is organised into thematic chapters which individually examine certain members of the $A\mathrm{UO}_4$ family of oxides, their solid state chemistry and associated properties. Although the focus of this body of work is the solid state chemistry of the $A\mathrm{UO}_4$ family oxides, the results will be discussed with respect to other ternary uranium oxides such as the $A\mathrm{U}_3\mathrm{O}_{10}$ triuranates and other ternary actinide oxides. Their specific literature will be discussed in associated chapters.

The 2^{nd} Chapter will describe the experimental techniques and methodologies used in this dissertation, The 3^{rd} Chapter builds on the previous *ex situ* works of the present author[43] by using *in situ* experimental and theoretical methods to thoroughly examine the irreversible transformation between α-SrUO_4 and β-SrUO_4. Oxygen defects were demonstrated to play a crucial role in this and these are explored further in the 4^{th} and 5^{th} Chapters. It was discovered that the implantation of a critical amount of oxygen defects into the rhombohedral $A\mathrm{UO}_4$ variants in space group $R\bar{3}m$ could allow symmetry lowering phase transformations to occur with heating, resulting in the formation of ordered high temperature superstructures.

The transformations were examined with respect to understanding the interplay between the chemical composition of the A site, the amount of defects that can generate, how this influences superstructure formation and the thermodynamics of this newly discovered type of phase transformation.

The 6^{th} Chapter seeks to initially understand the formation and structural properties of the $NiUO_4$ polymorphs described by Young[133], Hoekstra and Marshall[134] but questioned by Read *et al.*[128]. This chapter extends to structurally and spectroscopically examine at high resolution the orthorhombic *Pbcn*, *Cmmm* and *Imma* space group variants in an attempt to establish a hierarchical system that can be used to examine the structural trends and associated solid state chemistry across the known AUO_4 variants. The 7^{th} closely follows this work by focusing on the structural trends that occur within the rutile related orthorhombic AUO_4 in space group *Imma*, in particular understand the relation of these to similar β-$CdUO_4$ reported in the higher symmetry space group *Cmmm*.

The presence of the uranyl moiety in the AUO_4 oxides adds a pronounced degree of structural anisotropy to what would be otherwise regular $UO_{6\text{-}8}$ polyhedra. The theoretical studies Matar and co-workers[56,92] highlighted that if this anisotropy can be accessed with respect to pressure, bulk moduli could be produced which may rival archetype super and ultrahard materials cubic-BN and diamond.[167,168]. The 8^{th} and final Chapter, explores this by examining α-$SrUO_4$ and β-$SrUO_4$ under pressures towards 6 GPa *in situ* using neutron powder diffraction.

References

1. Taylor, S. R. *Geochimica Et Cosmochimica Acta* **28**, 1273–1285 (1964).

2. Cayrel, R., Hill, V., Beers, T. C., Barbuy, B., Spite, M., Spite, F., Plez, B., Andersen, J., Bonifacio, P., Francois, P., Molaro, P., Nordstrom, B., and Primas, F. *Nature* **409**(6821), 691–692 (2001).

3. McDiarmid, M. A., Keogh, J. P., Hooper, F. J., McPhaul, K., Squibb, K., Kane, R., DiPino, R., Kabat, M., Kaup, B., Anderson, L., Hoover, D., Brown, L., Hamilton, M., Jacobson-Kram, D., Burrows, B., and Walsh, M. *Environmental Research* **82**(2), 168–180 (2000).

4. Bleise, A., Danesi, P. R., and Burkart, W. *Journal of Environmental Radioactivity* **64**(2-3), 93–112 (2003).

5. Arnold, P. L., McMullon, M. W., Rieb, J., and Kuhn, F. E. *Angewandte Chemie-International Edition* **54**(1), 82–100 (2015).

6. Ephritikhine, M. *Dalton Transactions* (21), 2501–2516 (2006).

7. Hitch, C. J. and McKean, R. N. *The economics of defense in the nuclear age*. Harvard University Press, (1960).

8. Knorr, K. E. *On the Uses of Military Power in the Nuclear Age*. Princeton University Press, Princeton, NJ, (2016).

9. Gustafson, J. M. *The nuclear delusion: Soviet-American relations in the atomic age*, volume 39. Educational Foundation for Nuclear Science, Inc, (1983).

10. Hazen, R. M., Ewing, R. C., and Sverjensky, D. A. *American Mineralogist* **94**(10), 1293–1311 (2009).

11. Abram, T. and Ion, S. *Energy Policy* **36**(12), 4323–4330 (2008).

12. Lenzen, M. *Energy Conversion and Management* **49**(8), 2178–2199 (2008).

13. Burns, P. C. *Canadian Mineralogist* **43**, 1839–1894 (2005).

14. Burns, P. C., Miller, M. L., and Ewing, R. C. *Canadian Mineralogist* **34**, 845–880 (1996).

15. Zinkle, S. J. and Was, G. S. *Acta Materialia* **61**(3), 735–758 (2013).

16. Kleykamp, H. *Nuclear Technology* **80**(3), 221–246.

17. Kleykamp, H. *Journal of Nuclear Materials* **131**(2-3), 221–246 (1985).

18. Kashparov, V. A., Oughton, D. H., Zvarich, S. I., Protsak, V. P., and Levchuk, S. E. *Health Physics* **76**(3), 251–259 (1999).

19. Cohen, B. L. *Reviews of Modern Physics* **49**(1), 1–20 (1977).

20. Weber, W. J., Navrotsky, A., Stefanovsky, S., Vance, E. R., and Vernaz, E. *MRS Bulletin* **34**(1), 46–53 (2009).

21. Burns, P. C., Ewing, R. C., and Hawthorne, F. C. *Canadian Mineralogist* **35**, 1551–1570 (1997).

22. Desgranges, L., Baldinozzi, G., Simeone, D., and Fischer, H. E. *Inorganic Chemistry* **55**(15), 7485–7491 (2016).

23. Desgranges, L., Ma, Y., Garcia, P., Baldinozzi, G., Simeone, D., and Fischer, H. E. *Inorganic Chemistry* **56**(1), 321–326 (2017).

24. Banerjee, S. and Kutty, T. R. G. *Nuclear fuels*, 387–466. (2012).

25. Bots, P., Morris, K., Hibberd, R., Law, G. T. W., Mosselmans, J. F. W., Brown, A. P., Doutch, J., Smith, A. J., and Shaw, S. *Langmuir* **30**(48), 14396–14405 (2014).

26. Galuskin, E. V., Armbruster, T., Galuskina, I. O., Lazic, B., Winiarski, A., Gazeev, V. M., Dzierzanowski, P., Zadov, A. E., Pertsev, N. N., Wrzalik, R., Gurbanov, A. G., and Janeczek, J. *American Mineralogist* **96**(1), 188–196 (2011).

27. Galuskin, E. V., Galuskina, I. O., Dubrovinsky, L. S., and Janeczek, J. *American Mineralogist* **97**(5-6), 1002–1004 (2012).

28. Othmane, G., Allard, T., Menguy, N., Morin, G., Esteve, I., Fayek, M., and Calas, G. *American Mineralogist* **98**(2-3), 518–521 (2013).

29. Selbin, J., Holmes, L. H., and McGlynn, S. P. *Journal of Inorganic & Nuclear Chemistry* **25**(11), 1359–1369 (1963).

30. Ballhausen, C. J. and Gray, H. B. *Inorganic Chemistry* **1**(1), 111–122 (1962).

31. Denning, R. G. *Electronic structure and bonding in actinyl ions*, 215–276. Springer Berlin Heidelberg, Berlin, Heidelberg (1992).

32. Denning, R. G. *Journal of Physical Chemistry A* **111**(20), 4125–4143 (2007).

33. Vitova, T., Pidchenko, I., Fellhauer, D., Bagus, P. S., Joly, Y., Pruessmann, T., Bahl, S., Gonzalez-Robles, E., Rothe, J., Altmaier, M., Denecke, M. A., and Geckeis, H. *Nature Communications* **8**, 1–9 (2017).

34. Chermette, H., Rachedi, K., and Volatron, F. *Journal of Molecular Structure-Theochem* **762**(1-3), 109–121 (2006).

35. Gibson, J. K., Haire, R. G., Santos, M., Marcalo, J., and de Matos, A. P. *Journal of Physical Chemistry A* **109**(12), 2768–2781 (2005).

36. Polinski, M. J., Garner III, E. B., Maurice, R., Planas, N., Stritzinger, J. T., Parker, T. G., Cross, J. N., Green, T. D., Alekseev, E. V., Van Cleve, S. M., Depmeier, W., Gagliardi, L., Shatruk, M., Knappenberger, K. L., Liu, G., Skanthakumar, S., Soderholm, L., Dixon, D. A., and Albrecht-Schmitt, T. E. *Nature Chemistry* **6**, 387 (2014).

37. Denning, R. G. *Structure and Bonding* **79**, 215–276 (1992).

38. Krivovichev, S. V., Finch, R. J., and Burns, P. C. *Canadian Mineralogist* **40**, 193–200 (2002).

39. Krot, N. N. and Grigoriev, M. S. *Russian Chemical Reviews* **73**(1), 89–100 (2004).

40. Balboni, E. and Burns, P. C. *Journal of Solid State Chemistry* **213**, 1–8 (2014).

41. Severance, R. C., Smith, M. D., and zur Loye, H. C. *Inorganic Chemistry* **50**(17), 7931–7933 (2011).

42. Forbes, T. Z., Wallace, C., and Burns, P. C. *Canadian Mineralogist* **46**, 1623–1645 (2008).

43. Murphy, G., Kennedy, B. J., Johannessen, B., Kimpton, J. A., Avdeev, M., Griffith, C. S., Thorogood, G. J., and Zhang, Z. M. *Journal of Solid State Chemistry* **237**, 86–92 (2016).

44. Bertaut, E. F., Debergevin, F., Delapalme, A., Roult, G., Forrat, F., and Pauthenet, R. *Journal of Applied Physics* **33**(3), 1123–1126 (1962).

45. Zachariasen, W. H. *Acta Crystallographica* **1**(1-6), 281–285 (1948).

46. Kovba, T. M., Polunina, G. P., Ippolitova, E. A., Simanov, Y. P., and Spitsyn, V. I. *Zhurnal Fizicheskoi Khimii* **35**(4), 719–722 (1961).

47. Cordfunke, E. H. and Loopstra, B. O. *Journal of Inorganic & Nuclear Chemistry* **29**(1), 51–57 (1967).

48. Rudorff, W. and Pfitzer, F. *Zeitschrift Fur Naturforschung Section B-a Journal of Chemical Sciences* **9**(8), 568–569 (1954).

49. Takahashi, K., Fujino, T., and Morss, L. R. *Journal of Solid State Chemistry* **105**(1), 234–246 (1993).

50. Loopstra, B. O. and Rietveld, H. M. *Acta Crystallographica Section B-Structural Crystallography and Crystal Chemistry* **B 25**, 787–791 (1969).

51. Brisi, C. and Appendin.Mm. *Annali Di Chimica* **59**(5), 400–405 (1969).

52. Burns, P. C. *Reviews in Mineralogy ¡D¿* **38**, 23–90 (1999).

53. Liegeosi-Duyckaerts, M. *Spectrochimica Acta Part A-Molecular and Biomolecular Spectroscopy* **33**(6-7), 709–713 (1977).

54. Jakes, D. and Krivy, I. *Journal of Inorganic & Nuclear Chemistry* **36**(12), 3885–3885 (1974).

55. Read, C. M., Bugaris, D. E., and zur Loye, H. C. *Solid State Sciences* **17**, 40–45 (2013).

56. Matar, S. F. and Demazeau, G. *Journal of Solid State Chemistry* **182**(10), 2678–2684 (2009).

57. Allen, G. C., Griffiths, A. J., and Vanderheijden, A. N. *Transition Metal Chemistry* **6**(6), 355–360 (1981).

58. Allen, G. C. and Griffiths, A. J. *Journal of the Chemical Society-Dalton Transactions* **0**(2), 315–319 (1979).

59. Allen, G. C. and Griffiths, A. J. *Journal of the Chemical Society-Dalton Transactions* **6**(12), 1144–1148 (1977).

60. Fujino, T. and Morss, L. R. *Inorganica Chimica Acta* **94**(1-3), 123–123 (1984).

61. Anderson, J. S. and Barraclough, C. G. *Transactions of the Faraday Society* **59**(487), 1572–1576 (1963).

62. Tagawa, H., Fujino, T., and Yamashita, T. *Journal of Inorganic & Nuclear Chemistry* **41**(12), 1729–1735 (1979).

63. Holc, J. and Kolar, D. *Journal of Solid State Chemistry* **47**(1), 98–102 (1983).

64. Krasevec, V., Prodan, A., and Holc, J. In *8th European Congress on Electron Microscopy*, 1075–1076, (1984).

65. Prodan, A. and Boswell, F. W. *Acta Crystallographica Section B-Structural Science* **42**, 141–146 (1986).

66. Pialoux, A. and Touzelin, B. *Comptes Rendus De L Academie Des Sciences Serie Ii Fascicule B-Mecanique Physique Chimie Astronomie* **323**(10), 687–693 (1996).

67. Pialoux, A. and Touzelin, B. *Journal of Nuclear Materials* **255**(1), 14–25 (1998).

68. Goudochnikov, P. and Bell, A. J. *Journal of Physics-Condensed Matter* **19**(17), 176201 (2007).

69. Liu, X. C., Hong, R. Z., and Tian, C. S. *Journal of Materials Science-Materials in Electronics* **20**(4), 323–327 (2009).

70. Bhalla, A. S., Guo, R. Y., and Roy, R. *Materials Research Innovations* **4**(1), 3–26 (2000).

71. Tagawa, H. and Fujino, T. *Journal of Inorganic & Nuclear Chemistry* **40**(12), 2033–2036 (1978).

72. Tagawa, H. and Fujino, T. *Inorganic & Nuclear Chemistry Letters* **13**(10), 489–493 (1977).

73. Bugaris, D. E. and zur Loye, H. C. *Angewandte Chemie-International Edition* **51**(16), 3780–3811 (2012).

74. Hao, Y., Murphy, G. L., Bosbach, D., Modolo, G., Albrecht-Schmitt, T. E., and Alekseev, E. V. *Inorganic Chemistry* **56**(15), 9311–9320 (2017).

75. Hao, Y. C., Klepov, V. V., Murphy, G. L., Modolo, G., Bosbach, D., Albrecht-Schmitt, T. E., Kennedy, B. J., Wang, S., and Alekseev, E. V. *Crystal Growth & Design* **16**(10), 5923–5931 (2016).

76. Wang, S., Alekseev, E. V., Depmeier, W., and Albrecht-Schmitt, T. E. *Inorganic Chemistry* **50**(6), 2079–2081 (2011).

77. Wang, S. A., Alekseev, E. V., Depmeier, W., and Albrecht-Schmitt, T. E. *Inorganic Chemistry* **51**(1), 7–9 (2012).

78. Wang, S. A., Alekseev, E. V., Depmeier, W., and Albrecht-Schmitt, T. E. *Chemical Communications* **46**(22), 3955–3957 (2010).

79. Wang, S. A., Alekseev, E. V., Depmeier, W., and Albrecht-Schmitt, T. E. *Chemical Communications* **47**(39), 10874–10885 (2011).

80. Wang, S. A., Alekseev, E. V., Ling, J., Skanthakumar, S., Soderholm, L., Depmeier, W., and Albrecht-Schmitt, T. E. *Angewandte Chemie-International Edition* **49**(7), 1263–1266 (2010).

81. Wang, S. A., Alekseev, E. V., Stritzinger, J. T., Depmeier, W., and Albrecht-Schmitt, T. E. *Inorganic Chemistry* **49**(6), 2948–2953 (2010).

82. Roof, I. P., Smith, M. D., and zur Loye, H. C. *Journal of Crystal Growth* **312**(8), 1240–1243 (2010).

83. Roof, I. P., Smith, M. D., and zur Loye, H. C. *Journal of Chemical Crystallography* **40**(6), 491–495 (2010).

84. Roof, I. P., Smith, M. D., and zur Loye, H. C. *Solid State Sciences* **12**(12), 1941–1947 (2010).

85. Yeon, J., Smith, M. D., Sefat, A. S., and zur Loye, H. C. *Inorganic Chemistry* **52**(4), 2199–2207 (2013).

86. Fujino, T., Masaki, N., and Tagawa, H. *Zeitschrift Fur Kristallographie* **145**(3-4), 299–309 (1977).

87. Brisi, C., Montorsi, M., and Acquaron.G. *Revue Internationale Des Hautes Temperatures Et Des Refractaires* **8**(1), 37–41 (1971).

88. Pialoux, A. and Touzelin, B. *Canadian Journal of Chemistry* **77**(8), 1384–1393 (1999).

89. Ippolitova, E. A., Kovba, L. M., Simanov, Y. P., and Bereznikova, I. A. *Zhurnal Fizicheskoi Khimii* **35**(3), 145 (1961).

90. Yamashita, T., Fujino, T., Masaki, N., and Tagawa, H. *Journal of Solid State Chemistry* **37**(2), 133–139 (1981).

91. Tagawa, H. and Fujino, T. *Inorganic & Nuclear Chemistry Letters* **16**(2), 91–96 (1980).

92. Matar, S. F. *Chemical Physics Letters* **476**(4-6), 213–217 (2009).

93. Osman, H. H., Pertierra, P., Salvado, M. A., Izquierdo-Ruiz, F., and Recio, J. M. *Physical Chemistry Chemical Physics* **18**(27), 18398–18405 (2016).

94. Samson, S. and Sillen, L. G. *Arkiv for Kemi Mineralogi Och Geologi* **25**(6), 1–16 (1948).

95. Appel, H., Bickel, M., Melchior, S., Kanellakopulos, B., and Keller, C. *Journal of the Less-Common Metals* **162**(2), 323–334 (1990).

96. Bickel, M. and Kanellakopulos, B. *Journal of the Less-Common Metals* **163**(2), L19–L20 (1990).

97. Reis, A. H., Hoekstra, H. R., Gebert, E., and Peterson, S. W. *Journal of Inorganic & Nuclear Chemistry* **38**(8), 1481–1485 (1976).

98. Tanaka, K., Tokushima, K., Kurosaki, K., Ohishi, Y., Muta, H., and Yamanaka, S. *Journal of Nuclear Materials* **443**(1-3), 218–221 (2013).

99. Popa, K., Colineau, E., Wastin, F., and Konings, R. J. M. *Journal of Chemical Thermodynamics* **39**(1), 104–107 (2007).

100. Cordfunke, E. H. P. and Ijdo, D. J. W. *Journal of Physics and Chemistry of Solids* **49**(5), 551–554 (1988).

101. Cordfunke, E. H. P. and Ouweltjes, W. *Journal of Chemical Thermodynamics* **20**(2), 235–238 (1988).

102. Liu, J. H., Van den Berghe, S., and Konstantinovic, M. J. *Journal of Solid State Chemistry* **182**(5), 1105–1108 (2009).

103. Nakamura, A., Doi, Y., and Hinatsu, Y. *Journal of Solid State Chemistry* **184**(3), 531–535 (2011).

104. Nakamura, A. and Kenji, Y. *Physica B-Condensed Matter* **378-80**, 548–549 (2006).

105. Hinatsu, Y. *Journal of Alloys and Compounds* **193**(1-2), 113–115 (1993).

106. Matsuda, T., Yamanaka, S., Kurosaki, K., Uno, M., and Kobayashi, S. *Journal of Alloys and Compounds* **322**(1-2), 77–81 (2001).

107. Yamanaka, S., Kurosaki, K., Matsuda, T., and Uno, M. *Journal of Nuclear Materials* **294**(1-2), 99–103 (2001).

108. Cordfunke, E. H. P., Booij, A. S., SmitGroen, V., vanVlaanderen, P., and Ijdo, D. J. W. *Journal of Solid State Chemistry* **131**(2), 341–349 (1997).

109. Barrett, S. A., Jacobson, A. J., Tofield, B. C., and Fender, B. E. F. *Acta Crystallographica Section B-Structural Science* **38**, 2775–2781 (1982).

110. Frondel, C. and Barnes, I. *Acta Crystallographica* **11**(8), 562–563 (1958).

111. Cremers, T. L., Eller, P. G., Larson, E. M., and Rosenzweig, A. *Acta Crystallographica Section C-Crystal Structure Communications* **42**, 1684–1685 (1986).

112. Popa, K., Benes, O., Staicu, D., Griveau, J. C., Colineau, E., Raison, P. E., Vigier, J. F., Pagliosa, G., Sierig, M., Valu, O. S., Somers, J., and Konings, R. J. M. *Journal of Nuclear Materials* **479**, 189–194 (2016).

113. Konings, R. J. M., Popa, K., Colineau, E., and Wastin, F. *Journal of Chemical Thermodynamics* **40**(2), 220–224 (2008).

114. Zachariasen, W. H. *Acta Crystallographica* **7**(12), 788–791 (1954).

115. Guo, X. F., Tiferet, E., Qi, L., Solomon, J. M., Lanzirotti, A., Newville, M., Engelhard, M. H., Kukkadapu, R. K., Wu, D., Ilton, E. S., Asta, M., Sutton, S. R., Xu, H. W., and Navrotsky, A. *Dalton Transactions* **45**(11), 4622–4632 (2016).

116. Baur, W. H., Joswig, W., Pieper, G., and Kassner, D. *Journal of Solid State Chemistry* **99**(1), 207–211 (1992).

117. Bertaut, E. F., Delapalme, A., Forrat, F., and Pauthenet, R. *Journal De Physique Et Le Radium* **23**(8-9), 477–485 (1962).

118. Miyake, C., Kondo, T., Takamiya, T., and Yoneda, Y. *Journal of Alloys and Compounds* **193**(1-2), 116–118 (1993).

119. Bacmann, M. and Bertaut, E. F. *Journal De Physique* **30**(11-1), 949 (1969).

120. Bacmann, M. and Bertaut, E. F. *Journal De Physique* **27**(11-1), 726–730 (1966).

121. Ghodbane, O., Pascal, J. L., and Favier, F. *Acs Applied Materials & Interfaces* **1**(5), 1130–1139 (2009).

122. Kohler, T., Armbruster, T., and Libowitzky, E. *Journal of Solid State Chemistry* **133**(2), 486–500 (1997).

123. Chabre, Y. and Pannetier, J. *Progress in Solid State Chemistry* **23**(1), 1–130 (1995).

124. Guillot, M. and Pauthene.R. *Journal of Applied Physics* **36**, 1003–1005 (1965).

125. Bacmann, M. and Bertaut, E. F. *Bulletin De La Societe Francaise Mineralogie Et De Cristallographie* **90**(2), 257 (1967).

126. Bacmann, M., Bertaut, E. F., and Blaise, A. *Comptes Rendus Hebdomadaires Des Seances De L Academie Des Sciences Serie B* **266**(2), 45–49 (1968).

127. Bacmann, M., Bertaut, E. F., and Bassi, G. *Bulletin De La Societe Francaise Mineralogie Et De Cristallographie* **88**(2), 214–218 (1965).

128. Read, C. M., Smith, M. D., and zur Loye, H. C. *Solid State Sciences* **37**, 136–143 (2014).

129. Bacmann, M., Bertaut, E. F., Blaise, A., Chevalie.R, and Roult, G. *Journal of Applied Physics* **40**(3), 1131–1134 (1969).

130. Bacmann, M., Chevalie.R, Bertaut, E. F., Roult, G., and Belakhov.M. *Comptes Rendus Hebdomadaires Des Seances De L Academie Des Sciences Serie B* **267**(10), 518–522 (1968).

131. Greenblatt, M., Hornreich, R. M., and Sharon, B. *Journal of Solid State Chemistry* **10**(4), 371–376 (1974).

132. Althammer, M., Meyer, S., Nakayama, H., Schreier, M., Altmannshofer, S., Weiler, M., Huebl, H., Geprgs, S., Opel, M., Gross, R., Meier, D., Klewe, C., Kuschel, T., Schmalhorst, J.-M., Reiss, G., Shen, L., Gupta, A., Chen, Y.-T., Bauer, G. E. W., Saitoh, E., and Goennenwein, S. T. B. *Physical Review B* **87**(22), 224401 (2013).

133. Young, A. P. *Science* **153**(3742), 1380–1381 (1966).

134. Hoekstra, H. R. and Marshall, R. H. *Advances in Chemistry Series* **71**(71), 211–215 (1967).

135. Brisi, C. *Annali Di Chimica* **53**, 325 (1963).

136. Siegel, S. and Hoekstra, H. R. *Acta Crystallographica Section B-Structural Crystallography and Crystal Chemistry* **B 24**, 967–70 (1968).

137. Bacmann, M. and Bertaut, E. F. *Journal De Physique* **30**(11-1), 949–953 (1969).

138. Halcrow, M. A. *Chemical Society Reviews* **42**(4), 1784–1795 (2013).

139. Andersson, D. A., Baldinozzi, G., Desgranges, L., Conradson, D. R., and Conradson, S. D. *Inorganic Chemistry* **52**(5), 2769–2778 (2013).

140. Conradson, S. D., Manara, D., Wastin, F., Clark, D. L., Lander, G. H., Morales, L. A., Rebizant, J., and Rondinella, V. V. *Inorganic Chemistry* **43**(22), 6922–6935 (2004).

141. Hubert, S., Purans, J., Heisbourg, G., Moisy, P., and Dacheux, N. *Inorganic Chemistry* **45**(10), 3887–3894 (2006).

142. Bohler, R., Quaini, A., Capriotti, L., Cakir, P., Benes, O., Boboridis, K., Guiot, A., Luzzi, L., Konings, R. J. M., and Manara, D. *Journal of Alloys and Compounds* **616**, 5–13 (2014).

143. Aronson, S. and Clayton, J. C. *Journal of Chemical Physics* **32**(3), 749–754 (1960).

144. Dash, S., Parida, S. C., Singh, Z., Sen, B. K., and Venugopal, V. *Journal of Nuclear Materials* **393**(2), 267–281 (2009).

145. Anderson, J. S., Edgington, D. N., Roberts, L. E. J., and Wait, E. *Journal of the Chemical Society* , 3324–3331 (1954).

146. Popa, K., Prieur, D., Manara, D., Naji, M., Vigier, J. F., Martin, P. M., Blanco, O. D., Scheinost, A. C., Prussmann, T., Vitova, T., Raison, P. E., Somers, J., and Konings, R. J. M. *Dalton Transactions* **45**(18), 7847–7855 (2016).

147. Shannon, R. *Acta Crystallographica Section A* **32**(5), 751–767 (1976).

148. Miyake, C., Isobe, T., Yoneda, Y., and Imoto, S. *Inorganica Chimica Acta* **140**(1-2), 137–140 (1987).

149. Miyake, C., Kawasaki, O., Gotoh, K., and Nakatani, A. *Journal of Alloys and Compounds* **200**, 187–190 (1993).

150. Desgranges, L., Baldinozzi, G., Rousseau, G., Niepce, J. C., and Calvarin, G. *Inorganic Chemistry* **48**(16), 7585–7592 (2009).

151. Galuskin, E. V., Kusz, J., Armbruster, T., Galuskina, I. O., Marzec, K., Vapnik, Y., and Murashko, M. *American Mineralogist* **98**(11-12), 1938–1942 (2013).

152. Khoury, H. N., Sokol, E. V., and Clark, I. D. *Canadian Mineralogist* **53**(1), 61–82 (2015).

153. Weber, W. J., Ewing, R. C., Catlow, C. R. A., de la Rubia, T. D., Hobbs, L. W., Kinoshita, C., Matzke, H., Motta, A. T., Nastasi, M., Salje, E. K. H., Vance, E. R., and Zinkle, S. J. *Journal of Materials Research* **13**(6), 1434–1484 (1998).

154. Sickafus, K. E., Grimes, R. W., Valdez, J. A., Cleave, A., Tang, M., Ishimaru, M., Corish, S. M., Stanek, C. R., and Uberuaga, B. P. *Nature Materials* **6**(3), 217–223 (2007).

155. Sickafus, K. E., Minervini, L., Grimes, R. W., Valdez, J. A., Ishimaru, M., Li, F., McClellan, K. J., and Hartmann, T. *Science* **289**(5480), 748–751 (2000).

156. Wang, S. X., Wang, L. M., Ewing, R. C., Was, G. S., and Lumpkin, G. R. *Nuclear Instruments & Methods in Physics Research Section B-Beam Interactions with Materials and Atoms* **148**(1-4), 704–709 (1999).

157. Steele, B. C. H. *Materials Science and Engineering B-Solid State Materials for Advanced Technology* **13**(2), 79–87 (1992).

158. Steele, B. C. H. and Heinzel, A. *Nature* **414**(6861), 345–352 (2001).

159. Motohashi, T., Hirano, Y., Masubuchi, Y., Oshima, K., Setoyama, T., and Kikkawa, S. *Chemistry of Materials* **25**(3), 372–377 (2013).

160. Burschka, J., Pellet, N., Moon, S. J., Humphry-Baker, R., Gao, P., Nazeeruddin, M. K., and Gratzel, M. *Nature* **499**(7458), 316–318 (2013).

161. Kreuer, K. D., Paddison, S. J., Spohr, E., and Schuster, M. *Chemical Reviews* **104**(10), 4637–4678 (2004).

162. Wu, Z. S., Ren, W. C., Wen, L., Gao, L. B., Zhao, J. P., Chen, Z. P., Zhou, G. M., Li, F., and Cheng, H. M. *Acs Nano* **4**(6), 3187–3194 (2010).

163. Jiang, J., Li, Y. Y., Liu, J. P., Huang, X. T., Yuan, C. Z., and Lou, X. W. *Advanced Materials* **24**(38), 5166–5180 (2012).

164. Liu, C., Li, F., Ma, L. P., and Cheng, H. M. *Advanced Materials* **22**(8), E28–E35 (2010).

165. Ranson, P., Ouillon, R., Pinan-Lucarre, J. P., Pruzan, P., Mishra, S. K., Ranjan, R., and Pandey, D. *Journal of Raman Spectroscopy* **36**(9), 898–911 (2005).

166. King, G. and Woodward, P. M. *Journal of Materials Chemistry* **20**(28), 5785–5796 (2010).

167. Veprek, S. *Journal of Vacuum Science & Technology A* **31**(5), 0508221–05082233 (2013).

168. Veprek, S. *Journal of Nanoscience and Nanotechnology* **11**(1), 14–35 (2011).

Chapter 2

Experimental Techniques and Methodology

2.1 Introduction

This dissertation proposes to answer several scientific questions relating to the fundamental solid state chemistry of the $A\mathrm{UO}_4$ oxides and some other ternary actinide oxides. This involves established but in some instances modified experimental synthesis methodologies followed by in-depth analysis using data collected from high resolution structure and spectroscopic measurements. *Ab initio* techniques in the form of density functional theory were further utilized to develop a theoretical understanding of the physico-chemical phenomena uncovered in this dissertation. This chapter will describe both the theory and application of the synthetic, analytical and computational methodologies used in this thesis. Further chapters will finely detail the specific synthesis and analytical methods used for the material or structural system of interest.

2.2 Synthetic Methods

Solid state methods are generally based on subjecting homogeneously mixed reagents to elevated temperatures near to, but below, their melting points, either as powders or compacted pellets/rods. Unlike solution based synthesis methods, solid state synthesis proceeds without the use of solvents to provide reaction media and relies upon controlled proximity between reactants to allow procession of a reaction. Compacting mixtures into pellets/rods, in addition to intermittent mixing between heating cycles, is often necessary to ensure homogeneity and reaction completion. Solid state methods are restricted, as the use of high temperature environments overwhelmingly drives the reaction towards the thermodynamic rather than a kinetic product. Knowledge of the reactants thermo-structural properties and relation to other isostructural/electric materials, enables some control to be maintained in designing the synthesis condition. Furthermore without the application of a flux or at-least slow and controlled heating steps, the product is predominantly polycrystalline where the crystallites are often on the nanometre length scale. This confines analysis techniques to non-single crystal based methods.

Solid state synthesis was performed using binary uranium oxides in the form $\mathrm{U_3O_8}$, homogenously mixed with alkaline earth or transition metal compounds in oxide or carbonate form. The mixtures were subject to temperatures ranging from 400 to 1450 ^{o}C either as pellets or powders under variable atmospheres including air, argon, nitrogen, oxygen or hydrogen balanced with nitrogen. Sample purity and reaction progress was examined using X-ray powder (XRD) diffraction. If a reaction was found to

be incomplete or not of suitable purity, the sample would be re-mixed and heated under similar or new conditions until the product was satisfactory. The binary uranium oxides were obtained from sintering high purity uranium metal, in which uranium was in a depleted isotopic form with respect to the U-235 content. The uranium was supplied by ANSTO Minerals and synthesis was conducted in their specifically equipped laboratories for handling radioactive materials. Caution must be taken when handling uranium and other actinide materials due to their radioactive and radiotoxic properties. Synthesis experiments, and subsequent analysis of actinide materials, were conducted with sample quantities and exposure kept as low as reasonably possible to minimise radiation exposure.

2.2.1 High-Pressure Synthesis

For a reaction to proceed, it is a requirement that the reactants are placed in suitable proximity to each other, where they can experience adequate atomic mixing coupled with sufficient activation energy to allow bond formation and successful generation of products. This is achieved in solid state synthesis typically through the use of compacted pellets/rods as previously described. However such methods can fail for a variety of reasons, for instance if a sufficient activation energy is not obtained or if there is considerable size mismatch between the ionic radii of reactants. Methods such as co-precipitation or sol-gel can be used to aid this by providing more optimum homogeneity and reducing activation energy barriers, however they do not overcome size mismatch inadequacies between reactants and thus can fail in a similar fashion to that of solid state. High-pressure synthesis is considered an extreme method which may overcome several of these challenges. It is most often used in combination with high temperature to essentially draw reactants into highly compacted reaction state, which can often induce the modulation of atomic orbitals, followed by the delivery of sufficient activation energy through sufficient heat delivery, to allow reactivity, bond and subsequent product formation. The products obtained are often unique to high-pressure, containing peculiar structural distortions unlike those found from solid state and other conventional thermal methods conducted under ambient pressure conditions. As such the products obtained do not generally resemble those that are found in terrestrial nature albeit potentially within deep geological locations and other pressurised environments. Regardless, the method is scientifically desirably, as it allows the chemical-structural limitations of certain elements, under extreme conditions to be observed and examined. This is salient in the context of actinides, as their response to such environments is poorly known and pertinent considering the intentions to immobilise them within geological repositories.

High temperature high pressure (HT/HP) synthesis was performed using either binary uranium oxides in the form U_3O_8 or hydrous uranyl nitrate, $UO_2(NO_3)_2 \cdot 6\,H_2O$ (International Bioanalytical Industries, Inc.), homogenously mixed with alkaline earth or transition metal compounds in oxide or nitrate form. The mixtures were subject to pressures ranging from 2 to 10 GPa and temperatures ranging from 400 to 1450 ^oC. The HT/HP experiments were performed using a Voggenreiter LP 1000-540/50 instrument installed at the Division for Reactor Safety and Nuclear Waste Forms, Institute for Energy and Climate Research (IEK-6), Forschungszentrum Jülich, Germany. Sample purity and reaction progress was examined using X-ray powder diffraction (XRD) and single crystal laboratory X-ray diffraction (SC-XRD). The uranium oxides were obtained from sintering the uranyl nitrate. The uranium in all HT/HP experiments was in a natural isotopic state i.e natural abundance of U-235 with respect to U-238 and U-234. Natural uranium was used in these synthesis experiments due to both availability of material and the licensing conditions at the nuclear laboratories of IEK-6. All appropriate safety precautions and procedures were utilised when handling natural uranium materials.

2.2.2 Flux and Single Crystal Growth Synthesis Methods

As previously described, solid state synthesis methods often lead to the formation of polycrystalline phases where crystallites are often on the nanometre length scale. It can be desirable to obtain a sample with large crystallites, particularly for single crystal diffraction measurements. A plethora of crystal growth methods have been developed with many being utilized on actinide systems, of these, flux growth methods are the most commonly utilized [1] and these will be described.

Flux growth methods use chemical fluxes which are heated above their melting temperatures but below their boiling point where the reactants are submerged in this molten medium. The high temperature promotes reactivity and the partial slow evaporation of the flux increases the concentrations of the reactants, causing the product to agglomerate which promotes crystal growth. The reaction mixture is then very slowly cooled to further assist the crystal growth and to mitigate damage to crystals from otherwise large thermal gradients. At room temperature the crystals are either immediately mechanically separated or a solvent is applied to remove the flux or other impurities. If the flux growth synthesis experiment is well controlled, a single phase product can be readily obtained.

Flux growth synthesis methods were performed using either binary uranium oxides in the form U_3O_8 or hydrous uranyl nitrates, $UO_2(NO_3)_2 \cdot 6\,H_2O$ (international Bioanalytical Industries, Inc.), homogenously mixed with alkaline earth or transition metal compounds in oxide, chloride or nitrate form. The mixtures were subject to elevated temperature in the presence of excess flux. The mixtures were held at high temperature for extended amounts of time before being cooled very slowly to room temperature. The resulting product mixture was either treated with a solvent for purification or directly mechanically manipulated for crystal extraction. Sample purity and reaction progress was examined using XRD and SC-XRD. Details of specific flux synthesis experiments are contained in relevant chapters.

2.3 Scattering Techniques

To correctly describe the structure-property relationships of a crystalline material, precise knowledge of the chemical species present, their electronic states, the structural type and other solid state chemical properties must be obtained. Scattering techniques can be considered the most powerful available regarding these requirements, as they can precisely yield all this information often non-destructively. Although individual scattering techniques are often intended to probe specific chemical or physical properties, by using them in conjunction with other scattering techniques or other analysis methods, a complete chemical and physical description of a material can be obtained. In this dissertation several scattering techniques were used primarily centred upon material-particle or photon interactions. The physical principals behind the scattering techniques used in this dissertation will be discussed in the context of these radiation types in addition to technical information regarding radiation sources. Detailed information regarding the theory discussed in this chapter on scattering interactions can be found in references [2–6].

For the purposes of discussion, the term "photon" will be applied to described neutrons in addition to X-rays. When a photon of a certain initial wavelength, λ_i, interacts with a point like particle, along an initial wavevector, $\vec{k}_i$ at an angle, θ_i, parallel the scattering plane, x, it may become either elastically, inelastically scattered, or completely absorbed. For elastic scattering, the initial energy of the photon, E_i, will be equal to the energy of the photon after the scattering event, E_f, and the scattered photon will be directed away from its intended initial trajectory, $\vec{k}_{i'}$, along a scattered wavevector, $\vec{k}_f$. Under point like elastic conditions, both the wavelength and wavevector of the scattered photon, λ_f, and $\vec{k}_f$ will be equal to λ_i and $\vec{k}_i$ respectively (equation 2.2). The angle relative to the scattering plane of $\vec{k}_f$, θ_f will be

equal to θ_i. The difference between $\vec{k}_{i'}$and $\vec{k}_f$ is defined as the scattering vector, $\vec{Q}$, also known as the momentum transfer vector:

$$\vec{Q} = \vec{k}_f - \vec{k}_{i'} \tag{2.1}$$

since

$$|\vec{k}_f| = \frac{2\pi}{\lambda} \tag{2.2}$$

then for the elastic condition

$$\vec{Q} = \frac{4\pi sin\theta}{\lambda} \tag{2.3}$$

If the photon imparts some, but not all, of its energy, ω, during scattering, such that $E_f < E_i$, the process is inelastic and the scattered photon will have a wavelength $\lambda_f > \lambda_i$ by the de Broglie relation, and is thus red shifted. Furthermore by equation 2.2, $\vec{k}_f < \vec{k}_i$ and thus $\vec{Q}$ will be reduced. If all of the energy of the initial photon was imparted to the particle, the photon is said to have been completely absorbed. Subsequent electronic or nuclear based processes will result in the particle, these will be discussed in more detail in later sections of this dissertation. Experimentally, the total scattering function, $S(\vec{Q}, \omega)$, communicates the information that is obtained from the scattering process.

The description thus far describes that of an ideal scattering process of a perfectly static point like particle. Of course in nature particles are dynamic, several physical factors will contribute to the real scattering of a photon and by extension the measurement derived from the event. Fundamental to correctly interpreting scattering interactions is the concept of coherence. In the context of scattering, coherence can be described as the ability to know the wave properties of the photon in one moment of time and be able to reasonably predict its properties at another. If the scattering process between the photon and the particle previously described is perfectly coherent, the photon at the scattering event will contain the same information as the detected photon and thus $S(\vec{Q}, \omega)$ will perfectly describe the event. However if the scattering process is completely incoherent, the initial scattered photon will contain no information relatable to the detected photon and thus $S(\vec{Q}, \omega)$ cannot describe the event. Real scattering processes are a combination of both coherent and incoherent scattering interactions and therefore the total combined scattering coherence, the sum of the components, is important. It must be emphasized coherent or incoherent interactions can lead to elastic or inelastic interactions such that they are not mutually exclusive

processes. Both can be experimentally controlled, for instance through choice of instrumentation, radiation type and sample chemical/isotopic composition.

2.3.1 Diffraction

When several particles are brought together uniformly into an ideal crystal lattice in which monochromatic photons having a wavelength comparable to the distance between the particles are incident, the photons will be redirected into well-defined regions of space depending upon the scattering particle they encounter and the subsequent angle of incidence. As one photon labelled A follows the wave vector $\vec{k}_{Ai}$ and scatters from a particle labelled X at an angle θ it will be scattered along the wave vector $\vec{k}_{Af}$ producing a scattering vector $\vec{Q}_A$ (Figure 2.1). If another photon labelled B, in phase with A, follows the wave vector $\vec{k}_{Bi}$ and scatters from a particle labelled Y at distance, d, from X at an angle θ, its resulting wave vector, $\vec{k}_{Bf}$ with scattering vector $\vec{Q}_B$ will be out of phase with $\vec{k}_{Af}$ due to the extra distance traversed, xYz and interference effects will result between the photons. If the phase difference is equal to an integer number of wavelengths, nλ, and $\vec{Q}_A$ equals $\vec{Q}_B$, the interference will be perfectly constructive. If $\vec{Q}_A$ equals $\vec{Q}_B$, but the phase difference is equal to half integer number of wavelengths, $\frac{n\lambda}{2}$, the interference will be perfectly destructive. Constructive interference events follow Braggs law:

$$n\lambda = 2dsin\theta \tag{2.4}$$

This process is known as Bragg diffraction and forms the basis of crystallography which is a fundamental tool of solid state chemistry and materials science. Provided that $\vec{Q}$ for the interfering photons are both perpendicular to the scattering plane, Bragg reflections will be observed experimentally as θ is changed relative to the diffraction surface. The observable intensity of the Bragg reflection, $I(\vec{Q})$, will depend upon the detector and source efficiency, S, Lorentz and polarisation parameters of the photon beam, LP, and what is known as the structure factor, $F(\vec{Q})$:

$$I(\vec{Q}) = SLP|F(\vec{Q})|^2 \tag{2.5}$$

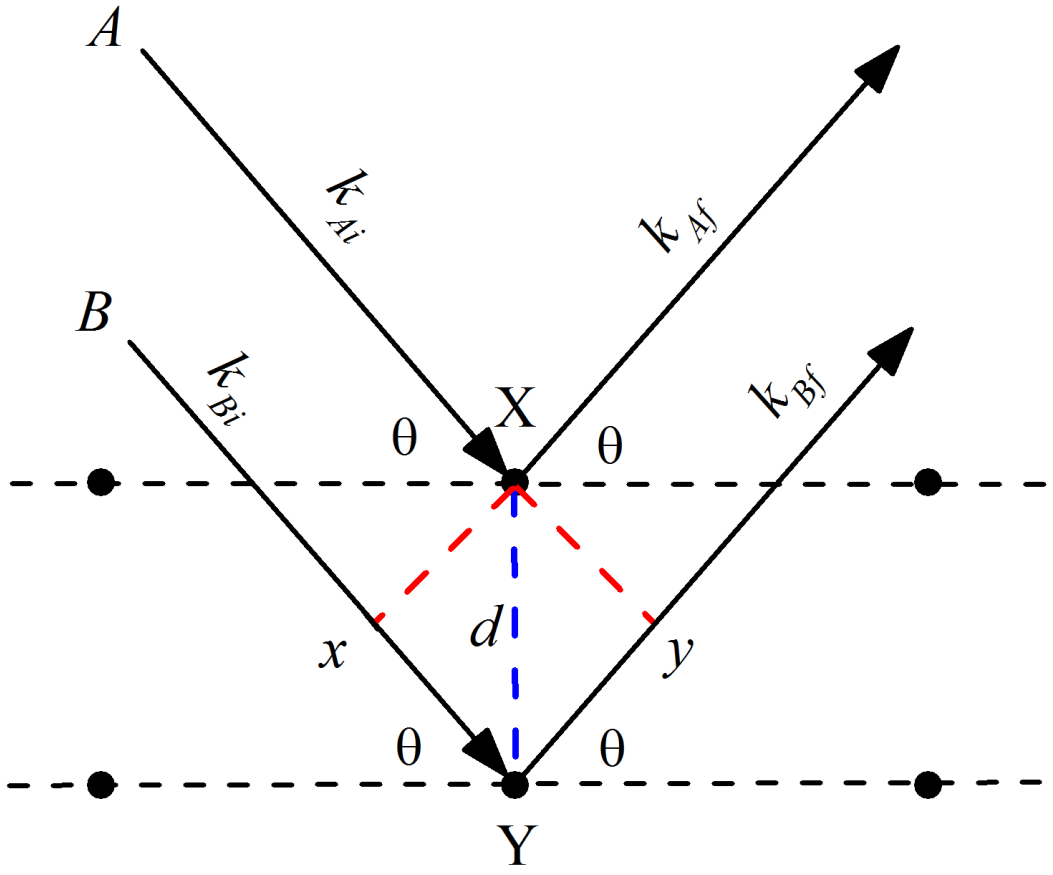

FIGURE 2.1: Incident photons k_{Ai} and k_{Bi} initially in phase are scattered by particles X and Y leading to an extra distance travelled by photon B, the interference of these photons constructively follows the Bragg condition.

$F(\vec{Q})$ essentially describes the atomistic contributions towards $I(\vec{Q})$ from a crystal lattice. It can be defined for X-ray scattering as:

$$F_{x-ray}(\vec{Q}) = F_{x-ray}(Q)e^{i\phi} = \left| f_i(\vec{Q}) \sum_i e^{i\vec{Q}\cdot\vec{r}_i} \right|^2 e^{\frac{-Q^2\langle u^2\rangle}{2}} \tag{2.6}$$

The term, $e^{\frac{-Q^2\langle u^2\rangle}{2}}$, is called the Debye-Waller factor, which measures the thermal displacement of atoms in the lattice and $\langle u^2\rangle$ is the average of the squared displacement of nuclei from their equilibrium lattice sites. ϕ is the phase of the diffracted photon over a scattering surface of radius, $\vec{r}$, assuming spherical distribution. Critical to $F_{x-ray}(\vec{Q})$ is the atomic scattering factor, $f_i(\vec{Q})$, defined as:

$$f_i(\vec{Q}) = \int \rho(\vec{r}) e^{-i\vec{Q}\cdot\vec{r}} d\vec{r} \tag{2.7}$$

$f_i(\vec{Q})$ for X-ray scattering, which quantifies the scattering strength of the particle relative to $\vec{Q}$ and thus determines $I(\vec{Q})$ relative to other particles, is equal to the Fourier transformation of the spatial density of the particle, $\rho(\vec{r})$, relative to the real and anomalous dispersion interactions of the photon. For X-rays, $\rho(\vec{r})$ corresponds to the electron charge density of the particle. When the Fourier transformation is calculated for $f_i(\vec{Q})$, and ultimately $I(\vec{Q})$, its magnitude will be proportional to the number of electrons of the atom or Z (Figure 2.2). However as $\vec{Q}$ from equation 2.3 decreases this causes $f_i(\vec{Q})$ and subsequently $I(\vec{Q})$ to reduce. This is a physical dilemma for X-ray scattering as most Bragg reflections and by extension detailed structural information is found at large θ.

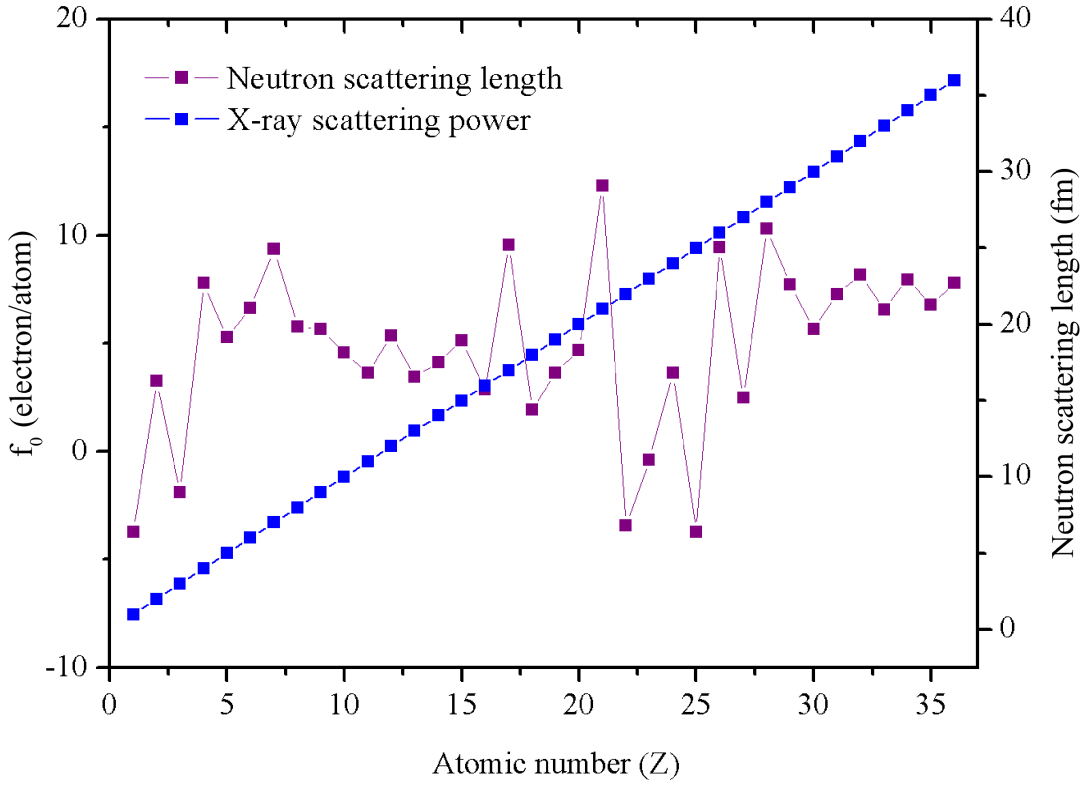

FIGURE 2.2: X-ray and neutron scattering lengths as a function of atomic number (Z).

For Neutron scattering $I(\vec{Q})$ is consistent with equation 2.5, but $F(\vec{Q})$ varies as follows:

$$F_{neutron}(\vec{Q}) = \left| b_{coh}(\vec{Q}) \sum_i e^{i\vec{Q}\cdot\vec{r}_i} \right|^2 e^{\frac{-Q^2\langle u^2\rangle}{2}} \tag{2.8}$$

From equation 2.8, $F_{neutron}(\vec{Q})$ is dependant upon the coherent scattering cross section of the neutron scattering particle, $b_{coh}(\vec{Q})$. A similar expression to equation 2.7 can be formulated for $b_{coh}(\vec{Q})$:

$$b_{coh}(\vec{Q}) \simeq \int \rho(\vec{x}) e^{-i\vec{Q}\cdot\vec{x}} d\vec{x} \tag{2.9}$$

Neutrons contain no charge and largely scatter through nuclear effects mediated via the short-range strong nuclear force of a particles nucleus. Since the strong nuclear force is derived from the presence of protons and neutrons in the nucleus of a particle, different isotopes will give rise to different values of $b_{coh}(\vec{Q})$. Thus when $b_{coh}(\vec{Q})$ is averaged over a specific element, a relatively spasmodic relationship between $I(\vec{Q})$ and Z is observed for neutron scattering (Figure 2.2). A further distinction between neutron and X-ray scattering for incident beams of similar λ, is the considerable size difference between the atoms electron density and its nucleus, the latter can be considered as an infinitesimal point or delta function. Thus when the structure factor is calculated for neutrons (equation 2.8), the exponential term which encapsulates this (and the θ dependency) results in unity, and there is thus no $I(\vec{Q})$ dependency on θ for neutron scattering.

Neutrons contain a nuclear spin and by extension are composite fermions which have magnetic moments. If an atom contains unpaired electrons that are below the Curie or Néel temperatures, these will induce an ordered magnetic moment on the nucleus. When neutrons are incident upon these magnetic moments, scattering events will occur between the incident moments of the neutron and particle, which in turn will interact and cause scattering of the incident neutron. However, unlike nuclear scattering which is isotropic, magnetic scattering is anisotropic due to the dipole nature of the induced magnetic moment. By extension, the strength of the scattering interaction will depend on the relative orientation of both the magnetic moment of the neutron and the atom. Similar to nuclear scattering it is a requirement $\vec{Q}$ be perpendicular to the scattering plane, but a further requirement for magnetic scattering is the atoms magnetisation vector component be parallel and in the same direction to $\vec{Q}$. As such magnetic neutron scattering has a strong angular dependence and is sensitive to the spatial distribution of both the direction and magnitude of the magnetization of a material.

2.3.1.1 Single Crystal Diffraction

When X-rays or neutrons are diffracted from a uniform crystal lattice over an appropriate angular range, several Bragg reflections result and it becomes possible to reconstruct and characterise the lattice through equation 2.5. This is essentially the method of single crystal diffraction. A single crystal can be loosely defined as a material with a continuous and unbroken lattice of repeating unit cells that define the symmetry and structure of the material. The orientation of the scattering planes that form between particles can be described by the Miller index notation, (*hkl*), which can be subsequently determined through their relation to *d*, equation 2.3 and equation 2.4. When the diffraction condition is satisfied, the values of $\vec{Q}$ will form observable points in reciprocal space that together form a reciprocal lattice. The reciprocal lattice and further structure determination from it can be understood from the Ewald Sphere construction. If the single crystal is placed at the centre of a sphere in reciprocal space in which the radii is equal $1/\lambda$, diffraction occurs when the sphere intersects a value for $\vec{Q}$. Since each value of $\vec{Q}$ will correspond to diffraction events from a specific scattering plane, defined by *hkl*, that plane, and all others that intersect the sphere can be determined in real space through the Laue equations:

$$\vec{a} \cdot \vec{Q} = h\lambda \tag{2.10}$$

$$\vec{b} \cdot \vec{Q} = k\lambda \tag{2.11}$$

$$\vec{c} \cdot \vec{Q} = l\lambda \tag{2.12}$$

By reorientating, the crystal and by extension the Ewald sphere, other scattering planes will intersect with the sphere and allow the crystal structure to be determined.

For single crystal diffraction to be correctly implemented it is a requirement firstly that an appropriately sized crystal which is free of twinning is selected (or at least has minimal twinning). For laboratory single crystal X-ray diffraction this is often achieved using single crystals with volumes as small as 0.001 mm^3. For single crystal neutron diffraction, owing to the much poorer interaction of neutrons with the sample and the often weaker source, it is a requirement that crystals are generally larger than 0.1 mm^3. This places strong emphasis on optimized synthesis and single crystal growth techniques. Furthermore, measurement

acquisition times are often prolonged, as the crystal needs to be continually re-orientated such that $\vec{Q}$ is perpendicular to the scattering plane for the diffraction condition to be satisfied.

Single crystal diffraction was undertaken in this thesis using laboratory single crystal X-ray diffraction (SC-XRD) and synchrotron single crystal X-ray diffraction (SSC-XRD). SC-XRD measurements were undertaken using an Agilent Technologies SuperNova diffractometer with Mo-Kα radiation ($\lambda = 0.71073$ Å) at room temperature. All measurements were corrected for Lorentz and polarization factors as well as absorption by the multi-scan method. SSC-XRD data were collected at 100(2) K on the MX2 beamline[7] at the Australian Synchrotron with Si double-crystal monochromator ($\lambda = 0.71085$ Å). All data were collected using BlueIce software[8]. Cell refinements and data reductions were undertaken using XDS software[9]. An empirical absorption correction was applied to the data using SADABS[10]. The structures were solved by direct methods using SHELXT[11], and the full-matrix least-squares refinements were carried out using SHELXL[12] via the Olex2 interface[13]. The one circle goniometer geometry of data collections at the MX2 beamline offers less opportunity for applying multi-scan absorption correction as is possible with the data collections on a four circle goniometer. Consequently, ripples around U atoms are often present due to ineffective absorption correction. In addition, the data completeness is relatively low for crystals in low symmetry space groups.

2.3.1.2 Powder Diffraction

For the reasons previously outlined it is not always practical to study diffraction quality single crystals. Powder diffraction can be seen as a faster and more easily applied method to obtaining structural characterisation of a compound or material. If a single crystal is broken down into a polycrystalline powder, when an X-ray or neutron beam is incident upon it, diffraction events will occur. Due to the random distribution of crystallites at any incident angle, θ, some crystallites will be correctly orientated such the $\vec{Q}$ is perpendicular to the scattering plane. This random but averaging process will cause the previously observed discrete points in reciprocal space from single crystal diffraction to average into concentric spheres, each of which corresponds to particular orientations of the scattering planes. In terms of the Ewald sphere construction, these spheres will overlap causing the diffracted photons to form a projection cone which is described by a specific *hkl* value. Thus it remains possible to determine the average lattice structure of a material similar to the method used to determine the structure of a single crystal.

Powder diffraction measurements were undertaken in this thesis using three methods. Laboratory X-ray powder diffraction (XRD) measurements were recorded using either a Bruker D8 advance diffractometer or a Bruker-AXS D4 Endeavour diffractometer. Both diffractometers used 40kV/40mA using Cu-Kα radiation source with a nickel filter and a linear silicon strip LynxEye Detector at room temperature.

Synchrotron X-ray diffraction (S-XRD) measurements were collected using the powder diffractometer at the beamline BL-10 of the Australian Synchrotron, Melbourne, Australia. Ground samples were contained in either 0.2 or 0.8 mm diameter glass or quartz capillaries that were rotated during the measurements. 0.8 mm capillaries were used for *in situ* gas flow experiments where the sample was diluted with quartz glass at a 50:50 ratio by weight to allow optimum gas flow-through. Variable temperature S-XRD measurements were achieved using an FMB-Oxford hot air blower. Measurements were collected from room temperature up to 1273 K. The wavelength was calibrated using a NIST standard LaB_6 crystal of which the precise value is given in subsequent chapters for specific experiments.

Neutron powder diffraction (NPD) measurements were undertaken using the Echidna high resolution diffractometer[14] and the Wombat high intensity diffractometer[15] at the ANSTO's OPAL nuclear reactor facility at Lucas Heights, Australia. The wavelength was controlled using a Ge(115) crystal monochromator with intended values of 1.622 and/or 2.439 Å, precise values are given in specific chapters. For these measurements each sample was contained in a cylindrical vanadium can which was mounted in a closed cycle refrigerator. Variable temperature NPD measurements were undertaken with the Echidna diffractometer using a ILL-type high vacuum furnace employing niobium elements and operating at greater than 6^{-10} torr. Measurements were taken from temperature down to 1.5 K for the cryostat and up to 1273 K for the high vacuum furnace where the wavelength was controlled using a double crystal monochromator. Detailed discussion on synchrotron and neutron radiation sources will follow in the coming sections of this chapter.

2.3.1.3 Diffraction Modelling and Refinement Methods

Despite the power in structure determination from both single crystal and powder diffraction, they are ultimately limited and cannot perfectly completely describe a lattice from measurement alone. This is in part due to what is known as the phase problem. Calculation of equation 2.8 involves taking the square modulus of complex quantities associated with the phase of the incident photon. Naturally this cannot be directly achieved, resulting in a considerable amount of scattering information related to the crystal

lattice being lost. The diffraction points, or cones, observed in reciprocal space are measures of the photon beams intensity and by the extension the amplitude. However, their distributions are still a result of the phase contributions such that it is possible to solve the phase problem indirectly and thus solve the crystal structure. Several structure modelling methods have been developed which attempt to overcome the phase problem for both single crystal and powder diffraction.

For single crystal diffraction measurements, the phase problem can be treated through such practises as direct methods, dual space methods, molecular replacement or the use of Patterson mapping. In this dissertation, a combination of Direct methods and Patterson mapping were used and these will be discussed. Direct methods use the reciprocal space measurements of $F(\vec{Q})$. By itself, $F(\vec{Q})$ measures the magnitude of the equation 2.6 and 2.8 and thus only reveals $f_i(\vec{Q})$, with the phase information absent. However the presence of atoms modulates both the phase and by extension the calculated magnitude of $F(\vec{Q})$. This allows a well-defined, rather than random relationship between the magnitude of $F(\vec{Q})$ and the photon phases to occur. Direct methods computationally exploit this to solve the phase problem. It is often advantageous if the square of $F(\vec{Q})$ is taken, as weak resolved Bragg reflections become resolvable, twinned structures become mathematically simpler to solve and Patterson Mapping becomes possible. Patterson Mapping, after Arthur Lindo Patterson, maps $F(\vec{Q})^2$ across reciprocal space, where observable peaks in this map correspond to vector distances between atoms. From the spatial distributions of these vectors, the real positions of atoms can be deduced. With this information, in addition to the determination of $f_i(\vec{Q})$, a model is constructed and refined against $F(\vec{Q})^2$, using a least-squares minimisation method. The refinement methods aim is to reduce the difference, M, between all measured values of $F(\vec{Q})^2$ and a calculated structure factor, $F(\vec{Q})^2_{calc}$, where a weighting factor is used, w, equal to $1/\sigma$, where σ equals the measurement uncertainty:

$$M = \sum w \left(F(\vec{Q})^2 - F(\vec{Q})^2_{calc} \right)^2 \tag{2.13}$$

Direct methods rely on a sufficiently large amount of independent resolvable Bragg reflections to be observed with minimal overlap. This is often achievable for single crystal diffraction in small to medium sized unit cells, $\sim$ 800 Å. However is it extremely difficult to apply for powder diffraction due to the smaller number of resolvable Bragg reflections. Effects such as reduced resolution at high 2θ for powder diffraction with X-rays coupled with signal to noise issues further compound this problem. Consequently

powder diffraction is generally not applied as a direct structure solution method. However if a suitable starting model is available, or a reasonable understanding of a materials solid state chemistry and associated crystallographic properties are known, precise structure determination can be obtained through refinement methods. Of the refinement methods available in powder diffraction, the Rietveld method is considered the most powerful and was implemented in this thesis through the programs GSAS [16,17], GSAS-II [18], Fullprof [19] and Topas [20,21]. The method is a whole pattern fitting technique that refines a model against $F(\vec{Q})$ in real space, i.e $I(\vec{Q})$ for both neutron and X-ray sources. The strength in the method relies on its ability to resolve overlapping weak Bragg reflections and extract scattering information which would otherwise be unobtainable in most other powder diffraction analysis methods. This achieved through calculating across every measured data point enabling independent intensity integration. This allows both the *hkl* values to be precisely obtained as well as atomic parameters to be deduced. The Rietveld method uses a least squared minimisation method as implemented in single crystal direct methods from equation 2.13. The experimental parameters associated with $I(\vec{Q})$, L, S and P are also refinable. The difference between the model and experimental measurement can be further quantified from a variety of R-factors, details of their calculation can be found in Appendix A.

2.4 X-ray Absorption Spectroscopy

As mentioned previously, an inelastic interaction between a photon and a particle will result, typically, in the transfer of energy from the photon to the particle. In the case of X-ray scattering, if the X-ray photon is incident upon an atom where the photon energy, E_{Photon} is greater than the energy of a core electron, $\mathrm{E}_{CoreElectron}$, X-ray absorption will occur. This is the fundamental process behind X-ray absorption spectroscopy (XAS) and is in principal described by the photoelectric effect (equation 2.14).

$$E_{Kinetic} = E_{Photon} - E_{CoreElectron} \tag{2.14}$$

As the X-ray photon interacts with the material with thickness, t, the change in intensity from its initial value, I_0, to its attenuated value, I, can be described by the Beer-Lambert Law, where μ is the X-ray absorption coefficient.

$$I = I_0 e^{-\mu t} \tag{2.15}$$

As the X-ray traverses the material, absorption mechanisms, assuming sufficient energy, will induce the excitation of a core electron causing it to leave its orbital leaving behind a core hole. Any excess energy from the incident X-ray photon will be transferred to the excited electron. The core electron hole can be filled either through an outer core electron descending orbitals and filling the hole with associated X-ray fluorescence or through the emission of an Auger electron. As the Auger electron leaves its orbital and is ejected it will induce an inner core electron to descend to fill the initial core hole and provide energy for the leaving Auger electron. These processes are illustrated in Figure 2.3. XAS measurements can use the X-ray fluorescence or Auger electron emissions to study the absorption interaction, but more often, as was used in this dissertation, the change in intensities of the initial X-ray photon beam, as it interacts with a material near a specific absorption "edge", is measured.

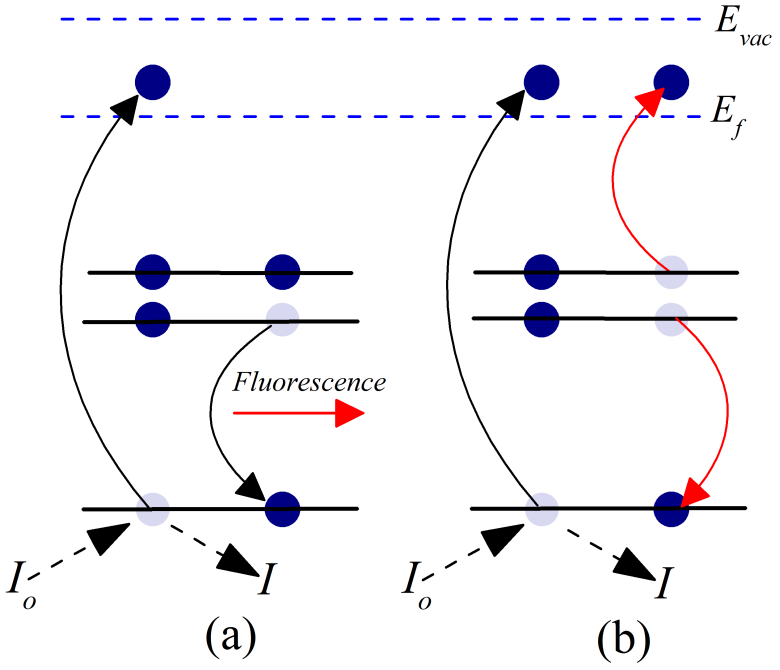

FIGURE 2.3: Schematic representations of physical processes contributing to X-ray absorption spectroscopy (XAS): photoabsorption of an X-ray creating a core hole followed by filling of the core hole by an electron in another level accompanied by (a) fluorescence or (b) emission of an Auger electron.

The uranium L_3-edge spectrum corresponds to the dipole transition of an electron from the $2p_{3/2}$ orbital to empty $6d$ states in the conduction band. Sufficient energy is required to cause this excitation,

without which, excitation cannot occur. With reference to Figure 2.4 this pre-excitation region is present in section (a), known as the pre-edge region. As the energy of X-ray beam is increased, it will be sufficient to overcome the binding energy of the electron allowing it to be excited into the 6*d* states. The absorption edge position depends on both the geometry and the valence state of the target atom. This makes XAS sensitive to oxidation state and allows it to be determined. For instance, an atom that is in a higher oxidation state compared to the same atom in a lower oxidation, will require more photon energy to cause the excitation due to electrostatic forces acting against this further increase in charge from excitation. Consequently when comparing their spectra, the XAS edge will be at higher energy for the higher oxidation state atom than the lower.

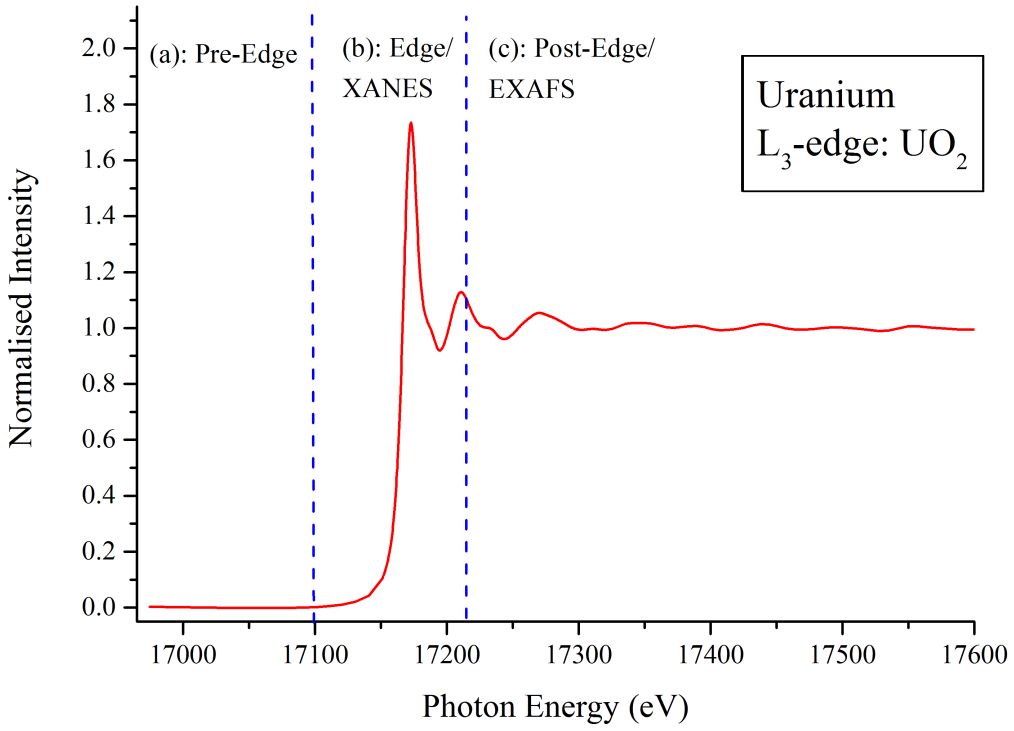

FIGURE 2.4: Uranium L_3 edge X-ray absorption spectrum for UO_2. The sections correspond to the (a) pre-edge, (b) XANES, and (c) EXAFS regions of the spectrum.

As excitation occurs, the photoelectron will be scattered by the atoms in the immediate coordination environment of the absorption atom. This will involve a transfer of energy from the photoelectron which will be reflected in the edge position and the line shape of the immediate XAS spectral edge (Figure 2.4 section (b)). This allows the oxidation state and coordination environment to be deduced. Analysing this region

near the absorption edge is a technique known as X-ray absorption near edge structure (XANES) analysis. The post edge region (c) corresponds to EXAFS oscillations resulting from the interferences between the outgoing photoelectron waves and the back scattered photoelectron waves from the neighbouring atoms. EXAFS analysis provides structural information such as bond distances, coordination number and the type of neighbouring atoms.

An essential component of an XAS measurement is having an X-ray source where the X-ray energy can be tuned and controlled across a continuous range of energies. For this a monochromator is most often used. X-ray tubes in laboratory machines use specific energies which do not offer the ability for this tuning process to occur. However synchrotron X-ray sources offer a wide variety of accessible X-ray energies at far greater flux. In this dissertation, XANES spectra were collected on a number of compounds whereas the EXAFS analysis was not undertaken although part of the data were collected in that region to enable XANES spectra normalisation. XANES spectra were collected at the U L_3 or L_2 edge using the X-ray absorption spectroscopy[22] and X-ray fluorescence microscopy[23] (XFM) beamlines at the Australian Synchrotron. A variety of experimental apparatus were employed to collect XANES spectra under different conditions and sample circumstances, these will be discussed in detail in associated chapters.

2.5 Synchrotron Photon Sources

In a standard X-ray tube, X-ray emission relies upon a cathode bombarding electrons at an anode target, such as copper, causing the removal of a core electron. As an outer core falls to fill this vacant hole, it releases a photon in the form of a characteristic X-ray. For instance, in the case of Cu X-rays, this uses the K edge transition where the $K_{\alpha 1}$ ($2p_{3/2} \rightarrow 1s$) is desired, where all other generated X-rays are near removed using filters. In conventional synchrotron light sources, electrons are accelerated to near the speed of light using a linear accelerator (linac) and a circular ring called a booster ring containing a large number of electromagnets. Once at sufficient velocity, the electrons are channelled into a secondary ring, called a storage ring. Here they become subject to either bending magnets or insertion devices for instance undulators or wigglers. Simplistically, these devices consist of magnets which alter the trajectory of the electron beam causing a dramatic change to their angular momentum. This change results in the spontaneous emission of light radiation which can vary in wavelength from infrared to Gamma ray depending upon the exact change to the angular momentum. Comparatively using characteristic X-ray

emission like in an X-ray tube, restricts the number of accessible wavelengths , which as an example restricts XAS measurements being performed (although XAS can potentially be obtained from the weaker Bremsstrahlung, but is predominantly inferior to synchrotron radiation). Further the intensity of photon emission, and more importantly, brilliance, from X-ray tubes is far less than that from a synchrotron. With respect to light sources brilliance can be defined as the number of photons at a particular wavelength falling upon a certain region of space over a certain period of time. This is opposed to intensity which is essentially the amount of power transferred per unit area. In essence brilliance is a measure of the ability to observe microscopic objects and events. Brilliance is a more important concept to consider in the context of this dissertation, since measuring an atomic scale event using light, a sufficient amount of coherent and focused photons are needed to scatter off a very small region of microscopic space. For this, angular divergence and band width need to be taken into account, which brilliance does and intensity does not.

The distinctive feature of synchrotron light, which enables such significantly greater brilliances over laboratory X-ray sources, is due to the ultra-relativistic velocity of the electron beam. As opposed to an electron at rest emitting light isotropically, light being emitted by an electron in motion will experience a bunching of wave pulses in the direction of movement, a minor blue-shift like effect. In the ultra-relativistic regime this will be considerably more pronounced as the light pulses bunch together leading to strong blue-shifted photons arising from the beam which in turn will experience high directionality based on its trajectory forming a very narrow cone. Therefore, instead of isotropic light beam emerging from the electron orbit in the synchrotron ring, a beam of light will emerge predominantly and at greatest brilliance parallel to the instantaneous trajectory of the beam. The orbit of the electron beam around the synchrotron ring continuously emitting light can be thought of as similar to a lighthouse. Synchrotrons are thus designed to capture this highly brilliant light by the construction of straight sections in the storage ring which capture and direct this light towards a point of measurement interest. By this bunching effect, synchrotron light is exceedingly more brilliant and intense than a standard laboratory X-ray source. In this thesis the Australian Synchrotron was used extensively. The Australian Synchrotron is a 3 GeV 3^{rd} generation synchrotron located in Clayton, Victoria, Australia (see Figure 2.5).

FIGURE 2.5: The Australian Synchrotron, ANSTO (https://www.synchrotron.org.au/research/facilities/australian-synchrotron/overview).

2.6 Neutron Sources

Typically there are two main methods of generating neutrons of a quantity and quality for use in neutron scattering experiments. The first is through utilisation of a nuclear reactor. Here heavy nuclei such as U-235 or Pu-239 are bombarded leading to their fission and subsequent neutron generation. The second is through a spallation source. A spallation source uses a heavy metal target, such as mercury, which is bombarded with protons. The collisional event causes the spontaneous discharge of neutrons. In nuclear reactors, the generation of neutrons is generally a continuous process. However in a spallation source the initial protons are imparted in pulses, meaning the subsequent neutron production is also pulsed. This means, with careful control, dynamical information can be extracted from a sample since the time structure of the beam can be determined. In this thesis a nuclear reactor source was solely used for neutron scattering experiments in the form of ANSTO's Open Pool Light Water (OPAL) nuclear reactor located in Sydney, New South Wales, Australia (see figure 2.6). OPAL uses low level enriched uranium in the chemical form U_2Si_3 as the neutron source operating at 20 MW. Upon initial fission the neutrons are classed as fast neutrons. Fast neutrons have energies too large, and by extension, wavelengths too small for neutron scattering purposes. The neutrons are thus moderated by a material which has a comparable mass to that of a neutron, in the case of the OPAL nuclear reactor, hydrogen, as water serves as the moderator. The collisions of the neutrons with the hydrogen atoms leads to reduction of their energies to what is known as the thermal energy range. Thermal neutrons have wavelengths on the angstrom scale and thus are suitable

for neutron scattering for materials on the atomic scale. The OPAL facility does possess the ability to further reduce the neutrons energies to what is known as the cold spectrum, where their wavelengths are suitable for neutron scattering in the macromolecular scale. After the neutron spectrum is chosen, the neutrons are subjected to a series of monochromators to select a specific wavelength of interest and filter out all else. Care must be taken when conducting neutron scattering experiments on actinides, isotopes such as Th-232, are fertile with thermal neutrons, such that they can undergo absorption of the thermal neutron, activate and rapidly undergo a series of radioactive decays resulting in a fissile material generating in the form of U-233. This was taken into account when conducting associated neutron scattering experiments on thorium or other fertile materials where appropriate risk assessments were undertaken with the support of ANSTO criticality officers.

FIGURE 2.6: The Open Pool Australian Light Water Reactor (OPAL), ANSTO (`https://www.ansto.gov.au/research/facilities/opal-multi-purpose-reactor`).

2.7 Electron Microscopy

Electron microscopy is a technique that is able to extend the resolution limitations of optical microscopy allowing the micro to nanolength scale to be observed using electron scattering. Several techniques and derivatives of electron microscopy have been developed, but in this dissertation scanning electron microscopy (SEM) was used and only this will be discussed here. SEM uses electrons obtained from a LaB_6 single crystal which are conveyed to a sample through a series of optics and apertures to create a relatively coherent beam. As the electron beam bombards a sample, two predominant scattering processes occur,

first is the back scattering of electrons (BSE) from the sample. This process is essentially ballistic, where the electron collides with an atomic nuclei and is scattered backwards towards the initial electron source where a detector is placed for measurement. Since electrons interact with atoms via their surrounding electron cloud, the collisional interaction will depend on the number of electrons present in the cloud of the nuclei and, by extension, the composition of the atom. This enables morphological features of a sample to be discerned based on element composition. BSE interactions are largely an elastic scattering process, but when high energy electrons collide with atoms they can impart their energy on them, causing the displacement of a core electron from that atom. This displaced electron, known as a secondary electron (SE), can be guided to a detector using a potential difference. Whereas BSE interactions are essentially a surface scattering process, SE can be generated beneath the upper layers of a sample. The generated SEs need to travel towards edges and corners of the sample before they can escape it. This enables enhanced resolution over BSE scattering for morphological and topological features of a sample towards the nano-length scale.

Since a SE electron is leaving a core hole position of an atom, an outer shell electron will descend and fill this vacancy. This will result in the emission of a characteristic X-ray corresponding to this change in energy, somewhat similar to the described XAS process. Measuring these X-rays is known as Energy-dispersive X-ray spectroscopy (EDS) and allows the chemical composition of a sample to be determined. Although BSE scattering can provide compositional information, EDS is superior since it can more readily determine the difference between atoms that have a similar number of electrons through their characteristic X-ray emissions.

Sample preparation involved spreading a small amount of power sample or carefully placed single crystals on carbon tape. The samples were coated with thin amount of carbon using a sputtering technique. This is to prevent charge effects occurring on the sample as measurements are undertaken which can interfere with analyses. SEM/EDS measurements were undertaken using a FEI Quanta 200F Environment Scanning Electron Microscope with low vacuum node at 0.6 mbar.

2.8 Thermal Analysis

Thermogravimetric analysis (TGA) is a method of monitoring changes to the mass of a material in response to thermal changes of temperature or time. This method is often combined with either differential scanning calorimetry (DSC) or differential thermal analysis (DTA). DSC monitors the amount of heat required to raise the temperature of a sample relative to a reference material. When a significant thermal event occurs, such as mass loss or a structural change, it will affect the required heat needed to change the temperature relative to the reference which, can be detected and quantifiably measured. This gives insight into the thermodynamics of a material, for instance if such changes are endothermic or exothermic in origin and further can be extended to extract properties like heat capacity. DTA is similar to DSC, but it is the heat flow that is held constant to both the sample and the reference instead of the temperature, which is measured. When the sample is heated and a thermal event occurs within the sample, this will change the temperature of the sample relative to the reference which is quantified. TGA and DTA measurements in this thesis were obtained using an SDT Q600 TGA/DTA.

2.9 *Ab Initio* Calculations

2.9.1 Overview of Density Functional Theory (DFT)

Core to DFT is considering the electronic ground state of the system of interest. To the describe the ground state energy of the system (E_0), several interactions are considered primarily based on the Kohn-Sham equations:

$$E_0 = min_{\rho \to N}\left(F[\rho] + \int \rho(\vec{r}) V_{ext} d\vec{r}\right) \tag{2.16}$$

E_0 is the ground state energy where an input wavefunction is minimised by evaluating the electron density (ρ) of the real number of electrons (N), calculated as a sum of the functional F[ρ], which contains the contribution of the associated kinetic energy T[ρ], the classical Coulomb interaction J(ρ) and the non-classical portion $E_{ncl}[\rho]$ and the integral of the electron density (ρ) over the volume (r) and the potential energy (V_{ext}).

The equation is derived from the two Hohenberg-Kohn theorems. The first states that the external potential $V_{ext}(\rho)$ is a unique functional of ρ(r). V_{ext}(r) fixes the Hamiltonian, H, which describes the system, leading the many-particle ground state to be a unique functional of ρ(r). There cannot be two different V_{ext}(r) values that give the same ρ(r) for the ground state and this results in the ground-state energy of a many bodied system having a unique functional for the particle density. Secondly, the functional returns a ground-state energy of the system at its lowest energy point, only if the input density is the true ground state density (variational principle). However from Equation 2.16, the kinetic energy and the non-classical interaction are unknown and can only be approximated.

Typically the kinetic energy of the system can be estimated by considering a reference non-interacting system. However not being the real kinetic energy of the actual interacting system it is offset by a difference which must be added to the calculation via the exchange-correlation energy term, E_{xc}, which attempts to describe and account for all unknown variables energetically in the simplistic case. E_{xc} at best can be approximated where the local-density approximation (LDA) is the basis of all approximate E_{xc} functionals. At the core of this model is the assumption that the electron distribution is a homogenous electron gas. This implies that within the gas there are no local perturbations which would lead to polarisation of regions containing positivity and/or negativity, the electron region is perfectly neutral. In practicality LDA is insufficient in accurately describing chemical systems and the generalized-gradient approximation (GGA) has been developed to overcome its limitations. GGA extends LDA by attempting to take into account the non-homogeneity of the electron density and locality but it is still limited, particularly by diffuse orbital overlap such as that encountered in actinide systems.

To model the interactions between electrons and ions, particularly within systems with boundary conditions, for instance unit cells, plane waves are used. However plane wave potentials incur high computational costs for heavy ions such as uranium. Consequently pseudopotentials are employed to reduce calculation times while maintaining a comparable level of accuracy in the calculations. The simplification works partially by assuming core electrons are frozen and do not play a role in the systems chemical dynamics. This is largely justifiable for chemical systems where core electrons do not participate in chemical interactions, however, in the case of actinides, where core electrons often participate in bonding, this approximation must be delicately applied, if used at all.

2.9.2 Hubbard *U* Parameter and Corrections Required for Actinide Systems

As eluded to in the previous section, the presence of actinide atoms in a chemical system adds a heightened degree of complexity to standard DFT calculations. Actinides contain a large amount of electrons which experience considerable correlation effects which coupled with the diffusivity of valence orbitals, leading to mixing between the *s*, *p*, *d* and *f* orbitals requiring the use of effective core potentials. Furthermore relativistic effects need to be taking into account, particularly the positioning of electron orbitals and localities. These factors are well known within the simple binary actinide oxides, AnO_2 (An = U, Np and Pu), which consequently are predicted by DFT to be metals whereas they are known to be insulators[24]. One of most common methods of approaching the challenge of actinide materials is using the Hubbard U correction. The principle of the U parameter is to treat the interactions of localized electrons, rather than the homogenous and uniform manor of LDA and GGA. This terms is added effectively in the form:

$$E_{DFT+U} = E_{DFT} + \sum_{a} \frac{U_{eff}}{2}(\rho^a - \rho^a\rho^a) \tag{2.17}$$

Here U_{eff} effectively accounts for on (U) and offsite (J) coulomb interactions arising from d and f electrons. The final term, so-called double-counting term, is used to eliminate the part of the interaction energy already contained in the U. These parameters can be extracted from *ab initio* calculations or also semi-empirically. In this thesis the U parameter was derived from first principles using the linear response approach of Cococcioni and de Girgoncoli[25]. DFT+U calculations were performed by Dr George Beridze and Dr Kowalski. Exact calculation methods used are described in detail in subsequent chapters.

References

1. Bugaris, D. E. and zur Loye, H. C. *Angewandte Chemie-International Edition* **51**(16), 3780–3811 (2012).

2. Pynn, R. *Neutron Scattering–A Non-destructive Microscope for Seeing Inside Matter*, 15–36. Springer US, Boston, MA (2009).

3. Santra, R. *Journal of Physics B: Atomic, Molecular and Optical Physics* **42**(2), 023001 (2009).

4. Als-Nielsen, J. and McMorrow, D. *Elements of Modern X-ray Physics*. Wiley, (2011).

5. Rubensson, J.-E. *Synchrotron Radiation*. 2053-2571. Morgan & Claypool Publishers, (2016).

6. Balcar, E. and Lovesey, S. *Theory of Magnetic Neutron and Photon Scattering*. Oxford Series on Neutron Scattering in Condensed Matter. Clarendon Press, (1989).

7. Aragao, D., Aishima, J., Cherukuvada, H., Clarken, R., Clift, M., Cowieson, N. P., Ericsson, D. J., Gee, C. L., Macedo, S., Mudie, N., Panjikar, S., Price, J. R., Riboldi-Tunnicliffe, A., Rostan, R., Williamson, R., and Caradoc-Davies, T. T. *Journal of Synchrotron Radiation* **25**, 885–891 (2018).

8. McPhillips, T. M., McPhillips, S. E., Chiu, H. J., Cohen, A. E., Deacon, A. M., Ellis, P. J., Garman, E., Gonzalez, A., Sauter, N. K., Phizackerley, R. P., Soltis, S. M., and Kuhn, P. *Journal of Synchrotron Radiation* **9**, 401–406 (2002).

9. Kabsch, W. *Acta Crystallographica Section D-Biological Crystallography* **66**, 133–144 (2010).

10. Blessing, R. H. *Acta Crystallographica Section A* **51**, 33–38 (1995).

11. Sheldrick, G. M. *Acta Crystallographica a-Foundation and Advances* **71**, 3–8 (2015).

12. Sheldrick, G. M. *Acta Crystallographica Section C-Structural Chemistry* **71**, 3–8 (2015).

13. Dolomanov, O. V., Bourhis, L. J., Gildea, R. J., Howard, J. A. K., and Puschmann, H. *Journal of Applied Crystallography* **42**, 339–341 (2009).

14. Liss, K. D., Hunter, B., Hagen, M., Noakes, T., and Kennedy, S. *Physica B-Condensed Matter* **385-86**, 1010–1012 (2006).

15. Studer, A. J., Hagen, M. E., and Noakes, T. J. *Physica B-Condensed Matter* **385-86**, 1013–1015 (2006).

16. Larson, A. C. and Dreele, R. B. V. Technical report, (2000).

17. Toby, B. H. *Journal of Applied Crystallography* **34**, 210–213 (2001).

18. Toby, B. H. and Von Dreele, R. B. *Journal of Applied Crystallography* **46**(2), 544–549 (2013).

19. Rodrguez-Carvajal, J. *Physica B: Condensed Matter* **192**(1), 55–69 (1993).

20. Coelho, A. A., Evans, J. S. O., Evans, I. R., Kern, A., and Parsons, S. *Powder Diffraction* **26**, S22–S25 (2011).

21. Evans, J. S. *Materials Science Forum* **651**, 1–9 9 (2010).

22. Glover, C., McKinlay, J., Clift, M., Barg, B., Boldeman, J., Ridgway, M., Foran, G., Garrett, R., Lay, P., and Broadbent, A. (2007).

23. Paterson, D., Jonge, M. D. d., Howard, D. L., Lewis, W., McKinlay, J., Starritt, A., Kusel, M., Ryan, C. G., Kirkham, R., Moorhead, G., and Siddons, D. P. *AIP Conference Proceedings* **1365**(1), 219–222 (2011).

24. Wen, X. D., Martin, R. L., Henderson, T. M., and Scuseria, G. E. *Chemical Reviews* **113**(2), 1063–1096 (2013).

25. Cococcioni, M. and de Gironcoli, S. *Physical Review B* **71**(3), 035105 (2005).

Chapter 3

Understanding the Rhombohedral to Orthorhombic Structural Phase Transformation in $SrUO_4$

This chapter is adapted from a manuscript titled "Nonstoichiometry in Strontium Uranium Oxide: Understanding the Rhombohedral-Orthorhombic Transition in $SrUO_4$" by G. L. Murphy *et al.* that has been published in the journal *Inorganic Chemistry*.

3.1 Introduction

Understanding the chemical origin of structural phase transformations, and the conditions at which certain phases exist, is pertinent in materials science, as it ultimately guides material application and usage. The δ phase of Bi_2O_3 is a prominent example, exhibiting superb ion conductivities at high temperatures that are inevitably lost at low temperature as it transforms to its γ form[1,2]. With respect to nuclear fuels and waste forms, phase transformations are particularly important macroscopically, as they have been found to influence cracking[3–5]. The plethora of fission daughters that arise from nuclear fuel burning leads to a variety of amorphous and crystalline phases forming which often experience phase separation at the nanometre length scale[6]. *In operando* crystallographic studies of these are near out of reach due to both the complexity of the materials and the associated radiation hazards. *Ex situ* systematic investigations of specific phases coupled with *in situ* studies of their structural-thermal dependence are pertinent in this aspect, as together with high level modelling[7], they enable both the structure-property relations of these phases to be determined and further, the chemical origin of their phase transformations to be understood.

As outlined in Chapter 1, the irreversible structural phase transformation that occurs between rhombohedral α-$SrUO_4$ and orthorhombic β-$SrUO_4$ has been investigated with various degrees of experimental precision, predominantly through thermodynamic methods[8–12]. In the authors published work of his B.Sc(Adv)(Hons) Honours thesis[13], the ability for $CaUO_4$, α-$SrUO_4$, β-$SrUO_4$ and $BaUO_4$ to host oxygen vacancies was related to the bonding requirements of the A site cation via *ex situ* measurements. This work showed that the over bonded Sr and Ca cations in the rhombohedral lattices could achieve stability through partial oxygen vacancy formation. In orthorhombic β-$SrUO_4$, the bonding of the Sr^{2+} cation is structurally satisfied and oxygen vacancy formation is not necessary. It is not immediately clear, though previously speculated[14], whether the difference in the structural chemistry between the $SrUO_4$ polymorphs is related to the reported[9,10,13] oxygen loss and gain phenomena associated with the α to β transition. Nor is it clear if the oxygen loss and gain phenomena is an essential component of the transformation and, if so, does it involve the sequential reduction and re-oxidation of the uranium.

This chapter is devoted to answering these scientific questions, using a combination of high resolution experimental and computational techniques. This involved *in situ* neutron and synchrotron X-ray powder diffraction measurements, performed under variable atmospheric conditions, with the intent to understand the oxygen loss and gain phenomena. *In situ* X-ray absorption near-edge spectroscopy measurements

on the uranium L_3-edge were used to probe the ability for uranium to undergo reduction during the transformation. The results of these experiments were then supplemented by *ab initio* calculations using density functional theory, in an attempt to obtain a near phenomenological understanding of the structural chemical relationship and phase transformation between rhombohedral α-$SrUO_4$ and orthorhombic β-$SrUO_4$.

3.2 Experimental

3.2.1 Synthesis

A polycrystalline sample of α-$SrUO_4$ was prepared by first weighing stoichiometric quantities of U_3O_8 and $SrCO_3$. These reagents were mixed in a mortar and pestle before being compacted into a pellet, placed into an alumina crucible and calcined at 900 ^{o}C for 60 hours using a muffle furnace with intermittent mixing. Laboratory XRD measurements were used to monitor the synthesis until a single phase sample of orthorhombic β-$SrUO_4$ was identified. A sub-sample of the yellow oxide was placed in an alumina boat as a fine powder and calcined at 1200 ^{o}C for 2 hours using a tube furnace whilst being exposed to a flowing 3.5% H_2/N_2 atmosphere. Post synthesis the sample was reddish-brown in colour and laboratory XRD measurements confirmed it to be rhombohedral α-$SrUO_4$. Given the synthesis conditions, and the known ability for α-$SrUO_4$ to readily form oxygen vacancies[13], the sample was then heated at 200 ^{o}C under flowing air to ensure it to be completely stoichiometric.

3.2.2 *Ex Situ* Neutron and Synchrotron X-ray Powder Diffraction

Accurate and precise structures of α-$SrUO_4$ and β-$SrUO_4$ were established by collecting ambient condition diffraction profiles using neutron (NPD) and synchrotron X-ray powder diffraction (S-XRD) and jointly refining the models against these using the Rietveld refinement method. For the NPD measurements, approximately 2 g of powdered material was placed in a vanadium can and data was collected at ANSTO's OPAL nuclear reactor using the high resolution neutron powder diffractometer ECHNIDA[15]. For the S-XRD measurements, approximately 5 mg of sample was ground into a fine power and placed in a 0.2 mm diameter glass capillary that was sealed. These S-XRD measurements were undertaken at the Australian

Synchrotron powder diffraction beamline[16]. Wavelengths of 1.622 and 0.82689 Å were used for these NPD and S-XRD measurements respectively, where the latter was determined using a NIST LaB_6 standard reference material.

3.2.3 *In Situ* Synchrotron X-ray Powder Diffraction

Approximately 5 mg of α-$SrUO_4$ was ground to a fine powder and loaded into a sealed 0.2 mm diameter quartz capillary. Temperature control was achieved using a FMB-Oxford hot air blower where measurements were taken incrementally from 25 to 1000 ^{o}C. The temperature was increased at 5 ^{o}C per minute and data collected after 30 seconds of holding at temperature to allow for thermal equilibration. These S-XRD measurements were undertaken at the Australian Synchrotron powder diffraction beamline[16]. The wavelength used in this experiment was 0.7260 Å determined from a NIST LaB_6 standard reference.

3.2.4 *In Situ* Neutron Powder Diffraction

Approximately 2 g of α-$SrUO_4$ was compacted into pellets and loaded into a thin walled vanadium can. The can was placed in an ILL type high vacuum furnace employing niobium elements and operating at $< 10^{-6}$ Torr. The can was not sealed during measurements and thus the sample was exposed to the high vacuum. The temperature was increased at 10 ^{o}C per minute and data was collected twice at each temperature for 2 h each. These NPD measurements were undertaken at ANSTO's OPAL nuclear reactor using the high resolution neutron powder diffractometer ECHNIDA[15]. Accurate structure models were developed by refining against the NPD and S-XRD data using the program GSAS[17,18] and GSAS-II[19]. The wavelength used in this experiment was 1.622 Å.

3.2.5 Thermogravimetric Analysis

Thermogravimetric analysis (TGA) measurements were collected from 25 to 1000 ^{o}C using a SFT Q600 TGA instrument. A sample of α-$SrUO_4$, approximately 20 mg, was contained in a quartz crucible and measurements were obtained at a heating rate of 5 ^{o}C under a flowing air atmosphere.

3.2.6 X-ray Absorption Spectroscopy

X-ray absorption spectroscopy near edge structure (XANES) measurements were collected on the U L_3-edge on the X-ray absorption spectroscopy (XAS) beamline at the Australian Synchrotron[20]. Approximately 2.7 mg of $CaUO_4$, α-$SrUO_4$ and $BaUO_4$ were mixed individually with 4.4 mg of BN as a diluent in a mortar and pestle. The three mixtures were loaded into open 2 mm diameter quartz capillaries and one mixed sample of α-$SrUO_4$ was additionally loaded in another open 2 mm diameter quartz capillaries that was sealed in air. The capillaries were placed into a water cooled Linkam TS1500 heating stage operating in an argon atmosphere[21], such that the samples in the open capillaries were exposed to the argon atmosphere whereas those in the closed capillary were not. The measurements were performed in transmission mode, using argon filled ionisation chambers, at temperatures between room temperature and 900 ^{o}C. The heating rate was set at 30 ^{o}C/min and data were collected after 10 minutes of holding time to allow for thermal equilibration. The beam intensity was monitored by an ionisation chamber located upstream from the sample position. XANES data was collected by a second ionisation chamber after the sample. A third ionisation chamber was located downstream to simultaneously measure a reference spectrum of a natural uranite (UO_2) sample. Energy steps as small as 0.25 eV were employed near the absorption edges with a counting time of 2 seconds per step. The energy scale of the monochromator was calibrated using the K-edge of Zr foil, the first derivative peak was set at 17995.8 eV, and the uranite sample was used to determine, and correct for, any energy shifts that may occur during the experiment. Data were analysed using the program ATHENA[22].

3.2.7 Density Functional Theory Calculations

Ab initio calculations using density functional theory (DFT) were used to calculate the energy for defect formation in α-$SrUO_{4-x}$ and β-$SrUO_{4-x}$ for $x = 0$ to 0.5. This was achieved using the DFT plane-wave package quantum-ESPRESSO[23]. In order to correctly account for the strongly correlated character of the f orbitals, the DFT + U method was used with the Hubbard U parameter derived directly from first principles using the linear response approach of Cococcioni and de Gironcoli[24]. The PBE[25] and PBEsol[26] exchange-correlation functionals and ultrasoft pseudopotentials[27] were used to account for the effects of the core electrons. All calculations were spin-polarised with the plane-wave energy cutoff of 50 Ryd. The α phase was modelled by a 48 atom supercell and the β phase by a 24 atom supercell. 2 x 2 x 2 and 4 x

3 x 3 Methfessel-Paxton k-point grids were used for the $SrUO_4$ polymorphs respectively[28]. The sizes of the grids were selected to give the convergence of the considered energies within 0.1 kJ/mol. Spin-orbit interactions were not taken into account during these calculations. These were separately tested and found to be negligible, less than 0.02 eV for uranium. These calculations were performed by Dr George Beridze and Dr Piotr M. Kowalski of Forschungszentrum Julich, Germany, using the JARA high-performance computational facility, Aachen, Germany.

3.3 Results and Discussion

3.3.1 *Ex Situ* Structural Characterisation

Room temperature NPD and S-XRD measurements of α-$SrUO_4$ and β-$SrUO_4$ confirmed their reported structural assignments of rhombohedral in space group $R\bar{3}m$ and orthorhombic in space group *Pbcm* respectively[13]13. The Rietveld refinement profiles of these structures for the NPD and S-XRD measurements are presented in Figure 3.1 with the associated structures in Figure 3.2. In both 2D layered structures, the edge sharing UO_6 (β-$SrUO_4$) and UO_8 (α-$SrUO_4$) polyhedra contain long U-O bonds parallel to the sheets and short oxo U-O(1) bonds orthogonal to this, consistent with the uranyl moiety[29]. The latter are directed at the Sr^{2+} cations. In β-$SrUO_4$ the U-O(1) bonds are noticeably less regular than the corresponding bonds in α-$SrUO_4$. Structural details, including refined lattice parameters and atomic coordinates are presented in Table 3.1 and 3.2.

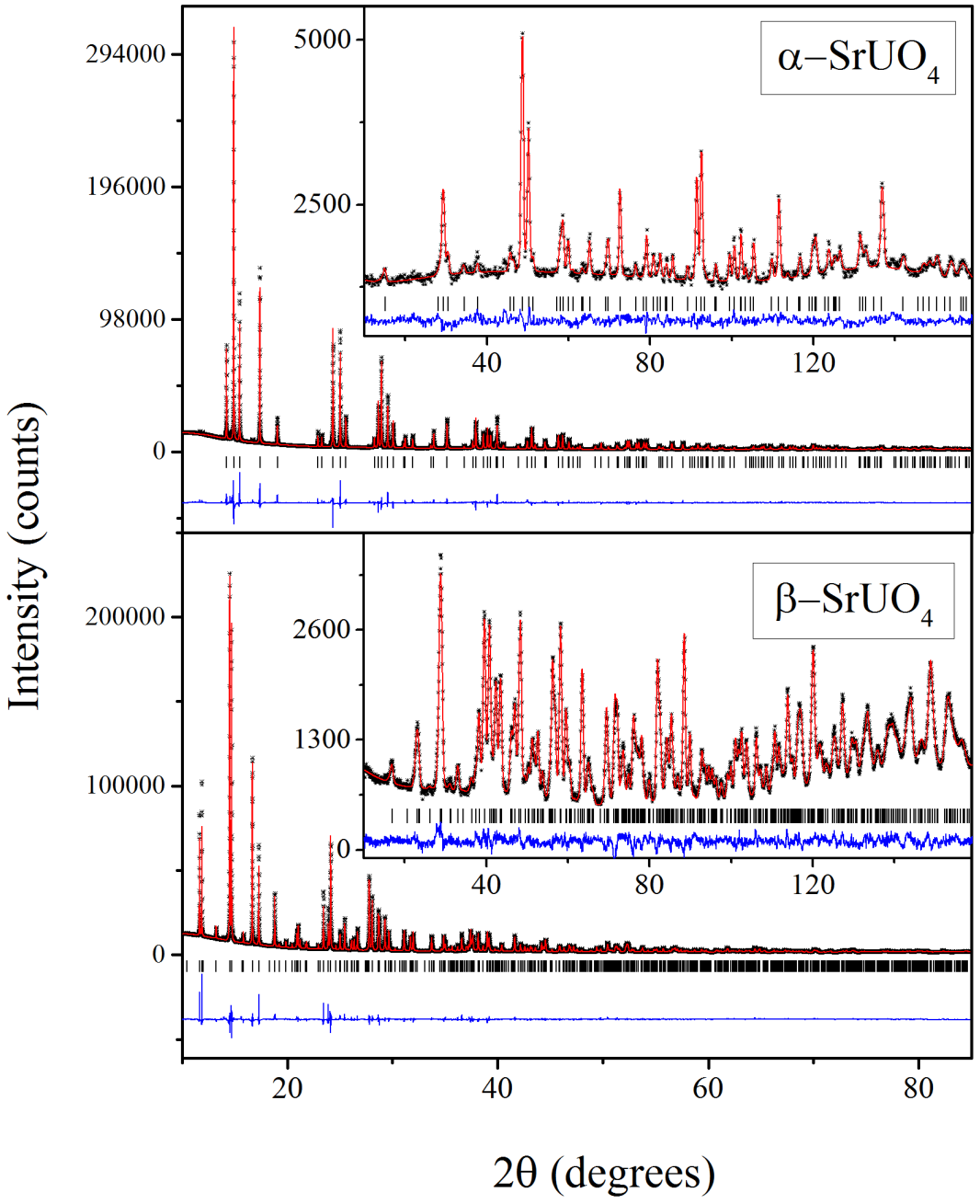

FIGURE 3.1: Rietveld refinement profiles of rhombohedral α-$SrUO_4$ in space group $R\bar{3}m$ α-$SrUO_4$ (top) and orthorhombic β-$SrUO_4$(bottom) in space group *Pbcn* against S-XRD and NPD (inset) data. The NPD and S-XRD measurement wavelengths of 1.622 and 0.8269 Å were used respectively.

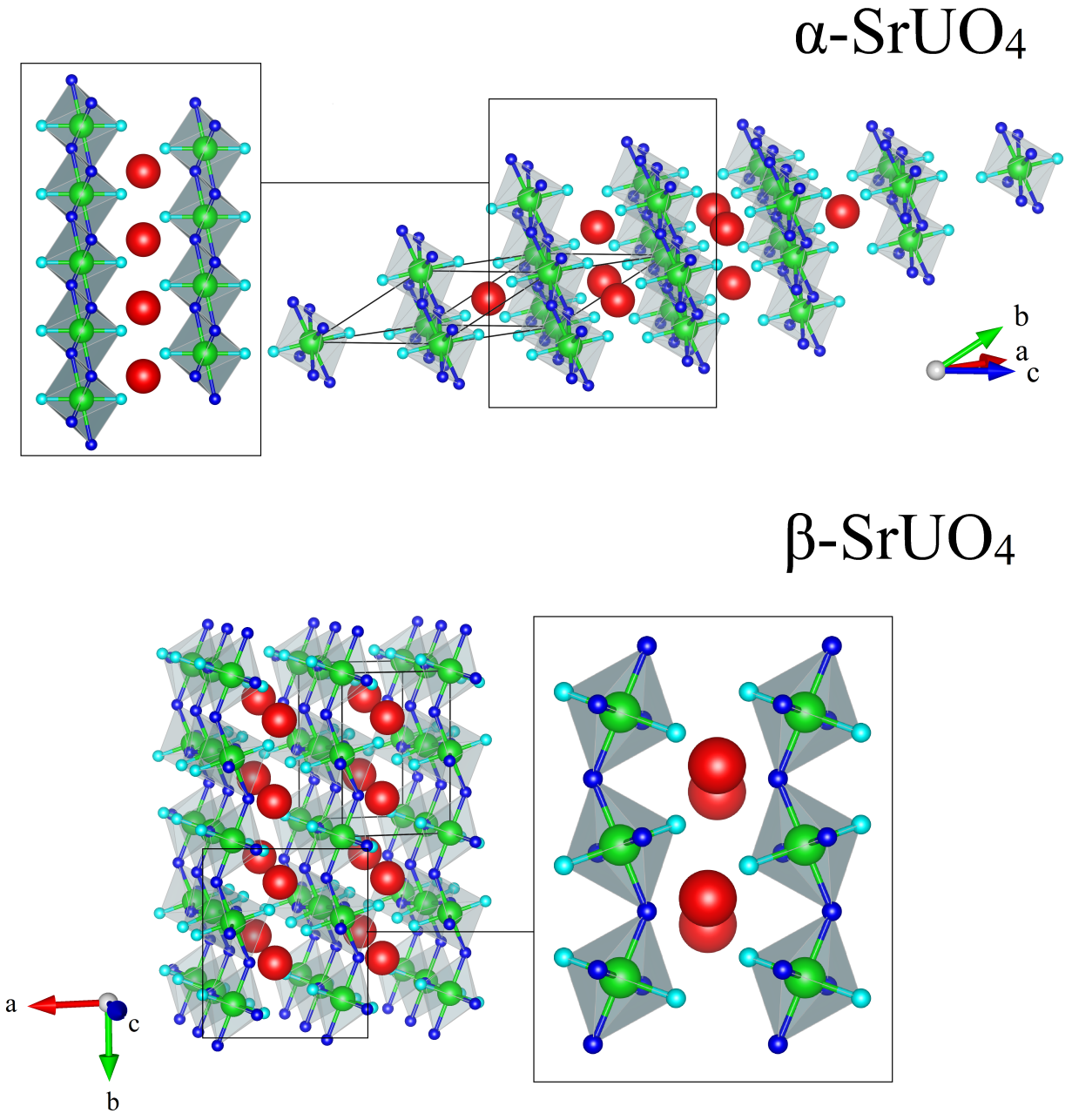

FIGURE 3.2: Structural Representations of rhombohedral α-$SrUO_4$ in space group $R\bar{3}m$ (top) and orthorhombic β-$SrUO_4$ (bottom) in space group *Pbcn* derived from Rietveld refinements against S-XRD and NPD data sets. Red, green, dark blue and aqua blue spheres represent strontium, uranium, non-uranyl oxygen and uranyl oxygen atoms.

TABLE 3.1: Structural data for α-$SrUO_4$ obtained from S-XRD and NPD data recorded at $\lambda = 0.82689$ and 1.622 Å respectively. The structure was refined in the rhombohedral space group $R\bar{3}m$ $a = 6.5119(4)$ Å, $\alpha = 34.8522(7)^o$ and cell volume = 80.499(8) Å^3, $wR_p = 3.17\%$, $R_p = 2.50\%$, $\chi^2 = 2.549$. *Equivalent values of the anisotropic results.

Atom	$x = y = z$	U_i/U_e*100 Å^2	$U^{11} = U^{22} = U^{33}$	$U^{12} = U^{13} = U^{23}$
Sr	0.5	0.57(8)	-	-
U	0	0.34(7)	-	-
O(1)	0.10672(15)	0.58*	0.57(10)	-0.37(2)
O(2)	0.35981(17)	0.62*	0.64(12)	-0.29(6)

TABLE 3.2: Structural data for β-$SrUO_4$ obtained from S-XRD and NPD data recorded at $\lambda = 0.82689$ and 1.622/2.439 Å respectively. The structure was refined in the orthorhombic space group $Pbcm$ $a = 6.5119(4)$ Å, b = 7.97629(20) Å, c = 8.12698(19) Å and cell volume = 355.999(14) Å^3, $wR_p = 4.76\%$, $R_p = 3.69\%$, $\chi^2 = 1.844$. *Equivalent values of the anisotropic results.

Atom	x	y	z	U_i/U_e*100 Å^2	U^{11}	U^{22}	U^{33}	U^{12}	U^{13}	U^{23}
Sr	0.4749(3)	0.20110(17)	0.25	1.05(3)	-	-	-	-	-	-
U	0	0	0	1.05(3)	-	-	-	-	-	
O(1)	0.2988(3)	0.91889(17)	0.07899(16)	1.06*	0.95(8)	1.27(7)	0.97(7)	0.12(7)	-0.30(6)	0.65(6)
O(2)	0.1712(3)	0.25	0	1.09*	0.56(10)	0.80(9)	1.91(10)	0	0	0.36(9)
O(3)	0.8606(4)	0.03204(23)	0.25	1.48*	2.07(12)	1.14(13)	1.24(11)	0.50(8)	0	0

3.3.2 *In Situ* Synchrotron X-ray Diffraction

The temperature of dependence of the structure of α-$SrUO_4$ was initially established using S-XRD for a sample in a sealed quartz capillary from ambient to 1000 ^{o}C. A portion of the diffraction profile is presented in Figure 3.3. Below approximately 500 ^{o}C the sample was essentially single phase α-$SrUO_4$ and displayed typical thermal expansive behaviour. Between 500 and 600 ^{o}C several Bragg reflections shift to lower 2θ, indicating an acceleration in the rate of thermal expansion. This persisted to between 700 and 800 ^{o}C where additional reflections were observed to grow into the diffraction pattern whilst, simultaneously, reflections corresponding to α-$SrUO_4$ began to lose intensity. This trend continued until approximately 900 ^{o}C, thereafter the sample was apparently single phase and reflections corresponding to α-$SrUO_4$ were no longer observable. This new phase could be refined against an orthorhombic structure in space group *Pbcm* corresponding to β-$SrUO_4$. That reflections corresponding to β-$SrUO_4$ emerge independently, with respect to α-$SrUO_4$ reflections, indicates the transformation is 1^{st} order. Cooling the sample to room temperature revealed β-$SrUO_4$ to remain, indicating that the transformation is irreversible, consistent with previous reports[9,30].

The S-XRD data were analysed using an α-$SrUO_4$ model to precisely determine the temperature dependence of the cell volume and the occupancy of the O(2) non-uranyl oxygen crystallographic site. These are presented together with TGA data collected under similar conditions in Figure 3.4. Three regions of interest are evident in the refined structural parameters. Up to 500 ^{o}C there is seemingly no anomalous behaviour apparent in the refined structural parameters. However, above 500 ^{o}C towards 800 ^{o}C, the thermal expansion of the unit cell volume increases, consistent with the observed accelerated shifting of Bragg reflections noted earlier. This coincides with an apparent reduction in the O(2) oxygen site occupancy, corresponding to loss of non-uranyl oxygen atoms. The O(1) site, (not shown in Figure 3.4) corresponding to the uranyl oxygen, does not exhibit any appreciable change in occupancy.

Interestingly upon heating beyond 800 ^{o}C the O(2) site occupancy is found to increase and this site becomes fully occupied by 1000 ^{o}C, indicating oxidation is occurring. Careful observation of the thermal expansion of the unit cell volume in this temperature range indicates that its rate of change has decelerated to a rate similar to that prior to 500 ^{o}C. These results strongly indicate that an oxygen loss and gain phenomena is associated with the transformation, consistent with previous reports[9,10,12,13] and confirms the report of Takahashi *et al.*[31] that the change in oxygen stoichiometry is associated with the O(2) site

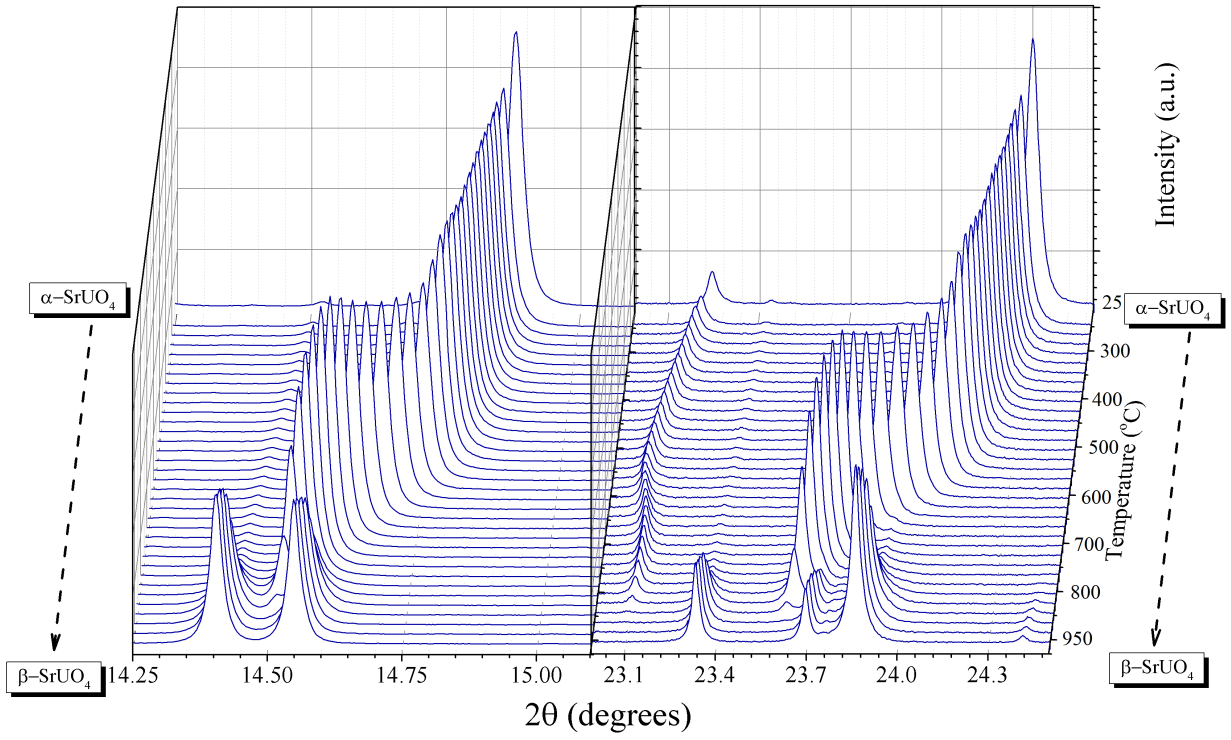

FIGURE 3.3: A portion of S-XRD ($\lambda = 0.7260$ Å) data collected for α-$SrUO_4$ heated in air to 1000 ^{o}C at $14.2 \leq 2\theta \leq 15.5^o$ and $23 \leq 2\theta \leq 25^o$. Note the accelerated shift of the two main reflections around 14.8 and 24.3^o (peak positions at RT) as a result of apparent the oxygen loss and uranium reduction from 600 ^{o}C.

exclusively. As described in Chapter 1, the uranyl bond is stronger than that of a regular U-O bond, such that the oxygens at the O(1) site are expected to be much more tightly held to the U cation than those at the O(2) site[32,33]. Consequently in α-$SrUO_4$, breaking the U-O(2) bond would require less energy than breaking the U-O(1) uranyl bond. However, at this point, it is still not clear what is the origin of this sequential reduction and oxidation and what is its relation to the phase transformation. Such behaviour is not observed in other materials that undergo thermally induced redox reactions[1,34,35]. Furthermore, the anomalous change in the unit cell volume expansion has not been described previously, due to the lack of structural studies present in literature. However Tagawa and Fujino[10] previously speculated that this oxygen loss and gain phenomena would correspond to a change in uranium oxidation state. Reduction of hexavalent uranium would correspond to an increase its ionic radii and subsequent oxidation would lead to a corresponding contraction in ionic radii[36]. The observed structural changes are indicative of this postulate that a uranium redox process is involved in the transformation.

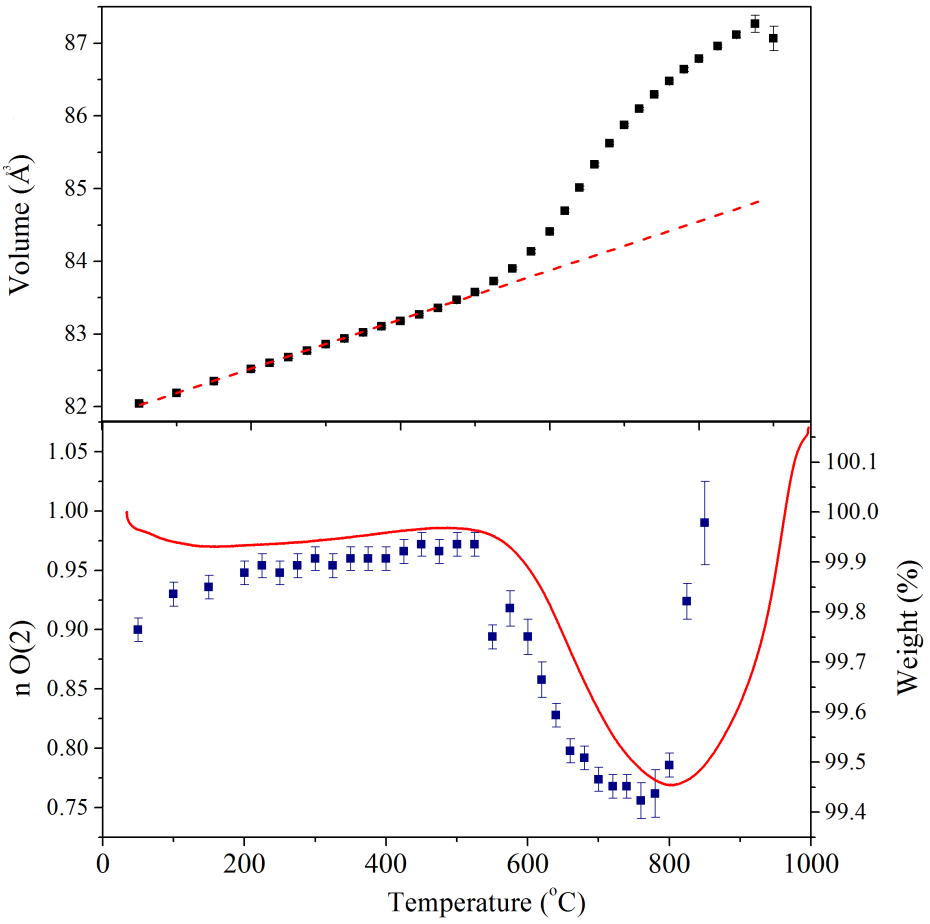

FIGURE 3.4: Temperature dependence of the unit cell volume (top) and oxygen O(2) site occupancy (bottom) for α-$SrUO_{4-x}$ obtained from Rietveld refinements against *in situ* S-XRD data. The solid red line is a result of thermogravimetric analysis measurement. The dashed red line is a linear fit for the refined volume data points between room temperature and 550 ^{o}C.

3.3.3 *In Situ* Neutron Powder Diffraction

Although the oxygen loss and gain phenomena, indicated by S-XRD measurements, is consistent with previous thermodynamic studies[9,10] the use of X-rays to measure anionic parameters in the presence of uranium is problematic. Consequentially *in situ* NPD measurements were used to corroborate the results of the S-XRD experiment. In these, the structure of α-$SrUO_4$ was studied from ambient temperature to 1000 ^{o}C. A notable distinction between the two experiments is the use of an ILL type furnace which operates under vacuum as opposed to the S-XRD experiment where the sample could access atmospheric oxygen. A portion of the NPD profile collected for α-$SrUO_4$ is presented in Figure 3.5. Interestingly,

upon heating the sample to 1000 ^{o}C, there was no indication from the diffraction profile that the sample underwent a phase transformation.

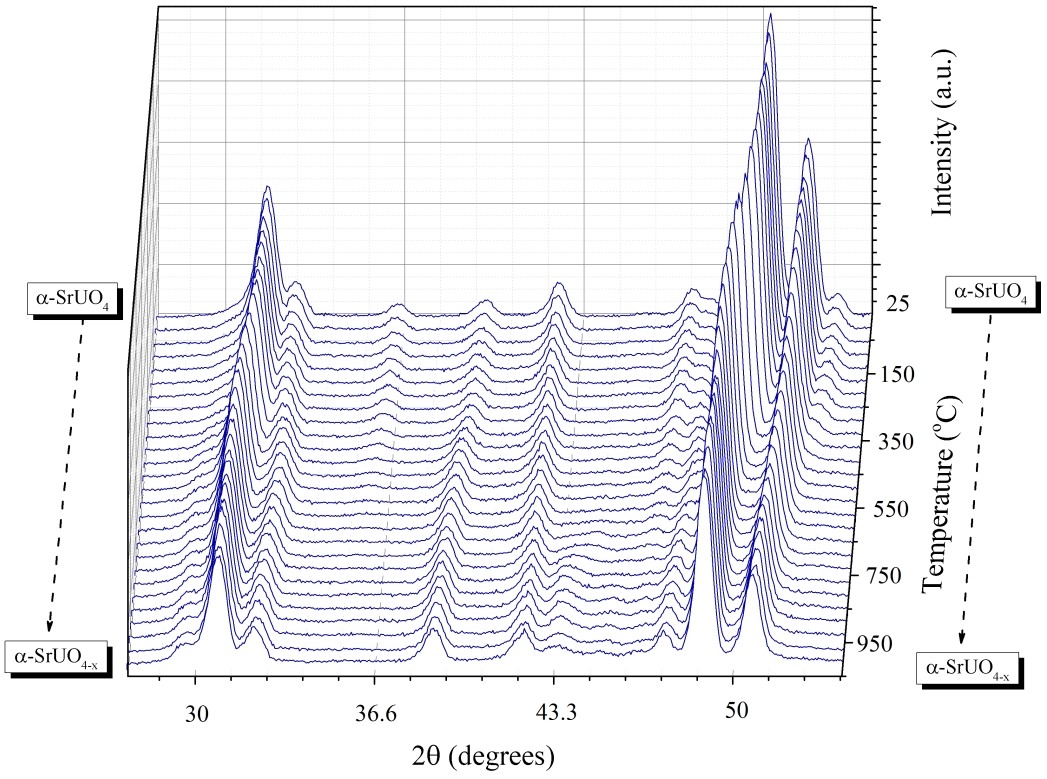

FIGURE 3.5: A portion of NPD collected for α-$SrUO_4$heated in vacuum to 1000 ^{o}C and cooled rapidly to 200 ^{o}C at $27.4 \leq 2\theta \leq 54^o$. Note loss of intensity of certain Bragg reflections such as that near 36.7 and 52^o, and that there is no apparent evidence for transformation behaviour occurring.

The temperature dependence of the unit cell volume, oxygen O(2) site occupancy, and atomic displacement parameters for α-$SrUO_4$ obtained from Rietveld refinements against the NPD data is presented in Figure 3.6. Similar to the S-XRD experiment, three regions of interest are evident in the refined structural parameters. Up to 500 ^{o}C thermal expansion is observed with approximately linear expansion of the unit cell volume. There is no significant change in the atomic displacement parameters over this temperature range, although a subtle reduction in the O(2) site occupancy is observed. From 500 to 800 ^{o}C, similar behaviour to that encountered in the S-XRD experiment is apparent. There is an acceleration in the rate of expansion of the unit cell volume coupled with the dramatic loss of occupancy of the O(2) oxygen site whereas the O(1) uranyl oxygen site remains fully occupied (Not shown in Figure 3.6). The difference in the occupancies of the two oxygen sites is reflected in the ADPs where a much greater increase is observed

above 500 ^{o}C for the O(2) site than for the O(1) site. Further heating the sample from 800 towards 1000 ^{o}C, results in the rate of volumetric expansion returning to a rate similar to that observed below 500 ^{o}C, and the sample remains sub-stoichiometric with a calculated stoichiometry of $SrUO_{3.6}$ at 1000 ^{o}C. These results evidently corroborate the oxygen loss phenomena observed in the S-XRD experiment, despite the difference in behaviour apparent above 800 ^{o}C. Cooling the sample to 200 ^{o}C whilst maintaining the vacuum, showed that the oxygen loss of the O(2) site persists and the lattice volume is still notably larger than what is observed in the corresponding heating sequence at 200 ^{o}C.

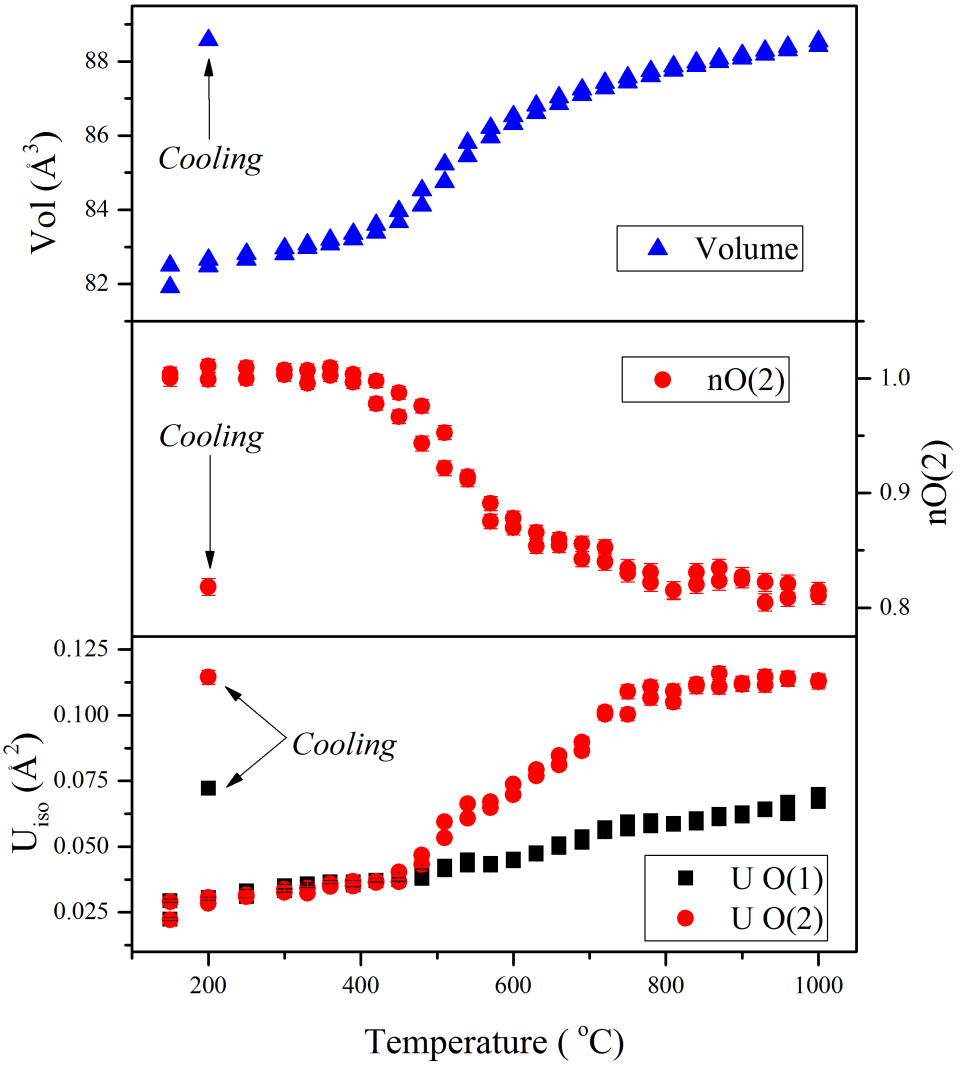

FIGURE 3.6: Temperature dependence of the unit cell volume (top), oxygen O(2) site occupancy (middle) and atomic displacement parameters for the O(1) and O(2) site oxygens (bottom) for α-$SrUO_{4-x}$ obtained from Rietveld refinements against *in situ* NPD data.

The crucial difference between the two diffraction experiments, such that the transformation occurs in one and not the other, is the atmospheres used. For sub-stoichiometric α-$SrUO_{4-x}$ to transform to stoichiometric β-$SrUO_4$ a source of oxygen is necessary. Tagawa *et al.*[9] argued that β-$SrUO_{4-x}$ only exists under a narrow sub-stoichiometry, x, whereas α-$SrUO_{4-x}$ can exist with a much wider range of x. Evidently under vacuum, there is insufficient oxygen to allow stoichiometric β-$SrUO_4$ to form in the NPD experiment, rather α-$SrUO_{4-x}$ persists. The initial oxygen loss process can be regarded as a crucial first step of the transformation, possibly reducing the activation energy barrier allowing it to proceed. That the sample does not reabsorb oxygen once cooled under vacuum, further demonstrates that the oxygen loss from the O(2) site is not simply a consequence of movement of anions into interstitial lattice positions and is a temperature activated phenomena, but rather it corresponds to total loss or extrusion of oxygen from the sample. This likely involves oxidation of the vanadium can in the NPD experiment. In the S-XRD experiment, only a small region ($\approx$ 3 mm) of the capillary ($\approx$ 35 mm long) is heated. The majority of the sample is away from hot zone and presumably does not transform, as illustrated graphically in Figure 3.7. Consequently during the oxygen loss step in the capillary, lattice oxygen diffuses to the cooler part of the sample, and this is reversed at higher temperature as the sample transforms to β-$SrUO_4$. This thermally regulated transport of oxygen is reminiscence of the electron beam induced annihilation and reappearance of tilted domains in $Li_{0.38}Nd_{0.54}TiO_3$ that is linked to Li cationic transport through the crystal lattice[37].

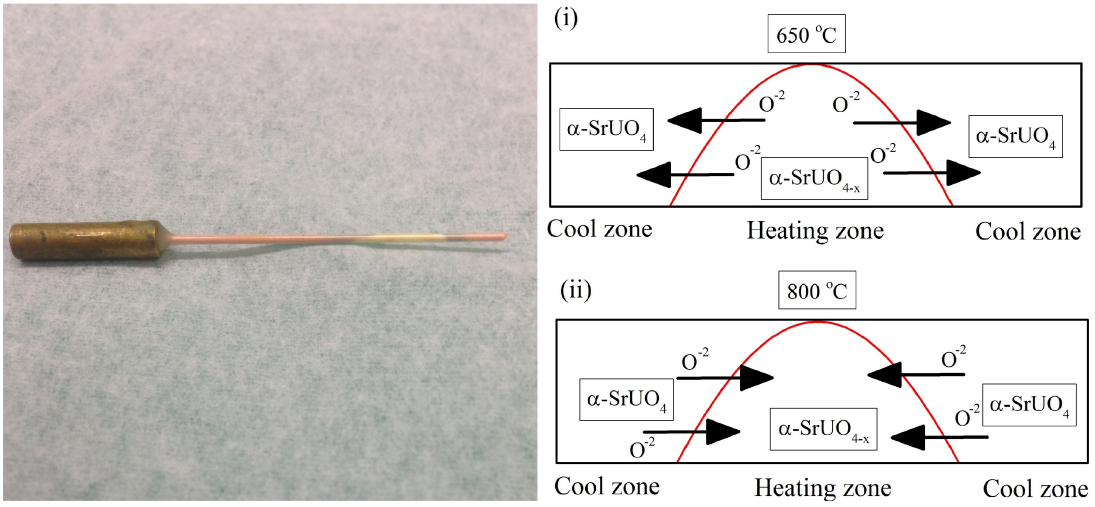

FIGURE 3.7: (Left) photo of α-$SrUO_4$ from the S-XRD experiment post-heating to 1000 ^{o}C and (right) schematic thermal distribution diagram of heat in capillary and apparent oxygen movement occurring in the same S-XRD experiment at (i) 650 and (ii) 800 ^{o}C. The small yellow region (β-$SrUO_4$) shows the approximate position of the hot zone in the measurement, the capillary is 0.2 mm in diameter.

3.3.4 *In Situ* X-ray Absorption Spectroscopy

The changes in oxygen stoichiometry of $SrUO_4$ during its α to β transformation strongly suggests that the uranium redox states are changing. *In situ* XANES measurements were collected at the U L_3-edge under argon and also in a sealed quartz capillary containing air to unequivocally establish firstly, the occurrence of redox behaviour and secondly, the extent of uranium reduction when α-SrUO4 is heated from room temperature to 1000 ^{o}C. *In situ* normalised XANES measurements collected under argon for α-$SrUO_4$, $CaUO_4$ and $BaUO_4$ are presented in Figure 3.9. From room temperature to 400 ^{o}C there is no apparent shift in the XANES spectra for α-$SrUO_4$, indicating no change to the U^{6+} oxidation state. Further heating from 400 to 600 ^{o}C shows a systematic shift of the XANES spectra towards lower photon energy indicating partial reduction of the U^{6+} oxidation state. In comparison, $CaUO_4$ and $BaUO_4$, which do not display transformative behaviour or change to the uranium valence, show no change in their XANES spectra when heated from room temperature to 1000 ^{o}C. No further changes were observed in the XANES spectra of α-$SrUO_4$ when heated to 900 ^{o}C and the XANES peak shape resembled that of α-$SrUO_4$ and not of β-$SrUO_4$ (Figure 3.8 shows the room temperature XANES spectra of $CaUO_4$, α-$SrUO_4$, β-$SrUO_4$ and $BaUO_4$ with standards reproduced from reference[13]). Some anomalous spectral shifting and strong changes to the peak shape were observed above 900 ^{o}C for α-$SrUO_4$, this is attributed to reactivity between the oxide and the BN matrix[38]. The continuity of the peak shape during heating indicates the sample is responding similar to the NPD experiment namely gradually generating vacancies and remaining sub-stoichiometric rhombohedral, α-$SrUO_4 \rightarrow \alpha$-$SrUO_{4-x}$.

To confirm and illustrate the phase transformation using *in situ* XANES, a sample of α-$SrUO_4$ was heated in a sealed quartz capillary containing air towards 950 ^{o}C and data collected on the U L_3-edge. The normalised first derivative of the data is presented in Figure 3.10. Subtle variation in the peak shape of the XANES spectra is evident for spectra recorded with the temperature above 650 ^{o}C indicating the sample is transforming to β-$SrUO_4$. This is particularly evident around 17185 eV. That the peak shape is changing in this region is a consequence of the different coordination environments for uranium as it transforms from α-$SrUO_4$ (CN = 8) to β-$SrUO_4$ (CN = 6). The final 1000 ^{o}C spectrum has a XANES peak shape consistent with the orthorhombic structure of β-$SrUO_4$[13].

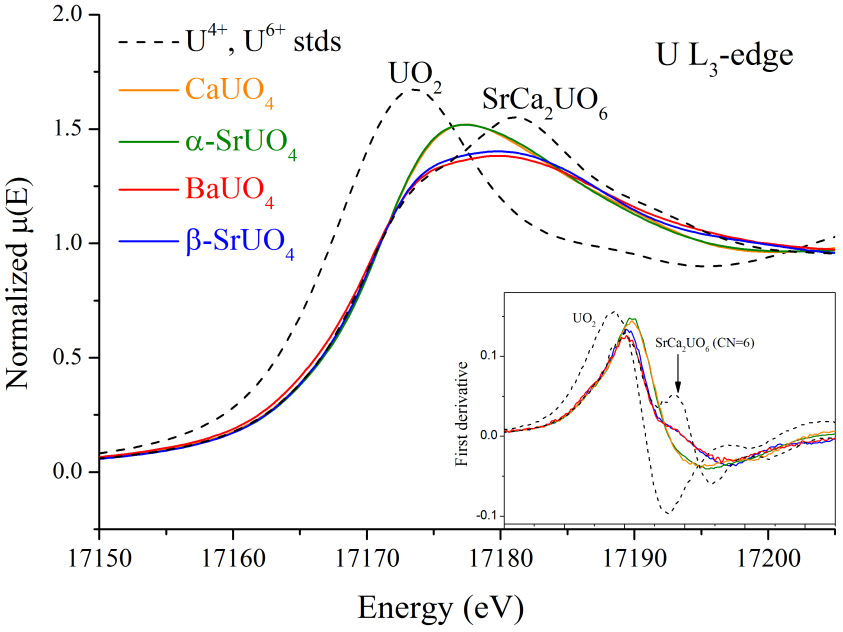

FIGURE 3.8: Normalised U L_3-XANES spectra from $CaUO_4$, α-$SrUO_4$, β-$SrUO_4$ and $BaUO_4$ and U^{4+} (UO_2) and U^{6+} ($SrCa_2UO_6$) standards at RT. Inset plots the first derivative.

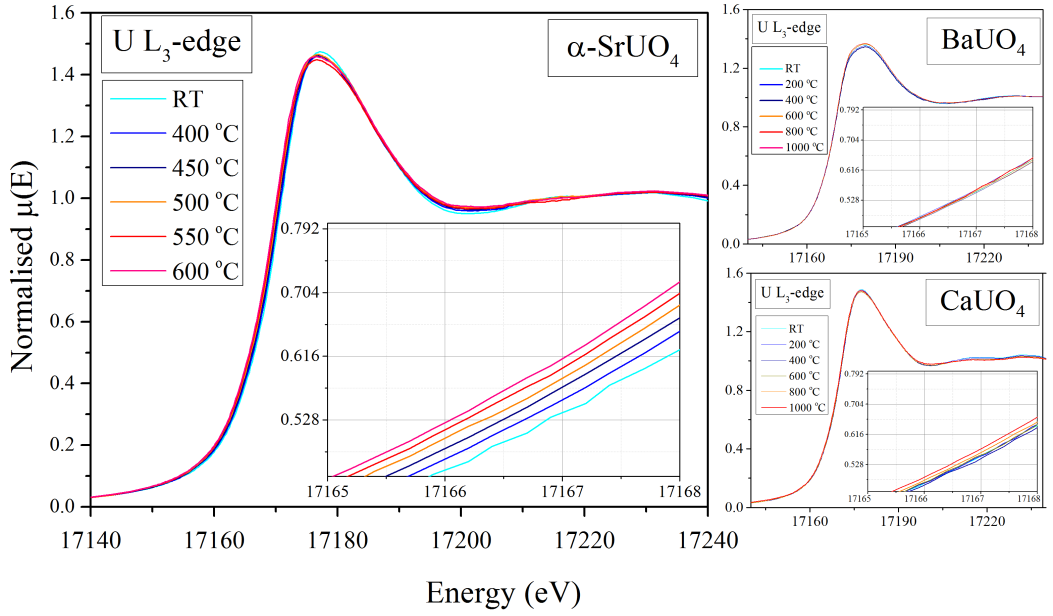

FIGURE 3.9: Normalised U L_3-edge XANES spectra collected from α-$SrUO_4$ *in situ* at temperatures ranging from 400 to 600 ^oC under an argon atmosphere. The inset (i) highlights the systematic edge shift towards lower energy with increasing temperature indicating reduction is occurring. The inset (ii) and (iii) correspond to $CaUO_4$ (isostructural to α-$SrUO_4$) and $BaUO_4$ (isostructural to β-$SrUO_4$) heated under similar conditions. No apparent edge shifting occurs in these samples indicating that the shifting observed α-$SrUO_4$ is consequence of reduction occurring during its higher temperature reduction step observed in the S-XRD and NPD experiments.

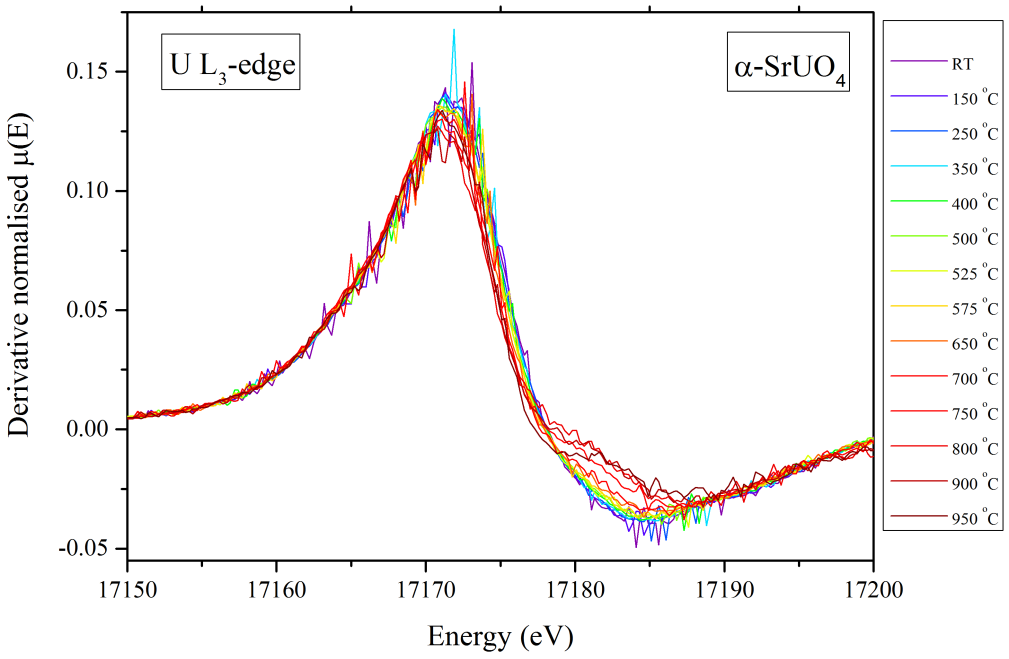

FIGURE 3.10: Normalised first derivative U L_3-edge XANES data collected from α-$SrUO_4$ in a sealed quartz capillary containing air heated from room temperature to 950 ^{o}C. The difference between the $SrUO_4$ spectra is attributed to the α to β phase transformation, apparent when inspecting the region near 171850 eV.

3.3.5 *Ab Initio* Calculations

To summarise so far, when rhombohedral α-$SrUO_4$ in space group $R\bar{3}m$ is heated above 700 ^{o}C it undergoes pronounced oxygen loss associated with reduction of uranium that apparently reduces the activation energy barrier for the transformation to stoichiometric orthorhombic β-$SrUO_4$in space group *Pbcm*. The transformation requires sequential steps of reduction, and re-oxidation, before the structural transformation can occur. Without the oxidation step, the transformation fails and α-$SrUO_{4-x}$ remains sub-stoichiometric. This is apparently related to the difference in the structural chemistry between α-$SrUO_4$ and β-$SrUO_4$, and particular the relative affinity for each to host oxygen defects. DFT+U calculations were performed to understand the relative energies of defect formation in the two structures.

The Hubbard U parameter was calculated to be 2.5 eV, in good agreement with previous studies on uranium solids[39]. The PBE+U and PBEsol+U methods were trialled with respect to the experimental measured volume to establish their appropriate use. This is presented in Figure 3.11. As evident, the PBE

functional slightly overestimates the volume by approximately 3.3%, a common feature of this functional [40]. This disparity is better accounted for with the PBEsol+U functional, which is intended to better reproduce the structural parameters of solids [26]. As evident in Figure 3.11, the calculated volume is seen to increase with increasing oxygen defects reflecting the increased presence of reduced uranium species and is in agreement with the observations of the *in situ* S-XRD and XANES experiments.

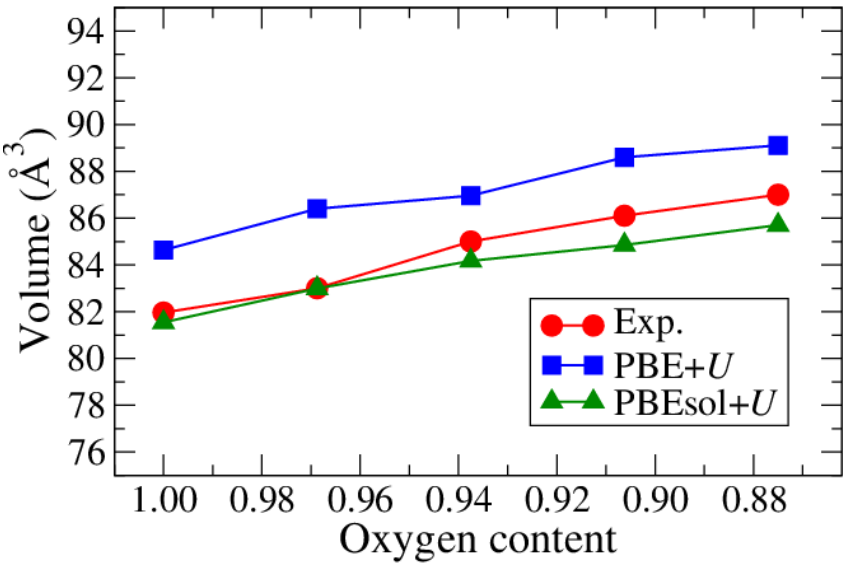

FIGURE 3.11: The comparison of variable temperature experimental (red circles) and calculated volumes of α-$SrUO_4$ with different oxygen occupancies (x) using the DFT+U method with PBE (blue squares) and PBEsol (green triangles exchange-correlation functionals).

For the two stoichiometric structures, the energy for defect formation is very similar where β-$SrUO_4$ is 0.22 eV lower in energy than α-$SrUO_4$. The energetic impact of oxygen vacancies on both structures was examined using a variety of configurations with single, double and triple oxygen defects. These results are summarised graphically in Figure 3.12. The energy required to create a single oxygen vacancy on the O(2) site of α-$SrUO_4$ (α-$SrUO_{3.875}$) was 0.29 eV more favourable than placing the vacancy on the O(1) uranyl site. In order to directly compare the two structures the constructed supercells had different sizes (48 atoms for α and 24 atoms for β), as such there are no calculations for β-$SrUO_{3.875}$ or β-$SrUO_{3.625}$. Among all possible permutations of arranging two oxygen defects in α-$SrUO_{3.75}$, the lowest energy configuration corresponds to two vacancies occurring on the O(2) site as opposed to involving the O(1) uranyl site. This is consistent with the understanding of the strength of the uranyl bond over the equatorial U-O

bonds[32], and with the diffraction studies described earlier in this chapter. In β-$SrUO_{3.75}$, an oxygen vacancy occurring at the O(3) site has a slightly lower energy than those containing a single defect at the O(1) uranyl, or the O(2) site, but its energy is still 0.5 eV higher than the most favourable configuration of defects in β-$SrUO_{3.75}$.

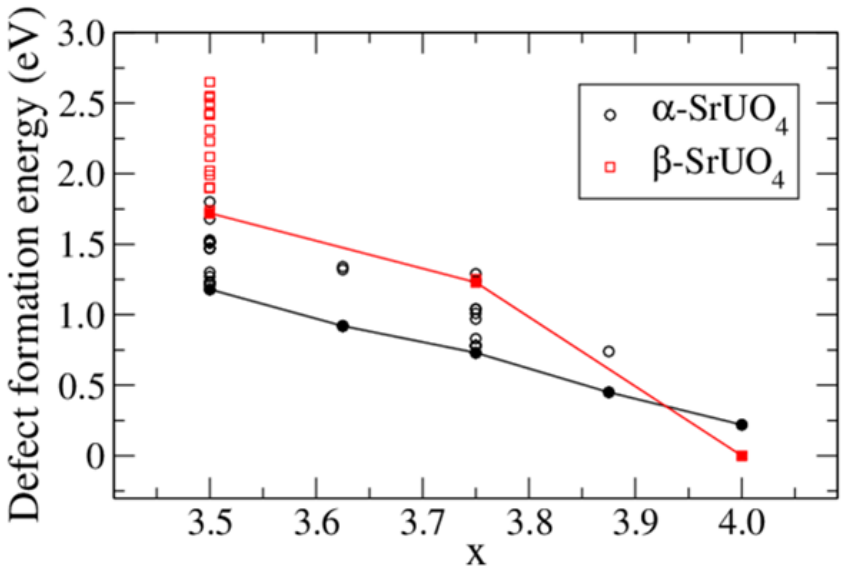

FIGURE 3.12: Defect formation energies of α (black circles) and β (red squares) as a function of oxygen content in $SrUO_x$, obtained using the PBE+U approach for various possible arrangements of vacancies allowed by the model system. The filled circles represent the most stable structures for each phase at specific oxygen content. Solid lines represent the trends as a function of oxygen content and are provided for visual guidance.

As evident in Figure 3.12, introduction of defects leads to an increase in energy for both phases when compared to the stoichiometric oxides. However, the α phase becomes lower in energy than the β in every case when defects are included in the structures. This explains why β-$SrUO_4$ cannot form without a source of resupplying oxygen during its transformation from α-$SrUO_4$. That a stoichiometric sample of α-$SrUO_4$ could be generated through low temperature treatment in an oxygen atmosphere is attributed to its metastability. The preference for α-$SrUO_4$ to retain defects, as indicated by the DFT+U calculations, may potentially be reflected in the initial reduction step when it is heated towards 400 ^{o}C that is a temperature activated loss of oxygen. It is postulated this process is synergistically coupled with the reduction of uranium and appears to reduce the activation energy barrier towards the transformation to β-$SrUO_4$.

With the results and calculations presented thus far, the phase transformation and structural relationship between α-$SrUO_4$ and β-$SrUO_4$ can be unequivocally understood. The unusual oxygen transport behaviour apparent in the phase transformation, shows that $SrUO_4$ must be an oxide conductor. Whilst oxygen diffusion via interstitial sites is crucial for oxygen mobility [1], diffusion along grain boundaries is also well documented [41]. Despite the contrasting designs of the S-XRD and NPD experiments used to study the α-$SrUO_4 \rightarrow \beta$-$SrUO_4$ phase transformation, it is still not clear whether the oxygen diffusion occurs interstitially, via grain boundaries or by a combination of both. It further remains an interesting question if the oxygen conduction present is of a magnitude suitable for oxygen ion conductor application. Although the use of a uranium oxide in such an application may be surprising, it is not a novel contemplation. UO_2 has been shown [42] to exhibit ionic conductivities at modest temperatures whereas some other studies have tailored their synthesis towards directly applying uranium oxide derivatives as oxygen ion fuel cell materials [43]. Subsequently, investigations utilising inelastic neutron scattering and also conductivity measurements are desirable to examine this potential application.

3.4 Chapter Conclusion

Using a combination of experimental and theoretical methods the critical role of anion vacancies and the oxygen potential of the atmosphere has upon the phase transformation between α-$SrUO_4$ and β-$SrUO_4$ has been revealed. Remarkably the α to β phase transformation is observed to involve the thermal regulation of oxygen ions through the sequential reduction and then re-oxidation of U^{6+} prior to transformation to stoichiometric β-$SrUO_4$. NPD measurements demonstrate this oxygen transport mechanism is discriminative, involving the non-uranyl oxygen O(2) site of α-$SrUO_4$ whilst the uranyl O(1) site is essentially a spectator. This is supported by DFT+U calculations which give insight into the inability for vacancies to form in β-$SrUO_4$and provides insight into the necessity for an oxidising atmosphere to be present for the transformation to proceed. That extensive vacancies form prior to the transformation is postulated to be synergistically coupled with the reduction of uranium, which reduces the activation energy barrier of the transformation. Although the oxygen transport pathways are not entirely clear, a considerable amount of ions are accessible for conduction, particularly when the maximum amount of vacancies are formed, even in the presence of oxygen this is $\sim SrUO_{3.6}$. It appears that $SrUO_4$ behaves as a temperature activated oxygen ion conduit, a desirable property often sort after in solid oxide fuel cell design and application.

References

1. Wind, J., Polt, J., Zhang, Z., Blom, D. A., Vogt, T., Withers, R. L., and Ling, C. D. *Chemistry of Materials* **29**(21), 9171–9181 (2017).

2. Battle, P. D., Catlow, C. R. A., Drennan, J., and Murray, A. D. *Journal of Physics C-Solid State Physics* **16**(17), L561–L566 (1983).

3. Sickafus, K. E., Grimes, R. W., Valdez, J. A., Cleave, A., Tang, M., Ishimaru, M., Corish, S. M., Stanek, C. R., and Uberuaga, B. P. *Nature Materials* **6**(3), 217–223 (2007).

4. Forgeron, T., Brachet, J. C., Barcelo, F., Castaing, A., Hivroz, J., Mardon, J. P., and Bernaudat, C. *Experiment and modeling of advanced fuel rod cladding behavior under LOCA conditions: Alpha-beta phase transformation kinetics and EDGAR methodology*, volume 1354 of *American Society for Testing and Materials Special Technical Publication*. (2000).

5. Sickafus, K. E., Matzke, H., Hartmann, T., Yasuda, K., Valdez, J. A., Chodak Iii, P., Nastasi, M., and Verrall, R. A. *Journal of Nuclear Materials* **274**(1), 66–77 (1999).

6. Kleykamp, H. *Journal of Nuclear Materials* **131**(2-3), 221–246 (1985).

7. Morelon, N. D., Ghaleb, D., Delaye, J. M., and Van Brutzel, L. *Philosophical Magazine* **83**(13), 1533–1550 (2003).

8. Fujino, T., Masaki, N., and Tagawa, H. *Zeitschrift Fur Kristallographie* **145**(3-4), 299–309 (1977).

9. Tagawa, H. and Fujino, T. *Journal of Inorganic & Nuclear Chemistry* **40**(12), 2033–2036 (1978).

10. Tagawa, H. and Fujino, T. *Inorganic & Nuclear Chemistry Letters* **13**(10), 489–493 (1977).

11. Tagawa, H., Fujino, T., and Yamashita, T. *Journal of Inorganic & Nuclear Chemistry* **41**(12), 1729–1735 (1979).

12. Pialoux, A. and Touzelin, B. *Canadian Journal of Chemistry* **77**(8), 1384–1393 (1999).

13. Murphy, G., Kennedy, B. J., Johannessen, B., Kimpton, J. A., Avdeev, M., Griffith, C. S., Thorogood, G. J., and Zhang, Z. M. *Journal of Solid State Chemistry* **237**, 86–92 (2016).

14. Tagawa, H. and Fujino, T. *Inorganic & Nuclear Chemistry Letters* **16**(2), 91–96 (1980).

15. Liss, K. D., Hunter, B., Hagen, M., Noakes, T., and Kennedy, S. *Physica B-Condensed Matter* **385-86**, 1010–1012 (2006).

16. Wallwork, K. S., Kennedy, B. J., and Wang, D. *The high resolution powder diffraction beamline for the Australian Synchrotron*, volume 879 of *AIP Conference Proceedings*, 879–882. Amer Inst Physics, Melville (2007).

17. Larson, A. C. and Dreele, R. B. V. Technical report, Los Alamos National Laboratory Report.

18. Toby, B. H. *Journal of Applied Crystallography* **34**, 210–213 (2001).

19. Toby, B. H. and Von Dreele, R. B. *Journal of Applied Crystallography* **46**(2), 544–549 (2013).

20. Glover, C., McKinlay, J., Clift, M., Barg, B., Boldeman, J., Ridgway, M., Foran, G., Garret, R., Lay, P., and Broadbent, A. *AIP Conference Proceedings* **882**(1), 884–886 (2007).

21. Johannessen, B., Hussain, Z. S., East, D. R., and Gibson, M. A. *An in-situ heater for the XAS beamline (12-ID) in Australia*, volume 430 of *Journal of Physics Conference Series*. (2013).

22. Ravel, B. and Newville, M. *Journal of Synchrotron Radiation* **12**(4), 537–541 (2005).

23. Giannozzi, P., Baroni, S., Bonini, N., Calandra, M., Car, R., Cavazzoni, C., Ceresoli, D., Chiarotti, G. L., Cococcioni, M., Dabo, I., Dal Corso, A., de Gironcoli, S., Fabris, S., Fratesi, G., Gebauer, R., Gerstmann, U., Gougoussis, C., Kokalj, A., Lazzeri, M., Martin-Samos, L., Marzari, N., Mauri, F., Mazzarello, R., Paolini, S., Pasquarello, A., Paulatto, L., Sbraccia, C., Scandolo, S., Sclauzero, G., Seitsonen, A. P., Smogunov, A., Umari, P., and Wentzcovitch, R. M. *Journal of Physics-Condensed Matter* **21**(39) (2009).

24. Cococcioni, M. and de Gironcoli, S. *Physical Review B* **71**(3), 035105 (2005).

25. Perdew, J. P., Burke, K., and Ernzerhof, M. *Physical Review Letters* **77**(18), 3865–3868 (1996).

26. Perdew, J. P., Ruzsinszky, A., Csonka, G. I., Vydrov, O. A., Scuseria, G. E., Constantin, L. A., Zhou, X. L., and Burke, K. *Physical Review Letters* **100**(13), 136406.

27. Vanderbilt, D. *Physical Review B* **41**(11), 7892–7895 (1990).

28. Methfessel, M. and Paxton, A. T. *Physical Review B* **40**(6), 3616–3621 (1989).

29. Vallet, V., Wahlgren, U., and Grenthe, I. *Journal of Physical Chemistry A* **116**(50), 12373–12380 (2012).

30. Tagawa, H. and Fujino, T. *Inorganic & Nuclear Chemistry Letters* **13**(10), 489–493 (1977).

31. Takahashi, K., Fujino, T., and Morss, L. R. *Journal of Solid State Chemistry* **105**(1), 234–246 (1993).

32. Denning, R. G. *Journal of Physical Chemistry A* **111**(20), 4125–4143 (2007).

33. Gibson, J. K., Haire, R. G., Santos, M., Marcalo, J., and de Matos, A. P. *Journal of Physical Chemistry A* **109**(12), 2768–2781 (2005).

34. Motohashi, T., Hirano, Y., Masubuchi, Y., Oshima, K., Setoyama, T., and Kikkawa, S. *Chemistry of Materials* **25**(3), 372–377 (2013).

35. Piovano, A., Agostini, G., Frenkel, A. I., Bertier, T., Prestipino, C., Ceretti, M., Paulus, W., and Lamberti, C. *Journal of Physical Chemistry C* **115**(4), 1311–1322 (2011).

36. Shannon, R. *Acta Crystallographica Section A* **32**(5), 751–767 (1976).

37. Zhu, Y., Withers, R. L., Bourgeois, L., Dwyer, C., and Etheridge, J. *Nature Materials* **14**, 1142 (2015).

38. Zhang, G. J., Zou, J., Ni, D. W., Liu, H. T., and Kan, Y. M. *Journal of Inorganic Materials* **27**(3), 225–233 (2012).

39. Beridze, G. and Kowalski, P. M. *Journal of Physical Chemistry A* **118**(50), 11797–11810 (2014).

40. Blanca-Romero, A., Kowalski, P. M., Beridze, G., Schlenz, H., and Bosbach, D. *Journal of Computational Chemistry* **35**(18), 1339–1346 (2014).

41. De Souza, R. A., Pietrowski, M. J., Anselmi-Tamburini, U., Kim, S., Munir, Z. A., and Martin, M. *Physical Chemistry Chemical Physics* **10**(15), 2067–2072 (2008).

42. Tsuji, T., Matsui, T., Abe, M., and Naito, K. *Journal of Nuclear Materials* **168**(1-2), 151–156 (1989).

43. Runge, H. and Greenblatt, M. *Solid State Ionics* **177**(3-4), 269–274 (2006).

Chapter 4

Creating Order from Disorder: Symmetry Lowering and Oxygen Defect Ordering with Heating in $SrUO_{4-x}$

This chapter is adapted from a manuscript titled "Unexpected Crystallographic Phase Transformation in Nonstoichiometric $SrUO_{4-x}$: Reversible Oxygen Defect Ordering and Symmetry Lowering with Increasing Temperature" by G. L. Murphy *et al.* that has been published in the journal *Inorganic Chemistry*.

4.1 Introduction

Recent investigations using total scattering methods and high resolution neutron diffraction have revealed the intricate nature of local anionic order within simple binary uranium oxides, UO_2 [1] and U_4O_9 [2], and the oxidation pathways that occur between these [3]. In these materials markedly different structural properties and physical phenomena can be realised through the subtle variation in short-range interactions and the interplay of anions and associated vacant sites. In Chapter 3 it was observed that under the high vacuum conditions of the NPD experiment, α-$SrUO_{4-x}$ achieves a maximum x value of approximately 0.4, and a similar value was observed during S-XRD experiment under oxidising conditions. This composition indicates that mixed uranium valence states are present (U^{6+} and U^{5+}). The ability for defects to form in materials is a consequence of a variety of structural and chemical factors where their inventory can be controlled and expanded further, for instance, through chemical and thermal pressure. Consequentially, it is postulated that the continued reduction of α-$SrUO_{\sim 3.6}$ leading to an increase in the number of oxygen defects, and electron occupancy in the uranium $5f$ orbitals, could result in the formation of a metastable structure, particularly if an oxygen stoichiometry of $SrUO_{3.5}$ corresponding to U^{5+} could be achieved. This possibility is reflected in literature with some tentative reports on the existence of $SrUO_{3+x}$ (with x = 0 to 0.5) structural variants [4,5]. These studies [4,5] suffer from low resolution measurements, leading to poor precision in the structural descriptions and a general paucity of structural-chemical information.

This chapter is directed at understanding the structural behaviour and response of α-$SrUO_4$ when pushed below the apparent sub-stoichiometric limit of $SrUO_{\sim 3.6}$, observed in Chapter 3. This involved using *in situ* synchrotron X-ray diffraction at high temperature under reducing conditions in the form of flowing high purity hydrogen gas employing a Norby-Flow cell apparatus [6]. The results obtained were supplemented with *ab initio* methods in the form of density functional theory in order to try and understand the anomalous transformative phenomena uncovered in this chapter, including the formation of a novel triclinic phase δ-$SrUO_{4-x}$, formed via reversible symmetry lowering and oxygen ordering at high temperatures.

4.2 Experimental

4.2.1 *In Situ* Synchrotron X-ray Powder Diffraction

Synchrotron X-ray diffraction (S-XRD) measurements were performed at the Australian synchrotron powder diffraction beamline[7]. A finely ground polycrystalline sample of α-$SrUO_4$ was mixed with coarse analytical grade quartz glass at a 50:50 ratio by w.t%. The mixture was loaded into a 0.8 mm diameter quartz capillary where the ends were loaded with course analytical grade quartz glass followed by glass wool in order to promote gas flow-through and mitigate against sample loss. The capillary was mounted on a goniometer equipped with a Norby-flow cell apparatus[6] that allowed rocking during S-XRD measurement to minimise the effects of preferred orientation. The Norby-flow cell equipped with a sample is presented in Figure 4.1. The gas inlet line was connected to the flow cell via a flow meter to ensure a constant flow of high purity hydrogen gas ($\geq$ 99.99% with oxygen $\leq$10 ppm and moisture $\leq$ 20 ppm). Below the capillary a FMB-Oxford hot air blower was placed to allow temperature control. Prior to variable temperature measurements the sample was flushed with high purity H_2 gas for 30 minutes at room temperature to ensure the sample was sufficiently soaked in gas and to ensure constant gas flow. Temperatures were increased at a ramp rate of 5 ^{o}C per minute and decreased at a rate of 25 ^{o}C per minute. The data collection was commenced after a 30 second delay at temperature to allow thermal equilibration. Data were collected for 5 minutes at each of the two positions of the MYTHEN detector at temperature steps from room temperature to 1000 ^{o}C. The wavelength was determined to be 0.77466 Å, calibrated using a NIST LaB_6 standard.

4.2.2 Superstructure Analysis

The structure of δ-$SrUO_4$ was analysed using TOPAS Academic (TA)[8,9] and ISODISTORT[10] against S-XRD data collected at 1000 ^{o}C by Dr Chun-Hai Wang. The high temperature structure of ordered δ-$SrUO_{4-x}$ (superstructure, lower symmetry) was considered to be a distortion of the low temperature disordered α-$SrUO_{4-x}$ phase (higher symmetry). The structural model was developed using the following steps to avoid possible over-parameterization and to obtain a stable refinement, reflecting the significantly lower X-ray scattering form factor of oxygen atoms relative to the heavier uranium atoms. Firstly, an average structural model of δ-$SrUO_{4-x}$, in space group $R\bar{3}m$, was refined without considering the supercell

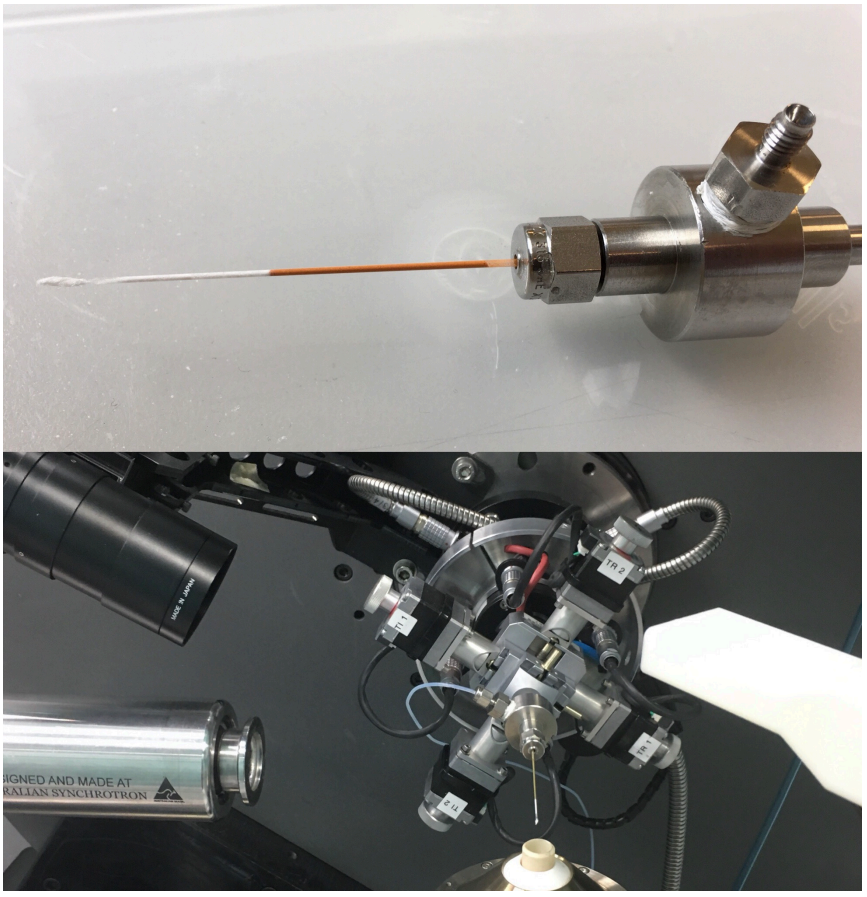

FIGURE 4.1: (Top) Norby-Flow cell equipped with a sample of α-$SrUO_{4-x}$ and (bottom) Norby-flow cell mounted on the Australian Synchrotron Powder Diffraction beamline diffractometer.

reflections. Then, symmetry representation analysis was applied in order to build a model for δ-$SrUO_{4-x}$, starting with the refined α-$SrUO_{4-x}$ model and taking into account the supercell reflections. A distortion model (triclinic cell in space group $P\bar{1}$) with commensurate distortion vector k = $[\frac{1}{4}\ \frac{1}{4}\ \frac{3}{4}]$ was used and distortion modes were refined to account for the positions of the observed supercell reflections. Bond distances restraints of 1.99 $\pm$ 0.02 and 2.33 $\pm$ 0.02 Å with a weighting of 1 were imposed for the uranyl oxo like and equatorial uranium-oxygen bonds respectively. In the final refinement cycles the structural model was fully relaxed with all free parameters refined.

4.2.3 Density Functional Theory Calculations

Ab initio calculations were performed with density functional theory (DFT) using the plain-wave Quantum-ESPRESSO simulations package[11]. The computational setup was exactly the same as that used in Chapter 3 for the α and β phases in $SrUO_{4-x}$. The plane-wave energy cut-off was set to 50 Ryd and ultrasoft pseudopotentials were used to mimic the presence of core electrons[12]. To be consistent with previous calculations PBE exchange-correlation functionals were applied. The stoichiometric δ phase was modelled by 2x2x2 supercell containing 192 atoms. Consequently, gamma point (k-point grid) calculations were sufficient to achieve a converged solution. The results of these calculations are consistent with the computation of a smaller 1x1x1 supercell but the larger supercell was used as it provided better flexibility to consider different O-vacancy arrangements. In order to account for electronic correlations the DFT+U method was applied, but with the Hubbard model computed *ab initio* using the linear response method of Cococcioni and de Gironcoli[13]. The same procedure has been successfully tested on large sets of uranium-bearing molecular and solid complexes[14] and applied in computation of the α and β phases of $SrUO_{4-x}$[15]. The derived Hubbard U parameter used in the current study is 2.5 eV, which is the same value as derived for the α and β phases of $SrUO_{4-x}$ in Chapter 3. This value is expected for U(VI) and U(V) compounds[14]. This analysis was conducted by Dr George Beridze and Dr Piotr Kowalski.

4.3 Results and Discussion

4.3.1 *In Situ* Synchrotron X-ray Powder Diffraction

The temperature dependence of α-$SrUO_4$ heated under high purity hydrogen to 1000 ^{o}C was established by S-XRD. The thermo-diffraction measurements could be divided into four regions of interest with respect to the temperature profile. From 25 to 75 ^{o}C the samples remains single (rhombohedral) phase with unexceptional thermal expansion. Considering the oxygen sensitivity of α-$SrUO_4$ described in Chapter 3 and previously[16,17] it is best to describe the sample below 125 ^{o}C as α-$SrUO_{4-x}$ due to the exposure to the hydrogen atmosphere. Heating the sample towards 150 ^{o}C resulted in the formation of weak reflections to the left of some strong Bragg reflections, most obvious near the reflections at $2\theta = 13.0$ and 13.7^o as evident in Figure 4.2. As the sample was further heated to 200 ^{o}C the intensity of these reflections increased while the reflections from rhombohedral α-$SrUO_{4-x}$ phase began to lose intensity, indicating that the sample was

undergoing a discontinuous first order phase transformation. The two-phase region co-exists up until 350 ^{o}C, thereafter the sample is single phase. This new phase was examined against reported $SrUO_{4-x}$ phases such as rhombohedral γ-$SrUO_{4-x}$ [17,18] and a reported perovskite-like phase [4] however the present phase did not match any of these. This novel phase is denoted disordered δ-$SrUO_{4-x}$. Examination of several of the Bragg reflections from α-$SrUO_{4-x}$ during the phase transformation, including the ones presented in Figure 4.2 shows they split upon heating, suggesting a structure relationship exists between the α and δ phases. That various Bragg reflections split indicates the crystallographic symmetry is lowered.

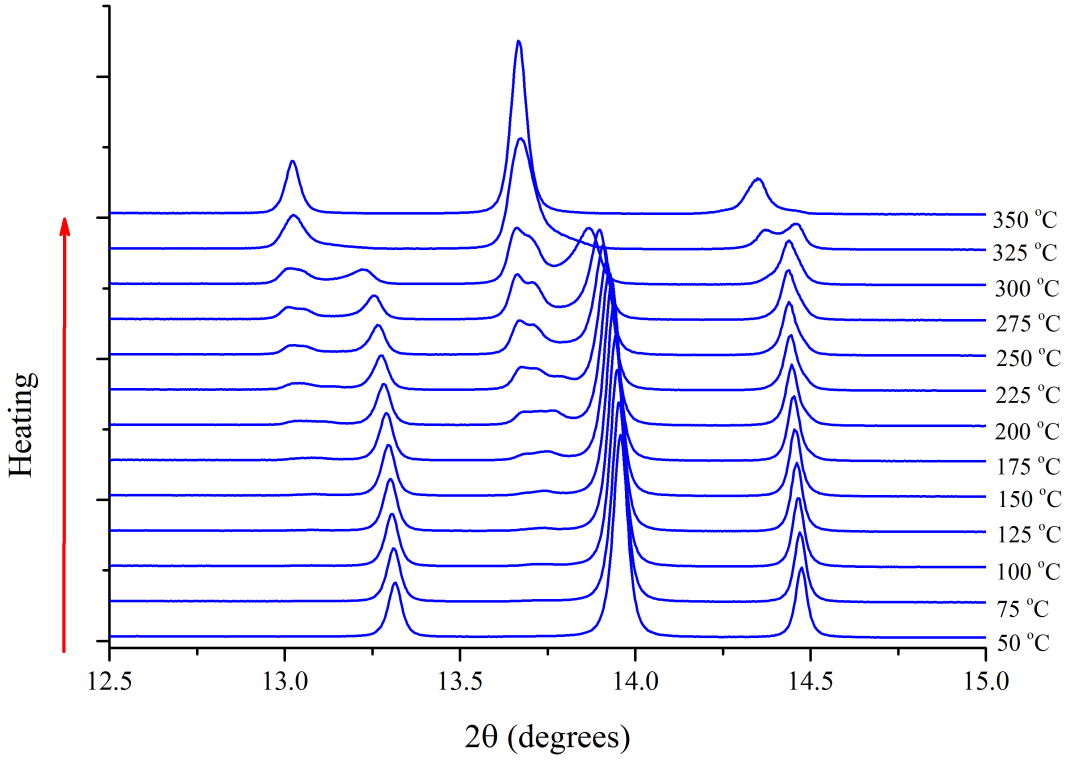

FIGURE 4.2: S-XRD data at 2θ ranging from 12.5 to 15^{o}, illustrating the temperature dependence of α-$SrUO_{4-x}$ heated from 50 to 350 ^{o}C under high purity hydrogen flow, where the onset of the disordered δ-$SrUO_{4-x}$ phase and loss of the α-$SrUO_{4-x}$ phase is apparent with increasing temperature. Note the splitting of the peak near 14^{o} indicating the lowering of symmetry with temperature.

The temperature dependence of the S-XRD patterns of δ-$SrUO_{4-x}$ from 350 to 1000 ^{o}C is presented in Figure 4.3. From 350 to 450 ^{o}C the diffraction profiles suggest that the sample remains single phase disordered δ-$SrUO_{4-x}$ where a gradual shift of Bragg reflections to lower angle is observed corresponding to thermal expansion. Interestingly there is variability in the relative shift of the Bragg reflections indicative of anisotropic thermal expansion such that some reflections do not seemingly shift whereas those that do

shift, do so until approximately 450 ^{o}C. Thereafter the thermal anisotropy is replaced by relative isotropic shifting of the Bragg reflections corresponding to, the as expected, thermal expansion. Coinciding with this loss of anisotropy was the appearance of extremely weak reflections at low 2θ as illustrated in the inset of Figure 4.3. Continued heating towards 1000 ^{o}C, while maintaining the constant flow of hydrogen, did not result in any changes to the diffraction patterns collected other than peak shifts due to thermal expansion. The intensity of the weak reflections does not seemingly vary with heating. Importantly these reflections can be considered as superlattice reflections indicative of symmetry lowering, likely involving the anionic sub-lattice considering their intensities, although it is also plausible they are a result of sample decomposition.

Maintaining the hydrogen flow, the sample was cooled to 50 ^{o}C relatively rapidly. Examination of the resultant S-XRD profile showed that it contained two phases both of which could be refined against rhombohedral models in space group $R\bar{3}m$. This is consistent with the re-formation of α-$SrUO_{4-x}$, albeit as two phases with slightly different oxygen stoichiometries and hence lattice parameters, see Figure 4.4 for refinement profiles. The two cation sites in both phases were completely occupied. It was not possible to refine the anion occupancies of the two phases, but it seems reasonable to propose that the larger cell contains more vacancies and hence the uranium is more reduced and the two phase anomaly is a consequence of variable amounts of defects between the two phases. Importantly, the observed high temperature weak reflections at low 2θ were no longer visible in the diffraction pattern. If they remained it would strongly suggest they were related to partial sample decomposition. That they are lost with the loss of the δ phase upon cooling suggests they are a structural feature of this and are indeed superlattice reflections, indicating a form of long range order is present at high temperature but absent at low temperature.

To further examine these tentative deductions the sample was reheated whilst under the hydrogen flow to 550 ^{o}C and re-cooled back to 50 ^{o}C in measurement increments of 50 ^{o}C. A portion of this data is presented in Figure 4.5. It was initially observed that the Bragg reflections corresponding to the larger rhombohedral cell phase began to lose intensity, whereas those of the smaller rhombohedral cell began to increase. This continued up until approximately 250 ^{o}C. This is consistent with thermally induced oxygen diffusion within the sample that allows it to achieve a near-equilibrium state in terms of oxygen stoichiometry. Around 300 ^{o}C additional Bragg reflections near 13.0 and 13.7^o in Figure 4.5, were observed to re-emerge in the diffraction profiles, consistent with reformation of the δ-$SrUO_{4-x}$ phase. A two-phase region persisted between 300 and 400 ^{o}C, thereafter the diffraction data was indicative of the sample being

single phase single δ-$SrUO_{4-x}$. Continual heating to above 450 ^{o}C resulted in the reappearance of the extremely weak superlattice reflections at $8^o < 2\theta < 12^o$. These persisted to 550 ^{o}C, at which time the sample was re-cooled towards 50 ^{o}C. The S-XRD profile revealed that cooling the sample results in the loss of the superlattice reflections below 250 ^{o}C, before the sample undergoes a transformation at 200 ^{o}C. The low temperature phase could be refined against a single phase rhombohedral structure in space group $R\bar{3}m$ consistent with α-$SrUO_{4-x}$. The Rietveld refinement profile is illustrated in Figure 4.4. That the superlattice reflections emerge upon heating and are lost upon cooling demonstrates that these are indicative of a reversible phase transformation and not sample decomposition as previously speculated. It should be noted that the loss of superlattice reflections with cooling occurs at a lower temperature than their appearance upon heating, this is likely a result of slow reaction kinetics as the cooling rate (25 ^{o}C/min) is much faster than the heating rate (5 ^{o}C/min). The maximum heating rate of the furnace is 5 ^{o}C/min, whereas faster cooling rates are possible.

Comparing the diffraction pattern at 50 ^{o}C after the heating cycle (Figure 4.4c) with that of α-$SrUO_{4-x}$ prior to heating to 1000 ^{o}C and 550 ^{o}C, showed (Figure 4.4a) it to be essentially identical, being fitted well against a rhombohedral α-$SrUO_{4-x}$ structure in space group $R\bar{3}m$. This demonstrates the sample stability against decomposition when heated to 1000 ^{o}C under a H_2 environment. To recapitulate, heating α-$SrUO_{4-x}$ under a H_2 gas flow results in a reversible first order transformation forming a novel phase denoted δ-$SrUO_{4-x}$. Further heating results in the appearance of weak superlattice reflections, most obvious in the region $8^o \leq \theta \leq 12^o$. This suggests the formation of a superstructure containing a long range ordered component, which considering the intensities of the superlattice reflections, is related to the anionic sublattice and most likely to oxygen vacancy ordering. Remarkably the intensities of these Bragg reflections seem to increase with increasing temperature, suggesting ordering increases with increasing temperature. When the temperature is reduced below 200 ^{o}C the long range ordering is lost as the structure transforms to α-$SrUO_{4-x}$ which apparently contains disordered oxygen vacancies. Heating the sample again to 550 ^{o}C and re-cooling demonstrates the transformation is completely reversible and pertinently, is not a consequence of reduction or structural degradation but indicates it is thermodynamic in origin. It is apparent that for the transformation to occur a critical number of vacancies must be generated in the rhombohedral structure. The transformation was not observed in the *in situ* neutron diffraction measurements described experiment in Chapter 3, presumably the vacuum atmosphere used there is not sufficiently reducing for the generation of the critical amount of vacancies.

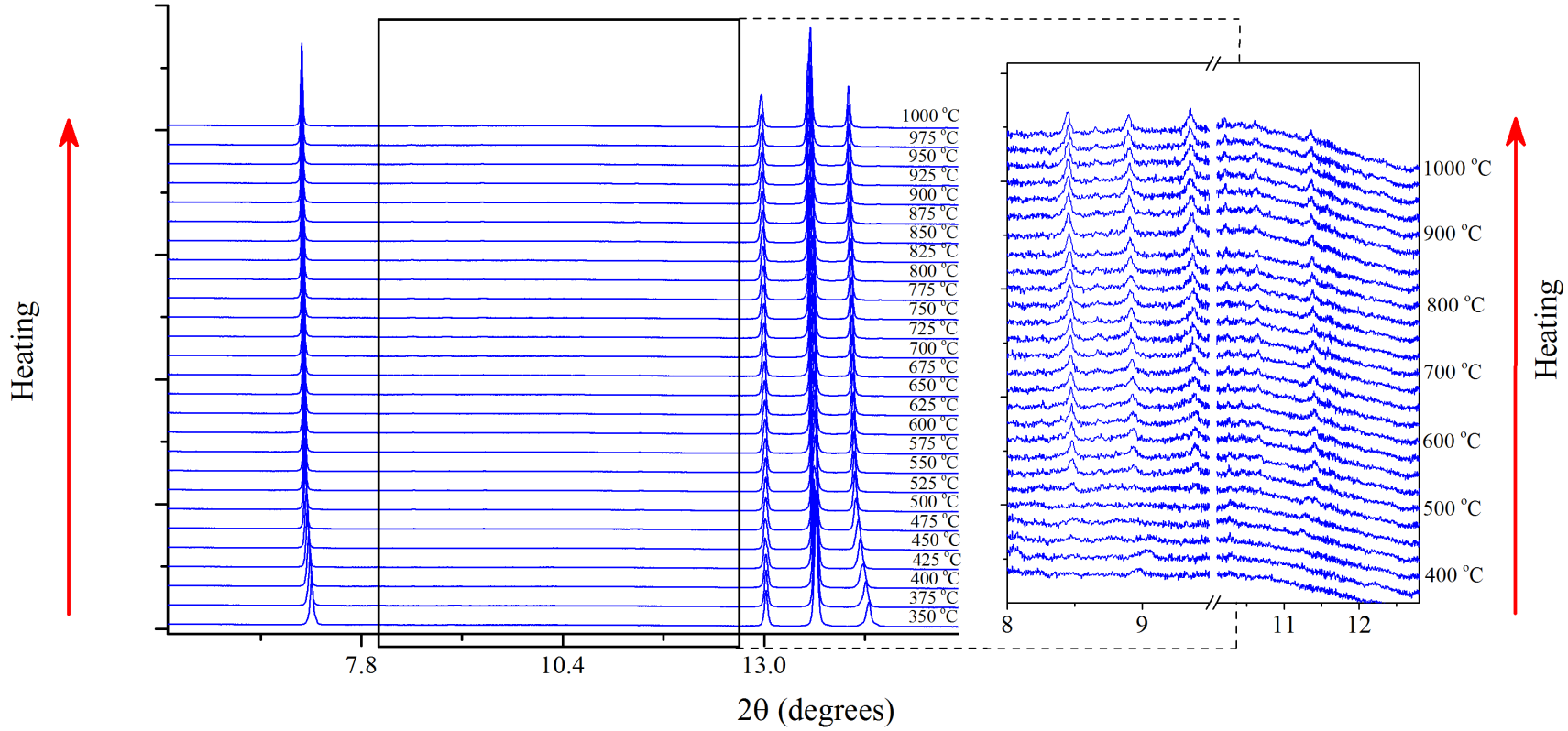

FIGURE 4.3: Variable temperature S-XRD data taken from δ-$SrUO_{4-x}$ at temperatures from 350 to 1000 ^{o}C, shown at 2θ ranging from 5.3 to 15.5^{o}. The inset illustrates the onset of superlattice reflections with heating to T $>$ 450 ^{o}C indicating the transition from the disordered δ-$SrUO_{4-x}$ to the ordered δ-$SrUO_{4-x}$.

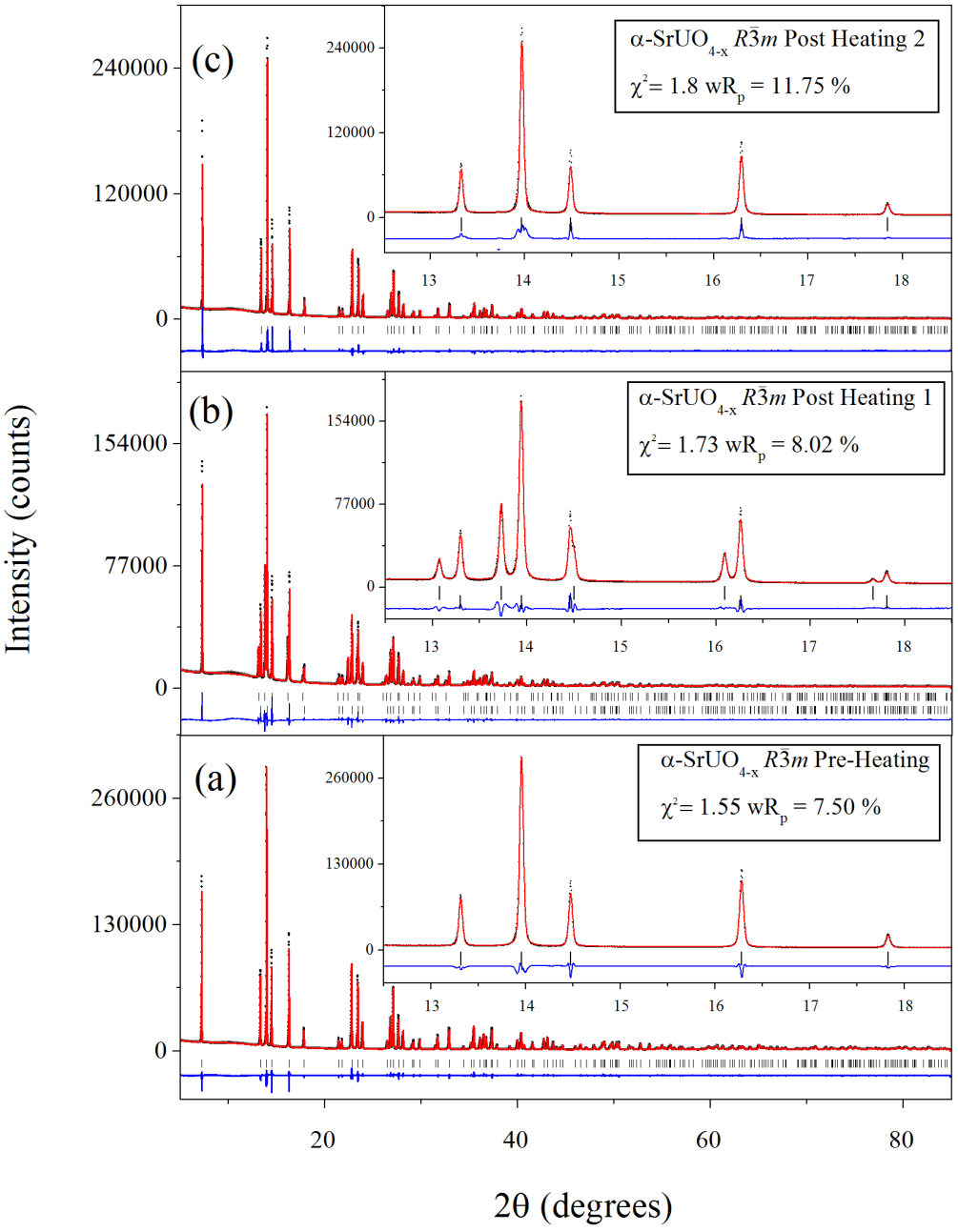

FIGURE 4.4: Rietveld profiles for α-$SrUO_{4-x}$ taken under high purity H_2 gas flow at 50 ^oC (a) before high temperature treatment, (b) after the first high temperature treatment to 1000 ^oC and (c) after the second high temperature treatment to 550 ^oC. The insets highlight the purity and absence of sample decomposition during the heating cycles. λ = 0.7746596 Å. Note the two phases apparent in the (b) profile where both phases could be refined against rhombohedral models in space group $R\bar{3}m$.

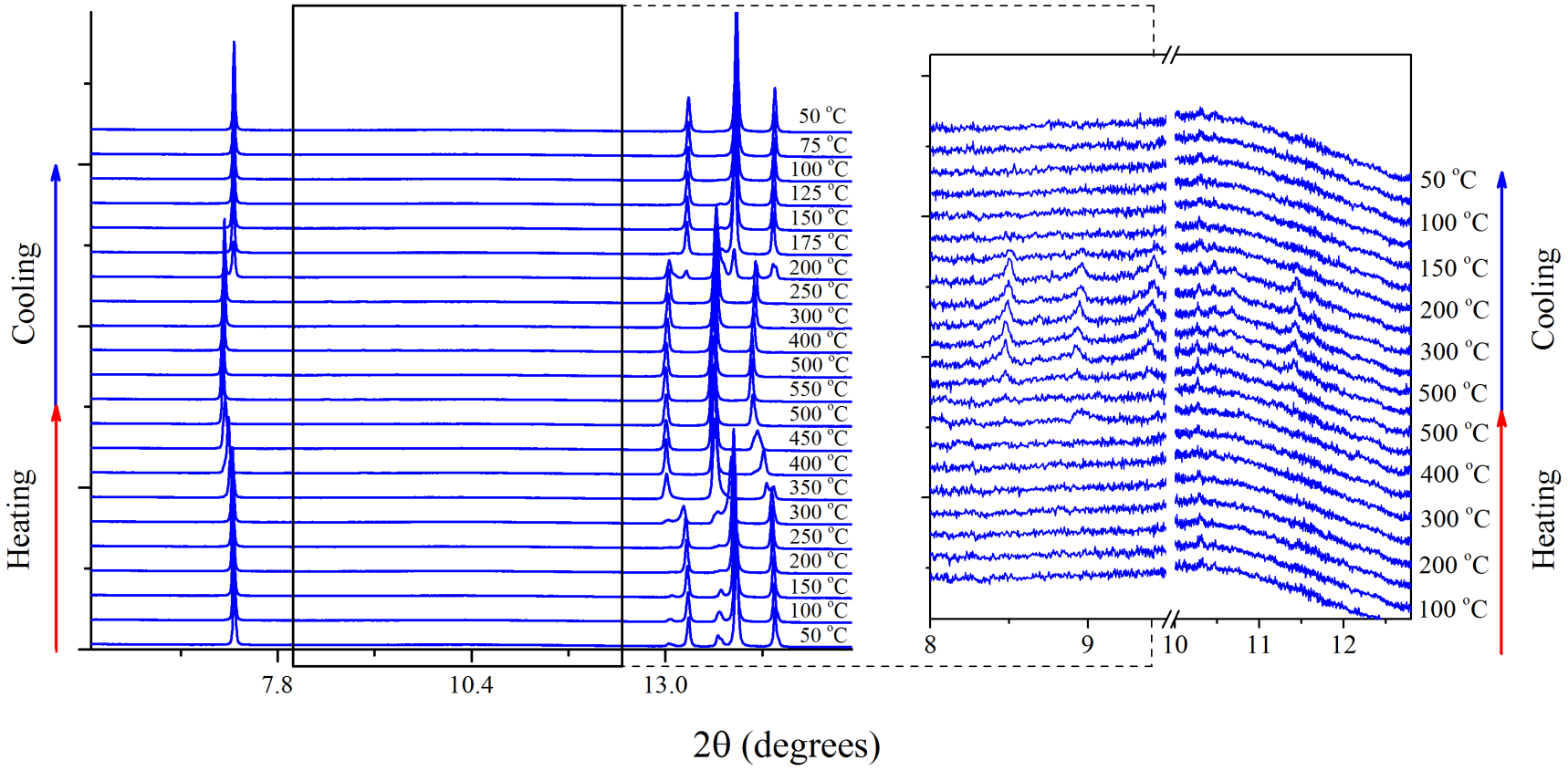

FIGURE 4.5: S-XRD heating data taken from $SrUO_{4-x}$ at temperatures ranging from 50 to 550 ^{o}C and cooling back to 50 ^{o}C under high purity hydrogen gas flow ($5.3 \leq 2\theta \leq 15.5^{o}$). The inset illustrates the onset of superlattice reflections with heating and loss thereof from cooling, highlighting the reversibility of the disorder (at lower temperatures) and order (at higher temperatures) transformation.

4.3.2 Structural Analysis and Solution of δ-$SrUO_{4-x}$ Superstructure

The structure of δ-$SrUO_{4-x}$ was determined using symmetry representation analysis. δ-$SrUO_{4-x}$ can be considered as a distortion from α-$SrUO_{4-x}$, evident by the observed superlattice reflections in the S-XRD pattern (Figure 4.3). These reflections follow a commensurate distortion vector k = $[\frac{1}{4}\ \frac{1}{4}\ \frac{3}{4}]$ derives from the parent sub-stoichiometric rhombohedral unit cell, α-$SrUO_{4-x}$. The structural analysis of δ-$SrUO_{4-x}$ was based on S-XRD data measured under H_2 at 1000 ^{o}C, as this data showed the best resolution of the superlattice reflections with the greatest intensities. The structural model of the ordered δ-phase was built and refined with the use of the program ISODISTORT. The pattern at 1000 ^{o}C was indexed to a triclinic unit cell in space group $P\bar{1}$ with cell volume of approximately 355 Å^3. The undistorted triclinic cell, where the atoms are constrained to the equivalent positions of the parent rhombohedral cell resulted in a wR_p factor of the refinement of 9.20% and this could be significantly improved through the introduction of one displacement distortion mode for the U and Sr cations, two anion displacement distortion modes and four anion occupancy distortion modes (wR_p = 3.98%). A further relaxation of the model to allow for refinement of the anion positional parameters resulted in a slight improvement to the refinement (R_{wp} = 3.21%) with the profile shown in Figure 4.6. In the final refinement cycles the atomic displacement parameters of the various ions were constrained to be equal and U-O bond length restraints were used to obtain a stable refinement. In Figure 4.6 the intensity (I) was plotted as $\sqrt{I}$ to highlight the details of the weak superlattice reflections. The structural model, described in Table 4.1, gives an excellent fit to the experimental data in addition the positions and relative intensities of the superlattice reflections are well described. This is apparently the first triclinic structural model for $SrUO_{4-x}$ reported to date and the first to contain an ordered superlattice[4,5].

A representation of the structure of δ-$SrUO_{4-x}$ is given in Figure 4.7. Similar to other $SrUO_{4-x}$ phases, δ-$SrUO_{4-x}$ adopts a layered structure. The U-O polyhedra form UO_{4-x} layers via edge-sharing connections and the Sr^{2+} cations sit between the layers. There are two types of oxygen sites with respect to the layers, the oxo-oxygens which possess uranyl structural character at sites O(1)-O(4) and the in plane oxygens at sites O(5)-O(8). The structural analysis suggested that the four oxygen sites O(1)-O(4) were fully occupied and this was assumed in the final refinements. The occupancies of the other four anion sites O(5) - O(8) were varied in the final refinement cycles and, with the exception of O(7), these are all partially occupied. The occupancy of the O^{2-} sites is illustrated by shading of the spheres in Figure 4.7, and is tabulated in

Table 4.1. The refined occupancies of the O(5), O(6), O(7) and O(8) sites are 0.90(2), 0.61(3), 1.00(3) and 0.89(3), respectively, corresponding to the compositional formula $SrUO_{3.70(3)}$. The out-of-plane oxo U-O bond length varies from 1.892(17) to 2.083(17) Å and the in plane U-O bond length ranges from 1.85(2) to 2.761(16) Å.

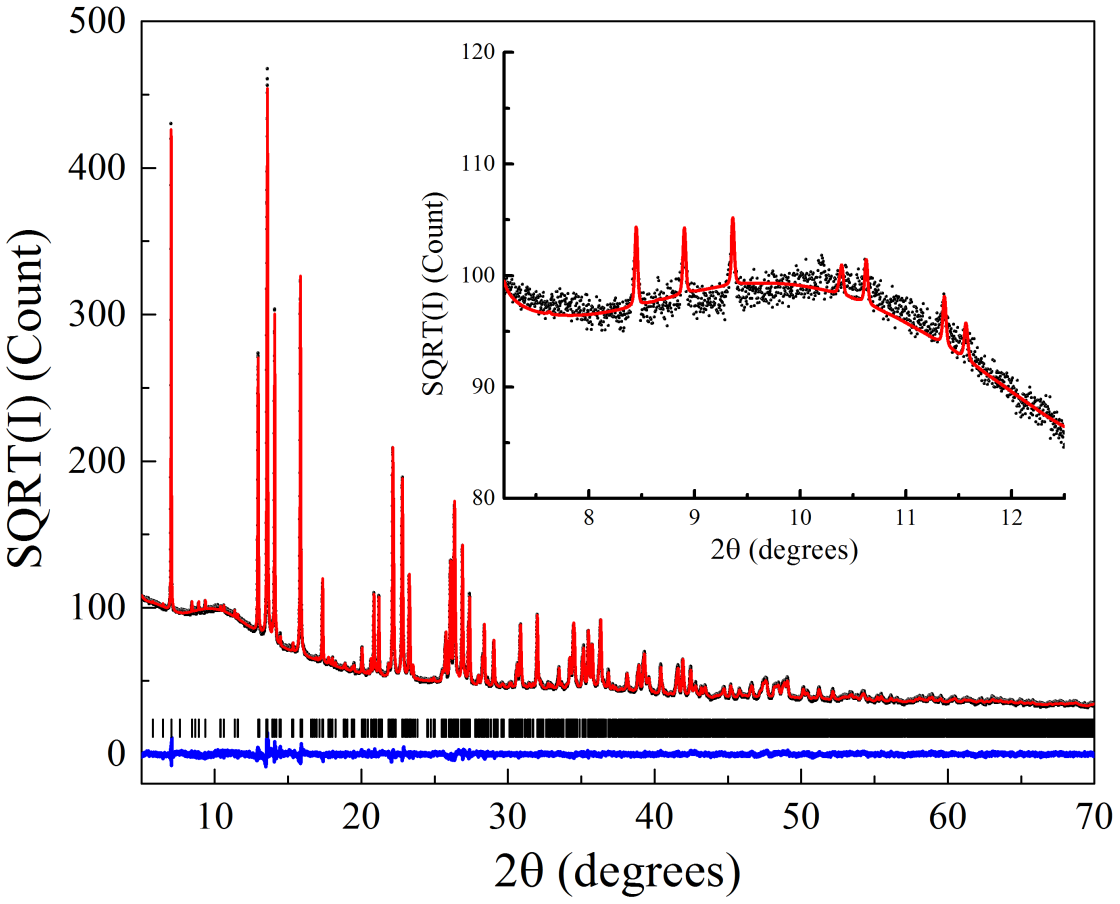

FIGURE 4.6: Rietveld refinement profile of the ordered δ-$SrUO_{4-x}$ against the S-XRD data at 1000 ^{o}C. Dots, observed; solid line, calculated curve; grey line below, difference curve; vertical tick marks, peak positions. wR_p = 3.21% and R_p = 2.42%. The square root of intensity was taken to highlight the superlattice reflections.

TABLE 4.1: Parameters of the ordered δ-$SrUO_{4-x}$ structure at 1000 ^{o}C from Rietveld refinement.

Space group:		$P\bar{1}$	Formula:		$SrUO_{3.70(3)}$
a(Å)		6.72851(3)	$\alpha(^{o})$		89.8732(6)
b(Å)		6.97217(6)	$\beta(^{o})$		107.3712(5)
c(Å)		8.06596(6)	$\gamma(^{o})$		99.9942(8)
V(Å^3)		355.159(4)	D_{theo} (g cm^{-}3)		7.20(1)
site	x	y	z	occupancy	B_{eq}(Å^2)
U(1)	0	0	0	1	2.283(9)
U(2)	0	0	0.5	1	2.283(9)
U(3)	0.0025(3)	0.4737(2)	0.2517(2)	1	2.283(9)
Sr(1)	0.4859(8)	0.7580(6)	0.6173(10)	1	2.99(3)
Sr(2)	0.4825(8)	0.7479(6)	0.1189(10)	1	2.99(3)
O(1)	0.299(3)	0.065(3)	0.067(3)	1	2.71(12)
O(2)	0.300(3)	0.073(3)	0.589(3)	1	2.71(12)
O(3)	-0.326(3)	0.444(3)	0.162(4)	1	2.71(12)
O(4)	0.323(3)	0.508(3)	0.325(3)	1	2.71(12)
O(5)	0.023(4)	0.128(3)	0.240(3)	1	2.71(12)
O(6)	-0.048(6)	0.812(4)	0.314(4)	0.90(2)	2.71(12)
O(7)	-0.035(3)	0.254(3)	-0.044(2)	0.61(3)	2.71(12)
O(8)	0.044(4)	0.297(3)	0.510(3)	0.89(3)	2.71(12)

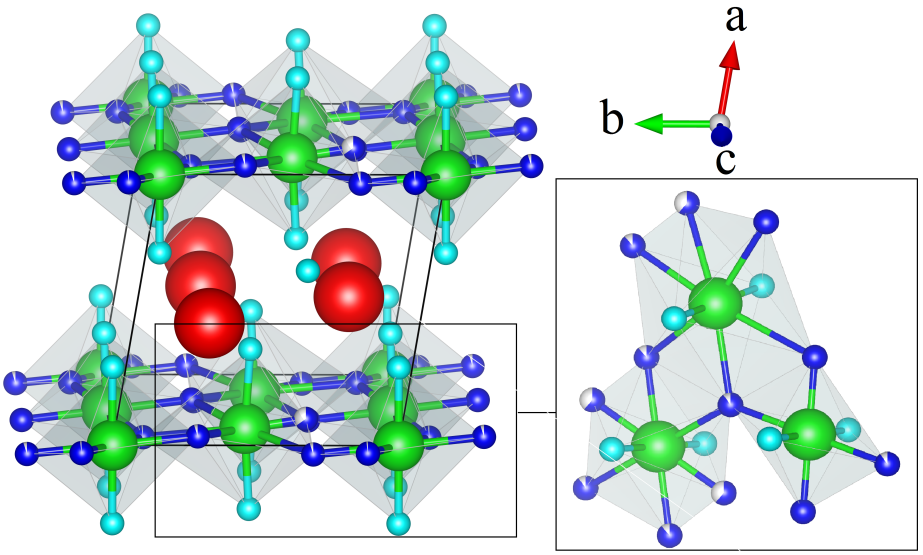

FIGURE 4.7: Representation of the ordered δ-$SrUO_{4-x}$ structure. Blue: in plane oxygen (partially shaded blue spheres denoting partial occupancy of the site), aqua: out of plane uranyl-like oxygen, green;: uranium and green: strontium.

δ-$SrUO_{4-x}$ can be regarded as a structural distortion of the rhombohedral α-$SrUO_{4-x}$ phase due to the preferential rearrangement of oxygen vacancies from selected in-plane sites. A comparison of the U-O layers in α-$SrUO_{4-x}$ and δ-$SrUO_{4-x}$ is shown in Figure 4.8. In α-$SrUO_{4-x}$ the uranium cations have (near) eight-fold coordination with oxygen forming UO_8 polyhedra where the oxygen vacancies are distributed evenly and randomly among all the in-plane oxygen sites. Each in plane oxygen atom is shared by three UO_8 polyhedra and sits at the centre of three neighbouring U atoms, forming a regular U3 triangle. This symmetry is broken in δ-$SrUO_{4-x}$ at temperatures above 450 ^{o}C. In ordered δ-$SrUO_{4-x}$ the U3 groups no longer retain a regular triangular configuration, due to the preferential loss of oxygen at the O(5), O(6), and O(8) sites. This results in a reduction of space group symmetry to triclinic. The appreciable loss at the O(6) site appears to be the main driving force for the symmetry lowering with O(6) moving away from the centre of the U3 triangles. This displacement results in a change in the effective coordination of the U(1) cation to 6 coordinate, whilst U(2) and U(3) cations remain 8-coordinate. Thus, 1/3 of the U atoms in δ-$SrUO_{4-x}$ exist as UO_6 octahedra and 2/3 as UO_8 polyhedra. Note that the U(3)-O(7) distance is relatively long at 2.761(16) Å. The refinement suggests that the anion vacancies are clustered around the U(2) and U(3) UO_8 polyhedra and are absent in the U(1) UO_6 polyhedra. This observation is similar to that made for α-$SrUO_{4-x}$ and β-$SrUO_{4-x}$ as described in Chapter 3, namely oxygen vacancies can be found in the UO_8 polyhedra of the former but are not observed in the UO_6 polyhedra of the latter.

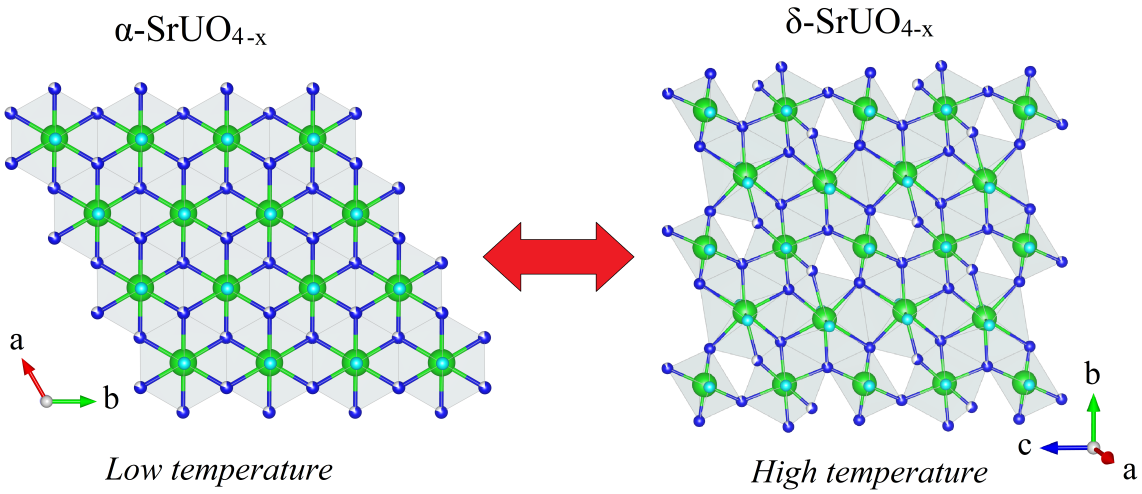

FIGURE 4.8: Representation of a U-O layer in disordered α-$SrUO_{4-x}$ and ordered δ-$SrUO_{4-x}$. Blue: in plane oxygen; aqua: out of plane oxygen, green: uranium. The apparent ordered oxygen defect sites in α-$SrUO_{4-x}$ are O(6) with occupancy of 0.61(3), as shown by the partially shaded blue spheres. The oxygen vacancies in δ-$SrUO_{4-x}$ are evenly distributed over the in plane O(2) sites i.e disordered, also shown using the partially shaded spheres.

4.3.3 *Ab Initio* Calculations

Having solved the δ-$SrUO_{4-x}$ structure its stability was examined computationally by calculating the energies for defect formation for various oxygen defect positons in a similar manor to α-$SrUO_{4-x}$ as undertaken in Chapter 3. Calculations were performed for stoichiometric, δ-$SrUO_{4-x}$, $x = 0.5$, $x = 0.25$ and $x = 0$. The three different structures were obtained by adjusting the content of the O(6) oxygen site, the site which the structural solution indicated defect formation was most prevalent (empty for $x = 0.5$ and full for $x = 0$). It is noted that the computed δ structure does not exactly represent the oxygen occupation of the observed superstructure since it does not account for the partial defects occurring on the O(5) and O(8) sites, therefore the results from the DFT calculation allow only a qualitative interpretation of the experimental results. The obtained energies are presented in Figure 4.9 together with those of the stable α and β phases calculated in Chapter 3. In the figure, the solid lines represents an apparent trend as a function of oxygen content and is provided for visual guidance. As indicated in Figure 4.9, stoichiometric δ-$SrUO_{4-x}$ is higher in energy than the corresponding δ phase by approximately 0.22 eV but has a very similar energy to the α phase. As the oxygen content is decreased, the α and δ phases become lower in energy relative to the β phase, where the calculations suggest the δ phase is slightly lower in energy than the α for all sub-stoichiometric contents.

That the δ phase is slightly lower energy than the α phase is at first glance contradictory to the experimental results, namely the α phase should be the lower energy structure as it is the low temperature structure or the δ phase should form irreversibly. However the DFT calculations do not take into account the entropic effects of the two structures. The random distribution of oxygen defects in α-$SrUO_{4-x}$ should result in additional configurational entropy (disordering) and will contribute to its stabilisation at ambient conditions. As described in Chapter 3, this sub-stoichiometric state will lead to mixed uranium valence states (namely U^{5+} and U^{6+}) forming, which allows for the possible short range ordering of, particularly, the U^{5+} cations. This local ordering should decrease as temperature is increased, giving rise to an increase in configurational entropy. Calculations support this, indicating significant short-range ordering of U^{5+} cations should be present in all phases at ambient conditions. For the δ phase a disordering energy of $\sim$ 4 kJ/mol at HT compared to 2.49 kJ/mol at ambient is calculated. This implies that disordering of U^{5+} cations should occur more easily in the δ phase than in the α phase and therefore at a critical temperature the defect ordered structure should become more favourable with respect to the overall free energy arising

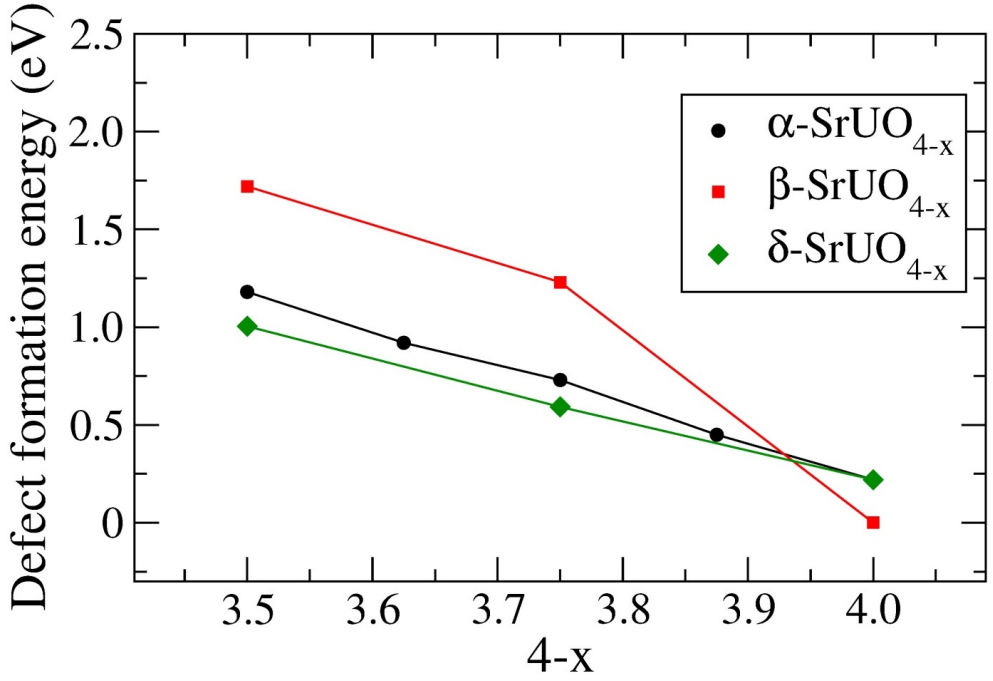

FIGURE 4.9: Defect formation energies, corresponding to the most stable oxygen vacancy arrangement, for α (black circle), β (red square) and δ (green diamond) structural phases as a function of oxygen content in $SrUO_{4-x}$, obtained using the PBE+U approach.

from this configurational electronic entropy contribution. In order to correctly describe these HT ordering effects at the quantitative level, a more complex thermodynamic modelling that accounts for short-range ordering should be applied that involves several *ab initio* sensitive U^{5+} ordered cation arrangements. This is out of the scope of the present dissertation. The importance of configurational electronic entropy has been noted[19] previously, however, with respect to literature, this appear to be the first demonstration that electronic entropy has a significant contribution towards a structure phase diagram.

4.3.4 Defect Ordering and Relation to Other Structural Systems

Ordering related to the formation of anion and cation defects in crystalline metal oxides is well known, for instance in the transition between the $A_{0.5}B_{0.5}O_{1.75}$ defect-fluorite and $A_2B_2O_7$ pyrochlore structures[20,21]. The thermally or chemically induced fluorite-pyrochlore transformation involves antisite defects, where the randomly distributed A and B type cations of the fluorite structure begin ordering in a manner that is correlated to the ordering of the anionic vacancies, ultimately leading to the formation of the ordered

pyrochlore structure[22–25]. Ionic defects have been investigated as a means of controlling the dimensionality of structures such as in the case of the reduction of the 3D structured perovskite $SrFeO_3$ to the layered 2D oxide $SrFeO_2$[26–29]. The gradual removal of lattice oxygen results in a succession of phase transformation, including the formation of the $Sr_2Fe_2O_5$ brownmillerite structure as the intermediate, which is coupled with the reduction of the Fe cation from tetravalent to trivalent. Examples of the influence of anion defects on ordering and structure transformation have also been found in actinide systems. For example the disordered fluorite structure of the mineral vorlanite, $(CaU)O_4$ can be transformed to the rhombohedral ordered protovorlanite structure $CaUO_4$ by heating[30–32]. The transition to the ordered lower symmetry triclinic δ-$SrUO_{4-x}$ from the disordered higher symmetry rhombohedral α-$SrUO_{4-x}$ does not involve a change in cation order nor is there any reduction occurring, such that it is driven purely by rearrangement of anion defects positions and is thermodynamic in origin. Whilst this ordering may be accompanied by charge ordering, it is distinct from the perovskite to brownmillerite transformation of $SrFeO_{3-x}$ in that once the ordered high temperature δ phase is formed it can reversibly transform back to the disordered low temperature α phase without a change in the average oxidation state of the uranium cations or in the concentration of oxygen vacancies. There are apparently no other examples of systems that reversibly transforms to a lower symmetry structure upon heating without a change in stoichiometry.

Prodan and Boswell postulated that the basic building elements in the defect structure of reduced $CaUO_{4-x}$ (with x = 0 - 0.5), which is isostructural with α-$SrUO_{4-x}$, are a central 6-coordinated U cation surrounded by six 7-coordinated Ca cations or a central 6-coordinated Ca cation surrounded by six 6-coordinated U cations[33]. Oxidation and reduction of $CaUO_4$ involves a change in the geometry of the uranium cations between UO_6 in reduced $CaUO_{3.5}$ and UO_8 in stoichiometric $CaUO_4$ through the formation of microdomains. That two reduced rhombohedral phases of α-$SrUO_{4-x}$ are observed in the first cooling cycle under hydrogen is in keeping with the earlier proposal of Prodan and Boswell[33]. It is postulated that the transformation from δ to α, that occurs as the sample is cooled, occurs at a temperature where oxygen conductivity and migration is inhibited, resulting in the formation of microdomains of two rhombohedral (α) phases with variable oxygen content. This may also be impacted by the rate of reformation of the intermediate disordered δ phase during cooling. It should be noted that the loss of the superlattice reflections with cooling occurs at a lower temperature than their appearance upon heating, this is likely a result of slower reaction kinetics as the cooling rate (25 ^{o}C/min) is much faster than the heating rate (5 ^{o}C/min), coupled with the coarser temperature steps used in the first cooling cycle. The

second heating/cooling cycle under hydrogen used a slower cooling rate (5 ^{o}C/min) which is believed to have allowed the oxygen to better equilibrate across the bulk sample, resulting in a single α phase. From this, oxygen conductivity in both the α and δ phases is expected to occur at modest temperatures, although this is yet to be directly established. That the oxygen defects are seemingly confined to the UO_8 polyhedra and absent in the UO_6 polyhedra is consistent with the idea propounded by Prodan and Boswell[33].

That uranium oxides can adopt complex structures is well illustrated by the recent work of Desgranges *et al.*[1] who showed that short-range order intrinsically exists in UO_2 which is best described in space group $Pa\bar{3}$ rather than $Fm\bar{3}m$ due to local distortions of the UO_8 polyhedra[1]. It is not known if similar short-range order also exists in the low temperature α-$SrUO_{4-x}$ structure and if such local order is a precursor to the formation of δ-$SrUO_{4-x}$. Examining the relaxed computed structure for the non-stoichiometric α-$SrUO_{3.5}$, as shown in Figure 4.10, it is noteworthy that there is an apparent mixture of UO_6 and UO_8 polyhedra similar to that observed in δ-$SrUO_{4-x}$. Though tentative, it is suggestive that short-range ordering could be occurring in non-stoichiometric α-$SrUO_{4-x}$, which might influence the peculiar transformation to the δ phase as observed here (see Figures 4.7 and 4.8). Further studies utilising atomic pair-distribution function analysis are desirable to address this possibility.

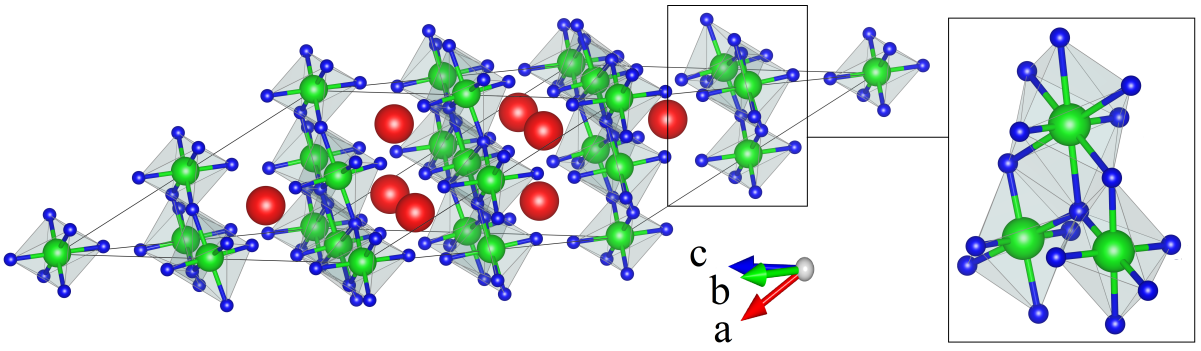

FIGURE 4.10: Computed structure for rhombohedral α-$SrUO_{3.5}$; note the apparent occurrence of both UO_6 and UO_8 as the inset highlights. Uranium, strontium, and oxygen atoms are represented as navy, green, and red respectively, in-plane and out-of-plane oxygens are not distinguished here.

The presence of the oxo uranium uranyl-like moieties in the α and δ phases is postulated to play a key role in the transformation. The structure and directionality of the uranyl-like moieties in the AUO_4 (A = Ca, Sr) oxides make them distinct from the tetragonal ABO_4 scheelite structural variants. The

scheelite structures do not display comparable ordering to that encountered here for $SrUO_4$. The oxo uranyl moiety, an example of the general actinyl moiety, is unique to the actinides and its use in chemical structural design has been limited, largely due to the difficulties in studying actinides. Although similar functional groups are known, for instance the structurally similar vanadyl group, its electronic structure and redox chemistry is markedly different from the actinyl groups[34,35]. Indeed more recent studies have demonstrated that the vanadyl group and other non-actinide surrogate elements do not replicate the unique chemistries and properties of the actinides[1,15,36–44].

The implications of the newly identified α-$SrUO_{4-x}$ to δ-$SrUO_{4-x}$ transition are potentially quite profound, as it implies materials that exist with desirable ordering properties at low temperature such as superconductors or topological insulators may be accessed at high temperature through controlled material design. Further studies are required to understand the thermodynamic origin of this fascinating phase transformation. A description is provided here based on DFT+U that reveals the importance of the entropy in the formation of the δ phase. However considering the known limitations of DFT, a more thorough experimental thermodynamic investigation is necessary to understand the origin of this novel phase transformation.

4.4 Chapter Conclusion

In summary, it is demonstrated that under highly reducing conditions oxygen deficient α-$SrUO_{4-x}$ in space group $R\bar{3}m$ undergoes a first order phase transformation above 200 ^{o}C to a new phase denoted as δ-$SrUO_{4-x}$: First as a disordered δ structure without long-range oxygen-vacancy ordering followed by an ordered δ structure at temperatures $>$ 450 ^{o}C. The ordered δ-$SrUO_{4-x}$ structure was refined against a triclinic model in space group $P\bar{1}$ and is characterised by ordering of the oxygen vacancies. Remarkably the transformation between α-$SrUO_{4-x}$ and δ-$SrUO_{4-x}$ is reversible, cooling the sample results in the reformation of the rhombohedral α-$SrUO_{4-x}$ phase in which the oxygen vacancies are disordered. That the transformation is reversible suggests that the formation of δ-$SrUO_{4-x}$ is a thermodynamically driven process, and is not caused by a change in the concentration of oxygen vacancies, which apparently remain constant under the hydrogen gas flow. This transformation has not been observed in less reduced samples of α-$SrUO_{4-x}$ demonstrating that a critical amount of oxygen defects must be present to allow their ordering and thus the formation of the δ phase. Nevertheless once obtained, ordering and symmetry lowering

with increasing temperature can be readily achieved at relatively low temperatures. Such phenomena are potentially unique to $SrUO_{4-x}$, while there are examples where oxygen vacancy ordering is favoured at high temperatures, such processes are generally irreversible [45,46]. With respect to literature there appears to be no other examples where oxygen disordering occurs upon lowering the temperature. Pertinently the transformation identified in the current study presents a novel direction for the design and acquisition of a new class of ordered materials that present their desirable ordering properties at high temperature. This is salient and relevant with respect to societally important materials such as next generation superconductors and topological insulators, which generally present their desirable ordering properties at low temperatures which are typically impractical for application and when heated, are lost to disordering processes.

References

1. Desgranges, L., Ma, Y., Garcia, P., Baldinozzi, G., Simeone, D., and Fischer, H. E. *Inorganic Chemistry* **56**(1), 321–326 (2017).

2. Desgranges, L., Baldinozzi, G., Simeone, D., and Fischer, H. E. *Inorganic Chemistry* **55**(15), 7485–7491 (2016).

3. Desgranges, L., Baldinozzi, G., Rousseau, G., Niepce, J. C., and Calvarin, G. *Inorganic Chemistry* **48**(16), 7585–7592 (2009).

4. Pialoux, A. and Touzelin, B. *Canadian Journal of Chemistry* **77**(8), 1384–1393 (1999).

5. Takahashi, K., Fujino, T., and Morss, L. R. *Journal of Solid State Chemistry* **105**(1), 234–246 (1993).

6. Norby, P. *In-situ time resolved synchrotron powder diffraction studies of syntheses and chemical reactions*, volume 228 of *Materials Science Forum*. Transtec Publications Ltd, Zurich-Uetikon (1996).

7. Wallwork, K. S., Kennedy, B. J., and Wang, D. *The high resolution powder diffraction beamline for the Australian Synchrotron*, volume 879 of *AIP Conference Proceedings*, 879–882. Amer Inst Physics, Melville (2007).

8. Coelho, A. A., Evans, J. S. O., Evans, I. R., Kern, A., and Parsons, S. *Powder Diffraction* **26**, S22–S25 (2011).

9. Evans, J. S. O. *Advanced Input Files & Parametric Quantitative Analysis Using Topas*, volume 651 of *Materials Science Forum*, 1–9. (2010).

10. Campbell, B. J., Stokes, H. T., Tanner, D. E., and Hatch, D. M. *Journal of Applied Crystallography* **39**, 607–614 (2006).

11. Giannozzi, P., Baroni, S., Bonini, N., Calandra, M., Car, R., Cavazzoni, C., Ceresoli, D., Chiarotti, G. L., Cococcioni, M., Dabo, I., Dal Corso, A., de Gironcoli, S., Fabris, S., Fratesi, G., Gebauer, R., Gerstmann, U., Gougoussis, C., Kokalj, A., Lazzeri, M., Martin-Samos, L., Marzari, N., Mauri, F., Mazzarello, R., Paolini, S., Pasquarello, A., Paulatto, L., Sbraccia, C., Scandolo, S., Sclauzero, G., Seitsonen, A. P., Smogunov, A., Umari, P., and Wentzcovitch, R. M. *Journal of Physics-Condensed Matter* **21**(39) (2009).

12. Vanderbilt, D. *Physical Review B* **41**(11), 7892–7895 (1990).

13. Cococcioni, M. and de Gironcoli, S. *Physical Review B* **71**, 035105 (2005).

14. Beridze, G. and Kowalski, P. M. *Journal of Physical Chemistry A* **118**(50), 11797–11810 (2014).

15. Murphy, G. L., Kennedy, B. J., Kimpton, J. A., Gu, Q. F., Johannessen, B., Beridze, G., Kowalski, P. M., Bosbach, D., Avdeev, M., and Zhang, Z. M. *Inorganic Chemistry* **55**(18), 9329–9334 (2016).

16. Murphy, G., Kennedy, B. J., Johannessen, B., Kimpton, J. A., Avdeev, M., Griffith, C. S., Thorogood, G. J., and Zhang, Z. M. *Journal of Solid State Chemistry* **237**, 86–92 (2016).

17. Tagawa, H. and Fujino, T. *Journal of Inorganic & Nuclear Chemistry* **40**(12), 2033–2036 (1978).

18. Fujino, T., Masaki, N., and Tagawa, H. *Zeitschrift Fur Kristallographie* **145**(3-4), 299–309 (1977).

19. Zhou, F., Maxisch, T., and Ceder, G. *Physical Review Letters* **97**, 155704 (2006).

20. Shamblin, J., Feygenson, M., Neuefeind, J., Tracy, C. L., Zhang, F. X., Finkeldei, S., Bosbach, D., Zhou, H. D., Ewing, R. C., and Lang, M. *Nature Materials* **15**(5), 507–511 (2016).

21. Ewing, R. C., Weber, W. J., and Lian, J. *Journal of Applied Physics* **95**(11), 5949–5971 (2004).

22. Zhang, Z. M., Avdeev, M., de los Reyes, M., Lumpkin, G. R., Kennedy, B. J., Blanchard, P. E. R., Liu, S., Tadich, A., and Cowie, B. C. C. *Journal of Physical Chemistry C* **120**(46), 26465–26479 (2016).

23. Zhang, Z. M., Middleburgh, S. C., de los Reyes, M., Lumpkin, G. R., Kennedy, B. J., Blanchard, P. E. R., Reynolds, E., and Jang, L. Y. *Journal of Physical Chemistry C* **117**(50), 26740–26749 (2013).

24. Saradhi, M. P., Ushakov, S. V., and Navrotsky, A. *Rsc Advances* **2**(8), 3328–3334 (2012).

25. Shlyakhtina, A. V., Knotko, A. V., Boguslavskii, M. V., Stefanovich, S. Y., Kolbanev, I. V., Larina, L. L., and Shcherbakova, L. G. *Solid State Ionics* **178**(1-2), 59–66 (2007).

26. Tsujimoto, Y., Tassel, C., Hayashi, N., Watanabe, T., Kageyama, H., Yoshimura, K., Takano, M., Ceretti, M., Ritter, C., and Paulus, W. *Nature* **450**(7172), 10621065 (2007).

27. Xiang, H. J., Wei, S. H., and Whangbo, M. H. *Physical Review Letters* **100**(16), 167207 (2008).

28. Piovano, A., Agostini, G., Frenkel, A. I., Bertier, T., Prestipino, C., Ceretti, M., Paulus, W., and Lamberti, C. *Journal of Physical Chemistry C* **115**(4), 1311–1322 (2011).

29. Maity, A., Dutta, R., Penkala, B., Ceretti, M., Letrouit-Lebranchu, A., Chernyshov, D., Perichon, A., Piovano, A., Bossak, A., Meven, M., and Paulus, W. *Journal of Physics D-Applied Physics* **48**(50) (2015).

30. Othmane, G., Allard, T., Menguy, N., Morin, G., Esteve, I., Fayek, M., and Calas, G. *American Mineralogist* **98**(2-3), 518–521 (2013).

31. Galuskin, E. V., Armbruster, T., Galuskina, I. O., Lazic, B., Winiarski, A., Gazeev, V. M.; Dzierzanowski, P., Zadov, A. E., Pertsev, N. N., Wrzalik, R., Gurbanov, A. G., and Janeczek. *American Mineralogist* **96**(5-6), 188–196 (2011).

32. Galuskin, E. V., Galuskina, I. O., Dubrovinsky, L. S., and Janeczek, J. *American Mineralogist* **97**(5-6), 1002–1004 (2012).

33. Prodan, A. and Boswell, F. W. *Acta Crystallographica Section B-Structural Science* **42**, 141–146 (1986).

34. Kauffman, G. *Angewandte Chemie International Edition* **46**(10), 1562–1563 (2007).

35. Ballhausen, C. J. and Gray, H. B. *Inorganic Chemistry* **1**(1), 111–122 (1962).

36. Makinen, M. W. and Mustafi, D. *Metal Ions in Biological Systems, Vol 31* **31**, 89–127 (1995).

37. Murphy, G. L., Kennedy, B. J., Zhang, Z. M., Avdeev, M., Brand, H. E. A., Kegler, P., and Alekseev, E. V. *Journal of Alloys and Compounds* **727**, 1044–1049 (2017).

38. Wang, S. A., Alekseev, E. V., Juan, D. W., Casey, W. H., Phillips, B. L., Depmeier, W., and Albrecht-Schmitt, T. E. *Angewandte Chemie-International Edition* **49**(6), 1057–1060 (2010).

39. Wang, S. A., Alekseev, E. V., Ling, J., Skanthakumar, S., Soderholm, L., Depmeier, W., and Albrecht-Schmitt, T. E. *Angewandte Chemie-International Edition* **49**(7), 1263–1266 (2010).

40. Hao, Y., Murphy, G. L., Bosbach, D., Modolo, G., Albrecht-Schmitt, T. E., and Alekseev, E. V. *Inorganic Chemistry* **56**(15), 9311–9320 (2017).

41. Hao, Y. C., Klepov, V. V., Murphy, G. L., Modolo, G., Bosbach, D., Albrecht-Schmitt, T. E., Kennedy, B. J., Wang, S., and Alekseev, E. V. *Crystal Growth & Design* **16**(10), 5923–5931 (2016).

42. Diwu, J., Nelson, A.-G. D., and Albrecht-Schmitt, T. E. *Comments on Inorganic Chemistry* **31**(1-2), 46–62 (2010).

43. Diwu, J., Nelson, A.-G. D., Wang, S., Campana, C. F., and Albrecht-Schmitt, T. E. *Inorganic chemistry* **49**(7), 3337–42 (2010).

44. Diwu, J. A., Wang, S. A., Liao, Z. L., Burns, P. C., and Albrecht-Schmitt, T. E. *Inorganic Chemistry* **49**(21), 10074–10080 (2010).

45. Back, D. F., de Oliveira, G. M., Ballin, M. A., and Corbellini, V. A. *Inorganica Chimica Acta* **363**(4), 807–812 (2010).

46. Burbano, M., Norberg, S. T., Hull, S., Eriksson, S. G., Marrocchelli, D., Madden, P. A., and Watson, G. W. *Chemistry of Materials* **24**(1), 222–229 (2012).

Chapter 5

Controlling Oxygen Defect Formation and the Effect on Reversible Symmetry Lowering and Disorder-Order Phase Transformations in Non-Stoichiometric Ternary Uranium Oxides

This chapter is adapted from a manuscript titled "Controlling Oxygen Defect Formation and its Effect on Reversible Symmetry Lowering and Disorder-Order Phase Transformations in Non-Stoichiometric Ternary Uranium Oxides" by G. L. Murphy *et al.* that has been accepted for publication in the journal *Inorganic Chemistry* at the time of writing.

5.1 Introduction

Chapters 3 and 4 demonstrated the significance of oxygen defect formation and behaviour in influencing phase transformations and structure formation in $SrUO_4$. In the broader context of defect engineering, a cascade of societally important materials ranging from solid oxide fuel cells to oxygen deficient high temperature superconductors have been realised through controlling and understanding the nature of defect formation[1–5]. Modification of materials by enhancing their defect properties requires controlled approaches that carefully balance improved performance, through increasing defect concentrations, against the loss of structural stability and/or performance associated with increasing defect interactions[6–9]. Nevertheless the approach of structural stabilisation through chemical modification leading to improved material properties has been effective and become quite topical in other avenues of materials science with several noteworthy recent successes[10–12]. Consequently elucidating the solid state chemistry that defines both the formation and behaviour of defects in materials is essential in advanced material design.

In the field of uranium oxide materials science, the majority of studies relating to defect phenomena have been focused on the binary oxides of uranium and changes to their thermal stabilities when fission daughter, or other reactor fuel related elements, partially substitute into the lattice[13–15]. However recent investigations have found appreciable ion conductivities can be achieved, through the partial substitution of aliovalent cations for uranium in the UO_2 lattice[16–18]. The majority of these studies have been confined to tetravalent uranium oxide containing materials, with few reports of materials with higher valence states. In the solid state, tetravalent uranium cannot simply undergo reduction through the formation of oxygen vacancies, unlike pentavalent and hexavalent uranium, as exemplified in Chapters 3 and 4 by $SrUO_4$. As described in Chapter 1, Bond Valence Sums (BVS) calculations indicate the ability for AUO_4 (A = Ca, Sr and Ba) oxides to host oxygen defects is a synergetic structural consequence of both the preferred bonding of the A and U cation sites and the ability for uranium to undergo reduction[19]. These calculations indicate that α-$SrUO_4$ can support more defects than the isostructural Ca analogue $CaUO_4$[19] partially due to the more over bonded nature of the Sr^{2+} cation than the Ca^{2+} cation where anion defects help to alleviate this over bonding.

Unlike α-$SrUO_4$, $CaUO_4$ is not reported to exhibit any transformative behaviour under oxidising conditions at high temperature[20–23], although it can support similar oxygen defects under reducing conditions[20,23]. Tagawa *et al.*[20] observed a two-step reduction process using thermogravimetric methods and

Prodan and Boswell[24] postulated that these events are related to interactions between the defects leading to the formation of microdomains with variable concentrations of oxygen defects. Oxygen ion transport, associated with the reduction and oxidation of the uranium cations, occurs between these micro-domains. However the few available *in situ* structural studies available do not provide any detail for this[22,23].

At room temperature α-$SrUO_4$ supports more oxygen defects on the O(2) site than $CaUO_4$ due to the over bonded environment of the Sr^{2+} cation leading to the reduction of the uranium[19]. The Ca^{2+} cation, being smaller than Sr^{2+}, is better accommodated in the structure and oxygen vacancies are not required to stabilise this. Considering this, it is not unreasonable to expect that the formation of additional oxygen vacancies in $CaUO_4$ may be enhanced through substitution of Ca^{2+} for Sr^{2+} cations in $CaUO_4$ and forming a solid solution of the type α-$Sr_xCa_{1-x}UO_4$. Consequently it is hypothesized that although $CaUO_4$ is not known to have an orthorhombic transformative partner, unlike α-$SrUO_4$, the introduction of Sr^{2+} cations into the lattice may coerce this. This hypothesized variation of defect inventory within the α-$Sr_xCa_{1-x}UO_4$ series must have consequences for the potential formation of δ phases.

This chapter is devoted to both understanding the ability for oxygen defects to form in AUO_4 oxides and how these effect ordering and δ phase superstructure formation following on from the results described in Chapters 3 and 4. This involved initially examining $CaUO_4$ using *in situ* neutron diffraction under vacuum, to probe the relative amount and position of oxygen defects in the lattice. This was followed by examining the solid solution α-$Sr_xCa_{1-x}UO_4$ using *ex situ* synchrotron X-ray diffraction. *In situ* synchrotron X-ray diffraction under air was then undertaken on select members of the α-$Sr_xCa_{1-x}UO_4$ series including $CaUO_4$ itself to establish the structural impact of variable amount of defects that may form under oxidising conditions. Finally the same chosen samples were examined using *in situ* synchrotron X-ray diffraction under flowing hydrogen to understand how the relative difference in defect formation may effect δ phase superstructure formation. These results were supplemented using *ab initio* methods using density functional theory to gain insight into the ability for these lattices to generate defects, the differences between these and how they influence the ordering of defects.

5.2 Experimental

5.2.1 Synthesis

A polycrystalline sample of $CaUO_4$ was prepared by first weighing stoichiometric quantities of U_3O_8 and $CaCO_3$. The reagents were mixed thoroughly using a mortar and pestle before being compacted into a pellet, placed in an alumina crucible and calcined at 900 ^oC for 60 hours in a muffle furnace with intermittent mixing. The series of oxides α-$Sr_xCa_{1-x}UO_4$, $0 < x < 1$ in steps of 0.1, were synthesized by weighing stoichiometric quantities of $CaCO_3$, $SrCO_3$ and U_3O_8. The reagents were mixed thoroughly using a mortar and pestle before being compacted into pellets and placed in alumina boats and calcined under reducing conditions (3% H_2/Ar) at 950 ^oC for 20 hours using a tube furnace with intermittent mixing. The oxides were then annealed at 200 ^oC in air for 20 hours to ensure the final products were stoichiometric with respect to oxygen content. Post synthesis the samples were examined using laboratory XRD to confirm reaction completion.

5.2.2 *Ex Situ* Neutron and Synchrotron X-ray Powder Diffraction

Room temperature structural characterisation was performed at the synchrotron X-ray powder diffraction (S-XRD) beamline at the Australian Synchrotron[25] for $CaUO_4$ and all members of the α-$Sr_xCa_{1-x}UO_4$ series. Due to beam time constraints neutron powder diffraction (NPD) measurements, using the ECHIDNA high resolution diffractometer at ANSTO's OPAL reactor[26], could only be performed on $CaUO_4$. For the S-XRD measurements approximately 5 mg of sample was finely ground and housed in 0.2 mm diameter glass capillaries and sealed. A wavelength of 0.82686 and 0.77466 Å were used for $CaUO_4$ and for members of the α-$Sr_xCa_{1-x}UO_4$ series respectively determined using a NIST LaB_6 standard reference material. The data were collected for 5 minutes at each of the two detector positions of the MYTHEN detector system. For NPD measurements approximately 2 g of $CaUO_4$ was pelletized and placed in a thin walled vanadium can and measured using a wavelength of 1.622 Å. Structural models were refined against the NPD and S-XRD data were executed using the program GSAS[27,28] and GSAS-II[29].

5.2.3 *In Situ* Synchrotron X-ray Powder Diffraction

In situ S-XRD measurements were performed at the Australian synchrotron powder diffraction beamline[25]. For sealed capillary air experiments finely ground polycrystalline samples of $CaUO_4$ and α-$Sr_xCa_{1-x}UO_4$ were loaded into 0.2 mm diameter quartz capillaries that were sealed. For gas flow experiments finely ground polycrystalline samples of $CaUO_4$ and α-$Sr_xCa_{1-x}UO_4$ were mixed at a 50:50 ratio by w.t%. The mixtures were loaded into a 0.8 mm diameter quartz capillaries where the ends were loaded with course analytical grade quartz glass followed by glass wool in order to promote gas flow and mitigate against sample loss. The capillary was mounted on a goniometer equipped with a Norby-flow cell apparatus[30] that allowed rocking during the S-XRD measurement to minimise the effects of preferred orientation. The gas inlet line was connected to the flow cell via a flow meter to ensure a constant flow of high purity hydrogen gas ($\geq$ 99.99% with oxygen $\leq$ 10 ppm and moisture $\leq$ 20 ppm) and also high purity oxygen gas (>99.9% with moisture $\leq$ 25 ppm and N_2 $\leq$ 500 ppm). A FMB-Oxford hot air blower was placed to allow temperature control below the capillary. Prior to variable temperature measurements the sample was flushed with high purity H_2 or O_2 gas for 30 minutes at room temperature to ensure the sample was sufficiently soaked in gas and to ensure constant gas flow. Temperatures were increased at a ramp rate of 5 ^{o}C per minute and decreased at a rate of 25 ^{o}C per minute, and the data collection was commenced after a 30 second delay at temperature to allow thermal equilibration. Data were collected for 5 minutes at each of the two positions of the MYTHEN detector from room temperature to 1000 ^{o}C. The structures refined against the S-XRD was done so using the program GSAS[27,28] and GSAS-II[29]. The wavelength was determined to be 0.77466 Å, calibrated using a NIST LaB_6 standard.

5.2.4 *In Situ* Neutron Powder Diffraction

Approximately 2 g of $CaUO_4$ was compacted into a pellet and loaded into a thin walled vanadium can. The can was placed in an Institute Laue Langevin (ILL) type high vacuum furnace employing niobium elements and operating at $< 10^{-6}$ Torr. The can was not sealed during measurements and thus was exposed to the high vacuum. The temperature was increased at 10 ^{o}C per minute and data was collected twice at each temperature for 2 h each. These NPD measurements were undertaken at ANSTO's OPAL nuclear reactor using the high resolution neutron powder diffractometer ECHNIDA[26]. The structures

refined against the NPD was done so using the program GSAS[27,28] and GSAS-II[29]. The wavelength used in this experiment was 1.622 Å.

5.2.5 Density Functional Theory Calculations

The *ab initio* calculations were performed by applying density functional theory (DFT) in a similar fashion to that undertaken in Chapters 3 and 4 using the Quantum-ESPRESSO simulations package[31]. A PBE exchange-correlation functional was applied using the plane-wave energy cut-off of 50 Ryd and ultrasoft pseudopotentials to mimic the presence of core electrons[32,33] were also used. The stoichiometric α and β phases were modelled by supercells containing 48 and 24 atoms, respectively. In order to account for electronic correlations the DFT+U method was applied, but with the Hubbard model computed *ab initio* using the linear response method of Cococcioni and de Gironcoli[34]. The Hubbard U parameter used in the current study is 2.5 eV, which is the same value as derived for the α and β phases in Chapters 3 and 4. This value is in the range expected for U(VI) and U(V) compounds[35]. In addition to $CaUO_{4-x}$, energies for α-$Sr_xCa_{1-x}UO_{4-x}$ were computed. The random distribution of Ca and Sr cations was modelled by a representative structure constructed using the quasi-random structure approach[36,37].

5.2.6 Superstructure Analysis

The structure of δ-$CaUO_{4-x}$ was analysed using TOPAS Academic (TA)[38,39] and Jana2006[40] against S-XRD data collected at 1000 ^{o}C. The 1000 ^{o}C pattern was chosen to serve as a comparison to the previous study of δ-$SrUO_{4-x}$ described in Chapter 4, which was analysed at the same temperature and where the protocol used for the structural analysis of δ-$SrUO_{4-x}$ was also followed here. First, an average structure of δ-$CaUO_{4-x}$ at 1000 ^{o}C that did not take into account the supercell reflections was developed. Then, the modulation vector that accounted for the observed superlattice reflections was investigated. Attempts were initially made to assign a commensurate distortion vector k, but none could be found and an incommensurate modulation vector k = $< \sim 0.27, \sim 0.16, \sim 0.29 >$ was then found. The structure of δ-$CaUO_{4-x}$ was then refined using Jana2006[40]. For each atomic position one modulation was applied per site. There should be an additional, occupancy, modulation of oxygen however this could not be identified reflecting the small relative scattering factor of oxygen in X-ray diffraction studies.

5.3 Results and Discussion

5.3.1 *Ex Situ* Structural Characterisation and Synthesis

From laboratory XRD $CaUO_4$ was found to be single phase and its structure could be refined against a rhombohedral model in space $R\bar{3}m$ showing it to be isostructural with α-$SrUO_4$ [19]. From joint refinement using NPD and S-XRD the sample is essentially stoichiometric with the refined occupancy of the O(1) and O(2) sites equal to 1.00(3) and 0.984(7) respectively. A structural model derived from these measurements is presented in Figure 5.1. In the series α-$Sr_xCa_{1-x}UO_4$, single phase samples could be prepared up to $x = 0.4$ and Rietveld refinement confirmed these were rhombohedral in space group $R\bar{3}m$ using S-XRD data. Surprisingly, despite the isostructural relationship of the end members of the series, above $x = 0.4$ phase separation occurred, as shown in a portion of the S-XRD data in Figure 5.2. Analysis shows both phases to be rhombohedral in space group $R\bar{3}m$. The two phases coexist until $x = 0.8$, thereafter a single phase rhombohedral structure, also in $R\bar{3}m$ forms. Attempts were made to re-synthesize the series with fresh reagents following the same method described but the identified miscibility gap was found to remain. The site occupancies of these phases were not refined, but considering that the samples were prepared under oxidising conditions, the difference in lattice parameter between the phases is likely related to one phase being Sr rich whereas the other is Ca rich.

5.3.2 *In Situ* Neutron Powder Diffraction

The temperature dependence of the structure of $CaUO_4$ heated to 1000 ^oC under vacuum was determined using NPD. As shown in Figure 5.3 approximately linear thermal expansion occurs to near 600 ^oC where an apparent increase in the rate of change of unit cell expansion is observed. This is reminiscent to what is observed in Chapter 3 when α-$SrUO_4$ was heated under air and vacuum. This change to the unit cell expansion is reflected in the occupancy of the O(2) oxygen site, which decreases rapidly above 600 ^oC reaching 0.826(14) or $CaUO_{3.65}$ at 1000 ^oC. Over the same temperature range the U-O(2) distance increased, in an approximately linear manner, by 1.58% from 2.2967(3) to 2.3331(13) Å, which is less than the 2.62% expansion in the unit cell parameter. The U-O(1) distance increased in a non-linear manner by 2.12% from 1.9604(12) to 2.002(5) Å over the measured temperature range. These increases are consistent with reduction of the U^{6+} cation similar to that described for α-$SrUO_4$ in Chapter 3.

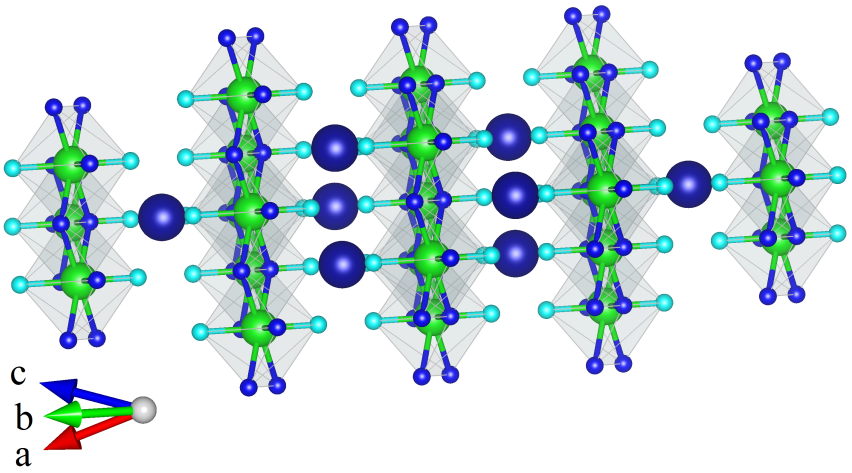

FIGURE 5.1: Representation of the rhombohedral $CaUO_4$ structure in $R\bar{3}m$. The U and Ca cations are represented by green and dark blue coloured spheres respectively, whereas the O(1) in-plane and O(2) out-of-plane site oxygen anions are represented by aqua and blue respectively.

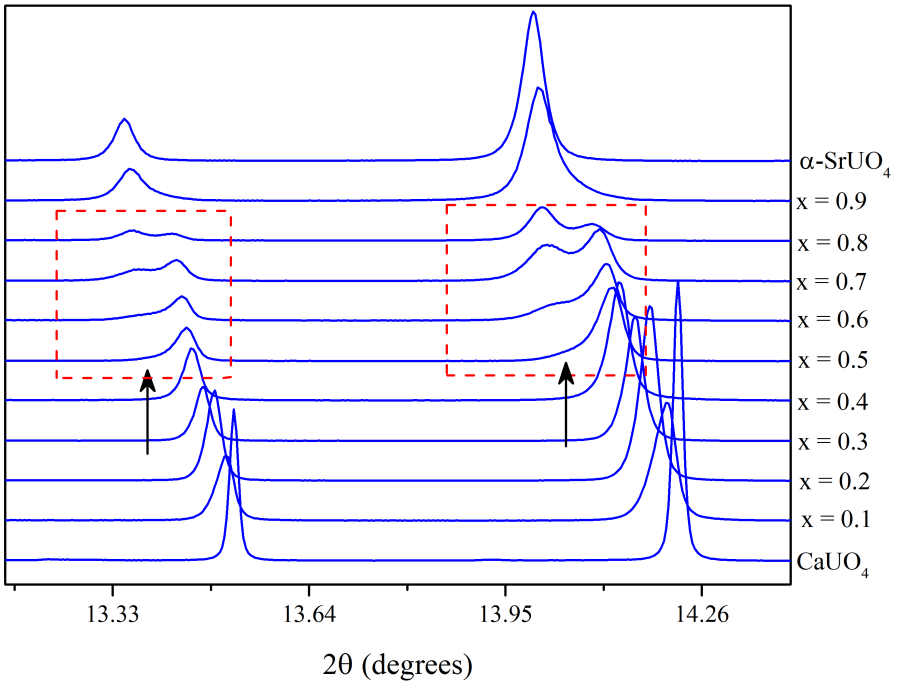

FIGURE 5.2: S-XRD patterns between 13.10 and 14.4 2θ for the α-$Sr_{0.4}Ca_{0.6}UO_4$ solid solution samples for $0 < x < 1$ in steps of 0.1.

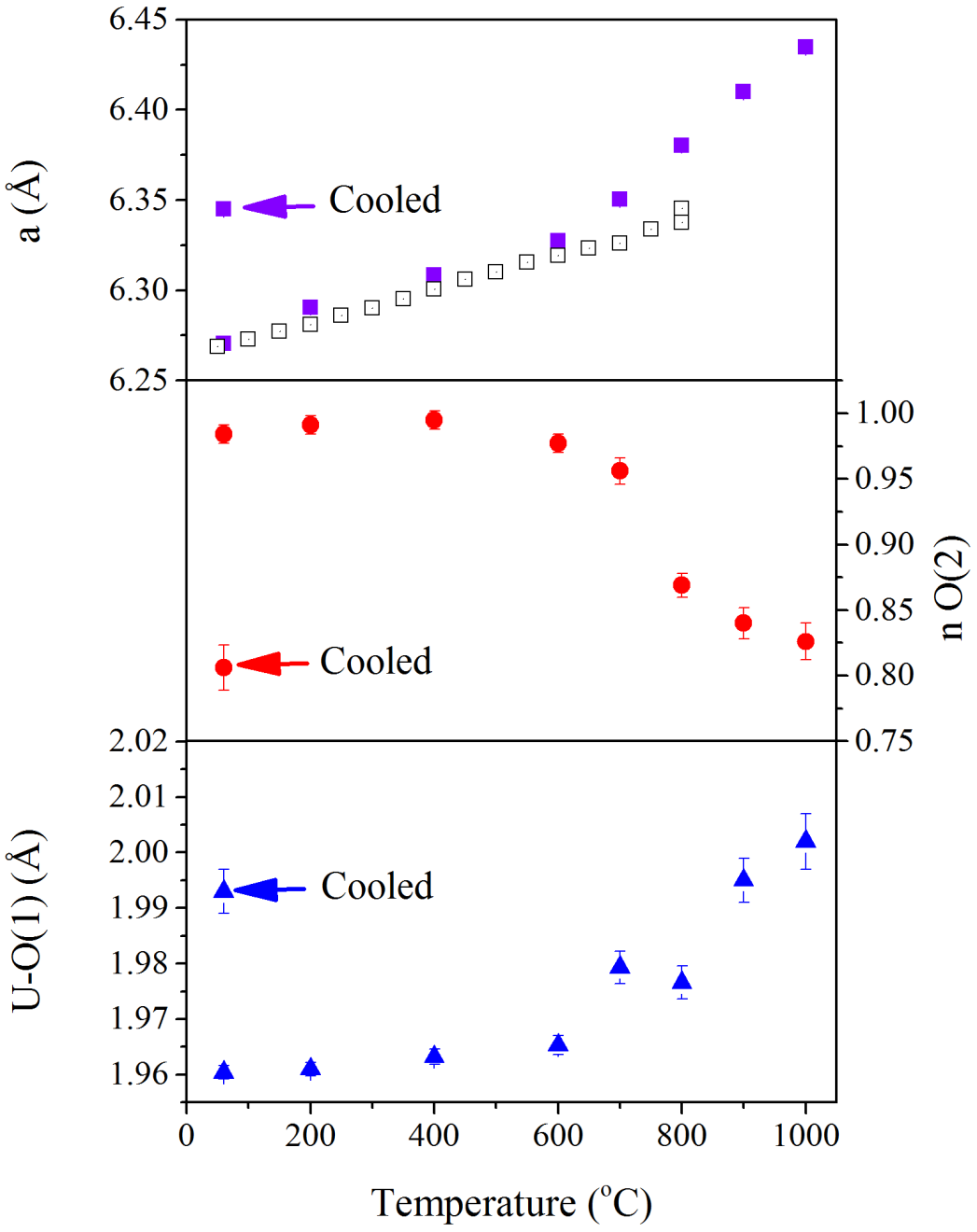

FIGURE 5.3: Temperature dependence of the unit cell volume, O(2) occupancy and isotropic displacement thermal parameter for O(1) and O(2) for $CaUO_4$ obtained from Rietveld refinements of *in situ* neutron powder diffraction patterns under vacuum.

5.3.3 *In Situ* Synchrotron X-ray Powder Diffraction 1. High Temperature Studies

Heating $CaUO_4$ in a sealed quartz capillary, containing air, and measuring using S-XRD resulted in linear thermal expansion to 700 ^oC and there is no evidence for any phase transitions to these temperatures. Continued heating to 1000 ^oC resulted in an increase in the rate of the thermal expansion of the $CaUO_4$ unit cell volume, see Figure 5.4, similar to that observed in the NPD experiment under vacuum for $CaUO_4$ and reminiscent to that observed in α-$SrUO_4$ under similar conditions described in Chapters 3 and 4. This is consistent with oxygen defect formation and partial reduction of the U cations occurring[20,41].

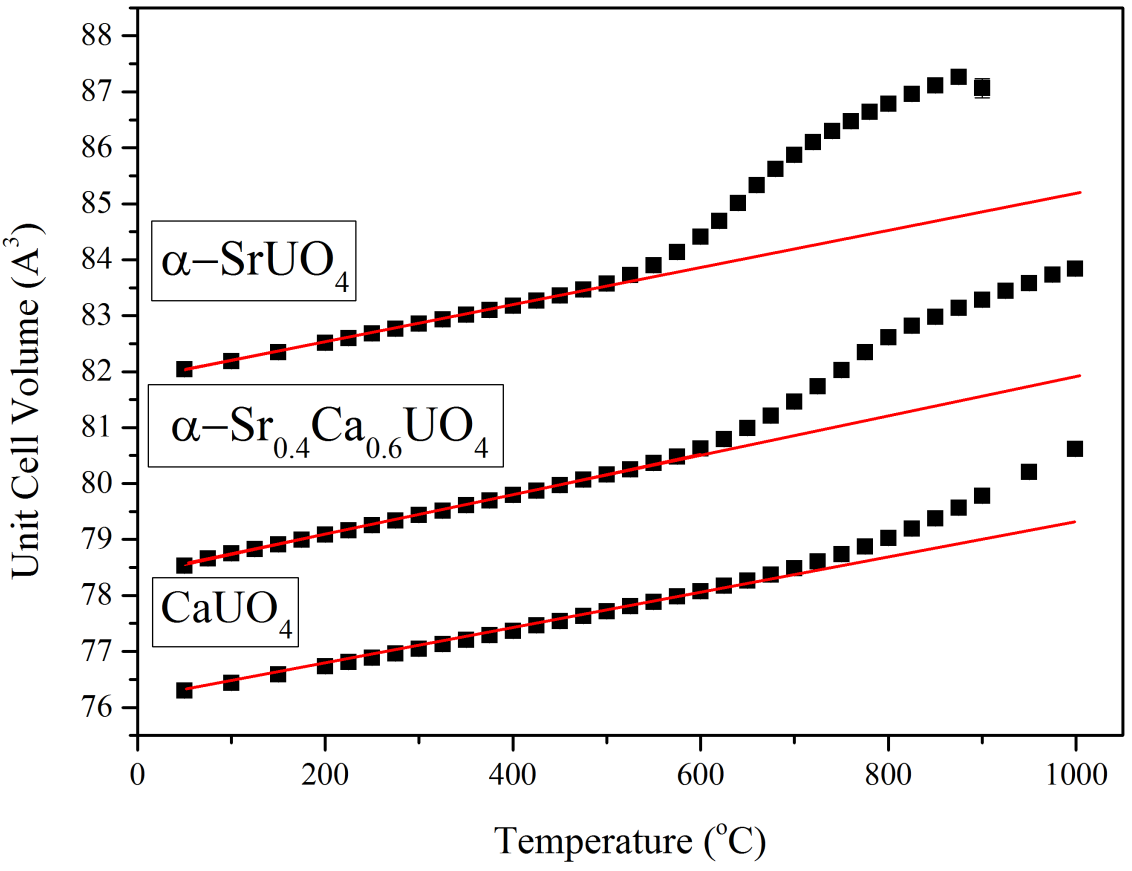

FIGURE 5.4: Temperature dependence of the unit cell volume of $CaUO_4$, α-$Sr_{0.4}Ca_{0.6}UO_4$ and α-$SrUO_4$ in sealed quartz capillaries containing air obtained from Rietveld refinements of *in situ* synchrotron X-ray powder diffraction patterns. The solid lines are a linear fit to the data between room temperature and 500 ^oC.

Considering the miscibility gap identified in the α-$Sr_xCa_{1-x}UO_4$ series, the highest single phase sample on the Ca rich of the series, $x = 0.4$, was chosen to be heated to 1000 ^{o}C in a sealed capillary containing air and measured using S-XRD. As evident in Figure 5.4 α-$Sr_xCa_{1-x}UO_4$ exhibits approximate linear thermal expansion until 600 ^{o}C. Between 600 and 1000 ^{o}C the rate of change of the thermal expansion of the unit cell volume was observed to increase. The rate of increase in the high temperature region is somewhat greater than that seen in undoped $CaUO_4$ and the change in slope occurs at a slightly lower temperature, 600 vs 700 ^{o}C in $CaUO_4$. If the observed cell volumes of α-$Sr_xCa_{1-x}UO_4$ and $CaUO_4$ are compared against the values expected if defect formation had not occurred, i.e linear expansion to 1000 ^{o}C, the cell volume of α-$Sr_xCa_{1-x}UO_{4-x}$ has increased by approximately 2% compared to the approximate 1% increase in $CaUO_{4-x}$. This indicates that the partial substitution of Sr^{2+} cations onto the Ca^{2+} site of $CaUO_4$ increases the amount of oxygen defects forming and, by extension, the amount of reduced uranium valence states. This trend is particularly apparent when the unit cell volume of α-$SrUO_4$ heated in a sealed capillary containing air (Chapter 3) is also considered (Figure 5.4). It is postulated that this trend is consequence of variation in defect-defect interactions between the oxides. Defect-defect interactions are generally unfavourable processes energetically contributing to an increase in free energy [42–46]. These interactions become more pronounced as the proximity between defects decreases. Since rhombohedral α-$SrUO_4$ has the largest unit cell, followed by α-$Sr_xCa_{1-x}UO_4$ and then $CaUO_4$, it is postulated that defect interactions are more significant in the latter structures, since the defects will be in closer proximity and it would be energetically more costly, and consequently greater temperatures are needed, for successive defects to form. This is evidently occurring by Figure 5.4.

5.3.4 *Ab Initio* Calculations

To examine the relationship and apparent differences within the α-$Sr_xCa_{1-x}UO_4$ series, DFT+U calculations were conducted to compare the relative energies of the $CaUO_4$, α-$SrUO_4$ and α-$Sr_{0.4}Ca_{0.6}UO_4$. In Table 5.1 the energy difference between the orthorhombic and rhombohedral phases of stoichiometric AUO_4 for A = Ca, $Sr_{0.4}Ca_{0.6}$ and Sr are presented. These energies clearly show that the stable phase of $CaUO_4$ is rhombohedral while the stable phase of $SrUO_4$ is orthorhombic. This is consistent with experimental observations. In the case of $Sr_{0.4}Ca_{0.6}UO_4$ the energy difference between the two phases is negligible suggesting a mixture of both may occur. This is consistent with previous experimental results [19] when the oxide is prepared under oxidizing conditions. Here, when prepared under reducing conditions,

the oxide is shown to be single phase rhombohedral. This is thought to be related to the inability of the orthorhombic structure to retain oxygen defects.

TABLE 5.1: The energy difference between rhombohedral and orthorhombic phases of stoichiometric AUO_4 for A = Ca, and Sr.

Composition	ΔE(rhombohedral-orthorhombic) [eV]
$CaUO_4$	-0.16
$Sr_{0.4}Ca_{0.6}UO_4$	0.01
$SrUO_4$	0.22

Although no phase transformation was observed in $CaUO_4$ or α-$Sr_xCa_{1-x}UO_4$ it is apparent that the introduction of Sr^{2+} cations reduces the temperature at which oxygen defects form. Since oxygen defect formation is critical in the transformation from α-$SrUO_4$ to β-$SrUO_4$, it is possible that an orthorhombic β transformation partner may exist for $CaUO_4$ and α-$Sr_xCa_{1-x}UO_4$ but only at temperatures above those accessible in these experiments. To examine this possibility *ab initio* DFT+U calculations were used to compare the energy of formation of rhombohedral $R\bar{3}m$ $CaUO_x$ and $Sr_{0.4}Ca_{0.6}UO_x$, structures and their theoretical orthorhombic forms in space group *Pbcm* for x = 4, 3.875, 3.75, 3.625 and 3.5. These are presented with the results of $SrUO_4$ from Chapter 3 in Figure 5.5. It is apparent that for the investigated oxygen contents, the orthorhombic partner is not favoured for either $CaUO_4$ or α-$Sr_{0.4}Ca_{0.6}UO_4$, suggesting neither could be accessed at higher temperatures.

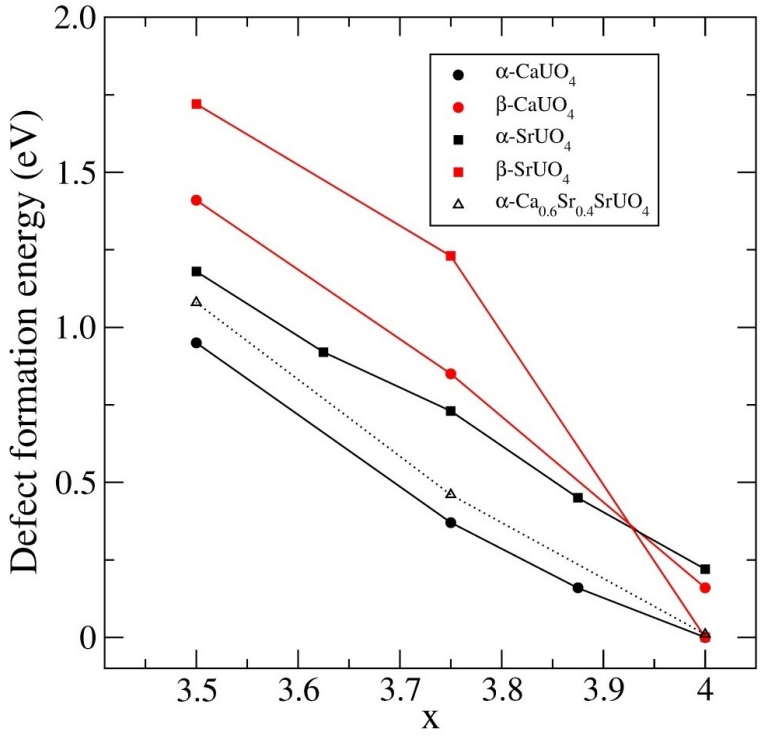

FIGURE 5.5: Defect formation energies for rhombohedral α (black symbol) and orthorhombic β (red symbol) for $CaUO_x$, $Sr_{0.4}Ca_{0.6}UO_x$ and $SrUO_x$ as a function of oxygen content, obtained using the PBE+U approach for various possible arrangements of vacancies allowed by the model systems.

5.3.5 *In Situ* Synchrotron X-ray Powder Diffraction 2. Superstructure Formation Studies

To recapitulate, when rhombohedral $CaUO_4$ is heated in a sealed capillary containing air, it is able to spontaneously generate oxygen defects on its O(2) site. The amount of defects that form can be increased via the substitution of the Ca^{2+} for the larger Sr^{2+} cation. This is thought to be related to defect-defect interactions, where the larger Sr^{2+} alleviates the effects of these by increasing the proximity at which these forms consequently allowing them to form at lower temperature. That the cationic lattice strongly influences the anionic lattice under oxidising conditions, it is likely a similar influence could be observed when δ phase superstuctures are formed. To examine this $CaUO_4$ and α-$Sr_{0.4}Ca_{0.6}UO_4$ were studied by S-XRD upon heating to 1000 ^{o}C under an atmosphere of flowing pure H_2. The temperature dependence of the S-XRD profiles for $CaUO_4$ and α-$Sr_{0.4}Ca_{0.6}UO_4$ under these conditions are presented in Figures 5.6 and 5.7 respectively.

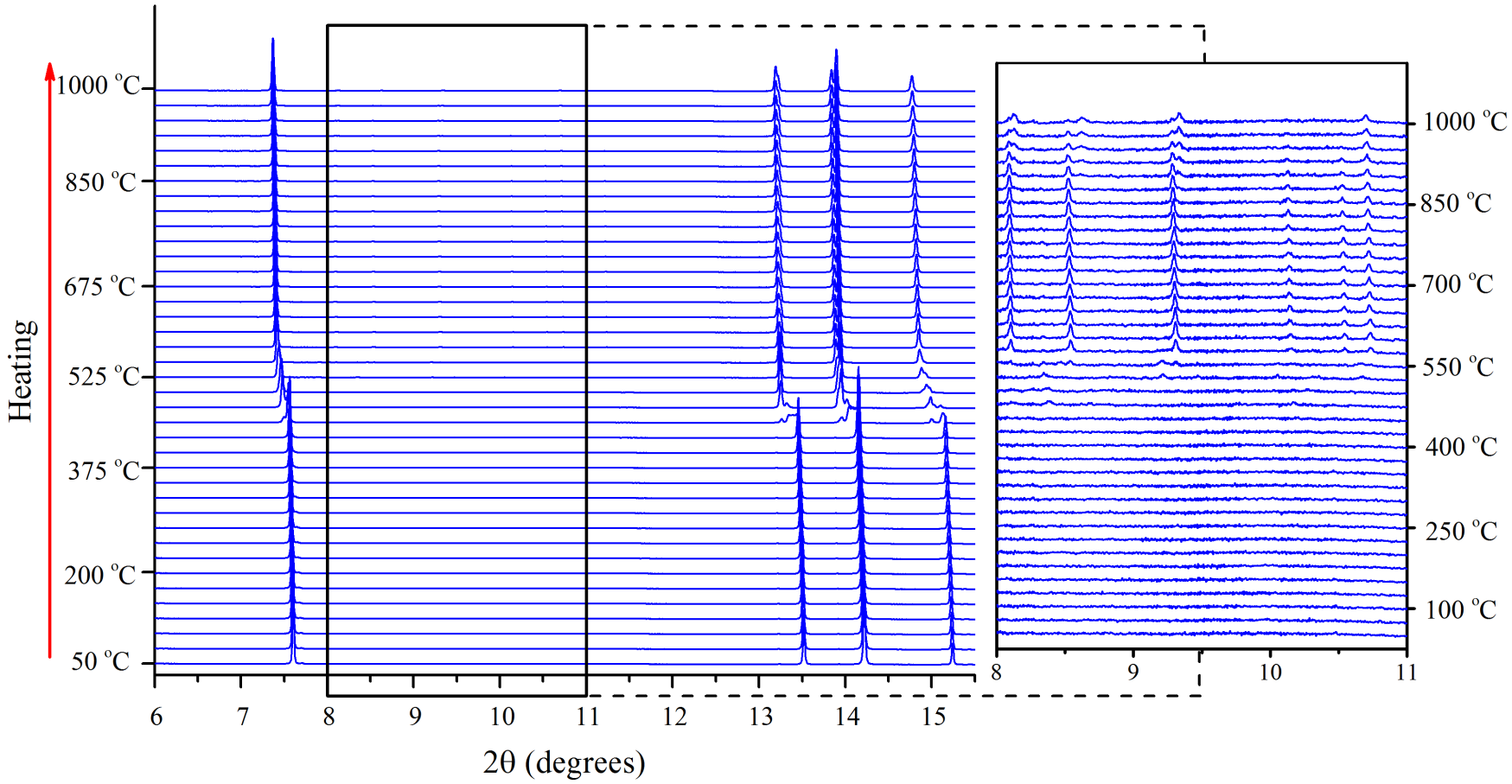

FIGURE 5.6: S-XRD patterns showing the temperature dependence of $CaUO_{4-x}$ heated under pure H_2 gas flow from RT to 1000 °C. The emergence of superlattice reflections corresponding to the formation of the ordered δ phase is illustrated in the inset.

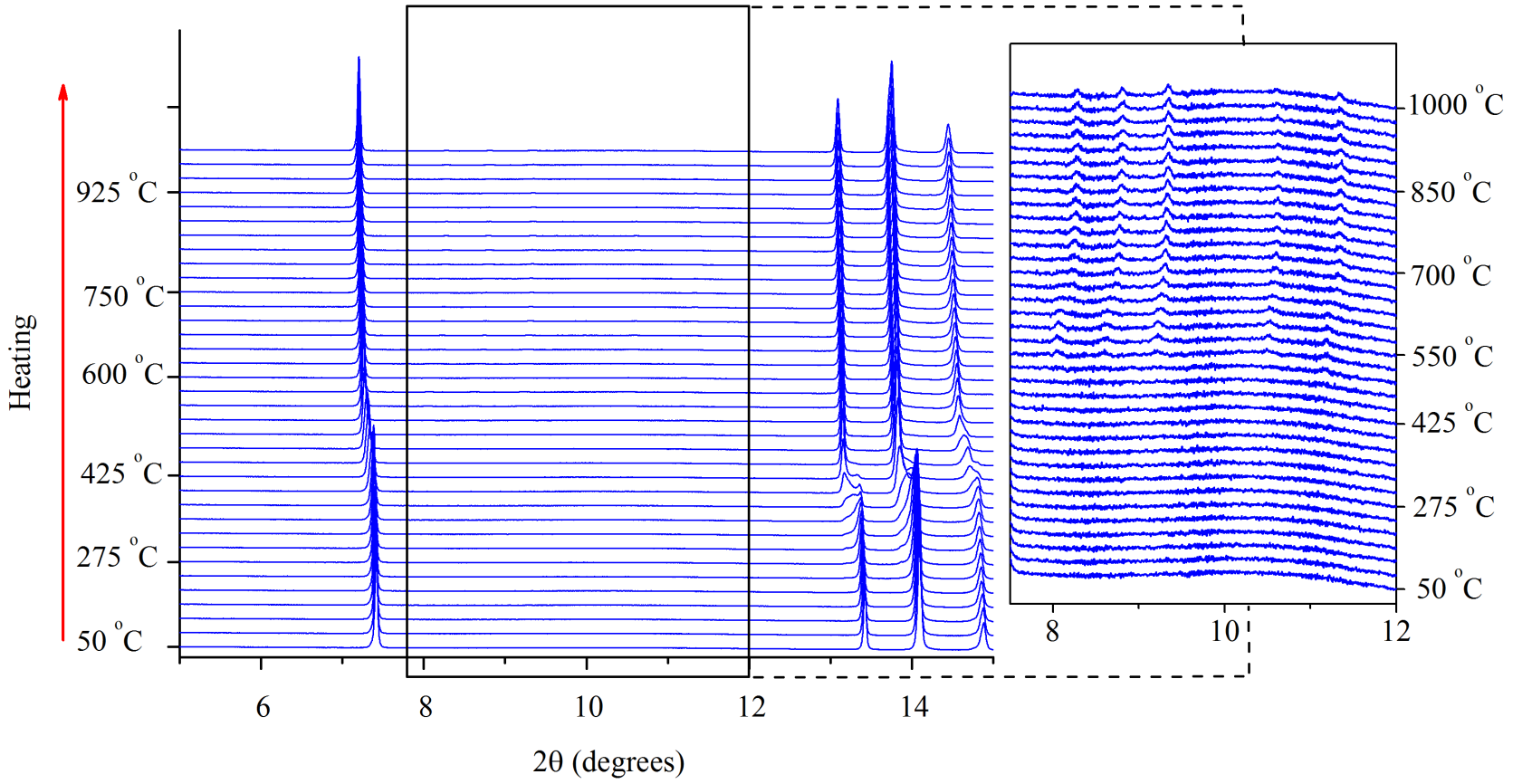

FIGURE 5.7: S-XRD patterns showing the temperature dependence of α-$Sr_{0.4}Ca_{0.6}UO_{4-x}$ heated under pure H_2 gas flow from RT to 1000 ^{o}C. The emergence of superlattice reflections corresponding to the formation of the ordered δ phase is illustrated in the inset.

The reducing environment enhances oxygen defect formation even at ambient temperature, consequently the oxides will be denoted as sub-stoichiometric, $CaUO_{4-x}$ and α-$Sr_{0.4}Ca_{0.6}UO_{4-x}$, in the following discussion. As shown in the Figures 5.6 and 5.7, the temperature dependence of the structure can be divided into three regions of interest. The S-XRD profiles show no changes upon heating $CaUO_{4-x}$ towards 350 ^{o}C other than the expected thermal expansion. Similar behaviour is observed for δ-$Sr_{0.4}Ca_{0.6}UO_{4-x}$ on heating to 200 ^{o}C. Heating $CaUO_{4-x}$, to 450 ^{o}C results in a first order phase transformation as evident by the appearance of new reflections in the S-XRD profile and the loss of peaks corresponding to the rhombohedral α phase, a similar transition occurs for α-$Sr_xCa_{1-x}UO_{4-x}$ albeit at a slightly lower temperature approximately 225 ^{o}C. These new phases are denoted δ and it is noteworthy that the temperature at which the transition for α-$Sr_{0.4}Ca_{0.6}UO_{4-x}$ occurs, $\sim$ 225 ^{o}C, is intermediate between that for $CaUO_{4-x}$, $\sim$ 450 ^{o}C, and α-$SrUO_{4-x}$, $\sim$200 ^{o}C.

Heating both oxides from 450 to 1000 ^{o}C under H_2 gas flow, results in the emergence of additional low intensity reflections at low 2θ angles most evident between $\sim$ 8 and 12^o in the diffraction patterns as shown in the insets of Figure 5.6 and 5.7. Similar to δ-$SrUO_{4-x}$, the appearance of these is indicative of the formation of an ordered superstructure, presumably due to the ordering of oxygen defects. The superlattice reflections for both δ phases are observed to persist, with continued heating, to 1000 ^{o}C where they apparently increase in intensity with heating, suggesting the structures are becoming more ordered with temperature. Some variation in the structure and positioning of these superlattice reflections, including some apparent peak splitting is observed for δ-$CaUO_{4-x}$ above 850 ^{o}C (see inset of Figure 5.6). However no changes are observed for the strong Bragg reflections.

The S-XRD profile of δ-$CaUO_{4-x}$, after rapidly cooling to room temperature whilst maintaining the H_2 gas flow, revealed the sample contained two phases both of which could be refined as rhombohedral structures in space group $R\bar{3}m$ (see Figure 5.8). Rapidly cooling δ-$Sr_{0.4}Ca_{0.6}UO_{4-x}$ to room temperature also resulted in the formation of two rhombohedral phases (see Figure 5.8).

The formation of multiple phases was also encountered in δ-$SrUO_{4-x}$when it was rapidly cooled after the first heating cycle under H_2. It was postulated rapid cooling inhibits oxygen ion transport across the sample, leading to the formation of microdomains with variable oxygen content, which in turn causes variability in unit cell sizes. Using a slower cooling rate a single phase sample of α-$SrUO_{4-x}$was formed. Consequently to both confirm the reversibility of the observed transformation and in an attempt to form a

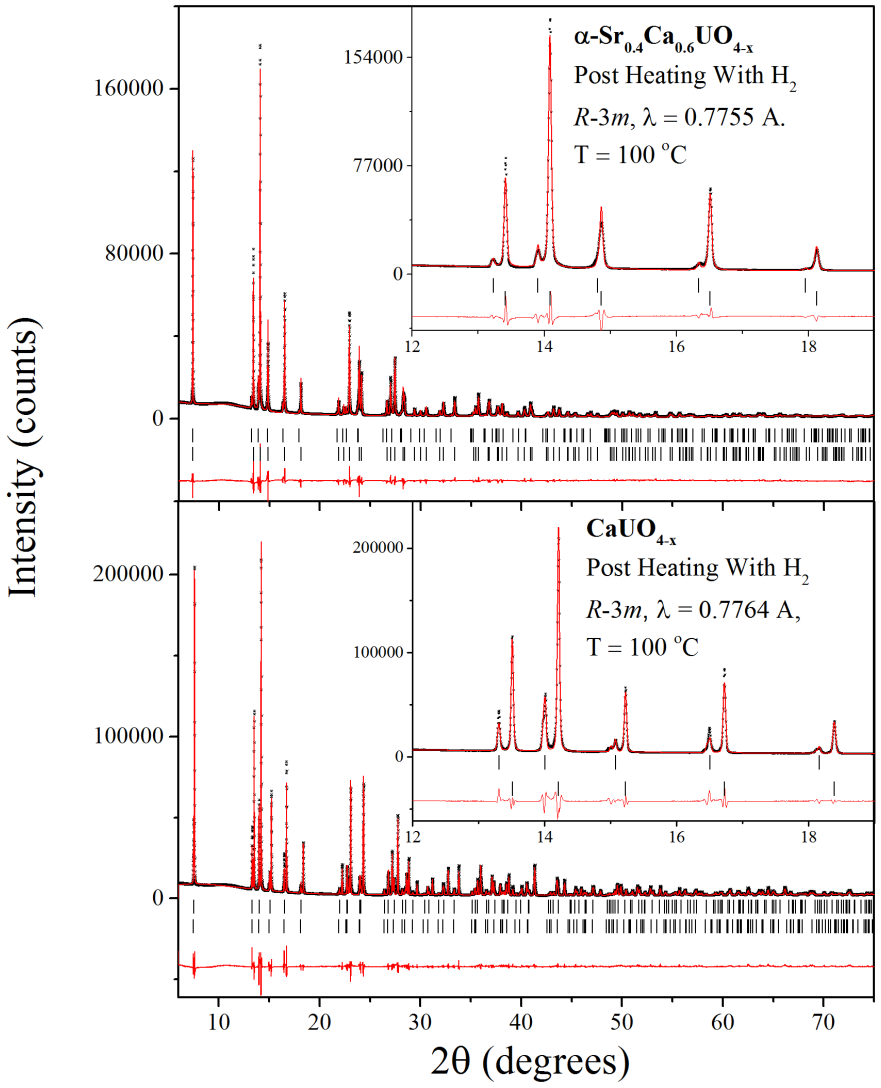

FIGURE 5.8: Rietveld refinement profile for α-$Sr_{0.4}Ca_{0.6}UO_{4-x}$ (top) and $CaUO_{4-x}$ (bottom) collected at 100 ^{o}C under H_2 gas flow atmosphere after exposure to high temperature and highly reducing conditions. Both data sets were refined against rhombohedral structures in space group $R\bar{3}m$. The inset highlights the two phase nature of the sample. The inset highlights the two phase nature of the samples. For $CaUO_{4-x}$ $\lambda = 0.7764$ Å, $wR_p = 30.67\%$, $R_p = 32.71\%$ and for α-$Sr_{0.4}Ca_{0.6}UO_{4-x}$ $\lambda = 0.7755$ Å, $wR_p = 9.98\%$, $R_p = 9.43\%$.

single phase sample of $CaUO_{4-x}$ upon cooling, the sample was then heated incrementally to 650 ^{o}C and then cooled slowly back to room temperature whilst under H_2 gas flow. As shown in Figure 5.10, in this second heating cycle the transformation to δ-$CaUO_{4-x}$ occurs at a lower temperature than observed in the initial heating cycle, at approximately 300 vs 450 ^{o}C. Some very weak super lattice reflections are apparent above 300 ^{o}C but these are lost on continued heating to 425 ^{o}C at which temperature relatively more intense (but still weak) super lattice reflections at become apparent. S-XRD patterns measured during cooling

reveal that the super lattice reflections indicative of the ordered δ phases are maintained until 250 ^{o}C before these are lost. This is similar to the behaviour of δ-$SrUO_{4-x}$, where superlattice reflections are lost at a lower temperature during cooling than the temperature these appear during heating. This hysteresis in the transition between the ordered and disordered structures is attributed to slow reaction kinetics. In contrast to that described for δ-$CaUO_{4-x}$ in Chapter 4, inspection of the data set measured at 100 ^{o}C shows that the sample remains a mixture of two phases which could both be refined against rhombohedral structures in space group $R\bar{3}m$.

To confirm the total reversibility of the transformation process in δ-$CaUO_{4-x}$ and in particular to determine if the original stoichiometric structure could be recovered the H_2 gas was replaced with O_2 and $CaUO_{4-x}$ heated to 700 ^{o}C then cooled to 25 ^{o}C. At about 250 ^{o}C, the diffraction data indicates that the sample converts to a single phase which is retained on heating to 700 ^{o}C and also when cooled to 100 ^{o}C. This process is illustrated in Figure 5.9. The 100 ^{o}C data set was fitted using a rhombohedral model in space group $R\bar{3}m$, consistent with the stoichiometric $CaUO_4$ structure and the Rietveld analysis provided no evidence for sample decomposition. The Rietveld profile is presented in Figure 5.11. This demonstrates that the process of reducing stoichiometric $CaUO_4$, to form δ-$CaUO_{4-x}$, is completely reversible.

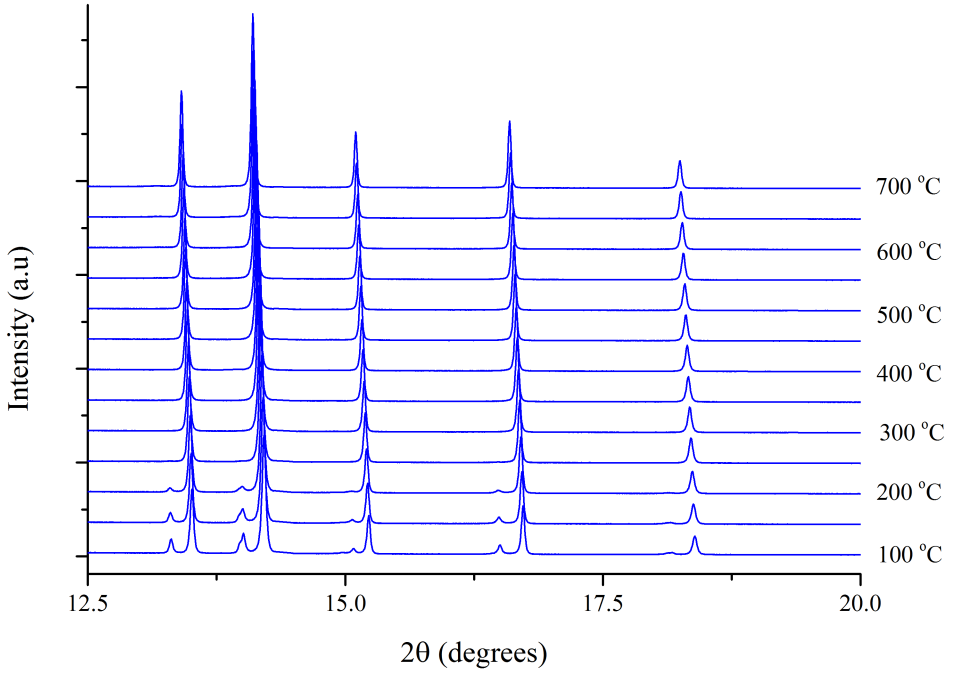

FIGURE 5.9: A portion of S-XRD data demonstrating the temperature dependence of $CaUO_{4-x}$ heated under pure O_2 from 100 to 700 ^{o}C.

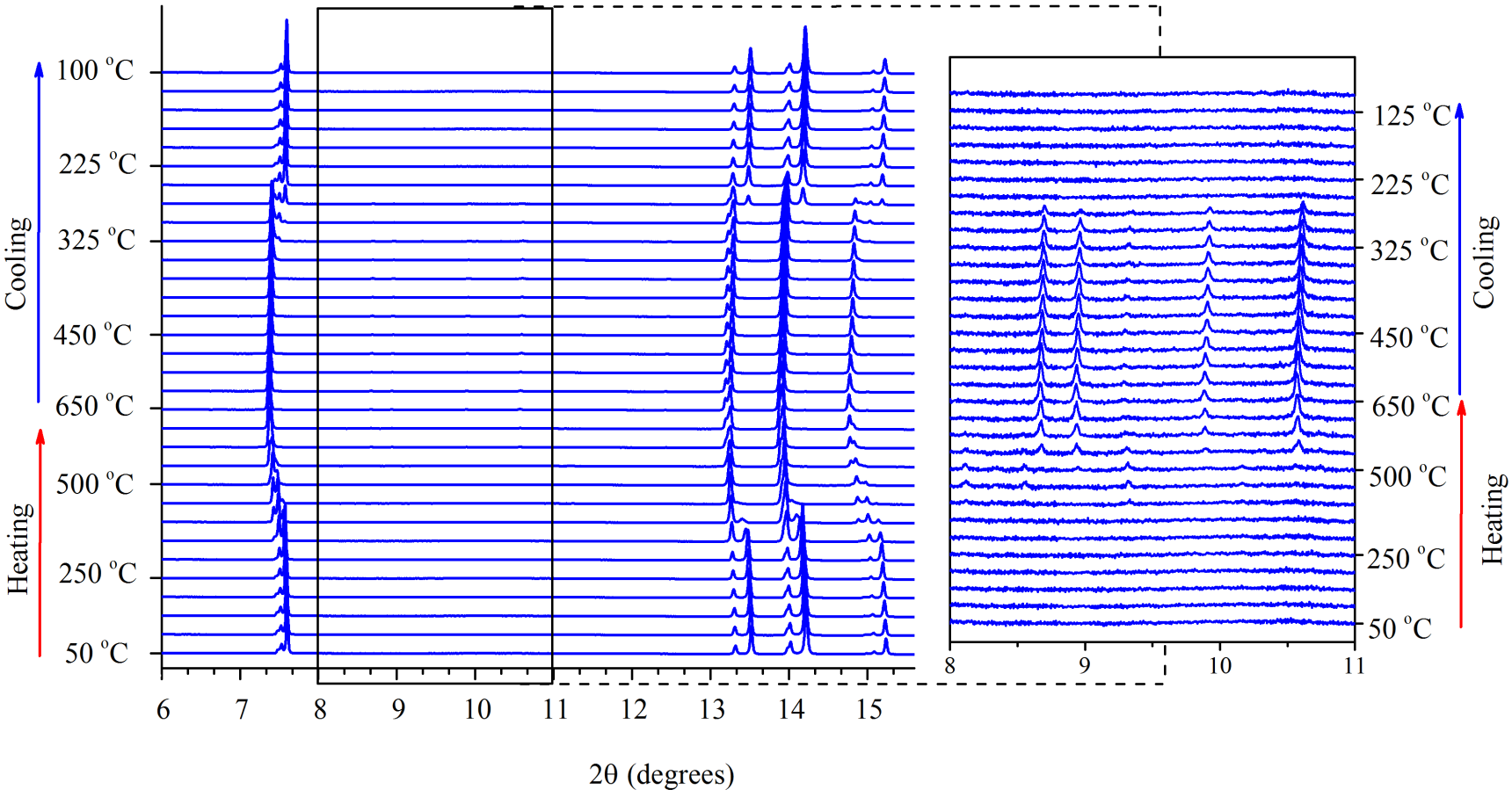

FIGURE 5.10: S-XRD patterns showing the temperature dependence of $CaUO_{4-x}$ heated under pure H_2 gas flow from 50 to 550 °C and back to 50 °C. The inset highlights the reversibility of the presence of superlattice reflections corresponding to the reversible formation of the ordered δ phase.

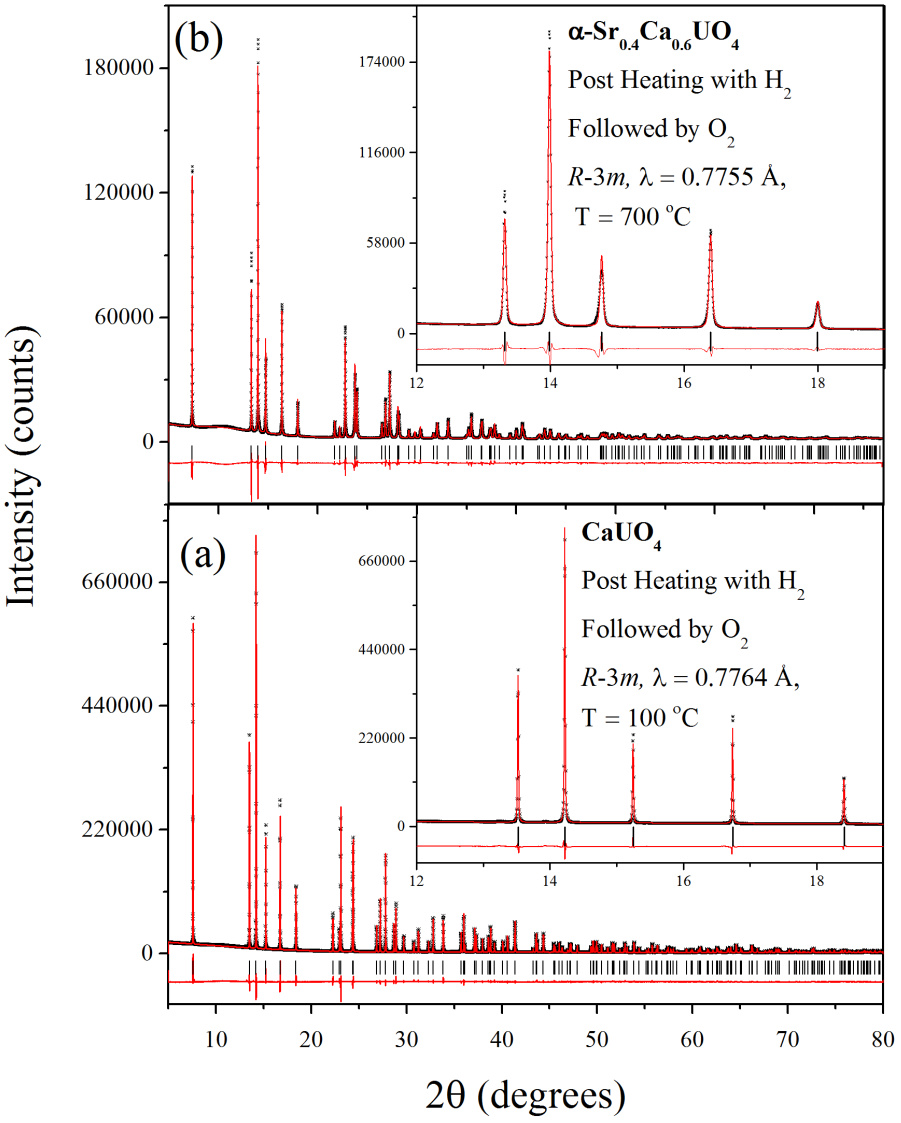

FIGURE 5.11: Rietveld profiles for α-$Sr_{0.4}Ca_{0.6}UO_4$ (top) at 700 ^{o}C and $CaUO_4$ (bottom) at 100 ^{o}C post H_2 gas flow and O_2 exposure taken using S-XRD data. The data was refined a rhombohedral structure in space group $R\bar{3}m$. The inset highlights the single phase nature of the sample. For $CaUO_4$ $\lambda = 0.7764$ Å, $wR_p = 10.52\%$, $R_p = 7.44\%$ and for α-$Sr_{0.4}Ca_{0.6}UO_{4-x}$ at 1000 ^{o}C $\lambda = 0.7755$ Å $wR_p = 4.84\%$, $R_p = 4.57\%$.

Due to beam time availability the reversibility of the ordering in δ-$Sr_{0.4}Ca_{0.6}UO_{4-x}$ under H_2 gas flow could not be examined. Rather the sample was heated to 1000 ^{o}C under O_2 gas flow to establish if the stoichiometric α-$Sr_{0.4}Ca_{0.6}UO_4$ could be recovered. This process is illustrated in Figure 5.12. During this oxidation heating cycle, the weak peaks due to the minor α-$Sr_{0.4}Ca_{0.6}UO_{4-x}$ phase are lost and there is no

evidence for any structural transformation or for the formation of any super lattice reflections. The profile measured at 700 ^{o}C could be fitted using a rhombohedral structure in space group $R\bar{3}m$. The Rietveld profile for the 700 ^{o}C data under O_2 gas flow is presented in Figure 5.11. Compared to $CaUO_4$ the peaks in α-$Sr_{0.4}Ca_{0.6}UO_4$ are considerably broader indicative of strain or reduced crystallinity. It is possible that longer heating times or heating to higher temperatures would improve the crystallinity. Comparing Figure 5.9 and 5.12, $CaUO_4$ reforms a single phase at a lower temperature then α-$Sr_{0.4}Ca_{0.6}UO_4$. Regardless these measurements demonstrate the reversibility of this transformation process.

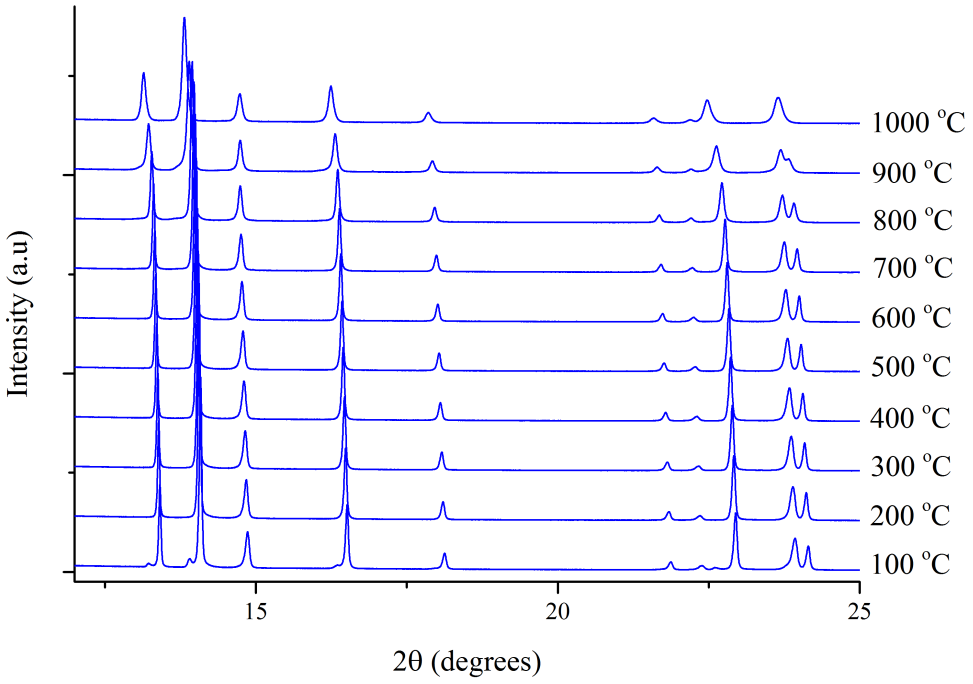

FIGURE 5.12: A portion of S-XRD data demonstrating the temperature dependence of α-$Sr_{0.4}Ca_{0.6}UO_{4-x}$ heated under pure O_2 from 100 to 1000 ^{o}C.

5.3.6 Superstructure Analysis and Discussion

As illustrated in Figure 5.13, there are noticeable variations, with respect to the temperature dependence, of the superlattice reflections of δ-$CaUO_{4-x}$ and δ-$Sr_{0.4}Ca_{0.6}UO_{4-x}$. From 550 to 750 ^{o}C the superlattice reflections of these two oxides are similar to each other and also similar to δ-$SrUO_{4-x}$ (Chapter 4) regarding position although differences are observed in their relative intensities. Interestingly as these samples are heated it is apparent that the reflections become more intense, suggesting the ordered defects are becoming

more ordered with temperature. However as noted previously, δ-$CaUO_{4-x}$ undergoes an abrupt change to its superlattice reflections above 875 ^{o}C and this is reflected in the inset of Figure 5.9 and Figure 5.13. This change involves the merging of some superlattice reflections while others are split into doublets. This suggests that the modulation of ordered superlattice of δ-$CaUO_{4-x}$ is changing with temperature and is thus temperature dependant. This change to the modulation of the superlattice is not observed in either δ-$Sr_{0.4}Ca_{0.6}UO_{4-x}$ or δ-$SrUO_{4-x}$, suggesting over the temperature range examined in these studies, the modulation of their superlattice is constant, although neutron diffraction measurements are required to confirm and better understand this.

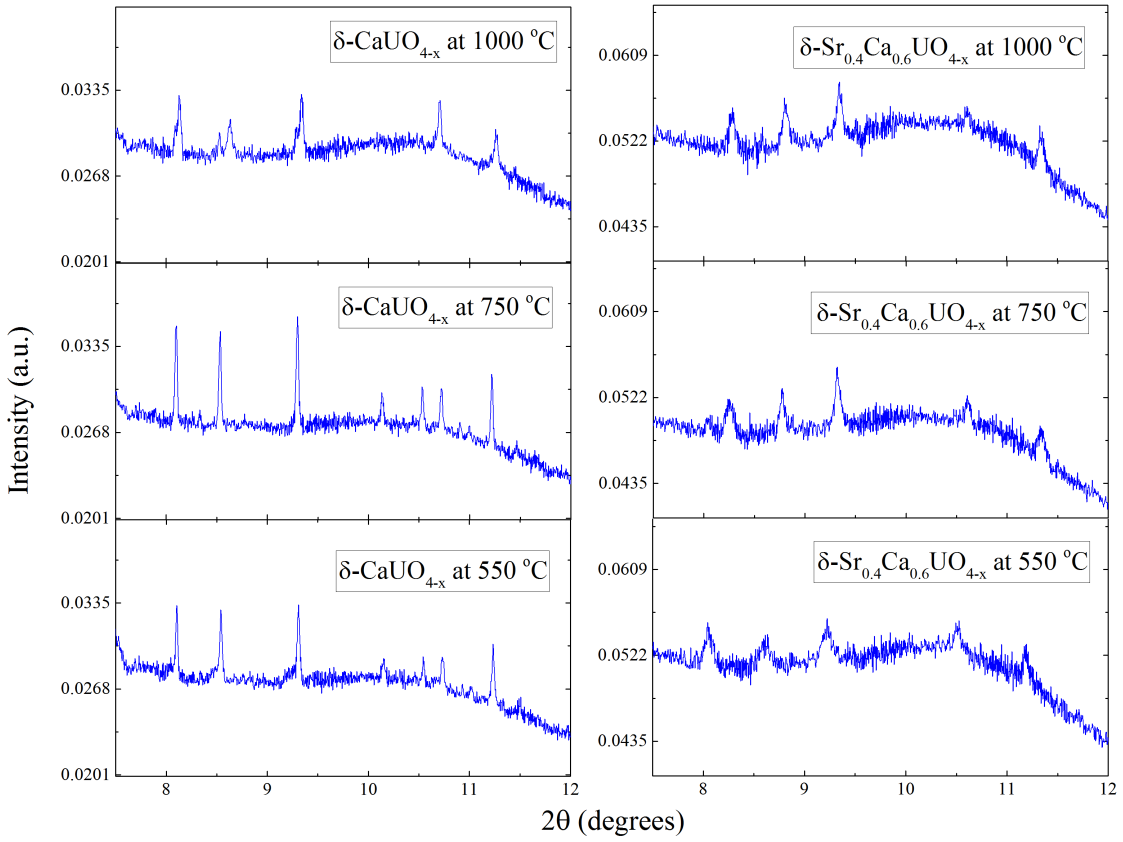

FIGURE 5.13: A portion of S-XRD data comparing the temperature dependence of the super lattice reflections for δ-$CaUO_{4-x}$ (left, $\lambda = 0.7764$ Å) and δ-$Sr_{0.4}Ca_{0.6}UO_{4-x}$ (right, $\lambda = 0.7755$ Å) between 7.5 and 12 2θ at 550, 750 and 1000 ^{o}C. Note the variation in reflections at 1000 ^{o}C for δ-$CaUO_{4-x}$ compared to lower temperature measurements presented here (intensities normalized to the strongest 100 main Bragg peak).

Considering the markedly different behaviour of the superlattice reflections of δ-$CaUO_{4-x}$ compared to δ-$Sr_{0.4}Ca_{0.6}UO_{4-x}$ or δ-$SrUO_{4-x}$, symmetry representation analysis was used in attempt to understand its peculiar high temperature ordering. The average structural model of δ-$CaUO_{4-x}$ at 1000 ^{o}C which does

not take into account the superlattice reflections is described in space group $P\bar{1}$ with $a = 6.4703$ Å, $b = 6.8856$ Å, $c = 3.9643$ Å, $\alpha = 89.78^o$, $\beta = 107.98^o$, $\gamma = 100.50^o$ with a cell volume = 164.9065(10) Å^3. The refined structural parameters for this are presented in Table 5.2. As described in the experimental section, the superlattice reflections were fitted using a modulation vector k = < 0.278, 0.159, 0.283 > based on the average cell. The refinement profile of this approximated structure is illustrated in Figure 5.14 and the structural parameters given in Table 5.3. Attempts were made to establish the occupancy modulation of oxygen in this model but the refinement could not converge to a stable value, presumably as a consequence of the comparatively weak scattering of the oxygen anions relative to the uranium cations. The average structure of δ-$CaUO_{4-x}$ is illustrated in Figure 5.15. The inability to assign a commensurate distortion vector to δ-$CaUO_{4-x}$and precisely determine its structure, highlights the markedly different superstructure topological and particularly, positional ordering of oxygen vacancies, between it, δ-$Sr_{0.4}Ca_{0.6}UO_{4-x}$ and δ-$SrUO_{4-x}$.

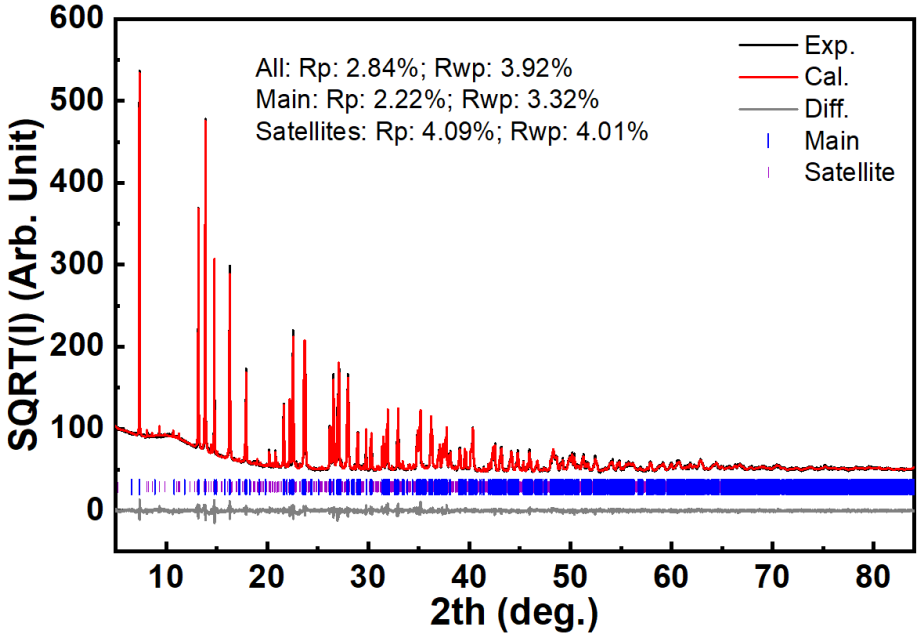

FIGURE 5.14: Rietveld refinement profile of ordered δ-$CaUO_{4-x}$. The black line represents experimental data, red line is the refined model, grey line is the difference plot, and the blue and purple vertical markers are the allowed space group reflections of the triclinic main structure and the satellite superstructure, respectively. The square root of the intensity of the peaks is used to make the satellite reflections clearer.

It is noteworthy that the transformation temperature from the stoichiometric rhombohedral α phase into the non-stoichiometric ordered δ phase is lowered as the Sr content increases for the three oxides

TABLE 5.2: Structural parameters for ordered δ-$CaUO_{4-x}$ average structure at 1000 ^{o}C from Rietveld refinement against S-XRD data.

a (Å)	6.47035(2)		$\alpha(^{o})$		89.8719(3)
b (Å)	6.88559(2)		$\beta(^{o})$		107.9814(3)
c (Å)	3.964331(13)		$\gamma(^{o})$		100.4957(3)
V (Å^3)	164.9065(10)		D_{theo} (g cm^{-3})		6.78
Space group	$P\bar{1}$ (No 2)		Formula		$CaUO_{4-x}$
Site	x	y	z	Occupancy	U_{iso} (Å^2)
U(1)	0	0.5	0	1	0.01228(8)
U(2)	0	0	0.5	1	0.01228(8)
Ca(1)	0.4934(17)	0.2448(16)	0.252(3)	1	0.0261(7)
O(1)	0.3277(4)	0.577(2)	0.163(3)	1	0.0046(15)
O(2)	0.3277(4)	0.035(2)	0.712(3)	1	0.0046(15)
O(3)	0.078(3)	0.210(2)	-0.047(5)	0.835(5)	0.0046(15)
O(4)	0.038(2)	0.677(2)	0.534(4)	0.835(5)	0.0046(15)

TABLE 5.3: Structural parameters for ordered δ-$CaUO_{4-x}$ modulation structure at 1000 ^{o}C from Rietveld refinement. The modulation vector for this refinement was: 0.278**a***+0.159**b***, 0.283**c***

a (Å)	6.47035(2)	$\alpha(^{o})$	89.8719(3)
b (Å)	6.88559(2)	$\beta(^{o})$	107.9814(3)
c (Å)	3.964331(13)	$\gamma(^{o})$	100.4957(3)
V (Å^3)	164.9065(10)	D_{theo} (g cm^{-3})	6.78
Space group	$P\bar{1}$ ($\alpha\beta\gamma$)	Formula	$CaUO_{4-x}$

$CaUO_{4-x}$, $Sr_{0.4}Ca_{0.6}UO_{4-x}$ and $SrUO_{4-x}$. Interestingly it is also observed that the transformation to the δ phase in $CaUO_{4-x}$ occurs at a lower temperature upon reheating, 300 vs 450 ^{o}C. It seems reasonable to postulate that the thermally induced transformation to the ordered δ phase requires both a critical amount of oxygen vacancies and sufficient thermal energy and that this combination is not initially achieved until the sample is heated to $\sim$ 450 ^{o}C under H_2. The necessary stoichiometry is maintained by cooling under H_2 such that the regeneration of the δ phase is simply controlled by temperature. Evidently defect interactions and their contribution to free energy seem to be playing a further role here [42–46]. More energy, and consequently greater temperatures, are required to overcome defect interactions in $CaUO_{4-x}$ to obtain the critical defect concentration necessary for the formation of the δ structure compared to α-$SrUO_4$ or α-$Sr_{0.4}Ca_{0.6}UO_4$ due to the difference in defect-defect interactions between these. Interestingly once the critical amount of defects has been obtained in $CaUO_{4-x}$, it can transform to the δ phase at lower

temperature upon reheating; this is consistent with what is observed in δ-$SrUO_{4-x}$. This suggests that the α to δ phase transformation is energetically less costly than the initial reduction from stoichiometric AUO_4 to the critical defect state.

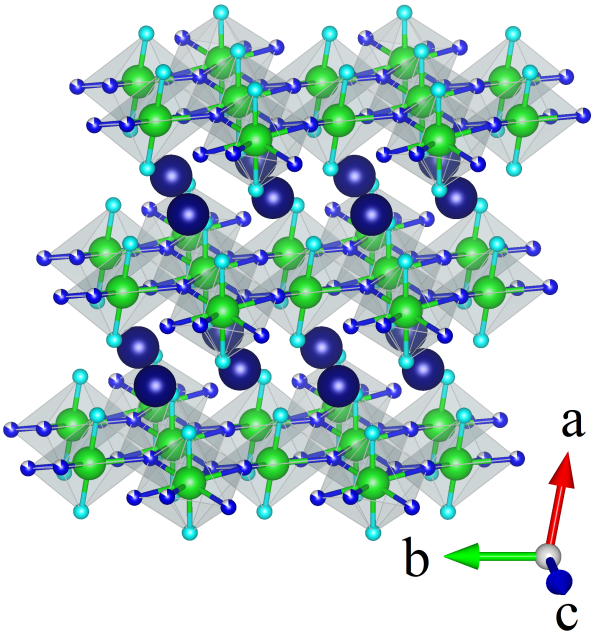

FIGURE 5.15: The average triclinic structure for δ-$CaUO_{4-x}$ and δ-$Sr_{0.4}Ca_{0.6}UO_{4-x}$ in $P\bar{1}$. The U and Ca cations are represented by blue and purple coloured spheres respectively, whereas the in-plane and out-of-plane oxo site oxygen anions are represented by blue and aqua respectively.

From the present work of this chapter it is apparent that the reversible symmetry lowering, through ordering of oxygen vacancies upon heating, is not unique to δ-$SrUO_{4-x}$ described in Chapter 4. There are several prominent examples of systems undergoing lowering in symmetry or exhibiting ordering with heating[47–49], however these are generally irreversible processes or require a change in composition. The reversible symmetry lowering, through ordering of oxygen vacancies upon heating, exhibited by the δ-AUO_4 family of oxides is distinct, occurring through thermodynamic response alone. Defect control is also important to consider here, apparently influencing both the temperature at which the ordered δ phase superstructures form and modulation used to describe their ordering. As mentioned in Chapter 4, the thermodynamic origin of these phase transformations is not clear, although by DFT+U calculations indicate that it involves a careful balance between the enthalpy and entropy of the system. These three ordered structures thus provide a platform to establish the thermal chemistry and particularly how

defect phenomena influences superstructure formation although this is beyond the scope of the present dissertation.

5.4 Chapter Conclusion

In summary it was demonstrated that the ability for rhombohedral $CaUO_4$ to host oxygen defects at high temperature under oxidising conditions can be controlled and increased by partially substituting Ca^{2+} ions for Sr^{2+} ions up to 40%. This leads to an increase in the unit cell volume, which presumably decreases defect interactions allowing more defects and by extension, reduced uranium valence states, to form with heating. When $CaUO_4$ and α-$Sr_{0.4}Ca_{0.6}UO_4$ are heated under highly reducing conditions they undergo reversible phase transformations involving the ordering of oxygen vacancies and lowering of crystallographic symmetry, forming layered triclinic structures denoted δ in space group $P\bar{1}$ from indexing diffraction data collected at 1000 ^{o}C. That the transformations are reversible demonstrates they are not related to any chemical changes such as decomposition or reduction, but instead are purely thermodynamic in origin. The transformation temperature from the stoichiometric oxide to the ordered δ phase is seemingly influenced by the size of alkaline metal cation and unit cell size. An increase in unit cell size results in a lowering of the transition temperature, and it is postulated that this is related to defect interactions increasing free energy. It was found that the solid solution α-$Sr_{0.4}Ca_{0.6}UO_4$ is not continuous for all x, only for $0 < x < 0.4$ and $0.9 < x$ 1.0, the intermediate composition in between separating into two rhombohedral phases. Despite the single phase regions being isostructural, when these are heated under highly reducing conditions they form δ phases with subtly different defect ordering arrangements as indicated by the appearance of the superlattice reflections. Observing the diffraction patterns of δ-$CaUO_{4-x}$ shows it contains markedly different superlattice reflections to that of δ-$Sr_{0.4}Ca_{0.6}UO_{4-x}$ and δ-$SrUO_{4-x}$ indicating that the modulation used to describe the ordering arrangement is temperature dependent. The stoichiometric structures can be readily recovered by heating under pure oxygen, demonstrating the total reversibility from ambient temperature stoichiometric AUO_4 to high temperature oxygen ordered δ-AUO_{4-x}. These are still the only examples of materials which can undergo reversible high temperature defect ordering and symmetry lowering phase transformations with heating.

References

1. Steele, B. C. H. and Heinzel, A. *Nature* **414**(6861), 345–352 (2001).

2. Shao, Z. P. and Haile, S. M. *Nature* **431**(7005), 170–173 (2004).

3. Attariani, H., Momeni, K., and Adkins, K. *ACS Omega* **2**(2), 663–669 (2017).

4. Lahiri, J., Lin, Y., Bozkurt, P., Oleynik, I., and Batzill, M. *Nature Nanotechnology* **5**(5), 326–329 (2010).

5. Suenaga, K. and Oomi, G. *Journal of the Physical Society of Japan* **60**(4), 1189–1192 (1991).

6. Wang, D. Y., Park, D. S., Griffith, J., and Nowick, A. S. *Solid State Ionics* **2**(2), 95–105 (1981).

7. Wilde, P. J. and Catlow, C. R. A. *Solid State Ionics* **112**(3-4), 173–183 (1998).

8. Steele, B. C. H. *Solid State Ionics* **129**(1-4), 95–110 (2000).

9. Bogicevic, A. and Wolverton, C. *Physical Review B* **67**(2) (2003).

10. Vantendeloo, G., Krekels, T., Milat, O., and Amelinckx, S. *Journal of Alloys and Compounds* **195**(1-2), 307–314 (1993).

11. Kuzmany, H., Matus, M., Faulques, E., Pekker, S., Hutiray, G., Zsoldos, E., and Mihaly, L. *Solid State Communications* **65**(11), 1343–1346 (1988).

12. Tsai, H., Nie, W., Blancon, J.-C., Stoumpos, C. C., Asadpour, R., Harutyunyan, B., Neukirch, A. J., Verduzco, R., Crochet, J. J., Tretiak, S., Pedesseau, L., Even, J., Alam, M. A., Gupta, G., Lou, J., Ajayan, P. M., Bedzyk, M. J., Kanatzidis, M. G., and Mohite, A. D. *Nature* **536**, 312 (2016).

13. Harada, Y. *Journal of Nuclear Materials* **238**(2), 237–243 (1996).

14. Cardinaels, T., Govers, K., Vos, B., Van den Berghe, S., Verwerft, M., de Tollenaere, L., Maier, G., and Delafoy, C. *Journal of Nuclear Materials* **424**(1-3), 252–260 (2012).

15. Sawbridge, P. T., Reynolds, G. L., and Burton, B. *Journal of Nuclear Materials* **97**(3), 300–308 (1981).

16. Badwal, S. P. S., Bannister, M. J., and Murray, M. J. *Journal of Electroanalytical Chemistry* **168**(1-2), 363–382 (1984).

17. Badwal, S. P. S. and Bevan, D. J. M. *Journal of Materials Science* **14**(10), 2353–2365 (1979).

18. Runge, H. and Greenblatt, M. *Solid State Ionics* **177**(3-4), 269–274 (2006).

19. Murphy, G., Kennedy, B. J., Johannessen, B., Kimpton, J. A., Avdeev, M., Griffith, C. S., Thorogood, G. J., and Zhang, Z. M. *Journal of Solid State Chemistry* **237**, 86–92 (2016).

20. Tagawa, H., Fujino, T., and Yamashita, T. *Journal of Inorganic & Nuclear Chemistry* **41**(12), 1729–1735 (1979).

21. Anderson, J. S. and Barraclough, C. G. *Transactions of the Faraday Society* **59**(487), 1572–1576 (1963).

22. Pialoux, A. and Touzelin, B. *Comptes Rendus De L Academie Des Sciences Serie Ii Fascicule B-Mecanique Physique Chimie Astronomie* **323**(10), 687–693 (1996).

23. Pialoux, A. and Touzelin, B. *Journal of Nuclear Materials* **255**(1), 14–25 (1998).

24. Prodan, A. and Boswell, F. W. *Acta Crystallographica Section B-Structural Science* **42**, 141–146 (1986).

25. Wallwork, K. S., Kennedy, B. J., and Wang, D. *The high resolution powder diffraction beamline for the Australian Synchrotron*, volume 879 of *AIP Conference Proceedings*, 879–882. Amer Inst Physics, Melville (2007).

26. Liss, K. D., Hunter, B., Hagen, M., Noakes, T., and Kennedy, S. *Physica B-Condensed Matter* **385-86**, 1010–1012 (2006).

27. Larson, A. C. and Dreele, R. B. V. Technical report, Los Alamos National Laboratory, (2000).

28. Toby, B. H. *Journal of Applied Crystallography* **34**, 210–213 (2001).

29. Toby, B. H. and Von Dreele, R. B. *Journal of Applied Crystallography* **46**(2), 544–549 (2013).

30. Norby, P. *In-situ time resolved synchrotron powder diffraction studies of syntheses and chemical reactions*, volume 228 of *Materials Science Forum*, 147–152. Transtec Publications Ltd, Zurich-Uetikon (1996).

31. Giannozzi, P., Baroni, S., Bonini, N., Calandra, M., Car, R., Cavazzoni, C., Ceresoli, D., Chiarotti, G. L., Cococcioni, M., Dabo, I., Dal Corso, A., de Gironcoli, S., Fabris, S., Fratesi, G., Gebauer, R., Gerstmann, U., Gougoussis, C., Kokalj, A., Lazzeri, M., Martin-Samos, L., Marzari, N., Mauri, F.,

Mazzarello, R., Paolini, S., Pasquarello, A., Paulatto, L., Sbraccia, C., Scandolo, S., Sclauzero, G., Seitsonen, A. P., Smogunov, A., Umari, P., and Wentzcovitch, R. M. *Journal of Physics-Condensed Matter* **21**(39) (2009).

32. Perdew, J. P., Burke, K., and Ernzerhof, M. *Physical Review Letters* **77**(18), 3865–3868 (1996).

33. Vanderbilt, D. *Physical Review B* **41**(11), 7892–7895 (1990). PRB.

34. Cococcioni, M. and de Gironcoli, S. *Physical Review B* **71**(3), 035105 (2005). PRB.

35. Beridze, G. and Kowalski, P. M. *Journal of Physical Chemistry A* **118**(50), 11797–11810 (2014).

36. Zunger, A., Wei, S. H., Ferreira, L. G., and Bernard, J. E. *Physical Review Letters* **65**(3), 353–356 (1990).

37. Li, Y., Kowalski, P. M., Blanca-Romero, A., Vinograd, V., and Bosbach, D. *Journal of Solid State Chemistry* **220**, 137–141 (2014).

38. Coelho, A. A., Evans, J. S. O., Evans, I. R., Kern, A., and Parsons, S. *Powder Diffraction* **26**, S22–S25 (2011).

39. Evans, J. S. O. *Advanced Input Files & Parametric Quantitative Analysis Using Topas*, volume 651 of *Materials Science Forum*, 1–9. (2010).

40. Petricek, V., Dusek, M., and Palatinus, L. Technical Report 5, (2014).

41. Tagawa, H. and Fujino, T. *Journal of Inorganic & Nuclear Chemistry* **40**(12), 2033–2036 (1978).

42. Beyerlein, I. J., Demkowicz, M. J., Misra, A., and Uberuaga, B. P. *Progress in Materials Science* **74**, 125–210 (2015).

43. Brewer, S. J., Cress, C. D., Williams, S. C., Zhou, H. H., Rivas, M., Rudy, R. Q., Polcawich, R. G., Glaser, E. R., Jones, J. L., and Bassiri-Gharb, N. *Scientific Reports* **7** (2017).

44. Grieshammer, S. *Journal of Physical Chemistry C* **121**(28), 15078–15084 (2017).

45. Grieshammer, S. and Martin, M. *Journal of Materials Chemistry A* **5**(19), 9241–9249 (2017).

46. Grieshammer, S., Zacherle, T., and Martin, M. *Physical Chemistry Chemical Physics* **15**(38), 15935–15942 (2013).

47. Tsujimoto, Y., Tassel, C., Hayashi, N., Watanabe, T., Kageyama, H., Yoshimura, K., Takano, M., Ceretti, M., Ritter, C., and Paulus, W. *Nature* **450**(7172), 1062–1066 (2007).

48. Shamblin, J., Feygenson, M., Neuefeind, J., Tracy, C. L., Zhang, F. X., Finkeldei, S., Bosbach, D., Zhou, H. D., Ewing, R. C., and Lang, M. *Nature Materials* **15**(5), 507–511 (2016).

49. Desgranges, L., Baldinozzi, G., Simeone, D., and Fischer, H. E. *Inorganic Chemistry* **55**(15), 7485–7491 (2016).

Chapter 6

Elucidating the Solid State Chemistry of the Ni-U-O System

This chapter is adapted from a manuscript titled "High Pressure Synthesis, Structural and Spectroscopic Studies of the Ni-U-O System" by G. L. Murphy *et al.* that has been published in the journal *Inorganic Chemistry*.

6.1 Introduction

Several of the structural phase transformations are known between the various structural types within the family of AUO_4 oxides. For instance the transformation between the alkaline earth metal rhombohedral and orthorhombic variants, described in Chapter 3, is irreversible between rhombohedral α-$SrUO_4$ and orthorhombic β-$SrUO_4$. The transformations that occur between U^{6+} oxides with rutile-related structures and the rhombohedral variants has been described for $CdUO_4$, where the rhombohedral α-$CdUO_4$ to orthorhombic β-$SrUO_4$ transformation is reported[1,2] to be irreversible. Whereas Chapters 4 and 5 have described the novel reversible symmetry lowering defect ordering transformations which the rhombohedral variants can access, provide they obtain suitable sub-stoichiometry. There appears to be no meaningful reports of phase transformations involving any of the U^{6+} orthorhombic oxides with rutile-related structures, for instance $MnUO_4$[3], $CoUO_4$[4] and $MgUO_4$[5] or for the orthorhombic U^{5+} oxides with the space group *Pbcn* seen in $CrUO_4$[6] and $FeUO_4$[3,7].

In 2014 Read *et al.*[3] published a structural hierarchy between the well-known AUO_4 variants based on the ratio of A to U site ionic radii. The hierarchy is largely consistent with the reported transformations but does highlight the paucity of information regarding transformations between U^{6+} orthorhombic oxides with rutile-related structures with the space group *Pbcn* orthorhombic U^{5+} oxides. Read *et al.*[3] suggest that an intermediate between these structural variants, based on ionic radii, would be $NiUO_4$, however they discount its existence arguing the Ni^{2+} cation is too small relative to the U^{6+} cation to allow formation of a rutile lattice. However this is in conflict with two reports from the 1960's which describe structures denoted α-$NiUO_4$[8] and β-$NiUO_4$[8,9] forming under high temperature and high pressure (HT/HP) conditions. Hoeskstra and Marshal[8] describe α-$NiUO_4$ as forming an orthorhombic structure isostructural to $CrUO_4$[6] and α-$NiUO_4$ as forming an orthorhombic structure isostructural to $MgUO_4$[5] under similar synthetic conditions around 4 GPa at 1000 ^{o}C for 30 min. Young[9] independently described the preparation of β-$NiUO_4$ at higher pressures and temperatures (6 GPa at 1100 ^{o}C), suggesting that the β-form might be preferred with increasing pressure/temperature. Neither the studies by Hoekstra and Marshal[8] or Young[9] provide any structural refinements and their structural assignments are based on only indexing laboratory XRD patterns. Further, there is no information regarding any phase transformation that would occur between the polymorphs of $NiUO_4$ and the oxidation states of their metal cations.

Since α-$NiUO_4$ is apparently isostructural to $CrUO_4$ which possesses trivalent Cr and pentavalent U cations[10], and β-$NiUO_4$ is isostructural to $MgUO_4$ in which the Mg is divalent and U hexavalent[10], it is possible that the relative stability of the two structures is related to electron transfer between the Ni and U cations. Generally Ni^{3+} is far less commonly encountered than Ni^{2+} owing to the stability of the $3d^8$ electron configuration of the latter. This presents an interesting hypothesis to be tested here: does an orthorhombic structure of $NiUO_4$ in space group *Pbcn* exist, and if so, does it require the presence of trivalent Ni and pentavalent U cations (isoelectric with $CrUO_4$ and $FeUO_4$), or can the structure be achieved with divalent Ni and hexavalent U cations?

Within the broader Ni-U-O system, other than the $NiUO_4$ polymorphs, the only other structures reported are NiU_2O_6 and NiU_3O_{10}. NiU_2O_6 has been well examined by single crystal X-ray diffraction[3], neutron power diffraction[11] and magnetic measurements[12]. NiU_2O_6 can be generated either from flux[3] or by heating its constituent oxides in an evacuated quartz tube[11,12] or in air[13]; where it forms a trigonal structure in space group $P321$ containing divalent nickel and pentavalent uranium. NiU_3O_{10} has been examined using single crystal X-ray diffraction analysis by Hoekstra and Marshal[8], who concludes it to be isostructural with CuU_3O_{10}[14] in space group $P\bar{1}$ but little other crystallographic information is available. Interestingly, both NiU_2O_6 and NiU_3O_{10} can be prepared under ambient pressure conditions, unlike the $NiUO_4$ polymorphs.

The literature suggests that there is apparent interplay between the ionic radii of the U and Ni site cations that effects, not only structure formation and type within both the AUO_4 oxides, but also within the Ni-U-O system. Consequently it is necessary to broaden the scope of this work, from the $NiUO_4$ polymorphs, towards others members of the Ni-U-O system in order to elucidate the solid state chemistry that underpins both the Ni-U-O system and the AUO_4 family of oxides. In this chapter, flux growth and HT/HP synthetic methods were used to firstly understand the conditions under which the oxides, NiU_3O_{10} and the two polymorphs of $NiUO_4$ form. Single crystal synchrotron X-ray diffraction measurements were used to determine the precise structures of these oxides. To determine the U oxidation state, X-ray absorption near edge structure (XANES) measurements were performed at the U L_3-edge from single crystals. The results are discussed with respect to the Ni-U-O system, the family and proposed hierarchy of AUO_4 oxides, and their relation to the general rutile family of oxides.

6.2 Experimental

6.2.1 High Temperature/Pressure Synthesis of $NiUO_4$

Stoichiometric quantities of NiO (obtained from sintering nickel nitrate, Alfa-Aesar, 99.9%) and U_3O_8 (obtained from sintering uranyl nitrate, International Bioanalytical Industries, Inc. 99%) were thoroughly mixed together, loaded into platinum crucibles and sealed. In order to understand the conditions at which the $NiUO_4$ polymorphs form, several synthesis experiments were undertaken using either piston cylinder or multi anvil apparatus (Voggenreiter LP 1000-540/50) located at IEK-6, Forschungszentrum Julich, Germany (Figure 6.1). The conditions of these are presented in Table 6.1, and the results of laboratory powder X-ray diffraction (XRD) and single crystal X-ray diffraction (SC-XRD) are also included in Table 6.1. Samples obtained from two synthesis experiments, one subjected to a pressure of 4 GPa and a temperature of 900 ^{o}C and another to a pressure of 10 GPa and temperature of 1200 ^{o}C, were selected for further analysis. The conditions for these and the corresponding $NiUO_4$ polymorph produced are described here:

- α-$NiUO_4$ (4 GPa and 900 ^{o}C): The sample was initially placed under a pressure of 4 GPa with a compression time of 30 minutes using a piston cylinder apparatus. Upon reaching the desired pressure, the sample was then rapidly heated to 900 ^{o}C in 20 minutes. These conditions were maintained for 12 hours before cooling to 600 ^{o}C over 48 hours and subsequently to room temperature rapidly. Then the pressure was gradually reduced to ambient over a period of 30 minutes.

- β-$NiUO_4$ (10 GPa and 1200 ^{o}C): The sample was initially placed under a pressure of 10 GPa with a compression time of 7.5 hours using a multi anvil apparatus. Upon reaching the desired pressure, the sample was then rapidly heated to 1200 ^{o}C using a ramp rate of 100 ^{o}C/min. These conditions were maintained for 1 hour before cooling to 600 ^{o}C over 3 hours and subsequently to room temperature, rapidly. Then the pressure was gradually removed over a period of 24 hours.

The crucibles from the described experiments were dismantled post-synthesis and found to contain either a mixture of α-$NiUO_4$ and NiU_3O_{10} (4 GPa and 900 ^{o}C) or a mixture of β-$NiUO_4$and NiU_3O_{10} (10 GPa and 1200 ^{o}C) as determined by XRD and SC-XRD. Fine single crystals of α-$NiUO_4$ (black), β-$NiUO_4$

(dark red), and NiU_3O_{10} (also black but much smaller in size) were mechanically separated for further analysis.

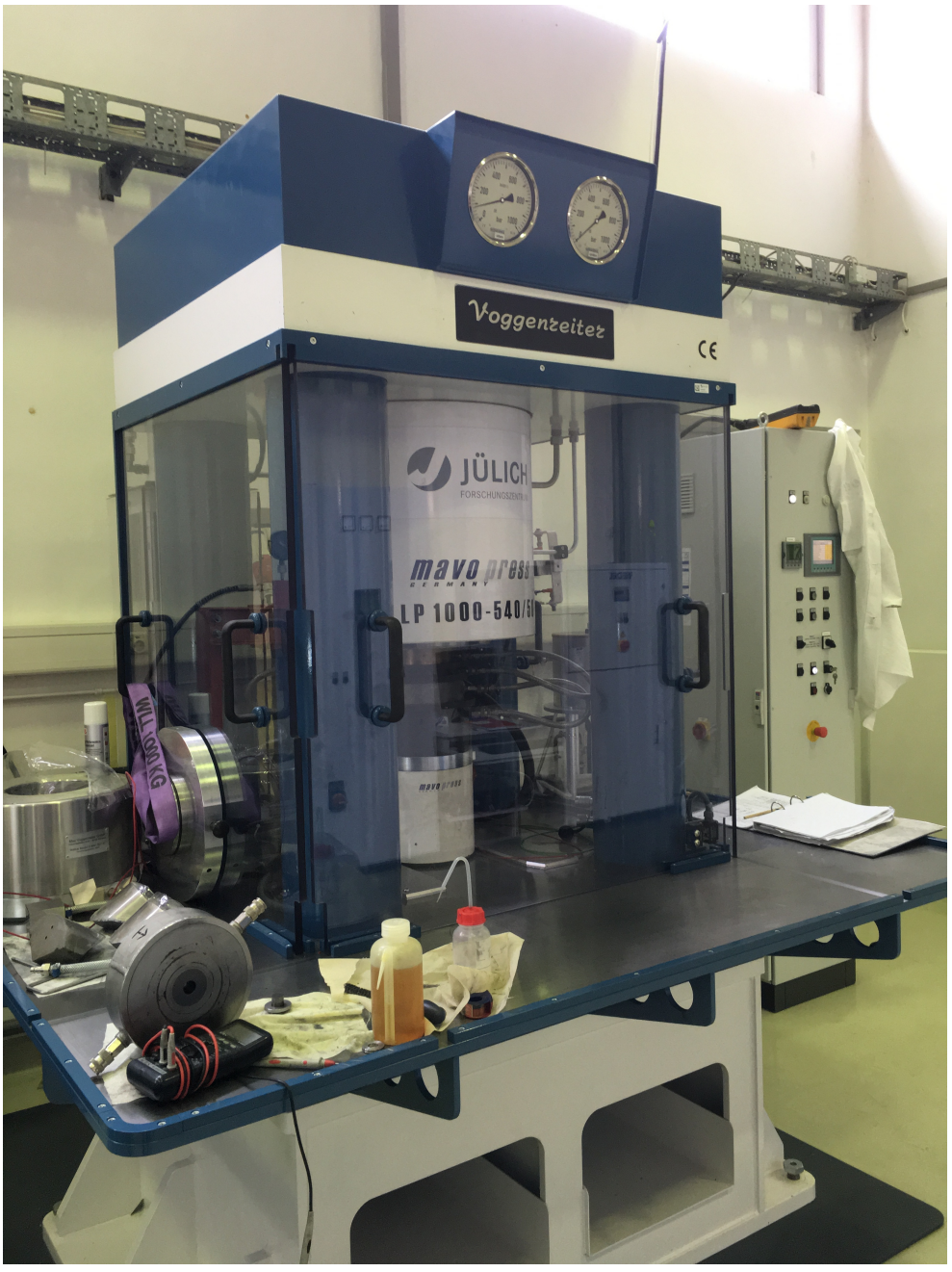

FIGURE 6.1: Voggenreiter LP 1000-540/50 high temperature high pressure apparatus installed at IEK-6, Forschungszentrum Julich, Germany.

TABLE 6.1: High temperature and high pressure conditions used to synthesize polymorphs of $NiUO_4$. Phases were determined using SC-XRD and powder XRD.

Temperature (^{o}C)	Pressure (GPa)	Phases present
900	2	NiU_3O_{10}
700	4	α-$NiUO_4$ + NiU_3O_{10}
900	4	α-$NiUO_4$ + NiU_3O_{10}
950	4	α-$NiUO_4$ + NiU_3O_{10}
1000	4	β-$NiUO_4$ + NiU_3O_{10}
1200	10	β-$NiUO_4$ + NiU_3O_{10}

6.2.2 Synthesis of NiU_3O_{10} (Ambient Pressure Conditions)

NiU_3O_{10} single crystals were readily recovered from the HT/HP experiments, but to confirm there was no structural modification associated with the use of high pressures, single crystals were also grown under ambient pressure conditions using a combined solid state and molten salt regrowth method. Stoichiometric quantities of NiO and U_3O_8 were intimately mixed and calcined for 72 hours using a platinum crucible in a box furnace at 1000 ^{o}C with intermittent mixing. The final product was mixed with excess $NiCl_2.6\,H_2O$ (Alfa Aesar 99.99%) and heated to 1100 ^{o}C at a ramp rate of 100 ^{o}C /hour, and the molten mixture was held at this temperature for 24 hours before being slowly cooled to 600 ^{o}C at 1 ^{o}C/min and then to room temperature at 10 ^{o}C/min. The final product was washed extensively with deionized water, to remove excess $NiCl_2$, before fine black single crystals of NiU_3O_{10} were mechanically separated for further analysis.

6.2.3 Single Crystal X-ray Diffraction

Single crystal X-ray diffraction (SC-XRD) data were collected to confirm crystal quality. SC-XRD measurements were undertaken at room temperature using an Agilent Technologies SuperNova diffractometer with Mo Kα radiation ($\lambda = 0.71073$ Å) equipped with a EOS CCD detector installed at IEK-6, Forschungszentrum Julich, Germany. All data sets were corrected for Lorentz and polarization factors as well as for absorption by the multiscan method.

6.2.4 Scanning Electron Microscopy and Energy Dispersive X-ray Spectroscopy

The morphology and elemental composition of the crystals were determined using a FEI Quanta 200F Environment Scanning Electron Microscope (SEM) fitted with an energy dispersive X-ray spectrometer (EDS) installed at IEK-6, Forschungszentrum Julich, Germany. This verified the sample compositions based on the SC-XRD structure solutions, see Figure 6.2 and Table 6.2.

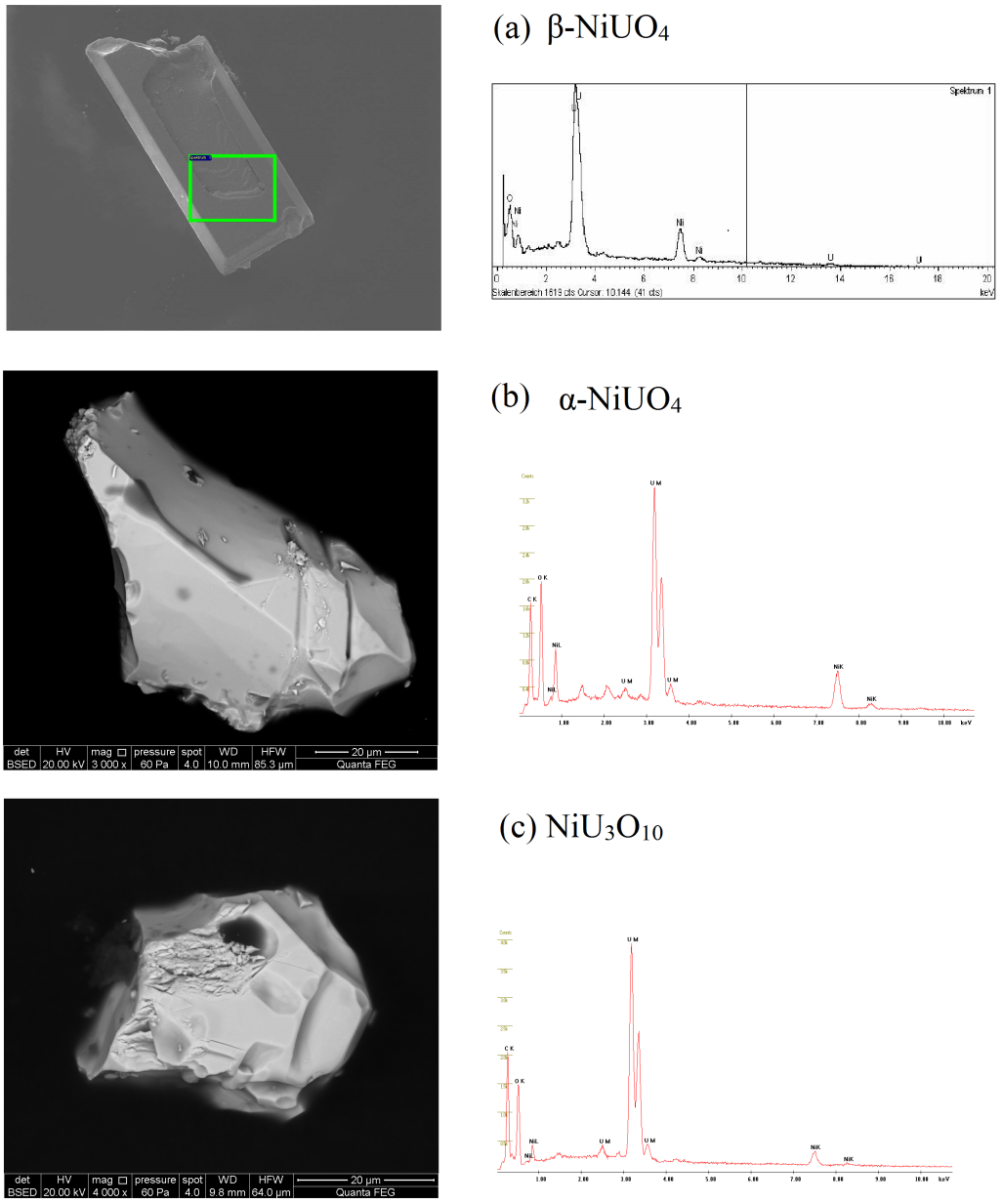

FIGURE 6.2: SEM and EDS analysis of (a) β-$NiUO_4$, (b) α-$NiUO_4$ and (c) NiU_3O_{10}.

TABLE 6.2: EDS measurements of some singe crystals for α-$NiUO_4$, β-$NiUO_4$ and NiU_3O_{10}.

sample	β-$NiUO_4$		α-$NiUO_4$		NiU_3O_{10}	
Element	U	Ni	U	Ni	U	Ni
Point 1	10.5	9.2	10.9	10.6	13.9	5.15
Point 2	10.8	9.2	11.1	13.3	13.6	5.21
Point 3	10.8	9.6	13.0	15.3	-	-
Average U:Ni	1.1	1	0.9	1	2.7	1

6.2.5 Laboratory Characterisation

Powder X-ray diffraction (XRD) measurements were made at room temperature using a Bruker AXS D8 Endeavor diffractometer (40 kV/40 mA) in Bragg-Brentano geometry installed at IEK-6, Forschungszentrum Julich, Germany. The diffractometer has a copper X-ray tube and a primary nickel filter, producing Cu Kα radiation. A linear silicon strip LynxEye detector (Bruker-AXS) was used. Data were collected in the range 2θ = 5-100^o with 10 sec/step and a step width of 0.02^o. The aperture of the fixed divergence slit was set to 0.2 mm and the receiving slit to 8 mm. The discriminator of the detector was set to an interval of 0.16 - 0.25 V. Samples were contained in domed sample holders due to their radioactive nature. Data were analysed by pattern matching using the program FullProf[15] where space group and lattice parameter information were obtained from single crystal X-ray measurements, as described below.

6.2.6 Synchrotron Single Crystal X-ray Diffraction

SSC-XRD data were collected at 100(2) K on the MX2 beamline[16] at the Australian Synchrotron with a Si double-crystal monochromator (λ = 0.71085 Å). All data were collected using Blu-Ice software[17]. Cell refinements and data reductions were undertaken using XDS software[18]. An empirical absorption correction was applied to the data using SADABS[19]. The structures were solved by direct methods using SHELXT[20], and the full-matrix least-squares refinements were carried out using SHELXL[21] via the Olex2 interface[22]. The one circle goniometer geometry of data collections at the MX2 beamline offers less opportunity for applying multi-scan absorption correction as is possible with the data collections on a four

circle goniometer. Consequently, ripples around U atoms are often present due to ineffective absorption correction. In addition, the data completeness is relatively low for crystals in low symmetry space groups.

6.2.7 X-ray Absorption Near Edge Structure (XANES) Measurements

XANES spectra were collected at the uranium L_3-edge for single crystals of α-$NiUO_4$, β-$NiUO_4$ and NiU_3O_{10}, as well as for powder samples of $CrU^{5+}O_4$ and $CoU^{6+}O_4$ (as U standards), on the X-ray Fluorescence Microscopy (XFM) beamline[23] at the Australian Synchrotron. The crystals were identified using SSC-XRD measurements. The measurements were performed at room temperature in fluorescence mapping mode using the Maia detector system[24,25]. Despite the excellent performance of the XFM monochromator, all specimens were measured in a single energy series to preclude errors resulting from any non-reproducibility of the X-ray energy; thus, while the individual energies may suffer some small uncertainty, all features are perfectly aligned. The potential impact of self-absorption effects, which suppress peak amplitudes in the XANES spectrum[26], are estimated to be less than 5% and this level of self-absorption is not detrimental to this study. Fluorescence data were analysed by fitting fluorescence spectra at each energy using a full forward model and with a moving edge formulation[27] within GeoPIXE[28]. The series of images were aligned using one of the lower-energy spectator elements and the fluorescence intensities for the three unknown and two reference specimens extracted from the entire specimen on the basis of their spatial location within the scan area. Further analysis on the fluorescence intensities was carried out using the software package ATHENA[29].

6.3 Results and Discussion

6.3.1 Syntheses

The two polymorphs of $NiUO_4$ were initially attempted to be synthesized using conventional solid state methods under ambient pressure, effective for other ternary uranium oxides[30], but as consistent with the reports of Hoekstra and Marshall[8], this was unsuccessful. Consequently HT/HP methods were employed. Hoekstra and Marshall[8] did not provide sufficient information to establish the optimal conditions to form either polymorph as in their synthesis they did not seem to be able to isolate a sample that was not mixed

with both polymorphs of $NiUO_4$. To understand the conditions under which each polymorph forms, a variety of temperature and pressure combinations was explored to understand which of the phases are preferred under given conditions. These are summarised in Table 6.1 where the phases were identified using both single crystal and powder XRD analysis. Although high pressure is necessary to obtain either polymorph of $NiUO_4$, temperature also plays a key role. 2 GPa is insufficient to stabilize either $NiUO_4$ polymorph at 900 ^{o}C whereas 700 ^{o}C was found to be sufficient to form α-$NiUO_4$ when the pressure was increased to 4 GPa. β-$NiUO_4$ is apparently favoured at both higher temperature and higher pressure conditions relative to α-$NiUO_4$ from Table 6.1. It is therefore expected that under a pressure of 4 GPa, α-$NiUO_4$ undergoes a phase transformation to β-$NiUO_4$ at a temperature between 950 and 1000 ^{o}C. Hoestra and Marshal[8] reported that both $NiUO_4$ polymorphs undergo decomposition above 920 ^{o}C under ambient pressure conditions to NiU_3O_{10} and NiO. From this it is deduced that high pressure is necessary for the phase transformation between the two $NiUO_4$ polymorphs to proceed. That the $NiUO_4$ polymorphs are recovered and stable from the HT/HP synthesis experiments is likely due to removing temperature first then pressure when finishing the experiments. Unfortunately, due to the time constraints a constant temperature variable pressure experiment could not be undertaken.

Small crystals of NiU_3O_{10} were readily identified and recovered from all the α-$NiUO_4$ or β-$NiUO_4$ HT/HP synthesis experiments. Analysis showed these to be structurally identical to the NiU_3O_{10} crystals obtained from the ambient pressure solid state and molten salt regrowth synthesis described above. Powder XRD patterns were analysed using profile matching, and examples for synthesis experiments at T = 900 ^{o}C and P = 4 GPa (α-$NiUO_4$) and T = 1000 ^{o}C and P = 4 GPa (β-$NiUO_4$) are presented in Figure 6.3. It is postulated that the presence of NiU_3O_8 reflects the non-isostatic conditions during synthesis. In general both $NiUO_4$ polymorphs were observed to form larger single crystals than NiU_3O_{10}, suggesting the preference of the former structures over the latter in high pressure conditions.

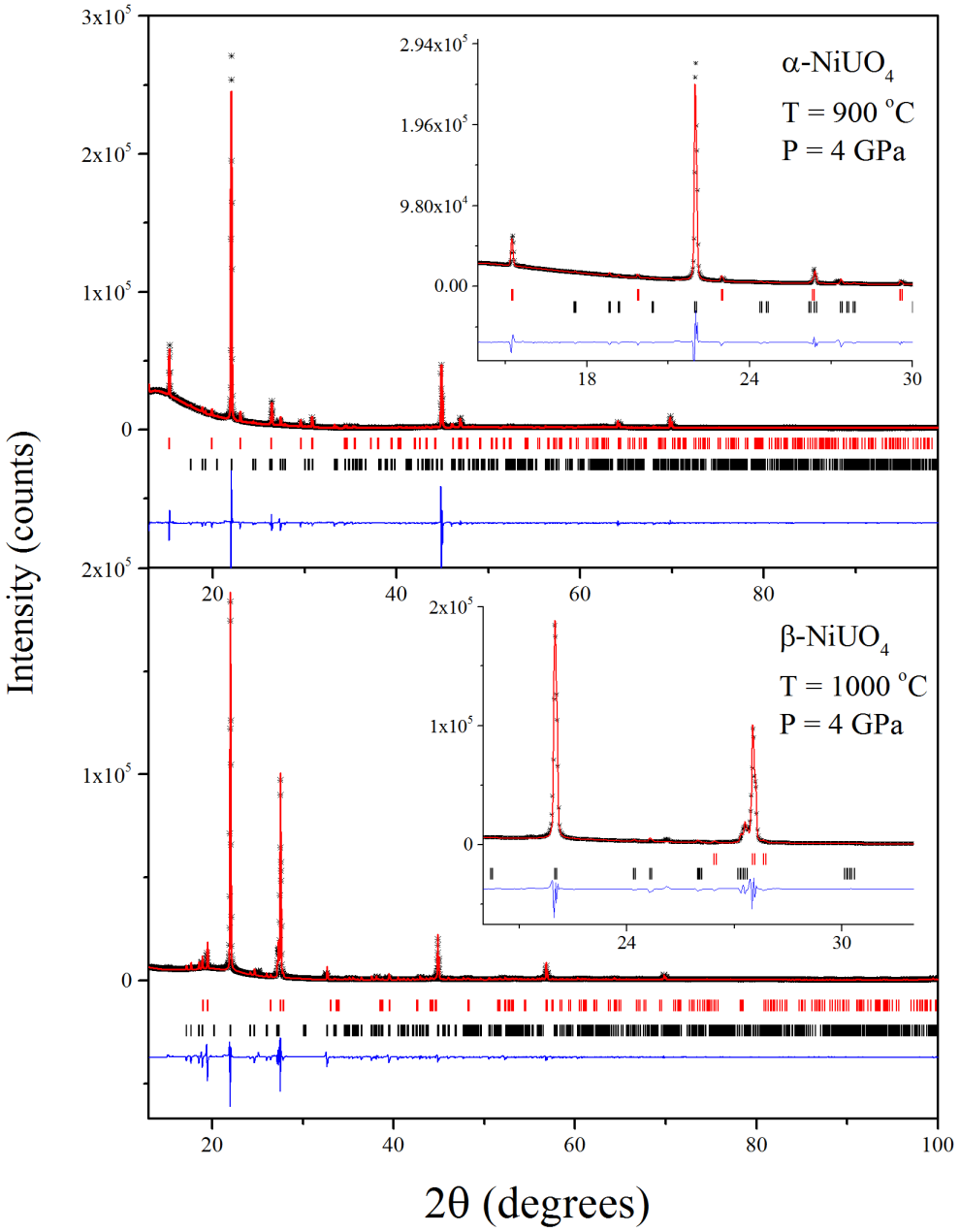

FIGURE 6.3: Powder XRD patterns collected from products of the synthesis experiments conducted at T = 900 °C and P = 4 GPa (top) and T = 1000 °C and P = 4 GPa (bottom), analysed using profile matching in the program FullProf. The top pattern was fitted against an α-$NiUO_4$ and NiU_3O_{10} model in their respective space groups *Pbcn* and $P\bar{1}$ using refined lattice parameters initially obtained from SC-XRD measurements. The bottom pattern was fitted against a β-$NiUO_4$ and NiU_3O_{10} model in their respective space groups *Ibmm* and $P\bar{1}$ using refined lattice parameters initially obtained from SC-XRD measurements. The red line, black dots, blue line, red vertical markers and black vertical markers correspond to the calculated model, collected data, difference curve, allowed reflections of the $NiUO_4$ polymorph in each pattern and allowed reflections of NiU_3O_{10}. The insets highlight the two phase nature of the samples. The low angle hump is a consequence of the sample dome used to house and contain the samples due to their radioactive and radiotoxic nature.

6.3.2 Structural Studies 1. α-$NiUO_4$

The structure of α-$NiUO_4$ was solved in the orthorhombic space group *Pbcn* using SSC-XRD measurements with a unit cell volume of 277.58(9) Å^3. Crystal data and refinement details are presented in Table 6.3, and structural parameters can be found in Table 6.4. Due to absorption issues thermal displacement parameters were constrained to isotropic. α-$NiUO_4$ is isostructural to $CrUO_4$[6] and FeUO4[3,7], and the structure is presented in Figure 6.4. This structural model is consistent with the early investigation by Hoekstra and Marshall[8] who concluded, based on the comparison of their powder XRD patterns, that α-$NiUO_4$ is isostructural with $CrUO_4$, although they placed $CrUO_4$ in a different space group (*Cmcm*).

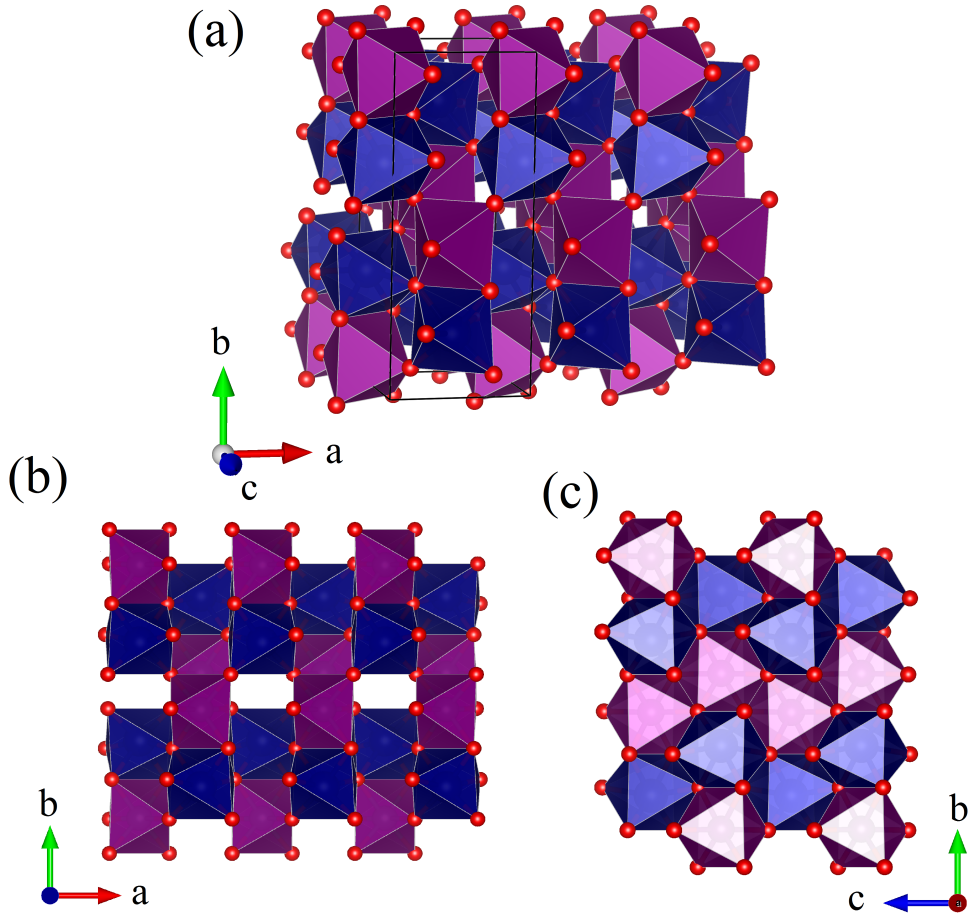

FIGURE 6.4: (a) Structural representation of α-$NiUO_4$ in space group *Pbcn*, (UO_6 and NiO_6 are represented as dark blue and purple grey polyhedra where oxygen atoms are represented as small red spheres). (b) Highlights corrugated 2D layers of corner sharing UO_6 polyhedra parallel to the (010) plane, and (c) highlights edge sharing 1D zig-zag rutile chains of NiO_6 polyhedra in the [001] direction.

The structure of α-$NiUO_4$ consists of corner sharing UO_6 polyhedra forming corrugated 2D-like layers parallel to the (010) plane. Between these layers NiO_6 polyhedra edge share forming zig-zag 1D chains in the [001] direction similar to the PbO_6 chains in the zig-zag rutile structure of α-PbO_2 [31]. None of the six U-O bonds are collinear, all forming O-U-O angles less than 170^o. Furthermore, the linkage between adjacent UO_6 polyhedra occurs through four of the six oxygens, the two remaining oxo U-O bonds are cis and not in the trans collinear configuration associated with the uranyl moiety [32]. The U-O bond lengths range from 1.949(10) to 2.227(10) Å and the Ni-O bond lengths range from 2.004(10) to 2.064(10) Å, details of bond distances can be found in Table 6.6. Considering the arrangement of the U-O bonds in the UO_6 polyhedra, the typical uranyl oxo moiety encountered in other ternary uranium oxides [30] is not present in α-$NiUO_4$. This is consistent with the remarks by Read *et al.* [3] in their study of $FeUO_4$. Bond valence sums (BVS) calculations for the Ni and U sites in α-$NiUO_4$ produced respective values of 2.18 and 6.46 suggesting the presence of divalent Ni and hexavalent U. It is interesting to note that although α-$NiUO_4$ is isostructural to $Cr^{3+}U^{5+}O_4$ and $Fe^{3+}U^{5+}O_4$, BVS calculations indicate that the oxidation states of Ni and U in α-$NiUO_4$ are divalent and hexavalent respectively. This difference in valence states is consistent with the longer U-O bond distances reported for $CrUO_4$ [10] and $FeUO_4$ [10] compared to those for α-$NiUO_4$.

TABLE 6.3: Crystal data and structure refinement details for α-$NiUO_4$, β-$NiUO_4$ and NiU_3O_{10}.

Compound	α-$NiUO_4$	β-$NiUO_4$	NiU_3O_{10}
Formula	$NiUO_4$	$NiUO_4$	NiU_3O_{10}
Formula weight	360.74	360.74	932.80
Crystal system	Orthorhombic	Orthorhombic	Triclinic
Space group	*Pbcn*	*Ibmm*	$P\bar{1}$
a (Å)	4.7500(9)	6.3840(13)	5.5010(11)
b(Å)	11.436(2)	6.3709(13)	5.5400(11)
c (Å)	5.1100(10)	6.7639(14)	7.5450(15)
α (^{o})	90	90	70.93(3)
β (^{o})	90	90	70.48(3)
γ (^{o})	90	90	72.94(3)
Volume (Å^3)	277.58(9)	275.10(10)	200.40(9)
Z / μ (mm^1)	4 / 64.846	4 / 65.431	1 / 62.771
Min./Max. θ [^{o}]	3.564/27.442	4.391/24.860	2.962/24.997
d_{calcd} (g cm^3)	8.632	8.710	7.729
GOF	1.108	1.195	1.196
Final R_1 [a] [$I > 2\sigma(I)$]	0.0353	0.0257	0.0501
Final wR_2 [b] [$I > 2\sigma(I)$]	0.0734	0.0699	0.1287

[a] $R_1 = \sum ||F_o| - |F_c|| / |F_o|$. [b] $wR_2 = (\sum[w(F_o{}^2 - F_c{}^2)^2] / \sum[w(F_o{}^2)^2])^{1/2}$

Table 6.4: Refined structural parameters for α-$NiUO_4$ in orthorhombic space group *Pbcn* from SSC-XRD data.

Atom	x	y	z	Ui/Ue (Å^3)	U^{11}	U^{22}	U^{33}
U	0.5	0.16996(6)	0.75	0.0021(4)	0.0025(5)	0.0019(5)	0.0020(5)
Ni	0.5	0.4371(2)	0.75	0.0021(4)	0.0025(5)	0.0019(5)	0.0020(5)
O1	0.244(2)	0.0594(8)	0.916(2)	0.0021(4)	0.0025(5)	0.0019(5)	0.0020(5)
O2	0.276(2)	0.3039(8)	0.903(2)	0.002(1)	0.0025(5)	0.0019(5)	0.0020(5)

Table 6.5: Refined structural parameters for β-$NiUO_4$ in orthorhombic space group *Ibmm* from SSC-XRD data.

Atom	x	y	z	Ui/Ue (Å^3)	U^{11}	U^{22}	U^{33}
U	0.03810(13)	0.5	0.25	0.03810(13)	0.0041(8)	0.0023(7)	0.0028(7)
Ni	0.5	0.5	0.5	0.0002(7)	-	-	
O1	0.0354(17)	0.802(2)	0.25	0.0023(17)	-	-	
O2	0.1936(17)	0.5	0.5269(18)	0.0023(17)	-	-	

6.3.3 Structural Studies 2. β-$NiUO_4$

The structure of β-$NiUO_4$ is described by the orthorhombic space group *Ibmm* based on SSC-XRD data and has a unit cell volume of 275.10(10) Å^3. Crystal data and refinement details are presented in Table 6.3, and structural parameters can be found in Table 6.5. Due to absorption issues thermal displacement parameters were constrained to isotropic. The structure is isostructural to that of $MgUO_4$ (described in the alternative space group of *Imma*)[5], and is presented in Figure 6.5. This is consistent with both Young's[9] and Hoekstra and Marshall's[8] original investigations of β-$NiUO_4$. The structure consists of UO_6 polyhedra edge sharing to form infinite 1D chains in the [001] direction similar to that in the archetype TiO_2 rutile structure. The UO_6 polyhedra form near tetragonal bipyramids where the shorter oxo-uranyl like collinear trans U-O(1) bonds (length = 1.921(13) Å) point towards Ni cations along the [010] direction. This uranyl length is considered long for hexavalent uranium[32] although is similar to α-$SrUO_4$ at 1.958(3) Å[30]. There are two longer U-O(2) bonds, labelled U-O(2)$_i$ and U-O(2)$_{ii}$, of length 2.113(12) and 2.120(12) Å, that link adjacent uranium polyhedra to form the 1D chains. The NiO_6 polyhedra form tetragonal bipyramids that edge share also forming infinite 1D chains along the [001] direction. Four long Ni-O(1) bonds are observed as a consequence of the coordination with the oxo-uranyl like O(1) oxygens at a length of 2.124(8) Å, and provide the edge sharing link of the NiO_6 chain. The two short Ni-O(2) bonds at 1.965(11) Å are collinear to each other and lie near parallel to the [100] direction. The UO_6 polyhedra are considerably distorted as highlighted in Figure 6.5a. Using the method of Robinson *et al.*[33] an approximate bond angle variance of 162.82 (^{o2}) is calculated for the UO_6 polyhedra compared to the NiO_6 polyhedra which are relatively free of distortion with an approximate bond angle variance of 108.08 (^{o2}). Refined bond lengths for β-$NiUO_4$ are listed in Table 6.6.

When the NiO_6 polyhedra in β-$NiUO_4$ are examined, a considerable off-axis tilt around the [010] axis is apparent as seen in Figure 6.5c. This is reminiscent to that observed in ABX_3 perovskite structures[34]. The ideal perovskite structure is cubic in space group $Pm\bar{3}m$, consisting of corner sharing BX_6 octahedra and AX_{12} cubo-octahedra. The structure can readily depart from the archetype cubic symmetry through a variety of distortion mechanisms including BX_6 tilting. This occurs when the A site cation is too small for the BX_6 corner-sharing connectivity. The BX_6 corner-sharing geometry is such that the tilting can either be in-phase or out-of-phase, described well by the Glazer notation[35]. The geometry of the edge sharing NiO_6 chains allows tilting to occur only along the edge. This acts as a fulcrum for the tilt to

occur along the chain linkage, causing the NiO_6 polyhedra to successively reverse tilt relative to the [010] axis, i.e., out-of-phase tilting. The U-O(2) bonds exhibit a consequential lengthening and shortening of the bonds which apparently induces the observed distortion in the UO_6 polyhedra.

TABLE 6.6: Selected bond distances (Å) for α-$NiUO_4$, β-$NiUO_4$ and NiU_3O_{10} obtained using SSC-XRD.

α-$NiUO_4$				β-$NiUO_4$				NiU_3O_{10}			
U	U	O1	1.949(10)	U	U	O1	1.921(13)	U1	U1	O2	1.936(19)
	U	O1	1.949(10)		U	O1	1.921(13)		U1	O2	1.936(19)
	U	$O2_i$	2.022(9)		U	$O2_i$	2.113(12)		U1	O3	2.020(17)
	U	$O2_i$	2.022(9)		U	$O2_i$	2.113(12)		U1	O3	2.020(17)
	U	$O2_{ii}$	2.227(10)		U	$O2_{ii}$	2.120(12)		U1	O5	2.287(18)
	U	$O2_{ii}$	2.227(10)		U	$O2_{ii}$	2.120(12)		U1	O5	2.287(18)
Ni	Ni	O1	2.004(10)	Ni	Ni	O2	1.965(11)	U2	U2	O1	2.122(18)
	Ni	O1	2.004(10)		Ni	O2	1.965(11)		U2	O1	2.27(2)
	Ni	O1	2.064(10)		Ni	O1	2.124(8)		U2	O2	2.450(17)
	Ni	O1	2.064(10)		Ni	O1	2.124(8)		U2	O3	2.525(19)
	Ni	O2	2.015(10)		Ni	O1	2.124(8)		U2	O3	2.34(2)
	Ni	O2	2.015(10)		Ni	O1	2.124(8)		U2	O4	1.835(17)
									U2	O5	1.894(17)
								Ni	Ni	O1	2.038(17)
									Ni	O1	2.038(17)
									Ni	O2	2.00(2)
									Ni	O2	2.00(2)
									Ni	O4	2.126(17)
									Ni	O4	2.126(17)

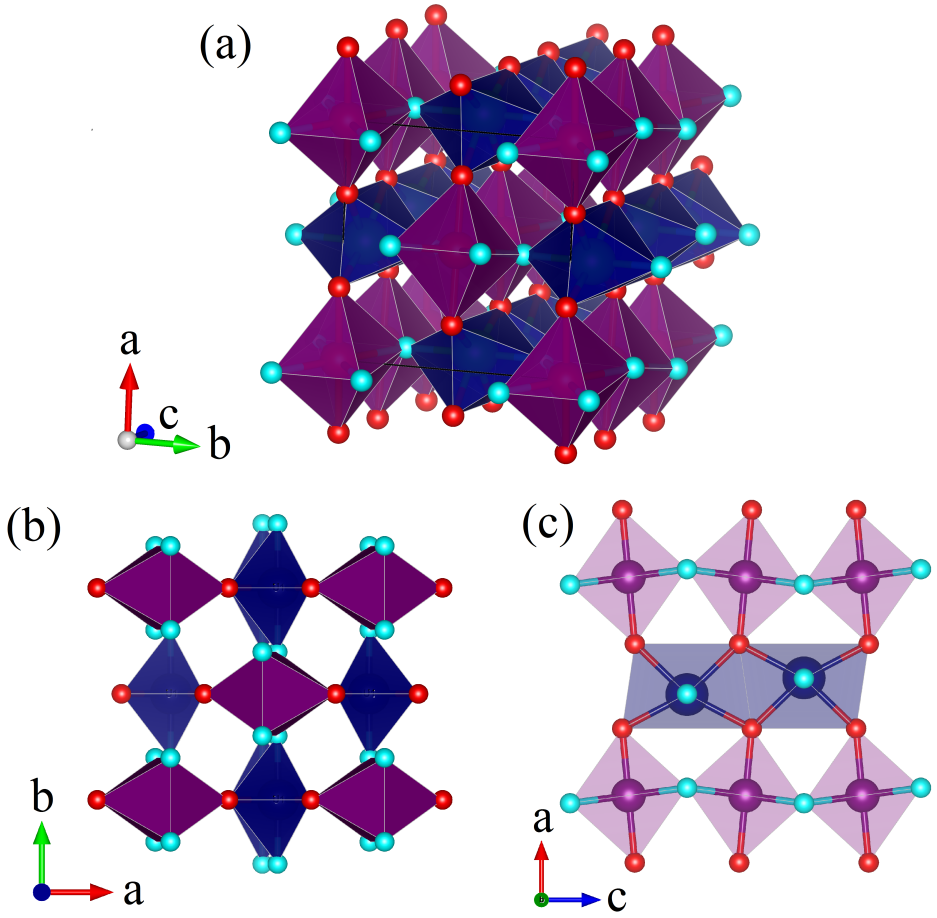

FIGURE 6.5: (a) Structural representation of orthorhombic β-$NiUO_4$ in space group *Ibmm* (UO_6 and NiO_6 are represented as dark blue and purple grey polyhedra where oxo and non-oxo oxygen atoms are represented as small aqua and red spheres respectively). (b) Highlights alternating 1D chains of UO_6 and NiO_6 polyhedra in the [001] direction similar to regular TiO_2 rutile, and (c) highlights the distortion of UO_6 polyhedra and the tilt of NiO_6 polyhedra.

BVS calculations were used to provide insight into the valence state of the metal cations in β-$NiUO_4$; values of 1.99 and 6.10 were obtained for Ni and U respectively suggesting the presence of divalent Ni and hexavalent U. Comparing the unit cell volumes between α-$NiUO_4$ and β-$NiUO_4$, the latter has a slightly smaller volume of 275.10(10) $Å^3$ compared to 277.58(9) $Å^3$. Typically smaller unit cell volumes are favoured by higher pressures, thus it is unsurprising that β-$NiUO_4$ was synthesized under higher pressure conditions, and consequently α-$NiUO_4$ is expected to undergo a phase transformation to the β polymorph with increasing pressure at constant temperature.

6.3.4 Structural Studies 3. NiU_3O_{10}

SSC-XRD measurements showed the structure of NiU_3O_{10} to be triclinic in space group $P\bar{1}$ with a unit cell volume of 200.40(9) Å^3. Crystal data and refinement details are presented in Table 6.3, and structural parameters can be found in Table 6.7. It is isostructural with CuU_3O_{10} [14] and the structure is related to that of $USbO_5$ [36]. The structure is represented in Figure 6.6 and consists of two distinct uranium sites, U(1) and U(2), forming $U(1)O_6$ and $U(2)O_7$ polyhedra respectively which link together to form a 3D framework like structure. Contained within the structure are NiO_6 polyhedra isolated from other NiO_6 groups by the UO_6/UO_7 framework. As presented in Figure 6.6b, the $U(2)O_7$ polyhedra edge share with other $U(2)O_7$ polyhedra forming 1D zig-zag chains along the [001] direction. The $U(1)O_6$ polyhedra bridge these chains via an in-plane edge and out-of-plane corner sharing motif. This edge sharing between the $U(1)O_6$ with the $U(2)O_7$ polyhedra involves U(1)-O(2) and U(1)-O(3) bonds where the former bonds corner share with the NiO_6 polyhedra. The $U(1)O_6$ polyhedra also corner share with $U(2)O_7$ polyhedra, linking the layers via the U(1)-O(5) bonds. The U(1)-O(2) bond is shorter, relative to the U(1)-O(3) and U(1)-O(5) bonds, with a refined length of 1.936(19) Å and it has a trans-collinear configuration with another U(1)-O(2) bond of the same length. This arrangement is suggestive of the presence of the uranyl moiety, despite it not being a terminal oxo as a consequence of its direct coordination to the $U(2)O_7$ polyhedra. The U(1)-O bond lengths in the $U(1)O_6$ polyhedra range from 1.936(19) to 2.287(18) Å forming relatively regular polyhedra whereas the bond lengths in the $U(2)O_7$ polyhedra range from 1.835(17) to 2.525(19) Å. The Ni-O distances in the NiO_6 polyhedra range from 2.00(2) to 2.126(17) Å. Details of the refined bond lengths can be found in Table 6.6. BVS calculations for the U(1), U(2) and Ni sites produce respective values of 6.28, 4.81 and 2.16. This seems to suggest that NiU_3O_{10} contains divalent nickel but surprisingly may contain mixed uranium valence states indicative of pentavalent and hexavalent uranium. However, this is not considered correct as it would imply a stoichiometry of NiU_3O_9, rather this reflects the limitation of using BVS calculations for uranium oxides materials [37]. This is also supported by XANES results in the following section.

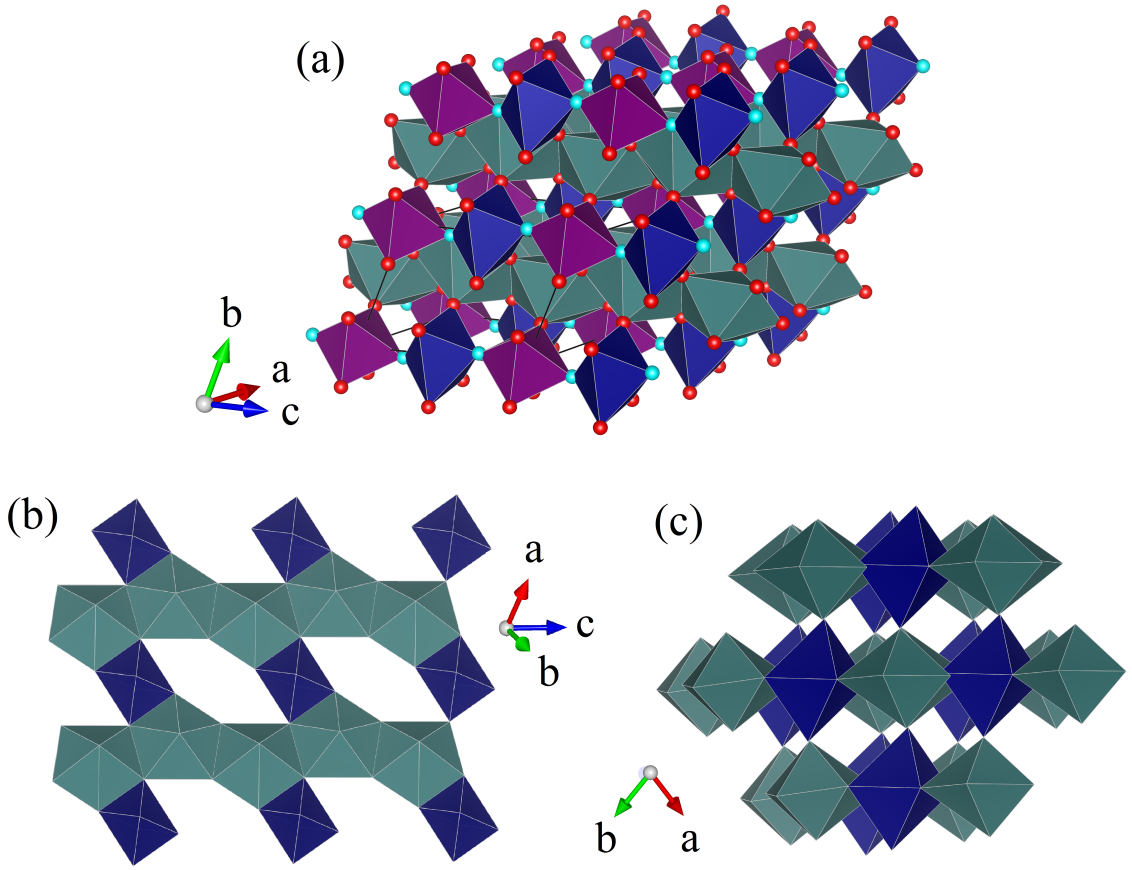

FIGURE 6.6: (a) Structural representation of NiU_3O_{10} in space group $P\bar{1}$ (UO_6, UO_7 and NiO_6 are represented as dark blue, silver-grey and purple polyhedra where uranyl-like oxygen and non-uranyl oxygen atoms are represented as small aqua and red spheres). (b) Highlights the UO_6-UO_7 edge sharing configuration, and the 1D zig-zag chains of U(2)O7 polyhedra along the [001] direction, and (c) highlights the UO_6 and UO_7 corner sharing configuration which forms the 3D UO_6-UO_7 framework. Note that NiO_6 polyhedra have been removed for clarity in (b) and (c).

TABLE 6.7: Refined structural parameters for NiU_3O_{10} in triclinic space group $P\bar{1}$ from SSC-XRD data.

Atom	x	y	z	Ui/Ue (Å^3)	U^{11}	U^{22}	U^{33}	U^{12}	U^{13}	U^{23}
Ni	0	0	0.5	0.0040(5)	0.0034(6)	0.0023(6)	0.0054(7)	-0.0013(4)	-0.0009(3)	0.0009(3)
O2	0.094(3)	-0.079(3)	0.251(3)	0.0040(5)	0.0034(6)	0.0023(6)	0.0054(7)	-0.0013(4)	-0.0009(3)	0.0009(3)
O3	0.094(3)	-0.079(3)	0.251(3)	0.0040(5)	0.0034(6)	0.0023(6)	0.0054(7)	-0.0013(4)	-0.0009(3)	0.0009(3)
O5	0.224(3)	-0.667(4)	0.352(3)	0.0040(5)	0.0034(6)	0.0023(6)	0.0054(7)	-0.0013(4)	-0.0009(3)	0.0009(3)
O4	0.710(3)	-0.234(3)	0.129(3)	0.0040(5)	0.0034(6)	0.0023(6)	0.0054(7)	-0.0013(4)	-0.0009(3)	0.0009(3)
O1	0.308(3)	-0.307(3)	-0.038(3)	0.0040(5)	0.0034(6)	0.0023(6)	0.0054(7)	-0.0013(4)	-0.0009(3)	0.0009(3)
U1	0	0	0.5	0.0040(5)	0.0034(6)	0.0023(6)	0.0054(7)	-0.0013(4)	-0.0009(3)	0.0009(3)
U2	0.47100(18)	-0.44730(18)	0.22696(15)	0.0040(5)	0.0034(6)	0.0023(6)	0.0054(7)	-0.0013(4)	-0.0009(3)	0.0009(3)

6.3.5 X-ray absorption Near Edge Structure (XANES) Studies

That α-$NiUO_4$ contains divalent nickel and hexavalent uranium cations, as suggested by BVS calculations, is in apparent conflict with the recent work of Guo *et al.*[10] who showed, using X-ray absorption spectroscopic measurements, that the isostructural $CrUO_4$ and $FeUO_4$ oxides contain trivalent chromium/iron and pentavalent uranium. As discussed by Burns *et al.*[37] BVS calculations involving uranium oxides are often compromised by the lack of precision in the structural determination (the heavy U cations dominate X-ray scattering hence reducing precision in the anion distances) and the impact of the uranyl group. Consequently XANES measurements were conducted in order to determine the oxidation states of the uranium cations in both $NiUO_4$ polymorphs as well as in NiU_3O_{10}. The persistent formation of multiphase samples in the HT/HP synthesis experiments precluded the option to prepare a pure phase powder sample suitable for standard XANES measurements. Mechanically isolating crystals of a sufficient quantity to generate a pure phase powder sample was found to be unreliable especially due to the similar morphologies and colours of crystals. To overcome this problem, XANES measurements at the U L_3-edge were undertaken by XANES mapping at the X-ray Fluorescence Microscopy (XFM) beamline of the Australian Synchrotron using single crystals of α-$NiUO_4$, β-$NiUO_4$, NiU_3O_{10} and powder standards of $Cr^{3+}U^{5+}O_4$ (isostructural to α-$NiUO_4$) and $Co^{2+}U^{6+}O_4$ (isostructural to β-$NiUO_4$). The U L_3 map of the crystals used in these measurements are presented in Figure 6.7, and the normalized U L_3-edge XANES spectra obtained from the three single crystal samples and the two powder standards are shown in Figure 6.8. The XANES spectra for the three nickel uranium oxide crystals are similar to that of $Co^{2+}U^{6+}O_4$ supporting the assignment of hexavalent uranium in all of them.

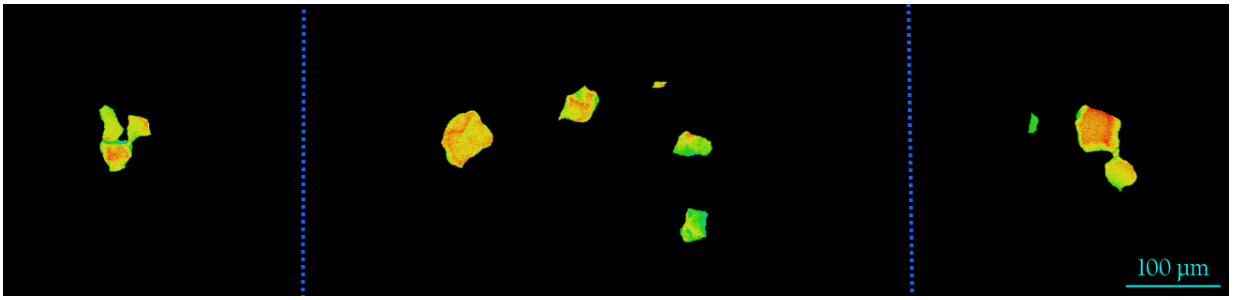

FIGURE 6.7: Uranium L_3 map of β-$NiUO_4$ (left), α-$NiUO_4$ (centre) and NiU_3O_{10} (right) crystals obtained using XFM. The intensity reflects both the U concentration as well as thickness of the crystals within each pixel area (1μm x 1μm).

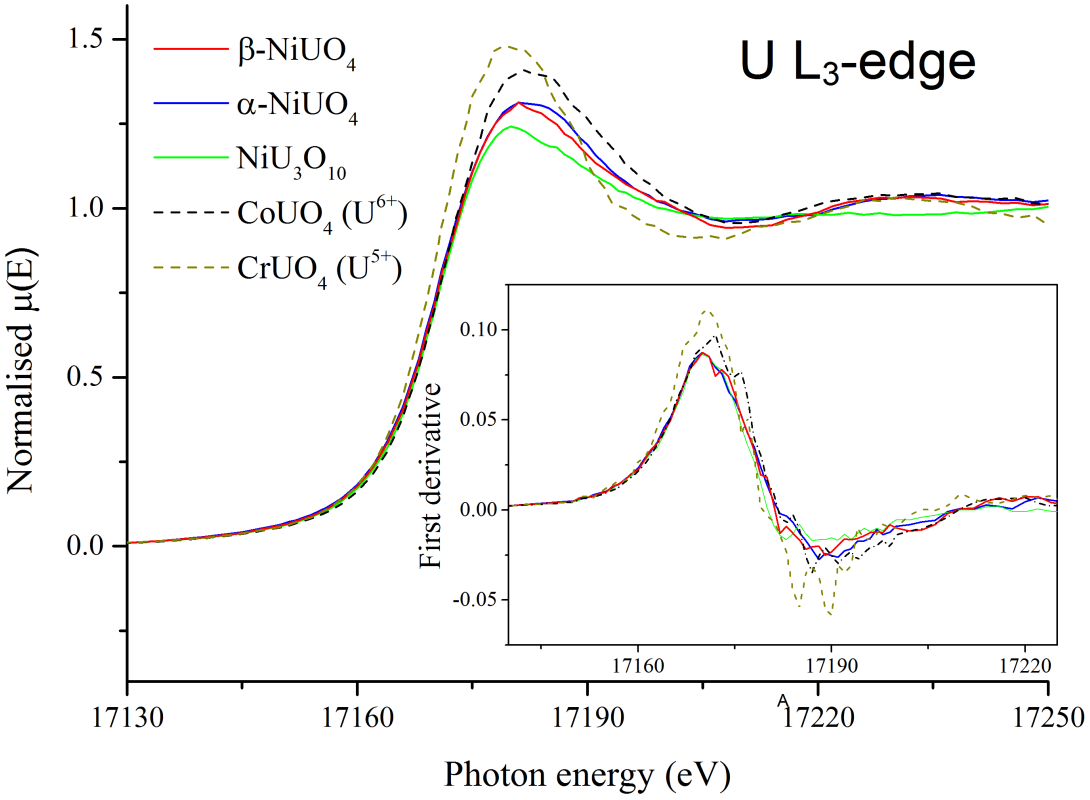

FIGURE 6.8: Normalized U L_3-edge XANES spectra from α-$NiUO_4$ (solid blue curve), β-$NiUO_4$ (solid red curve), NiU_3O_{10} (solid black curve), the U^{6+} standard $CoUO_4$ (dashed black curve), and the U^{5+} standard $CrUO_4$ (dashed gold curve).

6.3.6 Structural Relations within the Ni-U-O System

With the results acquired and presented thus far, the structural relations that occur between members of the Ni-U-O family of oxides can be more systematically understood. The structure of NiU_2O_6, as mentioned in the introduction, has previously been studied extensively using single crystal X-ray and neutron powder diffraction methods[3,12,13]. NiU_2O_6 crystallizes in the trigonal space group $P321$ forming a 3D framework structure based on corner sharing UO_6 polyhedra where isolated NiO_6 polyhedra sit within the framework of the structure. The structure contains divalent nickel and pentavalent uranium. The structure is represented in Figure 6.9. Pertinently both NiU_2O_6 and NiU_3O_{10} contain 3D framework connectivity of UO_6 (NiU_2O_6) or UO_6 and UO_7 (NiU_3O_{10}) polyhedra with isolated NiO_6 polyhedra, but unlike the two $NiUO_4$ polymorphs, do not contain interconnected NiO_6 polyhedra.

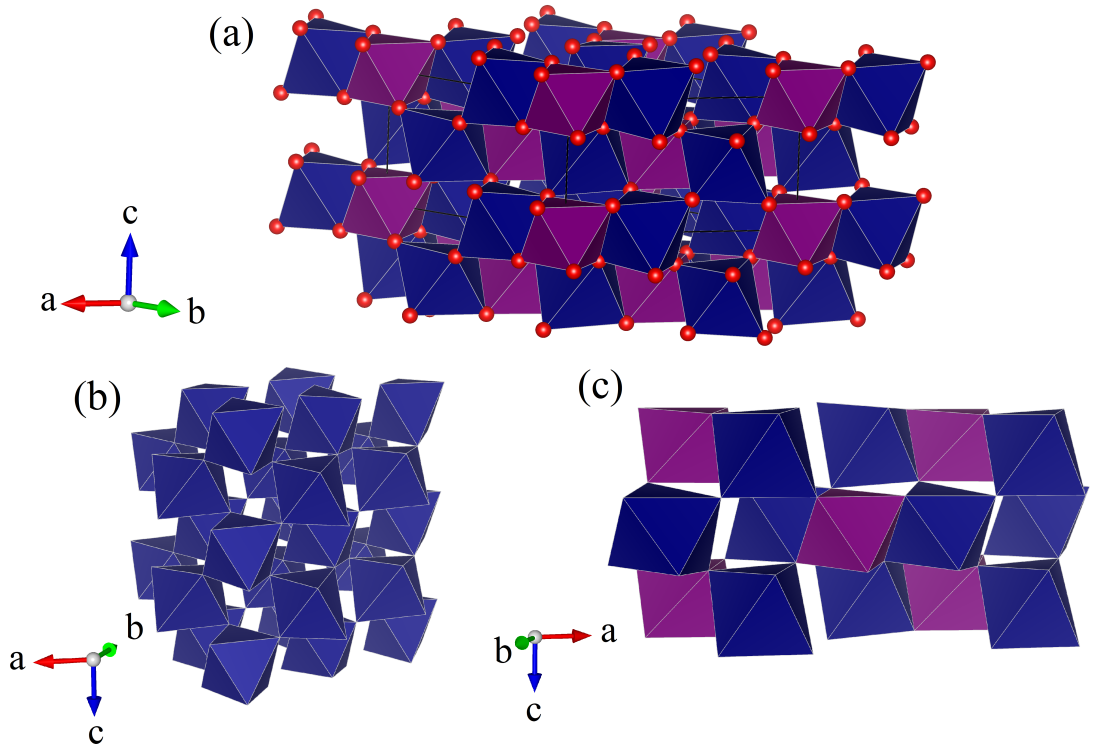

FIGURE 6.9: (a) Structural representation of NiU_2O_6 in space group $P321$[11]. Dark blue and purple polyhedra represent UO_6 and NiO_6, and small red spheres represent oxygen atoms. (b) Highlights the UO_6 corner sharing configuration (nickel polyhedra have been removed for clarity), and (c) highlights the edge and corner sharing motif of the UO_6 and NiO_6 polyhedra.

When comparing the two $NiUO_4$ polymorphs, β-$NiUO_4$ has the more regular rutile-like structure, with its UO_6 and NiO_6 polyhedra edge sharing forming alternate chains in the [001] direction (see Figure 6.5c), similar to that seen in TiO_2 (rutile) itself. Previously Baur *et al.*[38] derived a structural hierarchy relating rutile and $MgUO_4$, and hence β-$NiUO_4$, through a maximal nonisomorphic subgroup of order four. These authors argued that $MgUO_4$ in space group *Ibmm* could have been assigned to the more regular $CoReO_4$ structure in space group *Cmmm* if not for the presence of the uranyl moiety which leads to a distortion of the UO_6 polyhedra that requires the larger cell provided by *Ibmm*. The present investigation suggests that the impact of the uranyl group is even more profound. It is apparently able to assist in the formation of the β-$NiUO_4$ structure through the lengthening of the U-O(1) uranyl bond, providing the critical Ni-O(1) bond which allows successive NiO_6 polyhedra to link to form the described 1D chain (see Figure 6.5b).

α-$NiUO_4$, though less regular than β-$NiUO_4$, has a similar structure to the zig-zag distorted rutile of

α-PbO_2. The structure of α-PbO_2 consists of PbO_6 polyhedra edge sharing forming 1D zig-zag chains along the [001] direction and also corner sharing resulting in a corrugated 2D layered arrangement parallel to the (010) plane[31]. This is similar to the respective connectivity of the NiO_6 and UO_6 polyhedra in α-$NiUO_4$.

As mentioned previously, in contrast to the 1D connectivity of the NiO_6 groups in the two $NiUO_4$ polymorphs, NiU_2O_6 and NiU_3O_{10} form 3D framework structures, based on UO_6 (NiU_2O_6) or UO_6 and UO_7 (NiU_3O_{10}) connectivity, where the NiO_6 polyhedra are isolated from each other. Attempts were made to synthesize $NiUO_4$ with stoichiometric quantities of NiO and U_3O_8 using solid state methods under ambient pressure, but no ternary phases were identified. Evidently high pressures are essential for the formation of the 1D rutile-like chain in the Ni-U-O system, just as high pressure is needed to prepare the rutile form of SiO_2[39]. It is postulated that pressure enables the successive bonding of NiO_6 polyhedra in the two $NiUO_4$ polymorphs, which is not necessary in NiU_2O_6 and NiU_3O_{10} as they do not require interconnected NiO_6 polyhedra for the structural formation, instead forming framework structures based on interconnected UO_6 or UO_6 and UO_7 polyhedra respectively.

6.3.7 Crystal Chemistry of the $NiUO_4$ Polymorphs and Relation to Other AUO_4 Oxides

That the phase transformation from α-$NiUO_4$ to β-$NiUO_4$, which occurs through either temperature or pressure, is irreversible suggests that β-$NiUO_4$ is more stable. Although it is difficult to properly describe the α-$NiUO_4$ to β-$NiUO_4$ phase transformation without *in situ* measurements, it is postulated that it would be first order and reconstructive, transitioning from a partially 2D layered and 1D chain α-$NiUO_4$ structure to a more regular and completely 1D chain β-$NiUO_4$ structure. The change in volume between the structures is small, the $\sim 0.9\%$ reduction in β-$NiUO_4$ supports it being the preferred high pressure structure, which suggests difficulty in experimentally controlling the transition. This seems to be evident when comparing the synthesis conditions used in the present study to that of Hoekstra and Marshal[8] and also Young[9] in terms of phases recovered at specific pressures and temperatures.

Pertinently the α to β-$NiUO_4$ transition involves the emergence of the uranyl group that apparently plays the role of both a structurally anchoring and stabilizing group in β-$NiUO_4$, consistent with previous studies of similar uranium systems[40,41]. Its absence in α-$NiUO_4$ is thought to drive the increased

thermodynamic stability of β-$NiUO_4$. The enthalpy of formation of some other metal AUO_4 oxides in similar uranyl absent *Pbcn* ($FeUO_4$, $CrUO_4$) and uranyl present *Ibmm* ($MgUO_4$, $CoUO_4$) structures has been examined[10] previously, where it has been typically found that the *Pbcn* variants have a more positive enthalpy of formation. α-$NiUO_4$ is distinct to the other known AUO_4 variants in space group *Pbcn*, namely $CrUO_4$ and $FeUO_4$,[10] as it does not contain pentavalent uranium or a trivalent A-site metal cation. Guo *et al.*[10] postulated that the preferential oxidation of Cr and Fe to their trivalent oxidation states leads to the reduction of uranium from hexavalent to pentavalent in $CrUO_4$ and $FeUO_4$. Despite having the less stable $5f^1$ electron configuration, Guo *et al.*[10] argued that the presence of U^{5+} does not contribute significantly to the difference in enthalpy and stability. Generally, Ni^{3+} is encountered less frequently than Ni^{2+} although it does occur within lanthanide nickel perovskites of the form $Ln^{3+}Ni^{3+}O_3$, reflecting the preference for the lanthanoid cation to retain its trivalent state which coerces nickel to be trivalent[42,43]. Subsequently, it is argued that the presence of Ni^{2+} and U^{6+} in α-$NiUO_4$ is a consequence of their preferences to retain the relatively stable $3d^8$ and $5f^0$ electron configurations respectively, although the relative size between the two cations also plays a significant role, as previously discussed.

Although Read *et al.*[3] are incorrect in asserting that $NiUO_4$ does not exist, as demonstrated here, their proposed structural hierarchy remains valid and is expanded here to include α-$NiUO_4$ and β-$NiUO_4$ as well as the orthorhombic structures in *Pbcm*[30,44]. Table 6.8 summarises the present knowledge of the structures of the AUO_4 oxides, and Figure 6.10 displays a clear trend between the structure type and the ratio of the U to the A site cation ionic radii (r_A/r_U) (excluding the two anomalies discussed in the next paragraph). As presented in Figure 6.10, with decreasing r_A/r_U, AUO_4 oxides first adopt the orthorhombic structure in space group *Pbcm*, followed by the rhombohedral structure in $R\bar{3}m$, and the orthorhombic structure in *Ibmm* and finally the orthorhombic structure in *Pbcn*. A related trend between the enthalpy of formation and r_A was also identified by Guo *et al.*[10] but this contained far less data points. However when the results of Guo *et al.*[10] are considered with Table 6.8 and Figure 6.10, together they can be effectively used as means of predicting the thermodynamic stability of both known and unknown AUO_4 oxides.

TABLE 6.8: Comparison of AUO_4 structure types, ionic radii taken from the Shannon ionic radii tables[45]

.

Compound	Structural Type	Space group	Reference	Uranium Cation Valence	*A* Site Cation Valence	U Ionic Radii (Å)	*A* Ionic Radii (Å)	Cation Ratio r_A/r_U
$BaUO_4$	Orthorhombic	*Pbcm*	Murphy *et al.*[30]	6	2	0.73	1.35	1.85
$PbUO_4$	Orthorhombic	*Pbcm*	Cremers *et al.*[44]	6	2	0.73	1.19	1.63
β-$SrUO_4$	Orthorhombic	*Pbcm*	Murphy *et al.*[30]	6	2	0.73	1.18	1.61
α-$SrUO_4$	Rhombohedral	$R\bar{3}m$	Murphy *et al.*[30]	6	2	0.86	1.26	1.47
$CaUO_4$	Rhombohedral	$R\bar{3}m$	Murphy *et al.*[30]	6	2	0.86	1.12	1.30
α-$CdUO_4$	Rhombohedral	$R\bar{3}m$	Yamashita et al.[2]	6	2	0.86	1.1	1.28
β-$CdUO_4$	Orthorhombic	*Cmmm*	Yamashita *et al.*[2]	6	2	0.73	0.95	1.30
$MnUO_4$	Orthorhombic	*Ibmm*	Read *et al.*[3]	6	2	0.73	0.83	1.14
$CoUO_4$	Orthorhombic	*Ibmm*	Bertaut *et al.*[4]	6	2	0.73	0.745	1.02
$CuUO_4$	Monoclinic	$P2_1/n$	Siegel and Hoekstra[46]	6	2	0.73	0.73	1
$MgUO_4$	Orthorhombic	*Ibmm*	Zachariasen[5]	6	2	0.73	0.72	0.99
β-$NiUO_4$	Orthorhombic	*Ibmm*	Present investigation	6	2	0.73	0.69	0.95
α-$NiUO_4$	Orthorhombic	*Pbcn*	Present investigation	6	2	0.73	0.69	0.95
$FeUO_4$	Orthorhombic	*Pbcn*	Read *et al.*[3]	5	3	0.76	0.645	0.85
$CrUO_4$	Orthorhombic	*Pbcn*	Bacmann *et al.*[6]	5	3	0.76	0.615	0.81

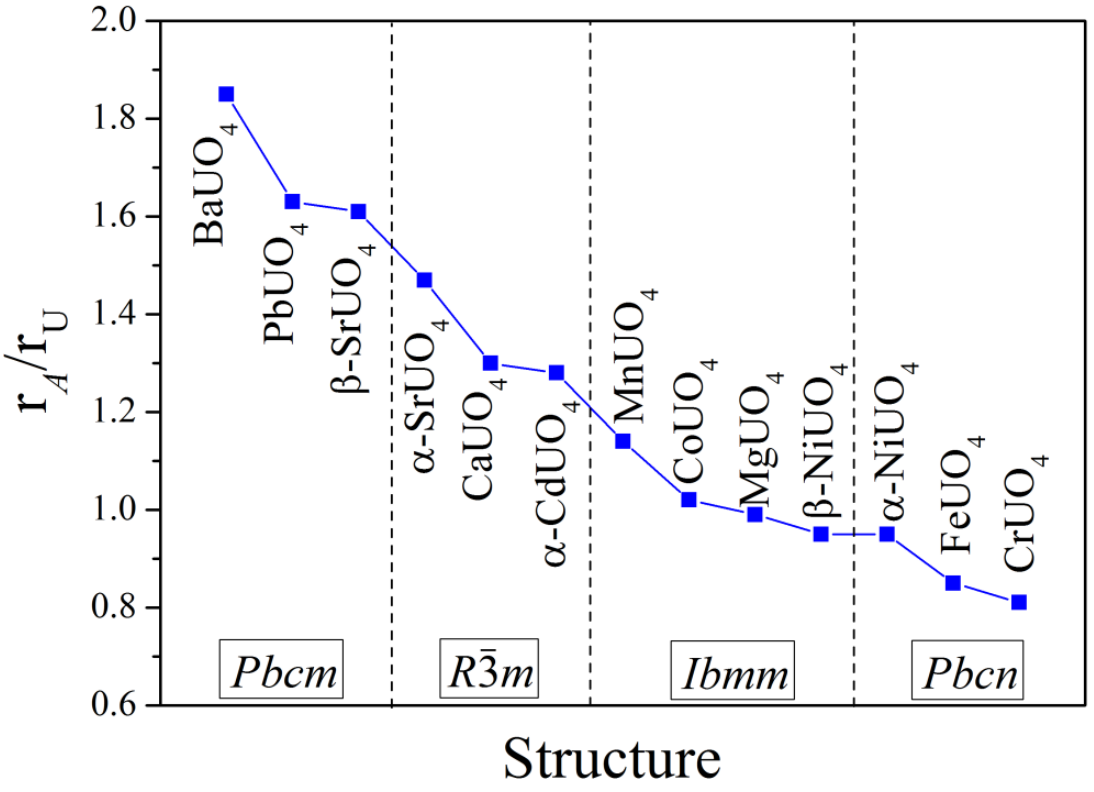

FIGURE 6.10: Trend between the ratio of the ionic radii of the A-site and uranium cations (r_A/r_U) and the structural types formed within the AUO_4 series of oxides.

As displayed in Figure 6.10, the two $NiUO_4$ polymorphs exist on the periphery of stability with respect to the *Pbcn* and *Ibmm* structural types. It was demonstrated that pressure is necessary to achieve a rutile-like 1D chain configuration of the NiO_6 polyhedra in either α-$NiUO_4$ or β-$NiUO_4$. This is reflected in the ionic radius of the divalent nickel cation being the smallest, when compared to the other A-site cations of the *Ibmm* AUO_4 series. Conversely Ni^{2+} is larger than Cr^{3+} and Fe^{3+} in the *Pbcn* AUO_4 series. It appears that pressure is necessary to mitigate this size problem and allow β-$NiUO_4$ and α-$NiUO_4$ to form.

The structures of $CuUO_4$ and β-$CdUO_4$ are somewhat anomalies in Table 6.8 (and hence excluded from Figure 6.10). Based on the relative size of the Cu^{2+} and U^{6+} cations, an orthorhombic structure in space group *Ibmm* would be expected for $CuUO_4$, instead it forms a monoclinic structure in space group $P2_1/n$[46]. This deviation from the structural trend is related to the presence of the Jahn-Teller active ($3d^9$) Cu^{2+} cation which lifts the degeneracy of the e_g orbitals resulting in a distortion of the UO_6 polyhedra[46]. This leads to two of the Cu-O bonds significantly lengthening whereas the other four shorten. This is

in contrast to the pattern of four long and two short A-O bonds observed in the *Ibmm* and *Pbcn* AUO_4 variants. Interestingly the tetragonal elongation of the UO_6 polyhedra seen in $CuUO_4$ is also observed in the NiO_6 polyhedra of NiU_3O_{10}. CuU_3O_{10} [8], which also contains the Jahn-Teller active Cu^{2+} cation, is isostructural to NiU_3O_{10}, and comparing these two there is no significant variation between the NiO_6 and UO_6 polyhedra. Consequentially it can be concluded that the atomic arrangement in the AU_3O_{10} structure better supports the presence of the Jahn-Teller active Cu^{2+} cation whereas the orthorhombic AUO_4 structures cannot.

The structure of β-$CdUO_4$ has been reported to be orthorhombic in space group *Cmmm* [2], unlike $MnUO_4$, $CoUO_4$, $MgUO_4$ and β-$NiUO_4$ which are all in space group *Ibmm*. The assignment of space group *Cmmm* rather than *Ibmm*, a result of a small differences in the anion sublattice, is a consequence of the laboratory X-ray powder diffraction used. It is hypothesized that a higher resolution measurement will reveal β-$CdUO_4$ to be better assigned to the *Ibmm* space group, particularly in light of the discussions by Baur *et al.* [38] and as there no apparent significant differences between the Cd^{2+} cation and other A site cations that would warrant it towards slightly higher symmetry. This will be examined and the findings presented in Chapter 7 of this dissertation.

Finally, it is noteworthy to consider the implications of α-$NiUO_4$ containing different metal and uranium oxidation states to those encountered in the isostructural $CrUO_4$ and $FeUO_4$. It is unclear whether a continuous solid solution would exist between these compounds, and if so, how the oxidation states in such a system would vary. Simplistically, it is postulated for a solid solution of the form, α-$Ni_xCr_{1-x}UO_4$ or α-$Ni_xFe_{1-x}UO_4$, the amount of nickel present would linearly increase the amount of U^{6+} that would form. However, considering the different affinities for the nickel, chromium or iron cations to oxidise from divalent to trivalent, this linear trend might not be realised. Consequentially such a system would potentially provide a means to measure the relative affinity for these transition metal cations to undergo oxidation in the presence of uranium. The knowledge is potentially relevant to the understanding of behaviour within spent nuclear fuel systems. Furthermore, it would provide a means to modulate the magnetism previously examined in these oxides [6,7,47–49].

6.4 Chapter Conclusion

To summarise, the ternary uranium oxides, α-$NiUO_4$, β-$NiUO_4$ and NiU_3O_{10} have been synthesized using a combination of high pressure and flux growth methods and their structures solved for the first time using SSC-XRD data supported by XANES measurements. All three oxides were found to only contain hexavalent uranium from the U L_3-edge via XANES mapping of selected single crystals. Both α-$NiUO_4$ and β-$NiUO_4$ were found to only form under HT/HP conditions and the synthesis conditions and data analysis suggests β-$NiUO_4$ is the preferred HT/HP phase. From *ex situ* synthesis experiments it is concluded that α-$NiUO_4$ will undergo a phase transformation to β-$NiUO_4$ irreversibly between T = 950 and 1000 ^oC when P = 4 GPa. That HT/HP conditions are necessary for the formation of α-$NiUO_4$ and β-$NiUO_4$ is argued to be a consequence of the size difference between the Ni^{2+} and U^{6+} cations. When compared to their isostructural orthorhombic counterparts in space group *Pbcn* ($Cr^{3+}U^{5+}O_4$, etc.) and *Ibmm* ($Mg^{2+}U^{6+}O_4$, etc.), the Ni^{2+} cation is essentially too large or too small relative to the U^{6+} cation, respectively, to form these structural types under ambient pressure conditions. Particularly, it is a requirement that for these structures to form they contain 1D chains of NiO_6 polyhedra, which the high pressure assists in obtaining. Comparatively NiU_3O_{10} and NiU_2O_6 [11] do not contain 1D chains of cations and mitigate this size problem and consequential high pressure synthesis conditions, by forming framework structures through connectivity among respective UO_6 or UO_6 and UO_7 polyhedra while NiO_6 polyhedra sit unconnected in void positions in both structures. Within the family of AUO_4 oxides, no phase transformations between the orthorhombic space group *Pbcn* (eg. $CrUO_4$ and $FeUO_4$) and *Ibmm* (eg. $MgUO_4$, $CoUO_4$ and $MnUO_4$) structures were known prior to this investigation. The identification of α-$NiUO_4$ and β-$NiUO_4$ and their position within the greater hierarchy of AUO_4 oxides firstly provides the missing link between the space group *Pbcn* and *Ibmm* variants then further allows the structural chemistry of the AUO_4 oxides to be more comprehensively understood in which structural type preference can be related to the ratio of the ionic radii of the *A*-site and uranium cations (r_A/r_U) and further to thermodynamic stability [10].

References

1. Tagawa, H. and Fujino, T. *Inorganic & Nuclear Chemistry Letters* **16**(2), 91–96 (1980).

2. Yamashita, T., Fujino, T., Masaki, N., and Tagawa, H. *Journal of Solid State Chemistry* **37**(2), 133–139 (1981).

3. Read, C. M., Smith, M. D., and zur Loye, H. C. *Solid State Sciences* **37**, 136–143 (2014).

4. Bacmann, M. and Bertaut, E. F. *Journal De Physique* **30**(11-12), 949–953 (1969).

5. Zachariasen, W. H. *Acta Crystallographica* **7**(12), 788–791 (1954).

6. Bacmann, M., Bertaut, E. F., and Bassi, G. *Bulletin De La Societe Francaise Mineralogie Et De Cristallographie* **88**(2), 214–218 (1965).

7. Bacmann, M. and Bertaut, E. F. *Bulletin De La Societe Francaise Mineralogie Et De Cristallographie* **90**(2), 257–258 (1967).

8. Hoekstra, H. R. and Marshall, R. H. *Advances in Chemistry Series* (71), 211–220 (1967).

9. Young, A. P. *Science* **153**(3742), 1380–1381 (1966).

10. Guo, X. F., Tiferet, E., Qi, L., Solomon, J. M., Lanzirotti, A., Newville, M., Engelhard, M. H., Kukkadapu, R. K., Wu, D., Ilton, E. S., Asta, M., Sutton, S. R., Xu, H. W., and Navrotsky, A. *Dalton Transactions* **45**(11), 4622–4632 (2016).

11. Hinatsu, Y., Doi, Y., and Nakamura, A. *Journal of Nuclear Materials* **385**(1), 49–52 (2009).

12. Hinatsu, Y. *Journal of Solid State Chemistry* **114**(2), 595–597 (1967).

13. Kemmlersack, S. *Zeitschrift Fur Anorganische Und Allgemeine Chemie* **358**(5-6), 226–230 (1968).

14. Dickens, P. G., Stuttard, G. P., and Patat, S. *Journal of Materials Chemistry* **3**(4), 339–341 (1993).

15. Rodrguez-Carvajal, J. *Physica B: Condensed Matter* **192**(1), 55–69 (1993).

16. Aragao, D., Aishima, J., Cherukuvada, H., Clarken, R., Clift, M., Cowieson, N. P., Ericsson, D. J., Gee, C. L., Macedo, S., Mudie, N., Panjikar, S., Price, J. R., Riboldi-Tunnicliffe, A., Rostan, R., Williamson, R., and Caradoc-Davies, T. T. *Journal of Synchrotron Radiation* **25**, 885–891 (2018).

17. McPhillips, T. M., McPhillips, S. E., Chiu, H. J., Cohen, A. E., Deacon, A. M., Ellis, P. J., Garman, E., Gonzalez, A., Sauter, N. K., Phizackerley, R. P., Soltis, S. M., and Kuhn, P. *Journal of Synchrotron Radiation* **9**, 401–406 (2002).

18. Kabsch, W. *Acta Crystallographica Section D-Biological Crystallography* **66**, 133–144 (2010).

19. Blessing, R. H. *Acta Crystallographica Section A* **51**, 33–38 (1995).

20. Sheldrick, G. M. *Acta Crystallographica Section C-Structural Chemistry* **71**, 3–8 (2015).

21. Sheldrick, G. M. *Acta Crystallographica a-Foundation and Advances* **71**, 3–8 (2015).

22. Dolomanov, O. V., Bourhis, L. J., Gildea, R. J., Howard, J. A. K., and Puschmann, H. *Journal of Applied Crystallography* **42**, 339–341 (2009).

23. Paterson, D., Jonge, M. D. d., Howard, D. L., Lewis, W., McKinlay, J., Starritt, A., Kusel, M., Ryan, C. G., Kirkham, R., Moorhead, G., and Siddons, D. P. *AIP Conference Proceedings* **1365**(1), 219–222 (2011).

24. Kirkham, R., Dunn, P. A., Kuczewski, A. J., Siddons, D. P., Dodanwela, R., Moorhead, G. F., Ryan, C. G., Geronimo, G. D., Beuttenmuller, R., Pinelli, D., Pfeffer, M., Davey, P., Jensen, M., Paterson, D. J., Jonge, M. D. d., Howard, D. L., Ksel, M., and McKinlay, J. *AIP Conference Proceedings* **1234**(1), 240–243 (2010).

25. Ryan, C. G., Siddons, D. P., Kirkham, R., Li, Z. Y., Jonge, M. D. d., Paterson, D. J., Kuczewski, A., Howard, D. L., Dunn, P. A., Falkenberg, G., Boesenberg, U., Geronimo, G. D., Fisher, L. A., Halfpenny, A., Lintern, M. J., Lombi, E., Dyl, K. A., Jensen, M., Moorhead, G. F., Cleverley, J. S., Hough, R. M., Godel, B., Barnes, S. J., James, S. A., Spiers, K. M., Alfeld, M., Wellenreuther, G., Vukmanovic, Z., and Borg, S. *Journal of Physics: Conference Series* **499**(1), 012002 (2014).

26. Goulon, J., Goulonginet, C., Cortes, R., and Dubois, J. M. *Journal De Physique* **43**(3), 539–548 (1982).

27. Etschmann, B. E., Donner, E., Brugger, J., Howard, D. L., de Jonge, M. D., Paterson, D., Naidu, R., Scheckel, K. G., Ryan, C. G., and Lombi, E. *Environmental Chemistry* **11**(3), 341–350 (2014).

28. Butler, S. Z., Hollen, S. M., Cao, L. Y., Cui, Y., Gupta, J. A., Gutierrez, H. R., Heinz, T. F., Hong, S. S., Huang, J. X., Ismach, A. F., Johnston-Halperin, E., Kuno, M., Plashnitsa, V. V., Robinson,

R. D., Ruoff, R. S., Salahuddin, S., Shan, J., Shi, L., Spencer, M. G., Terrones, M., Windl, W., and Goldberger, J. E. *Acs Nano* **7**(4), 2898–2926 (2013).

29. Ravel, B. and Newville, M. *Journal of Synchrotron Radiation* **12**(4), 537–541 (2005).

30. Murphy, G., Kennedy, B. J., Johannessen, B., Kimpton, J. A., Avdeev, M., Griffith, C. S., Thorogood, G. J., and Zhang, Z. M. *Journal of Solid State Chemistry* **237**, 86–92 (2016).

31. Filatov, S., Bendeliani, N., Albert, B., Kopf, H., Dyuzeva, T., and Lityagina, L. *Solid State Sciences* **7**(11), 1363–1368 (2005).

32. Burns, P. C. *Canadian Mineralogist* **43**, 1839–1894 (2005).

33. Robinson, K., Gibbs, G. V., and Ribbe, P. H. *Science* **172**(3983), 567–570 (1971).

34. Zhang, Z., Howard, C. J., Knight, K. S., and Lumpkin, G. R. *Acta Crystallographica Section B* **62**(1), 60–67 (2006).

35. Glazer, A. M. *Acta Crystallographica Section B-Structural Science* **B 28**(NOV15), 3384–3388 (1972).

36. Dickens, P. G. and Stuttard, G. P. *Journal of Materials Chemistry* **2**(7), 691–694 (1992).

37. Burns, P. C., Ewing, R. C., and Hawthorne, F. C. *Canadian Mineralogist* **35**, 1551–1570 (1997).

38. Baur, W. H., Joswig, W., Pieper, G., and Kassner, D. *Journal of Solid State Chemistry* **99**(1), 207–211 (1992).

39. Prakapenka, V. P., Shen, G., Dubrovinsky, L. S., Rivers, M. L., and Sutton, S. R. *Journal of Physics and Chemistry of Solids* **65**(8), 1537–1545 (2004).

40. Denning, R. G. *Journal of Physical Chemistry A* **111**(20), 4125–4143 (2007).

41. Gibson, J. K., Haire, R. G., Santos, M., Marcalo, J., and de Matos, A. P. *Journal of Physical Chemistry A* **109**(12), 2768–2781 (2005).

42. Tejuca, L. G. and Fierro, J. L. G. *Thermochimica Acta* **147**(2), 361–375 (1989).

43. Sarma, D. D., Shanthi, N., and Mahadevan, P. *Journal of Physics-Condensed Matter* **6**(48), 10467–10474 (1994).

44. Cremers, T. L., Eller, P. G., Larson, E. M., and Rosenzweig, A. *Acta Crystallographica Section C-Crystal Structure Communications* **42**, 1684–1685 (1986).

45. Shannon, R. *Acta Crystallographica Section A* **32**(5), 751–767 (1976).

46. Siegel, S. and Hoekstra, H. R. *Acta Crystallographica Section B-Structural Crystallography and Crystal Chemistry* **B 24**, 967–970 (1968).

47. Bacmann, M., Bertaut, E. F., and Blaise, A. *Comptes Rendus Hebdomadaires Des Seances De L Academie Des Sciences Serie B* **266**(2), 45–48 (1968).

48. Bacmann, M., Bertaut, E. F., Blaise, A., Chevalie.R, and Roult, G. *Journal of Applied Physics* **40**(3), 1131–1135 (1969).

49. Greenblatt, M., Hornreich, R. M., and Sharon, B. *Journal of Solid State Chemistry* **10**(4), 371–376 (1974).

Chapter 7

Structural and Spectroscopic Studies of the Rutile Related Orthorhombic AUO_4 Oxides

This chapter is adapted from a manuscript titled "Structural and Spectroscopic Studies of Orthorhombic MUO$_4$ Oxides (M = Cd, Co, Mn, Mg, Cr, $Cr_{0.75}Al_{0.25}$ and $Cr_{0.5}Fe_{0.5}$)" by G. L. Murphy *et al.* that is being prepared for submission at the time of writing.

7.1 Introduction

It was highlighted in Chapter 6 that the orthorhombic rutile related structure β-$NiUO_4$ in space group *Ibmm* exhibits tilting of the NiO_6 polyhedra reminiscent to that occurring in ABX_3 perovskites[1,2]. The tilting of the NiO_6 polyhedra was associated with the size mismatch between the U^{6+} and Ni^{2+} cations which require high pressure conditions for structure formation. The ideal perovskite structure is cubic in space group $Pm\bar{3}m$ where lowering of crystallographic symmetry can occur through BX_6 polyhedra tilting caused by a size mismatch between the A and B site cations. The corner sharing geometry of the BX_6 geometry is such that the tilting can occur either in phase or out of phase. The edge sharing chain structure of orthorhombic β-$NiUO_4$ in space group *Ibmm* is such that the observed tilting can only occur along one direction. Understanding these distortions and associated phase transformations in perovskites has been the topic of intense focus particularly due to the relevance of perovskite materials in energy[3,4] and solar devices[5,6] among other applications. Consequently understanding such mechanisms within AUO_4 oxides provide greater insight into their fundamental solid state chemistry and may promote further insights into related nuclear waste forms.

β-$NiUO_4$ is isostructural to $MgUO_4$[7], $CoUO_4$[8] and $MnUO_4$[9] which respectively have increasing A site cation sizes[10]. Considering that $MgUO_4$, $CoUO_4$ and $MnUO_4$ can be prepared under ambient pressure conditions[7–9], unlike β-$NiUO_4$, with an increasing r_A/r_U ratio, it is postulated this will be reflected in the tilting of the AO_6 polyhedra. Notably β-$CdUO_4$ is similar to these oxides, forming a rutile related structure with 1D chains of CdO_6 and UO_6 polyhedra, but it is reported in the higher symmetry space group of *Cmmm*[1]. Although it has been strongly speculated that this symmetry assignment is erroneously a consequence of the resolution of the laboratory X-ray powder diffraction used to describe it[11], that it has the largest r_A/r_U ratio of the rutile related orthorhombic AUO_4 oxides, it is plausible the *Cmmm* assignment could be related to this supposed tilting mechanism and a potentially associated phase transformation. Such transformations occurring through tilting have been identified in other ternary actinide oxide systems such as the perovskite $BaThO_3$[12] which undergoes a continuous phase transformation from space group *Pbnm* to *Ibmm* when heated above 800 ^{o}C via tilting of ThO_6 polyhedra.

This chapter is devoted to developing a comprehensive understanding of the rutile related orthorhombic AUO_4 oxides. This involved using a combination of neutron and synchrotron X-ray powder diffraction and also single crystal X-ray diffraction to generate precise structural models of β-$CdUO_4$, $CoUO_4$ and

$MnUO_4$ and $MgUO_4$ respectively. Of particular focus is the structure of β-$CdUO_4$ to determine whether it should be in space group *Cmmm*[11] or better placed in *Ibmm*. Of these previously described structures only $MgUO_4$ has been demonstrated[13] to unequivocally contain hexavalent uranium, although magnetism measurements give some insight into the valence states in $CoUO_4$[8,14] and $MnUO_4$[14,15]. Considering the somewhat unexpected observation of hexavalent uranium in α-$NiUO_4$, as described in Chapter 6, it is pertinent to definitively determine the U valence states of all members of the rutile related orthorhombic AUO_4 oxides. This was achieved using X-ray absorption spectroscopy performed on the U L_2-edge. The results are discussed with respect to the results of Chapter 6 and to the structural trends that occur between these rutile related AUO_4 oxides.

7.2 Experimental

7.2.1 Synthesis

The monouranates, β-$CdUO_4$, $CoUO_4$ and $MnUO_4$ were prepared by mixing appropriate stoichiometric quantities of CdO, $CoCO_3$ and $MnCO_3$ (Sigma-Aldrich: 99.98%) with U_3O_8. The powered mixtures for $CoUO_4$ and $MnUO_4$ were compacted into pellets and calcined in air at 1000 ^{o}C for 60 hours with intermittent mixing. For β-$CdUO_4$, it was synthesized in a similar method but at 825 ^{o}C in order to avoid loss of Cd. The reactions were monitored using powder X-ray diffraction (XRD) data measured on a Bruker D8 Advance diffractometer using Cu Kα radiation at room temperature. $CoUO_4$, $CrUO_4$ and $MnUO_4$ formed black powders whereas β-$CdUO_4$ was orange coloured.

Single crystals of $MgUO_4$ were prepared by mixing stoichiometric quantities of U_3O_8 and $MgCO_3$. The mixtures were compacted into pellets and calcined in air at 1000 ^{o}C for 20 hours. The resulting product was collected and mixed with excess $MgCl_2$ (20:1 molar ratio $MgCl_2$ to $MgUO_4$). The combined mixture was then heated to 1000 ^{o}C for 10 hours, cooled at a rate of 3 ^{o}C/hour to 400 ^{o}C before cooling to RT at a rate of 10 ^{o}C/minute. The mixture was washed with copious amounts of deionised water to remove the excess $MgCl_2$. The resulting product contained fine yellow single crystals of $MgUO_4$ which were mechanically separated. A sub-sample of $MgUO_4$ was speculated prior to treatment with $MgCl_2$. XRD measurements indicated this to be of suitable purity for analysis using X-ray absorption spectroscopy (XAS).

7.2.2 *Ex Situ* Neutron and Synchrotron X-ray Powder Diffraction

Synchrotron X-ray powder diffraction (S-XRD) data were collected at room temperature using the powder diffractometer at the beamline BL-10 of the Australian Synchrotron[16]. The samples were finely ground and housed in sealed 0.2 mm diameter quartz capillaries that were rotated during the measurements. Measurements for β-$CdUO_4$, $CoUO_4$ and $MnUO_4$ were conducted using a wavelength of 0.77435 Å. All wavelengths were determined using a NIST LaB_6 (660b) standard reference.

Neutron powder diffraction (NPD) data were measured at room temperature using the high resolution powder diffractometer Echidna[17] at ANSTO's OPAL facility at Lucas Heights using wavelengths of 1.6215 ($MnUO_4$) and 2.439 ($CoUO_4$) Å. The samples were placed in cylindrical vanadium cans that were mounted in a closed cycle refrigerator. The β-$CdUO_4$ sample was contained in a cylindrical annular vanadium can with an internal wall gap of 2 mm to minimise the effects of absorption due to Cd, a wavelength of 1.6215 Å was used for these measurements.

The structures described here were refined by the Rietveld method as implemented in the program GSAS[18] with the EXPUI GUI[19]. The peak shapes were modelled using a pseudo Voigt function and the background was estimated using a 12 term shifted Chebyschev function. The scale factor, detector zero point, lattice parameters, atomic coordinates and atomic displacement parameters were refined together with the peak profile parameters.

7.2.3 Single Crystal X-ray Diffraction

Single Crystal X-ray Diffraction (SC-XRD) measurements used an Agilent Technologies SuperNova diffractometer with Mo-Kα radiation (λ = 0.71073 Å) at room temperature. All data sets were corrected for Lorentz and polarization factors as well as for absorption by the multi-scan method. The structures of all compounds were solved by direct methods and refined by a full-matrix least-squares fitting on F^2 by SHELX-97. The result was checked for possible missing symmetry elements using PLATON with the ADDSYM algorithm, and no higher symmetry was found.

7.2.4 X-ray Absorption Near Edge Structure (XANES) Measurements

X-ray absorption near edge structure (XANES) spectra were collected from the samples, as well as U^{4+} (UO_2), U^{5+} ($CrUO_4$)[13] and U^{6+} ($CaUO_4$)[20] uranium standards, at the U L_2-edge on BL-12 at the Australian Synchrotron[21]. The measurements were performed at room temperature in transmission mode using three argon-filled ionisation chambers. The beam intensity was monitored by a flow through ionisation chamber located upstream from the sample. XANES spectra were collected by a second ionization chamber placed after the sample. A third ionization chamber was placed downstream to simultaneously measure the reference spectrum of a uraninite mineral sample. Powder samples of β-$CdUO_4$, $CoUO_4$, $MnUO_4$ and $MgUO_4$ were diluted with an appropriate amount of BN powder, sandwiched between two Kapton tapes, and positioned perpendicular to the X-ray beam. Energy steps as small as 0.25 eV were employed near the absorption edge with a counting time of 2 s per step. The energy scale of the monochromator was calibrated using the K-edge of a Mo foil at 20000 eV, and the uraninite reference spectra were used to align scans from different samples during the experiment (if the energy scale drifts slightly). Data analysis was performed using the software package ATHENA[22].

7.3 Results and discussion

7.3.1 Structural Studies 1. β-$CdUO_4$

S-XRD data sets collected on β-$CdUO_4$ could be indexed against an orthorhombic structure. Orthorhombic space groups were explored in describing β-$CdUO_4$ with the focus being, but not limited to, *Cmmm* and *Ibmm*. The S-XRD data was sufficient in ruling out other space groups, the subtle variation between *Cmmm* and *Ibmm* stemming from the anionic sub-lattice meant they could not be discerned using the S-XRD data unequivocally. Although careful inspection and comparison of the refined models shows the *Ibmm* assignment is the preferred, see Figure 7.1. Nevertheless NPD measurements were undertaken to definitively resolve this which are better suited to detect the difference between the anionic sub-lattices. The diffraction data were absorption corrected, to account for the annular can used during measurement to minimise the effects of the high thermal neutron absorption problems of the Cd-113 isotope. The refinement returned lower fitting measurement factors for *Ibmm* compared to *Cmmm* when refining against this NPD

data. The refinement profiles of the NPD and S-XRD for β-$CdUO_4$ are presented in Figure 7.2 where they are refined against the *Cmmm* and *Ibmm* space groups comparatively.

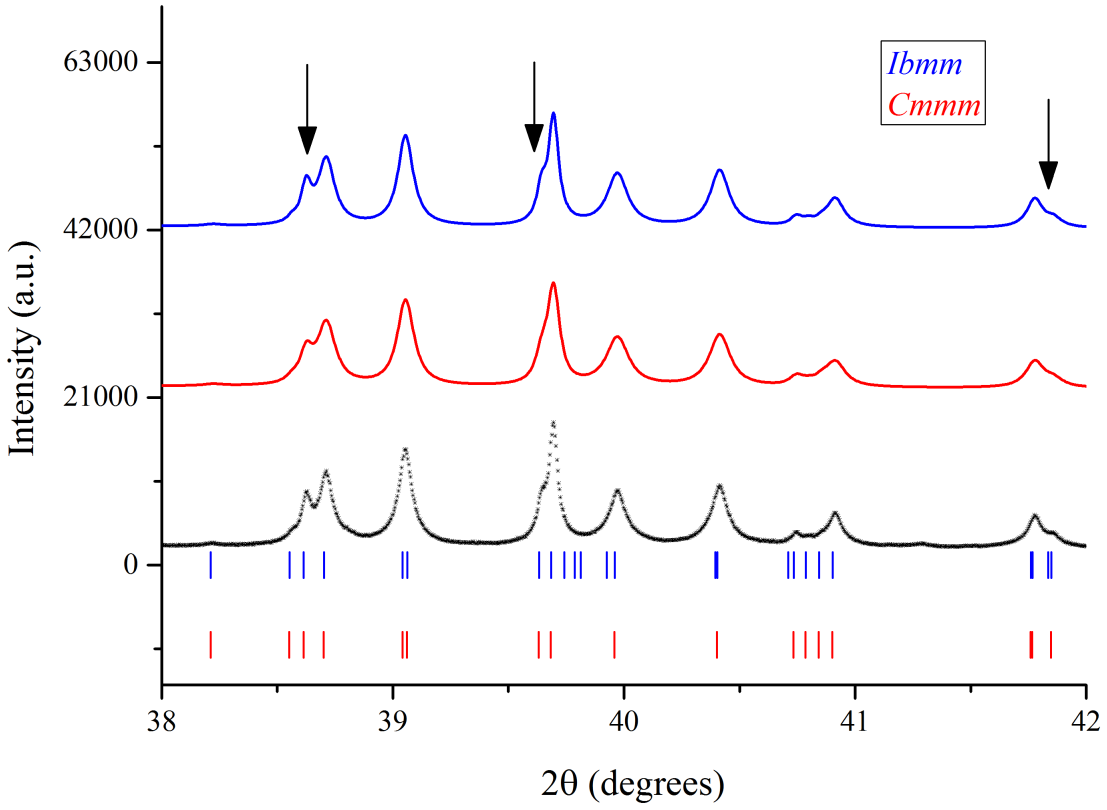

FIGURE 7.1: S-XRD data (black) for β-$CdUO_4$ between 38 and 42^o where the refined models and allowed reflections of the space groups are presented in blue (*Ibmm*) and red (*Cmmm*), note the improved replication of the experimental data in the *Ibmm* model indicated by the arrows.

In these the χ^2 values and observation of fitted peaks from the two data sets indicated the space group *Ibmm* compared to *Cmmm* was the preferred descriptor. Consequently with this affirmation, the NPD and S-XRD data sets were jointly refined using the Rietveld method, accounting for the variable statistics, the bond lengths are presented in Table 7.1 and the refined structural parameters in Table 7.2. The structure of β-$CdUO_4$ has not been previously studied using neutron or synchrotron X-ray diffraction, consequently the structure reported here is both the first reporting it in the *Ibmm* space group and the most accurate and precise reported to date.

β-$CdUO_4$ can be considered to adopt a rutile related structure similar to β-$NiUO_4$ described in Chapter 6, where the CdO_6 and UO_6 polyhedra align along the [001] direction forming an infinite set of edge-sharing

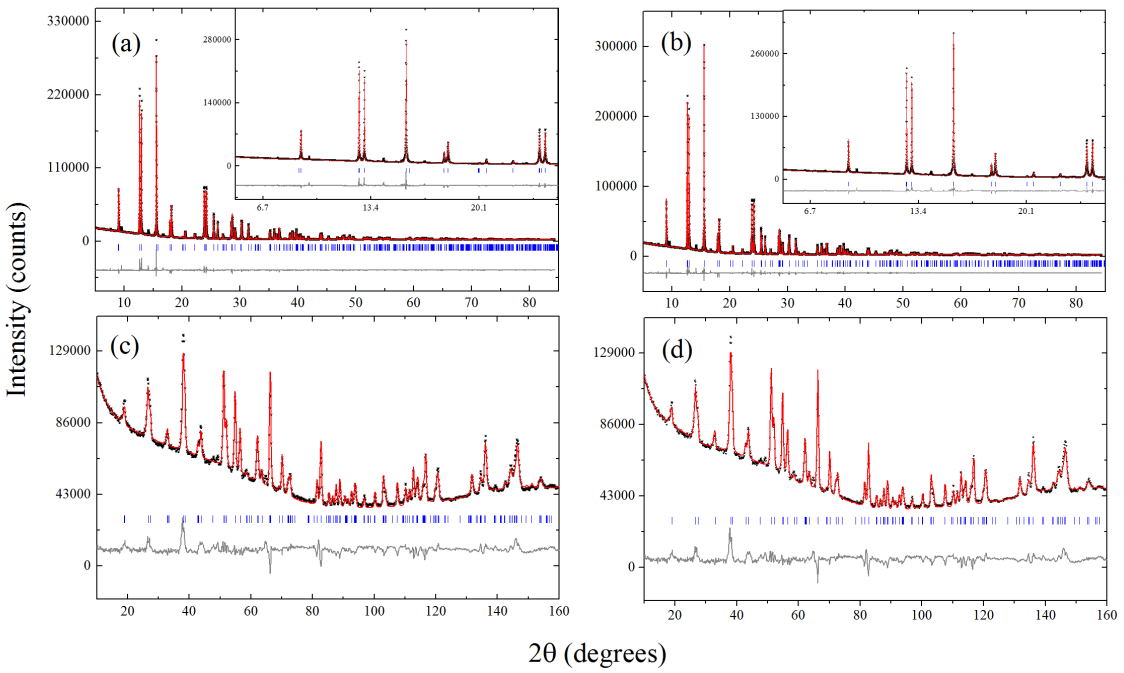

FIGURE 7.2: Rietveld refinement profiles for orthorhombic β-$CdUO_4$ in space group *Ibmm* against (c) NPD and (a) S-XRD and also in space *Cmmm* against (d) NPD and (b) S-XRD data. Dots, observed; solid line, calculated curve; grey line below, difference curve; vertical tick marks, peak positions. For *Ibmm* $wR_p = 3.31$ % $R_p = 2.37$% (NPD), $wR_p = 4.74$% $R_p = 3.11$% (S-XRD) and $wR_p = 4.26$% $R_p = 2.84$% χ^2 **= 14.59** (S-XRD and NPD combined). For *Cmmm* $wR_p = 3.18$% $R_p = 2.21$% (NPD), $wR_p = 5.02$% $R_p = 3.25$% (S-XRD) and $wR_p = 3.77$% $R_p = 2.87$% χ^2 **= 26.19** (S-XRD and NPD combined).

1D chains. The structure is illustrated in Figure 7.3. Similar to β-$NiUO_4$, the UO_6 polyhedra in β-$CdUO_4$ form two types of U-O bonds. U-O(2) and U-O(3) bonds link between adjacent UO_6 polyhedra creating the edge sharing motif in the [001] direction. The U-O(1) bonds are orthogonal to this and collinear with an oxo configuration consistent with uranyl[23] directed at the Cd atoms. The CdO_6 polyhedra contain two coordination bond types, *A*-O(1) and *A*-O(2). Two axial *A*-O(2) bonds are orientated in the [010] direction coordinating into the equator of the UO_6 polyhedra. Four *A*-O(1) bonds are directed into the [011] direction, derived from the coordination of the uranyl oxygens, corresponding to the U-O(1) bond in the UO_6 polyhedra.

TABLE 7.1: Bond distances obtained from structural refinements using NPD, S-XRD, SC-XRD and SSC-XRD for the AUO_4 structures reported here (A = β-Cd, Co, Mn and Mg).

	β-$CdUO_4$	$CoUO_4$	$MnUO_4$	$MgUO_4$
U-O(1)/Å	1.9255(18)x 2	1.923(4) x 2	1.890(4)x 2	1.939(4)x 2
U-$O(2)_i$/Å	2.160(15)x 2	2.184(4) x 2	2.155(8)x 2	2.157(3) x 2
U-$O(2)_{ii}$/Å	2.194(15)x 2	2.170(5) x 2	2.186(8) x 2	2.167(3) x 2
A-O(1)/Å	2.3129(12) x 4	2.200(3) x 4	2.263(3) x 4	2.183(2) x 4
A-O(2)/Å	2.2317(18) x 2	1.973(4) x 2	2.099(4) x 2	2.020 (4) x 2

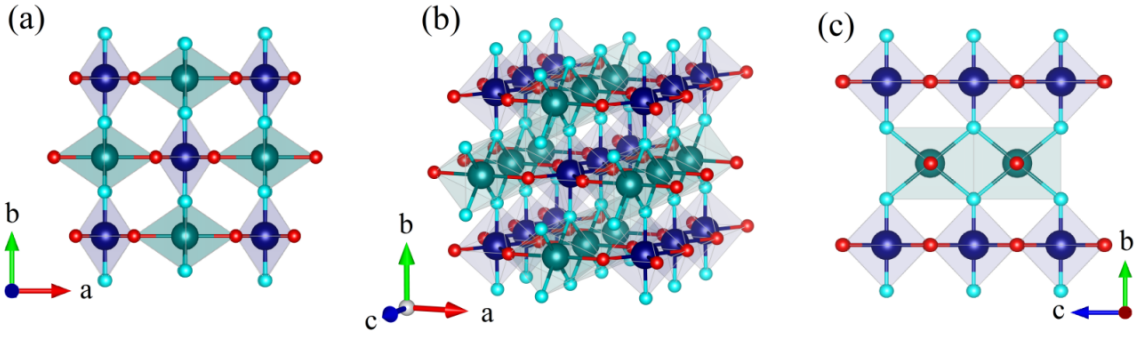

FIGURE 7.3: Structural representations of orthorhombic β-$CdUO_4$ in space group *Ibmm*. (a) projected in the [001] direction, (b) perspective on the structure with respect to the chain configuration and (c) projected in the [100] direction. Blue grey, dark blue, red and aqua spheres represent U, Cd, O(2) and O(1) uranyl oxygen atoms respectively.

7.3.2 Structural Studies 2. $CoUO_4$, $MnUO_4$ and $MgUO_4$

S-XRD and NPD patterns were collected for $CoUO_4$ and $MnUO_4$. Using a joint refinement method theses could be both well refined against orthorhombic structures in *Ibmm*, isostructural with β-$CdUO_4$ and β-$NiUO_4$ and consistent with previous reports[8,9,15]. $MnUO_4$ was found to have the larger unit cell of 313.9541(21) Å^3 compared to 294.09(4) Å^3 due to the larger Mn^{2+} cation ionic radii (0.83 Å CN = 6) compared to the smaller Co^{2+} (0.745 Å CN = 6). The Rietveld profiles for both $CoUO_4$ and $MnUO_4$ are presented in Figure 7.4, Refined bond lengths in Table 7.1 and structural parameters are given in Table 7.3 and 7.4 respectively.

The synthetic method used to generate single crystals of $MgUO_4$, using a solid state followed by molten regrowth approach, was found to be successful. Fine orange crystals of $MgUO_4$ could be readily separated and identified. The structural solution of $MgUO_4$ using SC-XRD measurements, demonstrated it crystallises in an orthorhombic structure in space group *Ibmm* isostructural with β-$CdUO_4$, $CoUO_4$ and $MnUO_4$. With respect to the aforementioned structures discussed so far, $MgUO_4$ was observed to form a smaller unit cell than β-$CdUO_4$ and $MnUO_4$ but greater than $CoUO_4$ and β-$NiUO_4$. Refined bond lengths and atomic parameters are shown in Table 7.1 and 7.5 respectively. The original study of $MgUO_4$ by Zachariasen in 1954[7] reports structural parameters of less precision than that here, Zachariasen describes challenges associated with absorption problems. In the present work an optimum crystal was chosen for the structural analysis and which the absorption was corrected using a multi scan method.

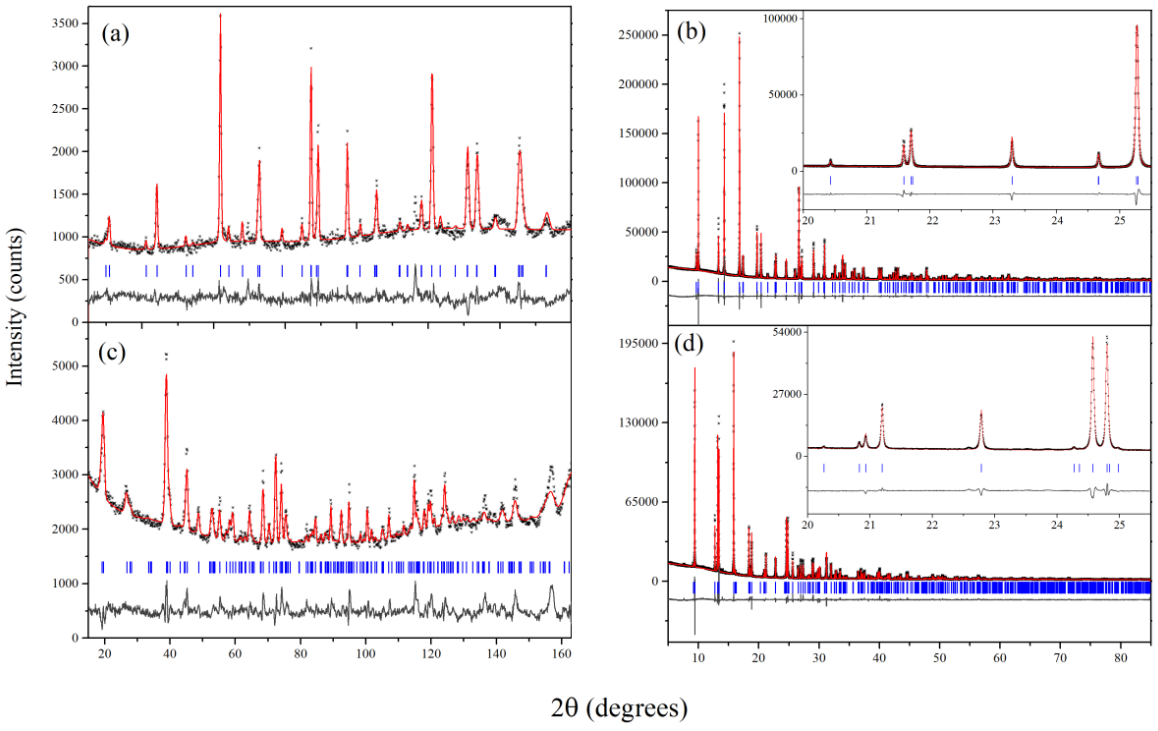

FIGURE 7.4: Rietveld profiles for $CoUO_4$ (a and b) and $MnUO_4$ (c and d) refined against NPD (left) and S-XRD (right) data sets in space group *Ibmm*. Dots, observed; solid line, calculated curve; grey line below, difference curve; vertical tick marks, peak positions. The background in (c) is a consequence of using small sample volume during the neutron measurement due to the limited amount of sample available.

TABLE 7.2: Refined structural parameters for β-$CdUO_4$ obtained from NPD and S-XRD data recorded at λ = 1.6215 and 0.77435 Å respectively. The structure was refined in the orthorhombic space group *Ibmm*.

Atom	x	y	z	Ui/Ue*100 Å^3
U	0.0000(4)	0	0.25	1.070(10)
Cd	0.5	0	0	0.441(16)
O1	0.0042(17)	0.28094(25)	0.25	1.144(5)
O2	0.18240(25)	0	-0.0030(26)	1.65(3)

a = 7.02652(11) Å, b = 6.85299(11) Å, c = 7.03729(11) Å, Cell volume = 338.864(16) Å^3. wR$_p$ = 4.26%, R$_p$ = 2.84%, χ^2 = 14.59 (S-XRD and NPD combined). *Equivalent values of the anisotropic results.

TABLE 7.3: Refined structural parameters for $CoUO_4$ obtained from NPD and S-XRD data recorded at λ = 2.4395 and 0.77466 Å respectively. The structure was refined in the orthorhombic space group *Ibmm*.

Atom	x	y	z	Ui/Ue*100 Å^3	U^{11}	U^{22}	U^{33}	U^{12}	U^{13}	U^{23}
U	0.03162(5)	0	0.25	0.693(5)	-	-	-	-	-	-
Co	0.5	0	0	0.957(29)	-	-	-	-	-	-
O1	0.0343(7)	0.2956(6)	0.25	1.3*	0.024(3)	0.008(3)	0.0060(23)	0	0.0049(28)	0
O2	0.1975(6)	0	-0.0231(6)	0.0*	0.0027(21)	0.0114(24)	0.008(3)	0	0	0.0014(18)

a = 6.4990(11) Å, b = 6.5055(11) Å, c = 6.9558(10) Å, Cell volume = 294.09(4) Å^3. wR$_p$ = 11.04%, R$_p$ = 7.75% (S-XRD), wR$_p$ = 5.57%, R$_p$ = 4.65% (NPD), χ^2 = 3.93 (S-XRD and NPD combined). *Equivalent values of the anisotropic results.

TABLE 7.4: Refined structural parameters for $MnUO_4$ obtained from NPD and S-XRD data recorded at $\lambda = 1.6215$ and 0.77466 Å respectively. The structure was refined in the orthorhombic space group *Ibmm*.

Atom	x	y	z	Ui/Ue*100 Å^3	U^{11}	U^{22}	U^{33}	U^{12}	U^{13}	U^{23}
U	0.01434(9)	0	0.25	1.1206(7)	-	-	-	-	-	-
Mn	0.5	0	0	1.139(3)	-	-	-	-	-	-
O1	0.0135(11)	0.2843(6)	0.25	2.0*	0.0204(26)	0.0193(28)	0.0201(29)	0	0.001(3)	0
O2	0.1896(5)	0	-0.0129(13)	2.1*	0.0203(27)	0.021(3)	0.0215(28)	0	0	-0.001(4)

a = 6.75463(3) Å, b = 6.65046(2) Å, c = 6.98896(2) Å, Cell volume = 313.9541(21) Å^3. wR_p = 10.87%, R_p = 7.65% (S-XRD), wR_p = 7.69%, R_p = 5.3% (NPD), χ^2 = 3.85 (S-XRD and NPD combined). *Equivalent values of the anisotropic results.

TABLE 7.5: Refined structural parameters for $MgUO_4$ obtained from SC-XRD data recorded at $\lambda = 0.71073$ Å. The structure was refined in the orthorhombic space group *Ibmm*.

Atom	x	y	z	Ui/Ue*100 Å^3	U^{11}	U^{22}	U^{33}	U^{12}	U^{13}	U^{23}
U	0.47697 (2)	0	0.25	0.4*	0.00346(8)	0.00239(8)	0.00608(8)	0	0	0
Mg	0	0	0.5	0.7*	0.0078(80)	0.0087(8)	0.0043(6)	0.0005(5)	0	0
O1	0.4759(3)	0.2974(4)	0.25	0.79*	0.0048(11)	0.0075(11)	0.0115(11)	0	0.0004(8)	0
O2	0.3057(4)	0	0.5171(3)	0.77*	0.0115(12)	0.0068(10)	0.0049(9)	-0.0009(7)	0	0

a = 6.595(5) Å, b = 6.519(5) Å, c = 6.923(5) Å, Cell volume = 297.6(4) Å^3. wR_p = 2.25%, R_p =0.90% , χ^2 = 1.077. *Equivalent values of the anisotropic results.

7.3.3 X-ray Absorption Near Edge Structure (XANES) Results

As described previously in both this dissertation and in published works[13,20,24] the AUO$_4$ oxides can host a variety of uranium valence states. Prior to this dissertation it could be reasonably assumed that a specific AUO$_4$ structure type would host a particular uranium valence state and corresponding A site cation valence. Chapter 6 highlights the limitation of this assumption, that despite being isostructural to CrU(V)O$_4$[13] and FeU(V)O$_4$[9,25,26], α-NiUO$_4$ contains hexavalent uranium. Further, as described previously in this dissertation bond valence sums (BVS) calculations are of limited value[23] in assigning correct valence states in actinide materials because of precision in initial measurement and the presence of the actinyl group. Direct valence state determination methods, such as XANES, are thus necessary. XANES measurements are particularly pertinent here when considering the presence of cations such as Co and Mn which can readily exist as divalent or trivalent leading to the possibility of hexavalent or pentavalent uranium respectively. XANES measurements were performed on β-CdUO$_4$, CoUO$_4$ and MnUO$_4$ and MgUO$_4$ on the U L$_2$-edge. This spectra originates from the dipole transition of the U $2p_{1/2}$ core electrons into the empty $6d$ states in the conduction band. As shown in Figure 7.5 the U L$_2$ edge position of all four AUO$_4$ oxides investigated here is essentially the same as that of CaUO$_4$[20] corresponding to the presence of hexavalent uranium in these oxides.

When these spectroscopic results are considered, together with β-NiUO$_4$, it is apparent that all known orthorhombic AUO$_4$ oxides in space group *Ibmm* exist with hexavalent uranium. It seems implausible to observe these possessing pentavalent uranium in the case of β-CdUO$_4$ and MgUO$_4$ as this would require trivalent Cd and Mg which is not possible. However it is reported[27] that when β-CdUO$_4$ is heated towards 1000 ^{o}C it undergoes a pronounced oxygen loss involving a phase transformation. This behaviour is reminiscent to that observed in SrUO$_4$ in Chapter 3, namely oxygen vacancy formation accompanied by mixed U^{6+} and U^{5+} oxidation states. Although these results stem from thermal analysis and there are little structural studies to confirm this. Such a study is out of the scope of the presented investigation. Nevertheless it would be worthwhile to examine this, particularly if it is related the anomalous reversible high temperature oxygen defect ordering observed in similar SrUO$_4$ and CaUO$_4$.

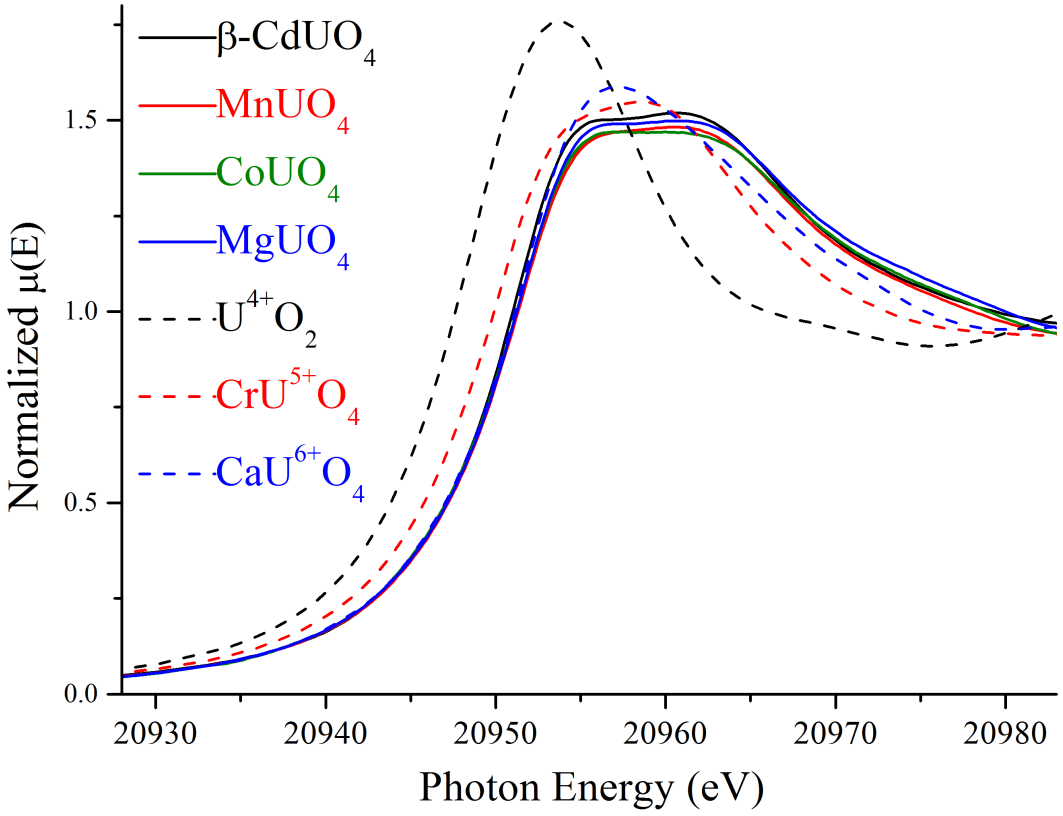

FIGURE 7.5: Normalized U L_2-edge XANES spectra of β-$CdUO_4$ (solid black line), $MnUO_4$ (solid red line), $CoUO_4$ (solid green line), and $MgUO_4$ (solid blue line), as well as U^{4+} (dash black line), U^{5+} (dash red line) and U^{6+} (dash blue line) standards.

7.3.4 Structural Chemistry and Trends in the Rutile Related Orthorhombic AUO$_4$ Oxides

With the precise structures and spectroscopic measurements presented so far for the orthorhombic AUO$_4$ oxides in space group *Ibmm*, it is pertinent to systematically compare and contrast them. Table 7.6 comparatively details the refined lattice volume, BVS values for each metal cation, U-O(1) uranyl bond length, A site cation radii, and UO_6 bond angel variance calculated for β-$CdUO_4$, $MnUO_4$, $CoUO_4$, $MgUO_4$ and β-$NiUO_4$. Although BVS are relatively inaccurate in oxidation state determination in uranium oxides as described, they can provide a crude means to look at the relative stability of cations as has been done previously[20]. These have been calculated for each of the metal cations as presented in Table 7.6. Of the orthorhombic *Ibmm* AUO$_4$ oxides, β-$CdUO_4$ has the largest unit cell whereas β-$NiUO_4$ has the smallest, a consequence of the respective large and small Cd^{2+} and Ni^{2+} cations, where the other oxides follow

this trend consistently. That the small Ni^{2+} cation requires high pressure synthesis conditions to form β-$NiUO_4$, is consistent with the calculated BVS that shows it to be the most under bonded U cation of the series. It was highlighted in Chapter 6 that the UO_6 polyhedra in β-$NiUO_4$ undergo considerable distortion to accommodate this, this is evident in the large U-O(1) uranyl bond length of 1.921(13) Å and, particularly, the large approximate bond angle variance of 162.82 ^{o2}, calculated using the method of Robinson *et al.*[28]. As the *A* site cation size increases towards Cd, the uranium distortion is reduced as shown by the reduction of the bond angle variance for the UO_6 polyhedra. This suggests structural instability is partially alleviated through distortion of the uranium polyhedra.

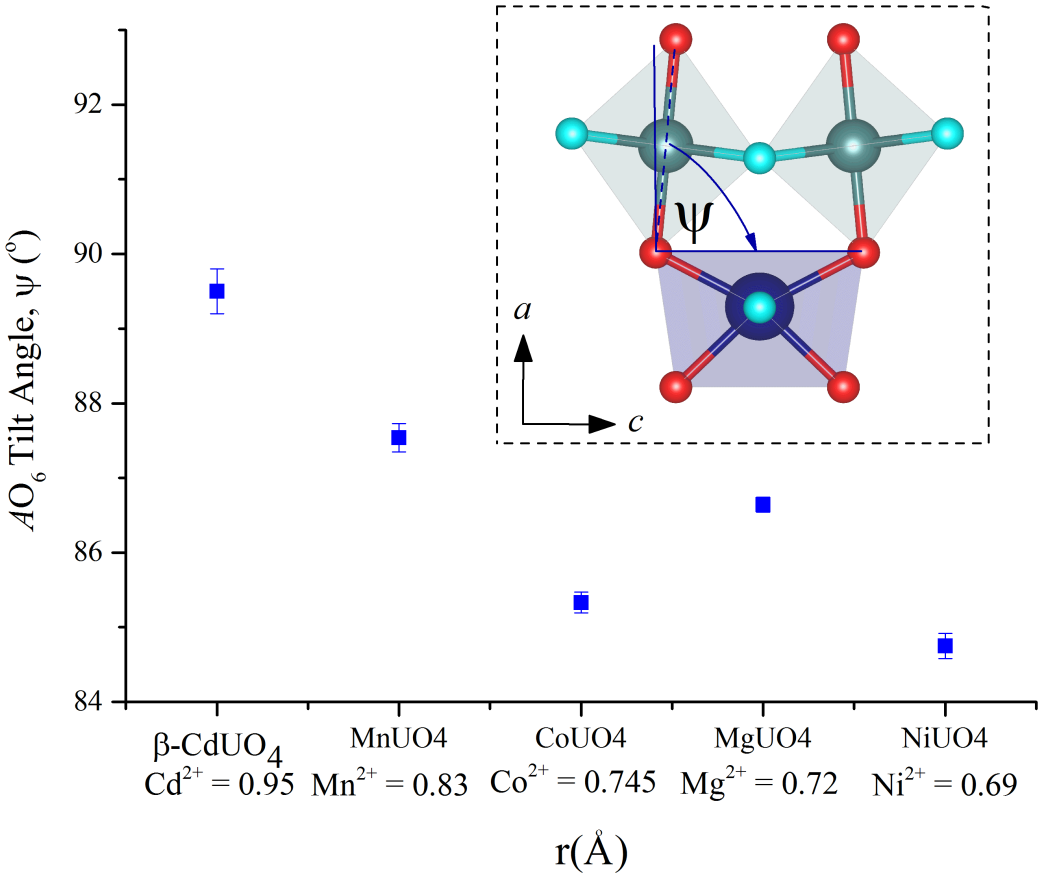

FIGURE 7.6: Calculated angular tilt, ψ, of AO_6 polyhedra in the AUO_4 oxides in space group *Ibmm* for A = β-Cd, Co, Mn, Mg, and β-Ni.

It was noted in Chapter 6 that when the NiO_6 polyhedra of β-$NiUO_4$ show a subtle tilt away from the [010] direction. This is particularly apparent when comparing to the CdO_6 polyhedra in β-$CdUO_4$ which does not seem to present much tilting (Compare Figure 7.3 with Figure 6.5, Chapter 6). Calculating the tilt angle for the rest of the orthorhombic *Ibmm* AUO_4 oxides shows they follow a trend of increasing the ionic radii resulting in the reduction of this tilt. This trend is graphically illustrated in Figure 7.6. This tilting phenomena is similar to that observed in ABX_3 perovskites. However the rutile like geometry of the AUO_4 orthorhombic oxides in space group *Ibmm* means the tilting can only occur in one dimension and it seems to be reduced to zero in β-$CdUO_4$. β-$CdUO_4$ is reported to undergo a first order phase transformation at high temperature[27]. That the structure cannot undergo a reverse tilt like motion, because of the rutile configuration, is suspected to contribute to the apparent first order nature of the transformation. Many phase transformations in ABX_3 perovskites occur through changes to the tilt of BX_6 polyhedra, resulting in 2^{nd} order phase transformations occurring[12]. The inability for a reverse tilt like motion in the orthorhombic *Ibmm* AUO_4 oxides seemingly prevents this as the tilting can only occur along one axis here, whereas the perovskite structure has two fulcrum points. However the transformation of β-$CdUO_4$ has only been examined using thermal analysis methods. It is desirable to examine these using *in situ* structural methods to determine the nature of the transformation.

TABLE 7.6: Structural parameters for the orthorhombic AUO_4 oxides in space group *Ibmm* for A = β-Cd, Co, Mn, Mg, and β-Ni. BVS calculated using the values of Burns *et al.*[23].

Oxide	Unit cell volume (Å^3)	A BVS	U BVS	uranyl length (Å)	A site radii (Å)[10]	UO_6 Bond angle variance (^{o2})
β-$CdUO_4$	338.864(16)	2.15	6.04	1.9255 (18)	0.95	116
$MnUO_4$	313.9541(21)	2.10	5.95	1.890(4)	0.83	119
$CoUO_4$	294.09(4)	1.95	6.05	1.923(4)	0.75	140
$MgUO_4$	297.6(4)	1.89	6.05	1.939(4)	0.72	123
β-$NiUO_4$	286.85(10)	1.99	6.10	1.921(13)	0.69	162

7.4 Chapter Conclusion

Accurate and precise structures for β-$CdUO_4$, $MnUO_4$, $CoUO_4$ and $MgUO_4$ have been determined using a combination of NPD, S-XRD and SC-XRD supported by XANES measurements. These all form orthorhombic oxides in space group *Ibmm* isostructural to β-$NiUO_4$ described in Chapter 6 where they all are demonstrated to contain hexavalent uranium. This is the first reported description of β-$CdUO_4$ being in space group *Ibmm*, determined through accurate measurements using NPD and S-XRD. Examining the

precise structural models presented shows they possess a tilting like arrangement of AO_6 polyhedra which is proportional to the size of A site cation and a consequence of mismatched sizing between the A site and U cations. This is most pronounced in β-$NiUO_4$ and least in β-$CdUO_4$. Furthermore considerable distortions are identified in the UO_6 polyhedra that seem to allow structure formation and alleviate instability caused by the cation mismatching. That the highlighted tilting mechanism occurs over one axis, unlike that found in ABX_3 perovskites, is suspected to contribute to the first order nature of the reported[27] of β-$CdUO_4$.

References

1. Glazer, A. M. *Acta Crystallographica Section B-Structural Science* **B 28**(NOV15), 3384–3389 (1972).

2. Zhang, Z., Howard, C. J., Knight, K. S., and Lumpkin, G. R. *Acta Crystallographica Section B* **62**(1), 60–67 (2006).

3. Bhalla, A. S., Guo, R. Y., and Roy, R. *Materials Research Innovations* **4**(1), 3–26 (2000).

4. King, G. and Woodward, P. M. *Journal of Materials Chemistry* **20**(28), 5785–5796 (2010).

5. Tsai, H., Nie, W., Blancon, J.-C., Stoumpos, C. C., Asadpour, R., Harutyunyan, B., Neukirch, A. J., Verduzco, R., Crochet, J. J., Tretiak, S., Pedesseau, L., Even, J., Alam, M. A., Gupta, G., Lou, J., Ajayan, P. M., Bedzyk, M. J., Kanatzidis, M. G., and Mohite, A. D. *Nature* **536**, 312 (2016).

6. Burschka, J., Pellet, N., Moon, S. J., Humphry-Baker, R., Gao, P., Nazeeruddin, M. K., and Gratzel, M. *Nature* **499**(7458), 316–322 (2013).

7. Zachariasen, W. H. *Acta Crystallographica* **7**(12), 788–791 (1954).

8. Bacmann, M. and Bertaut, E. F. *Journal De Physique* **30**(11-1), 949 (1969).

9. Read, C. M., Smith, M. D., and zur Loye, H. C. *Solid State Sciences* **37**, 136–143 (2014).

10. Shannon, R. *Acta Crystallographica Section A* **32**(5), 751–767 (1976).

11. Yamashita, T., Fujino, T., Masaki, N., and Tagawa, H. *Journal of Solid State Chemistry* **37**(2), 133–139 (1981).

12. Murphy, G. L., Kennedy, B. J., Zhang, Z. M., Avdeev, M., Brand, H. E. A., Kegler, P., and Alekseev, E. V. *Journal of Alloys and Compounds* **727**, 1044–1049 (2017).

13. Guo, X. F., Tiferet, E., Qi, L., Solomon, J. M., Lanzirotti, A., Newville, M., Engelhard, M. H., Kukkadapu, R. K., Wu, D., Ilton, E. S., Asta, M., Sutton, S. R., Xu, H. W., and Navrotsky, A. *Dalton Transactions* **45**(11), 4622–4632 (2016).

14. Bertaut, E. F., Delapalme, A., Forrat, F., and Pauthenet, R. *Journal De Physique Et Le Radium* **23**(8-9), 477–485 (1962).

15. Bacmann, M. and Bertaut, E. F. *Journal De Physique* **27**(11-1), 726–732 (1966).

16. Wallwork, K. S., Kennedy, B. J., and Wang, D. *The high resolution powder diffraction beamline for the Australian Synchrotron*, volume 879 of *Aip Conference Proceedings*, 879–882. Amer Inst Physics, Melville (2007).

17. Liss, K. D., Hunter, B., Hagen, M., Noakes, T., and Kennedy, S. *Physica B-Condensed Matter* **385-86**, 1010–1012 (2006).

18. Larson, A. C. and Dreele, R. B. V. Technical report, Los Alamos National Laboratory, (2000).

19. Toby, B. H. *Journal of Applied Crystallography* **34**, 210–213 (2001).

20. Murphy, G., Kennedy, B. J., Johannessen, B., Kimpton, J. A., Avdeev, M., Griffith, C. S., Thorogood, G. J., and Zhang, Z. M. *Journal of Solid State Chemistry* **237**, 86–92 (2016).

21. Glover, C., McKinlay, J., Clift, M., Barg, B., Boldeman, J., Ridgway, M., Foran, G., Garrett, R., Lay, P., and Broadbent, A. *Status of the x-ray absorption spectroscopy (XAS) beamline at the Australian synchrotron*, volume 882 of *AIP Conference Proceedings*, 884–888. (2007).

22. Ravel, B. and Newville, M. *Journal of Synchrotron Radiation* **12**(4), 537–541 (2005).

23. Burns, P. C., Ewing, R. C., and Hawthorne, F. C. *Canadian Mineralogist* **35**, 1551–1570 (1997).

24. Popa, K., Prieur, D., Manara, D., Naji, M., Vigier, J. F., Martin, P. M., Blanco, O. D., Scheinost, A. C., Prussmann, T., Vitova, T., Raison, P. E., Somers, J., and Konings, R. J. M. *Dalton Transactions* **45**(18), 7847–7855 (2016).

25. Bacmann, M. and Bertaut, E. F. *Bulletin De La Societe Francaise Mineralogie Et De Cristallographie* **90**(2), 257–261 (1967).

26. Bacmann, M., Bertaut, E. F., Blaise, A., Chevalie.R, and Roult, G. *Journal of Applied Physics* **40**(3), 1131–1134 (1969).

27. Tagawa, H. and Fujino, T. *Inorganic & Nuclear Chemistry Letters* **16**(2), 91–96 (1980).

28. Robinson, K., Gibbs, G. V., and Ribbe, P. H. *Science* **172**(3983), 567–561 (1971).

Chapter 8

Variable Pressure Neutron Diffraction Studies of $SrUO_4$

This chapter is adapted from a manuscript titled "High Pressure Neutron Diffraction Studies of $SrUO_4$: A Departure in Badger's Rule and Bond Lengthening with Pressure" by G. L. Murphy *et al.* that is being prepared for submission at the time of writing.

8.1 Introduction

As highlighted in Chapter 6, high pressures can be used as an alternative compared to traditional solid state methods to synthesise new structural phases. In the context of actinide chemistry they can also be used to examine the exotic behaviour of $5f$ electron delocalisation and how these electrons can contribute to bonding[1–3]. It is reasonably well understood that the relative compressibility of actinide elements is related to the number of $5f$ electrons present, and particular, how iterant they can become[3,4]. Metallic uranium, neptunium and plutonium contain electrons within the valence ($6d/5f$) shell that lead to heightened itinerancy and pronounced incompressibility[3]. Conversely the early and transplutonium actinides either do not have a significant amount of valence ($6d/5f$) electrons or experience increased screening of the f states, both of which inhibit electron itinerancy and consequently, these actinides are generally softer than uranium, neptunium and plutonium[3,4]. The above discussion is largely a generalized overview and somewhat arbitrary[3] as several controversies remain, for instance the extent of partial localisation of the $5f$ states in the harder actinides. Furthermore understanding the nature of $5f$ electron response to pressure becomes more convoluted when complex oxides are considered which may contain structural groups such as the actinyl moiety which modulate electron density away from the generalised metallic state. Specific structural dimensionality may further impact electron delocalisation and the general response to pressure.

The structures of uranyl group containing rhombohedral $CaUO_4$[5], orthorhombic β-$CdUO_4$[6] (in space group *Cmmm*) and also UO_2F_2[7] have been previously calculated using density functional theory. These three compounds were predicted to exhibit relatively unexceptional bulk moduli from isotropic compression but could obtain much higher values under anisotropic compression along the uranyl bond directed axis, the calculated bulk moduli being comparable to that of diamond[8]. *In situ* high pressure studies of actinides have largely been confined to the metallic state with few studies looking at binary and ternary oxides. Despite the absence of contemporary experimentation, computational studies have progressed the interest and understanding of complex actinide oxides under pressure. Notably it was argued recently by Osman *et al.*[9] using computational methods in the form of density functional theory, that $Cs_2UO_2Cl_4$ is able to exhibit anomalous lengthening of the uranyl bond under pressure, suggesting this may be in violation of Badger's rule[10]. The rule essentially relates bond strength to its vibrational mode and as such is useful in spectroscopy for assessing the changes to bonding within a material and its interactions. Other studies[11,12] have noted the inability for actinide materials to be understood using Badger's rule, although

there are apparently none that have looked at this departure with *in situ* high pressure diffraction methods, particularly to examine how lengthening of the uranyl bond will affect the bulk compressibility of the material.

This chapter is devoted to investigating and understanding the theorised departure of Badger's rule through *in situ* high pressure studies of the 2D layered uranyl group containing α-$SrUO_4$ and β-$SrUO_4$. The structures contain 2D layers of UO_8 and UO_6 polyhedra respectively. A subtle but potentially pertinent difference between the polymorphs is the direction and lengths of the uranyl groups, as illustrated in Figure 8.1, the uranyl bonds in α-$SrUO_4$ are normal to the Sr^{2+} layers whereas in β-$SrUO_4$ they partially tilt away from normal incidence with the Sr^{2+} layers. Further the uranyl bond in α-$SrUO_4$ is longer at 1.958(3) Å than is in β-$SrUO_4$ with a length of 1.879(2) Å. Extension of the theoretical results of Osman *et al.*[9] suggests a gradual lengthening of the uranyl bond should occur upon application of pressure but it is not clear to the extent at which it will lengthen, since the Sr^{2+} cations should sterically hinder this based on their close proximity to the uranyl bonds in both polymorphs. These subtle differences are hypothesized to contribute to potentially significant difference in the structural behaviour and response when these oxides are subject to high pressure. Consequently the pressure dependence of the structures of α-$SrUO_4$ and β-$SrUO_4$ were examined *in situ* using neutron powder diffraction. The results obtained are discussed with respect to previously described theoretical results, the relation to other actinides under pressure and general high pressure materials science.

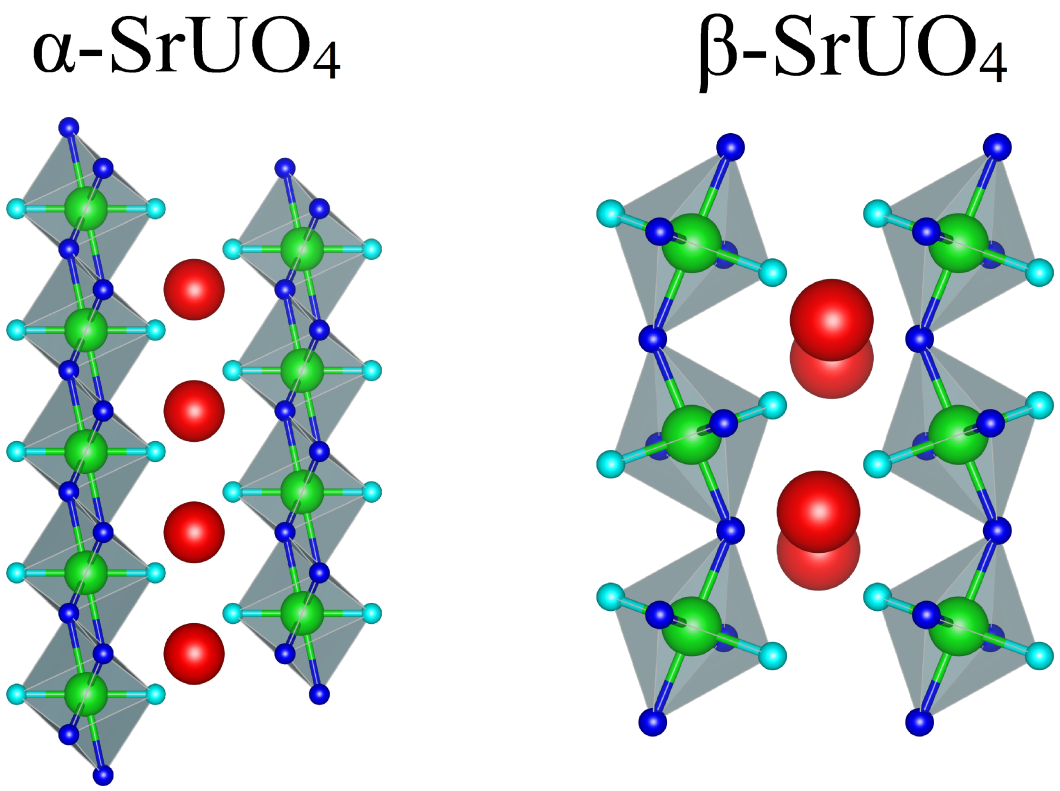

FIGURE 8.1: Structural representations of the layered structure motifs of α-$SrUO_4$ (left) and β-$SrUO_4$ (right). Green, red, blue and aqua blue spheres represent uranium, strontium, oxygen and uranyl oxygen atoms.

8.2 Experimental

8.2.1 Sample Preparation and *In Situ* High Pressure Neutron Powder Diffraction

A polycrystalline sample of α-$SrUO_4$ and β-$SrUO_4$ were prepared as outlined previously in Chapter 3. The oxides ($\approx$ 100 mg) were mixed with lead metal ($\approx$ 50 mg) that acts as an internal pressure standard and a small amount of deuterated ethanol mixed with methanol which acts as the pressure transmittance medium. The resulting slurry was loaded into a TiZr null matrix alloy sample holder, which was placed in a VX-5 Paris-Edinburgh hydraulic press equipped with boron nitride anvils [13] (see Figure 8.2). Neutron powder diffraction (NPD) data were acquired using the high intensity neutron diffractometer WOMBAT [14]

at ANSTO's OPAL reactor. WOMBAT employs an area detector that continuously covers 120^o, however only data in the angular range $16^o < 2\theta < 100^o$ was suitable. Data was collected for 10-30 minutes at each pressure increment using the instruments oscillating collimator active and neutrons with a wavelength of 1.6369 Å were used as determined using a LaB_6 reference. α-$SrUO_4$ and β-$SrUO_4$ were pressed incrementally towards maximum load pressures of respectively 1200 and 1000 bar. Using the lead standard these load pressures were determined to corresponds to maximum pressures of 6.15 and 5.7 GPa respectively on the samples. Analysis of the collected NPD data was undertaken using the programs GSAS [15,16] and GSAS-II [17]. The program EoSFit7 [18] was used to determine the bulk moduli.

.

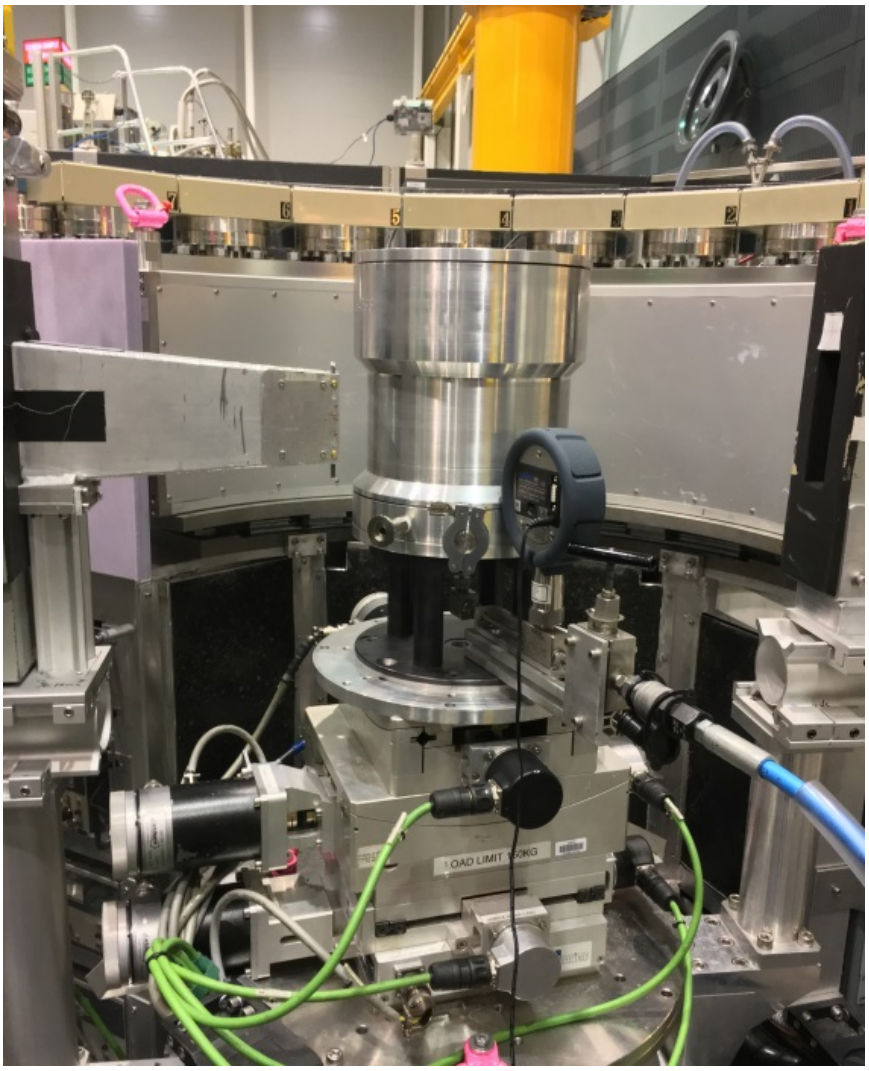

FIGURE 8.2: Paris-Edinburgh cell equipped to the WOMBAT high intensity neutron diffractometer at ANSTO's Opal Reactor [14].

8.3 Results and Discussion

8.3.1 *In Situ* High Pressure Neutron Powder Diffraction Studies

The pressure dependence of the NPD patterns for α-$SrUO_4$ to 6.15 GPa is presented in Figure 8.3. Inspecting the peaks corresponding to α-$SrUO_4$ it is apparent they exhibit considerable broadening, associated with strain, as the pressure is increased towards 6.15 GPa. This is in contrast to the lead standard which relatively maintains crystallinity over the studied pressure range. Critical, pressure induced shifts in the peak positions to lower 2θ, indicative of contraction with pressure, for α-$SrUO_4$ are small compared to the lead. This suggests α-$SrUO_4$ is quite incompressible.

The pressure dependence of the NPD patterns for β-$SrUO_4$ to 5.7 GPa is presented in Figure 8.4. Similar to what was observed for α-$SrUO_4$, the diffraction peaks corresponding to β-$SrUO_4$ exhibit considerable broadening associated with strain as it pressed towards 5.7 GPa. Also similar to α-$SrUO_4$, the pressure induced peak shifting of β-$SrUO_4$ is quite subtle compared to the lead standard, although it seems to be greater than α-$SrUO_4$, suggesting the α phase is less compressible than the β phase. This is confirmed when the change to unit cell volume (V/V_0) determined from Rietveld refinements against NPD data as a function of pressure is plotted for α-$SrUO_4$and of β-$SrUO_4$ as presented in Figure 8.5. It is apparent that both oxides are relatively incompressible, but this particularly so for α-$SrUO_4$ as by near 6 GPa the unit cell volume has contracted by only approximately 1%.

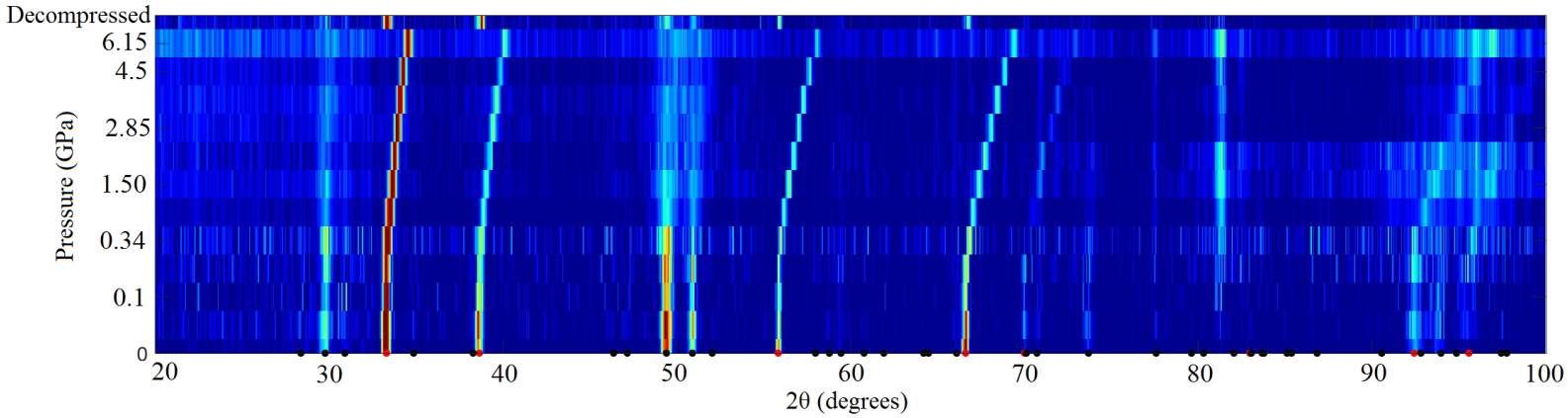

FIGURE 8.3: NPD data collected for α-$SrUO_4$ from ambient pressure to 6.15 GPa and decompressed at 2θ values ranging from 20 to 100^o.

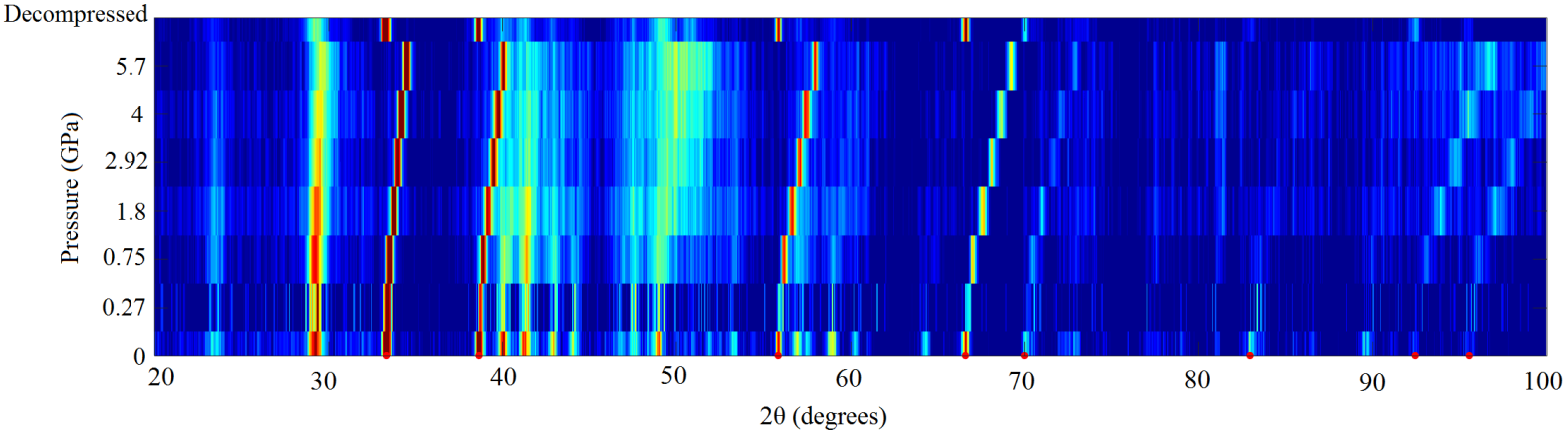

FIGURE 8.4: NPD data collected for β-$SrUO_4$ from ambient pressure to 5.7 GPa and decompressed at 2θ values ranging from 20 to 100^o.

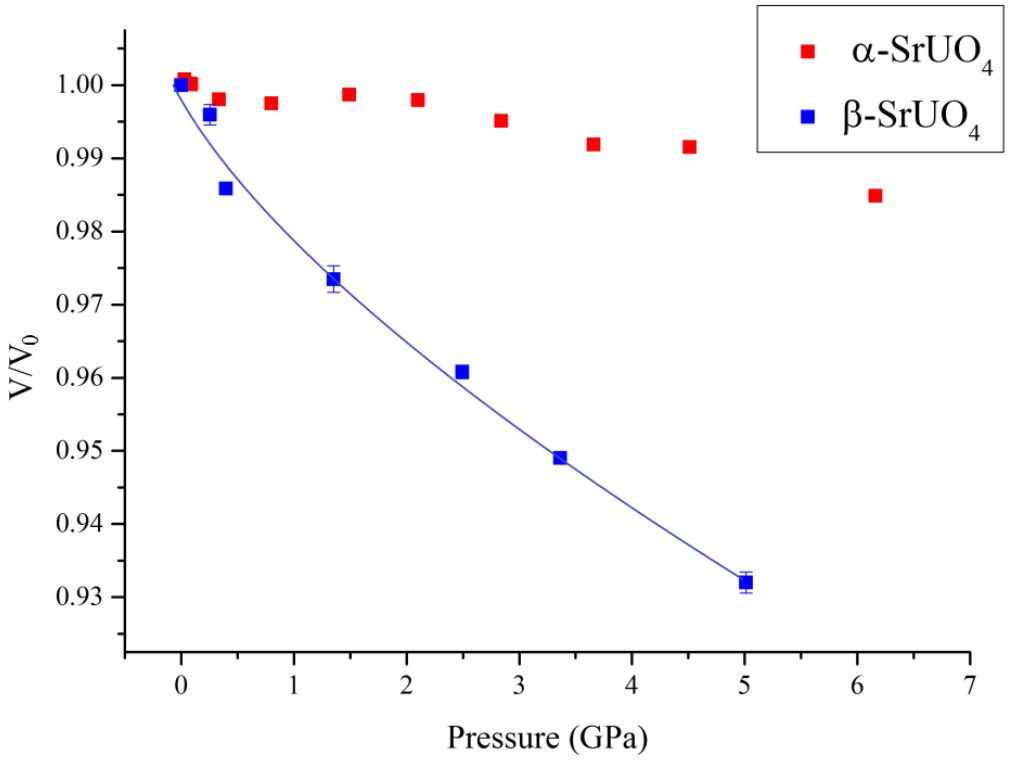

FIGURE 8.5: Unit cell volume dependence of α-$SrUO_4$ and β-$SrUO_4$ as a function of pressure. The plotted line for β-$SrUO_4$ is derived from the Murnaghan EoS assigned for it ($\chi^2 = 0.07$).

Equations of state (EoS) were estimaed for each oxide using the software EoSFit7[18] using the refined lattice volume against the determined pressures. The pressure dependence of β-$SrUO_4$ to 5.17 GPa could be fitted well to a Murnaghan[19] EoS model:

$$P(V) = \frac{K_0}{K_0'}[\frac{V^{-K_0}}{V_0} - 1] \tag{8.1}$$

For β-$SrUO_4$ initial volume, V_0, is 347.1(6) Å ^{3}, bulk modulus, K_0, 55(8) GPa and its first derivative of, K_0', 12(4) GPa, and the EoS curve is presented in Figure 8.5. The Murnaghan EoS curve is shown to well describe the pressure dependence of β-$SrUO_4$. A calculated K_0 of 55(8) GPa is similar to that found for the uranyl peroxide nano-cluster material $U_{60}([UO_2(O_2)(OH)]_{60}{}^{60-}$ at 25 GPa but well away from the isotropically calculated value for orthorhombic β-$CdUO_4$ (calculated in space group *Cmmm*) at 166 GPa.

Attempts were made to fit an EoS against the α-$SrUO_4$ V/V_0 obtained from the NPD measurements but no reliable model could be determined. This is suspected to be a consequence of the pronounced incompressibility of α-$SrUO_4$ and limited pressure range studied. The estimated value of K_0, based on the collected data, was above 400 GPa suggesting α-$SrUO_4$ may be a super or ultrahard material similar to c-BN[20] and diamond[21,22]. Although it is stressed this is speculation and further measurements of α-$SrUO_4$ at higher pressure are required to determine a suitable equation of state and determine an accurate K_0. Nevertheless that α-$SrUO_4$ exhibits such a large K_0 is consistent with the results of Mater and Demazeau[5] who calculated isostructural $CaUO_4$ to have a K_0 of 410 GPa when compressed anisotropically.

The pressure dependence of U-O(1) uranyl and U-O(2) bonds for α-$SrUO_4$ is presented in Figure 8.6. As evident from this figure, increasing pressure results in an increase in the length of both the U-O(1) uranyl and U-O(2) bonds in α-$SrUO_4$. The bond lengthening is most pronounced in the uranyl bond which increases from an initial value of 1.97(3) to 2.27(8) Å at 6.15 GPa. This corresponds to a 15% increase in length from 6.15 GPa of pressure. This remarkable but counter intuitive observation, is consistent to the theoretical results of Osman *et al.*[9], where they attributed the bond lengthening to be a consequence of charge transfer towards the uranyl bond causing the effective charge of the uranyl group, UO_2^{2+}, to decrease. This violates what is expected from Badger's rule as predicted by Osman *et al.*[9]. A uranyl bond length of greater than 2.00 Å is not expected for hexavalent uranium[23,24] and is more consistent with penatavalent uranium, similar to the uranyl lengths observed in Chapter 3 and 4 for sub-stoichiometric α-$SrUO_{4-x}$ and δ-$SrUO_{4-x}$ with respective lengths of 1.973(2) and 1.892(17) - 2.083(17) Å .

To recapitulate with respect to observations made in this chapter, theoretical discussions[9] and previous literature[3], placing α-$SrUO_{4-x}$ under pressures up to 6.15 GPa results in an electron delocalisation process to occur where charge is transferred to the uranyl bond, reducing the effective uranyl charge and leading to the bond length increasing. As described in the introduction to this chapter, the uranyl bonds in α-$SrUO_4$ are directed perpendicular to the UO_8 layers normal to the Sr^{2+} cations. This geometry allows little flexibility for the structure to contract or respond to the increased pressure, and this is likely related to the origin of the pronounced incompressibility of α-$SrUO_{4-x}$.

The pressure dependence of the U-O(1) uranyl, U-O(2) and U-O(3) bonds for β-$SrUO_4$ is presented in Figure 8.7. Towards 1 GPa the U-O(1) uranyl bond gradually contracts, however increasing pressure towards 5.7 GPa shows an overall expansion of 12% of initial length at ambient conditions. The U-O(2)

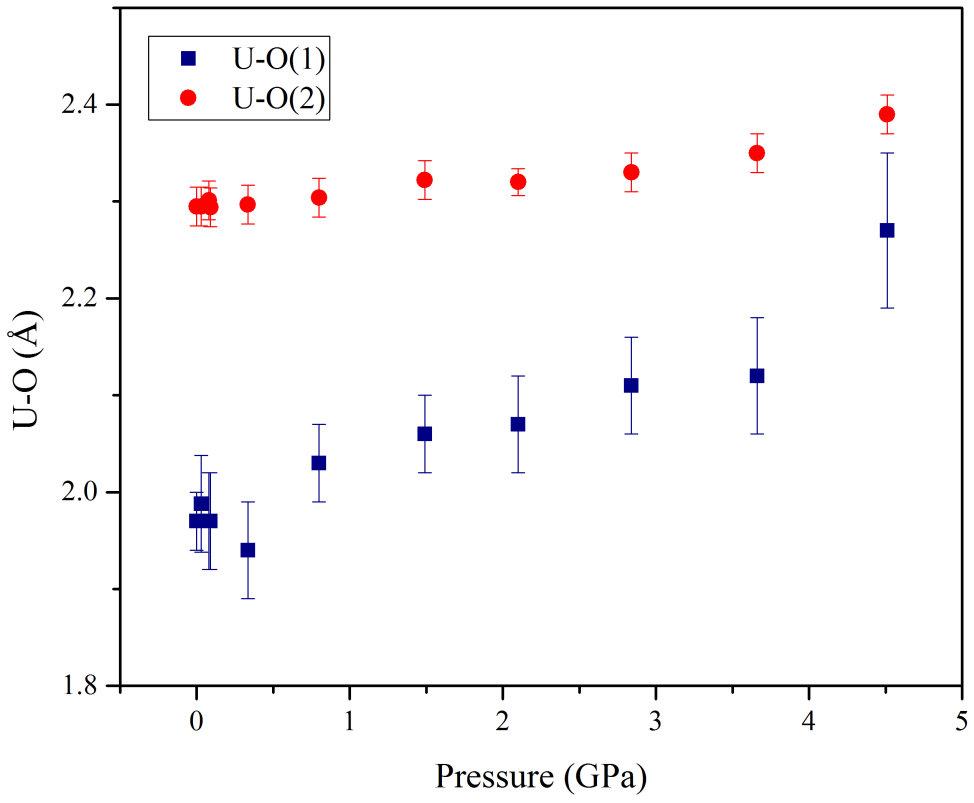

FIGURE 8.6: Uranium-Oxygen bond lengths in the UO_8 polyhedra in α-$SrUO_4$ from ambient towards 5 GPa determined from Rietveld refinements against NPD measurements. Note the exceptional expansion of the uranyl U-O(1) bond length.

and U-O(3) bonds, like the U-O(2) bonds in α-$SrUO_4$ show overall expansion over the pressure range from 2.162(6) and 2.221(7) Å to 2.270 and 2.274(18) Å respectively. This dramatic increase in the uranyl and also equatorial U-O(2) and U-O(3) bond lengths in β-$SrUO_4$, is similar to that observed in α-$SrUO_4$. Consistent with the previous discussion for α-$SrUO_4$ an apparent electron transfer process is occurring which is causing the lengthening of the uranyl bond. It further demonstrates the departure from what is predicted by Badger's Rule. The partial contraction at low pressure of the uranyl bond in β-$SrUO_4$ is also observed in α-$SrUO_4$ when Figure 8.6 is inspected carefully. It is difficult to speculate as to the exact origin of this but it is suspected that it is related to the occurrence of a specific activation pressure which is necessary to initiate electron delocalisation and bond lengthening. This is in keeping with some of the behaviours previously observed[3] in actinide metals under pressure.

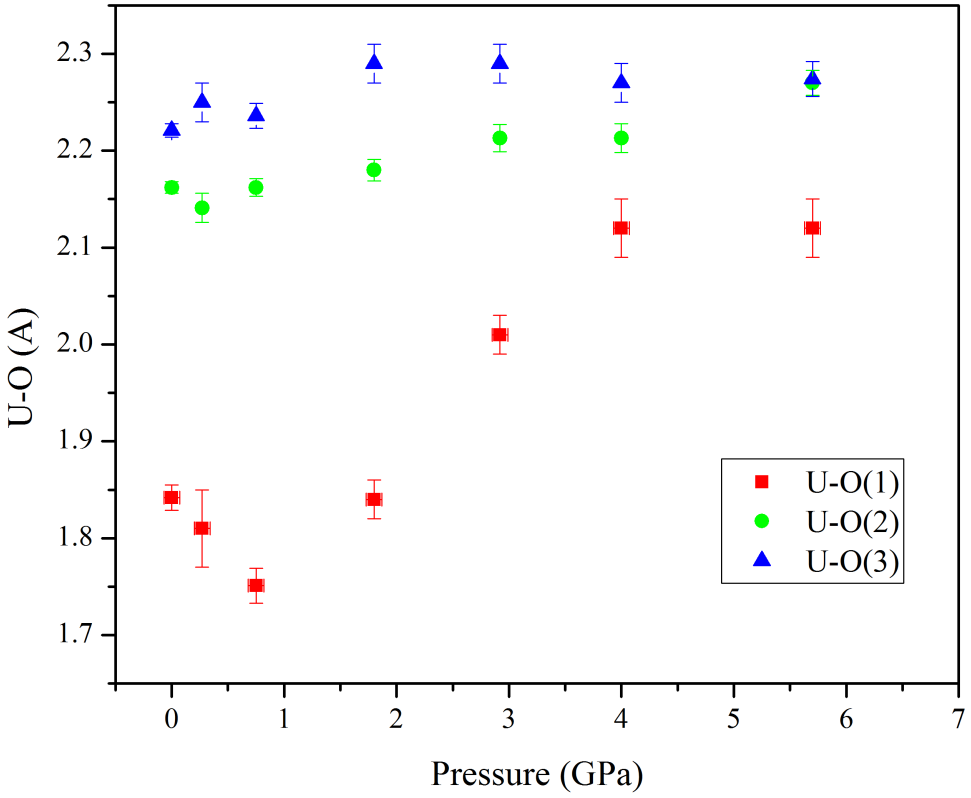

FIGURE 8.7: Uranium-Oxygen bond lengths in the UO_6 polyhedra in β-$SrUO_4$from ambient towards 5.7 GPa determined from Rietveld refinements against NPD measurements. Note the exceptional expansion of the uranyl U-O(1) bond length.

This is apparently the first study to demonstrate the departure of Badger's rule in uranyl containing materials through anomalous bond expansion under pressure. This phenomena, present in both α-$SrUO_4$ and β-$SrUO_4$, is quite significant as based on the geometry of the structure, the expanding uranyl bonds would place considerable chemical pressure on the Sr^{2+} layers. Although chemical pressure has been discussed well in literature[25,26], most studies use chemical substitution to achieve necessary chemical pressure effects. α-$SrUO_4$ and β-$SrUO_4$ are novel in this aspect as by providing physical pressure to the oxides causes a secondary form of pressure to occur via the expansion pf the uranyl bonds against the Sr^{2+} cation layers. This novel *in situ* chemical pressure process could be useful and relevant in high pressure science such as for example, attempting to obtain metallic hydrogen[27] if hydrogen could be inserted in the α-$SrUO_4$ structure or similar which some[28] have speculated as a way to access it. For reasons previously discussed the incompressibility of the $SrUO_4$ poloymorphs is most pronounced in α-$SrUO_4$,

although further high pressure *in situ* studies are required to properly ascertain a suitable EoS and K_0 for it. Nevertheless when the change in volume of α-$SrUO_4$ and also β-$SrUO_4$ are considered, with the reference materials diamond[21], anatase[29] and c-BN[30], Figure 8.8, it is apparent that α-$SrUO_4$ exhibits considerable incompressibility, very similar to diamond and c-BN.

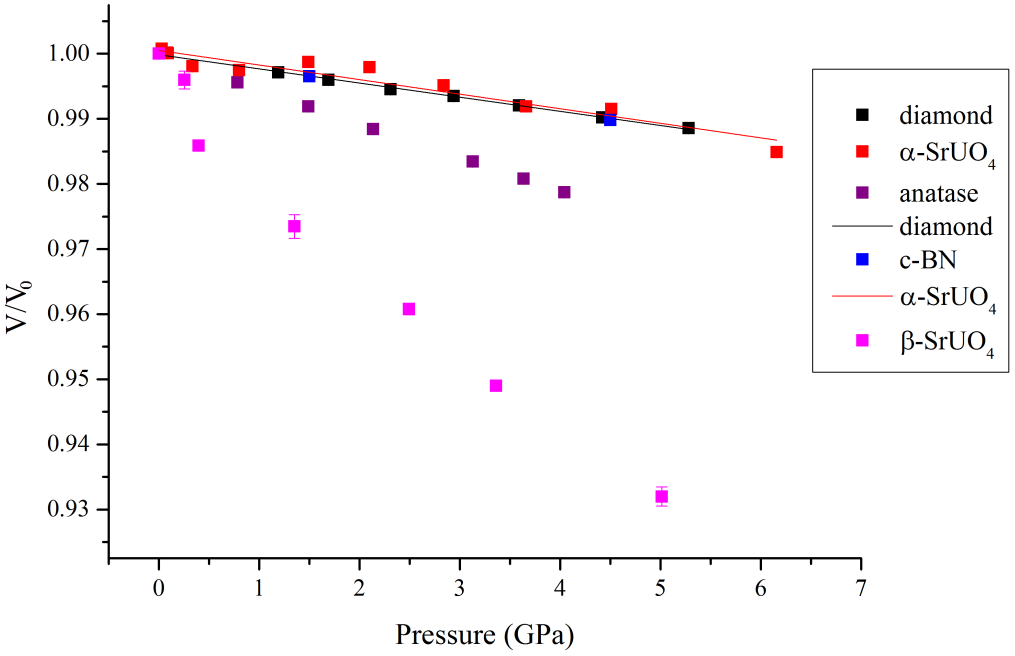

FIGURE 8.8: Comparison of V/V_0 for α-$SrUO_4$, β-$SrUO_4$, diamond[21], anatase[29] and c-BN[30]. The red and black lines are fitted to illustrate the similar incompressibility of α-$SrUO_4$ and diamond respectively.

8.4 Chapter Conclusion

It is demonstrated that when pressured towards 6.15 and 5.7 GPa respectively both α-$SrUO_4$ and β-$SrUO_4$ undergo anomalous bond expansion most pronounced in the uranyl bond. NPD measurements, consistent with the theoretical predictions of Osman *et al.*[9] indicate this is a consequence of charge transfer and resulting reduction of effective charge from the uranyl, UO_2^{2+}, group towards the uranyl bonds. Both oxides are quite incompressible, however the incompressibility is most pronounced in α-$SrUO_4$ where measurements indicate it has a very large bulk modulus consistent with superhard materials c-BN and diamond. However further high pressure measurements at higher pressures are needed to confirm this

as an EoS could not be fitted against the NPD refined volumetric data for it. An EoS based on the Murnaghan model could be fitted against data collected for β-$SrUO_4$ which returned a much lower bulk modulus compared to α-$SrUO_4$ of 55(8) GPa. The dramatically different incompressibilitys of the two isostructural oxides is reminiscent to that of diamond and graphite [8] and is attributed to the subtly different bonding arrangements and geometries between the structures. This work demonstrates that significant superhard properties can be realised within actinide oxides based on electron delocalisation and also the associated importance of subtle bonding arrangements and geometries in influencing material hardness and incompressibility.

References

1. Benedict, U., Haire, R. G., Peterson, J. R., and Itie, J. P. *Journal of Physics F: Metal Physics* **15**(2), L29 (1985).

2. Jha, P. K. and Sanyal, S. P. *Journal of Physics and Chemistry of Solids* **64**(8), 1237–1240 (2003).

3. Lindbaum, A., Heathman, S., Bihan, T. L., Haire, R. G., Idiri, M., and Lander, G. H. *Journal of Physics: Condensed Matter* **15**(28), S2297 (2003).

4. Idiri, M., Le Bihan, T., Heathman, S., and Rebizant, J. *Physical Review B* **70**(1) (2004).

5. Matar, S. F. and Demazeau, G. *Journal of Solid State Chemistry* **182**(10), 2678–2684 (2009).

6. Matar, S. F. *Chemical Physics Letters* **476**(4-6), 213–217 (2009).

7. Matar, S. F. *Solid State Sciences* **11**(8), 1380–1385 (2009).

8. Zhao, Z. S., Xu, B., and Tian, Y. J. *Recent Advances in Superhard Materials*, volume 46 of *Annual Review of Materials Research*, 383–406. (2016).

9. Osman, H. H., Pertierra, P., Salvado, M. A., Izquierdo-Ruiz, F., and Recio, J. M. *Physical Chemistry Chemical Physics* **18**(27), 18398–18405 (2016).

10. Cioslowski, J., Liu, G., and Mosquera Castro, R. A. *Chemical Physics Letters* **331**(5), 497–501 (2000).

11. Schnaars, D. D. and Wilson, R. E. *Inorganic Chemistry* **53**(20), 11036–11045 (2014).

12. Vallet, V., Wahlgren, U., and Grenthe, I. *Journal of Physical Chemistry A* **116**(50), 12373–12380 (2012).

13. Besson, J. M., Nelmes, R. J., Hamel, G., Loveday, J. S., Weill, G., and Hull, S. *Physica B: Condensed Matter* **180-181**, 907–910 (1992).

14. Studer, A. J., Hagen, M. E., and Noakes, T. J. *Physica B-Condensed Matter* **385-86**, 1013–1015 (2006).

15. Larson, A. C. and Dreele, R. B. V. Technical report, Los Alamos National Laboratory, (2000).

16. Toby, B. H. *Journal of Applied Crystallography* **34**, 210–213 (2001).

17. Toby, B. H. and Von Dreele, R. B. *Journal of Applied Crystallography* **46**(2), 544–549 (2013).

18. Gonzalez-Platas, J., Alvaro, M., Nestola, F., and Angel, R. *Journal of Applied Crystallography* **49**(4), 1377–1382 (2016).

19. Murnaghan, F. D. *Proceedings of the National Academy of Sciences* **30**(9), 244–247 (1944).

20. Knittle, E., Wentzcovitch, R. M., Jeanloz, R., and Cohen, M. L. *Nature* **337**, 349 (1989).

21. Gillet, P., Fiquet, G., Daniel, I., Reynard, B., and Hanfland, M. *Physical Review B* **60**(21), 14660–14664 (1999).

22. Cohen, M. L. *Physical Review B* **32**(12), 7988–7991 (1985).

23. Burns, P. C., Miller, M. L., and Ewing, R. C. *Canadian Mineralogist* **34**, 845–880 (1996).

24. Burns, P. C., Ewing, R. C., and Hawthorne, F. C. *Canadian Mineralogist* **35**, 1551–1570 (1997).

25. Zhang, D. W., Tang, G. D., Xu, X. B., Qiu, L., Wang, Z. H., and Du, Y. W. *Modern Physics Letters B* **26**(31) (2012).

26. Hegger, H., Petrovic, C., Moshopoulou, E. G., Hundley, M. F., Sarrao, J. L., Fisk, Z., and Thompson, J. D. *Physical Review Letters* **84**(21), 4986–4989 (2000).

27. Ashcroft, N. W. *Physical Review Letters* **21**(26), 1748–1749 (1968).

28. Feng, J., Grochala, W., Jaro, T., Hoffmann, R., Bergara, A., and Ashcroft, N. W. *Physical Review Letters* **96**(1), 017006 (2006).

29. Arlt, T., Bermejo, M., Blanco, M. A., Gerward, L., Jiang, J. Z., Olsen, J. S., and Recio, J. M. *Physical Review B* **61**(21), 14414–14419 (2000).

30. Datchi, F., Dewaele, A., Le Godec, Y., and Loubeyre, P. *Physical Review B* **75**(21), 214104 (2007).

Chapter 9

Conclusions and Perspectives

Structural elucidation of uranium oxide compounds is a pertinent task due to the relevance such materials have towards the operational efficiency of UO_2 nuclear fuels and the processing and storage of nuclear waste forms. However, despite the protracted focus on nuclear related technologies, the fundamental chemistry of uranium remains poorly understood, even in binary oxide form, as illustrated by the recent works of Desgranges and co-workers [1,2]. This dissertation was directed at systematically examining ternary uranium oxides of the form AUO_4 to elucidate the solid state chemistry which underpins them, and further, understand the role uranyl bonding and $5f$ electron chemistry play in influencing their physicochemical properties. This begins with Chapter 3, where the α to β transition in $SrUO_4$ was examined *in situ* using neutron and synchrotron X-ray diffraction, X-ray absorption spectroscopy and supported by *ab initio* calculations. It was shown that the α rhombohedral polymorph in space group $R\bar{3}m$ undergoes an irreversible phase transformation to the β orthorhombic polymorph in space group *Pbcm* above 600 ^{o}C. Crucial to the transformation is the generation of oxygen vacancies and reduced uranium valence states in the rhombohedral α polymorph as it is heated in the presence of oxygen. This process is believed to lower the activation energy. For the transformation to progress it is essential that oxygen is present to re-oxidise sub-stoichiometric α-$SrUO_{4-x}$, otherwise the orthorhombic β polymorph will not form. *Ab initio* calculations indicate the origin of this phenomena lies in the ability for the α polymorphs UO_8 polyhedra to be thermodynamically preferred when containing oxygen vacancies whereas the UO_6 in β-$SrUO_4$ are not thermodynamically disposed to contain vacancies. Overall, the phase transformation is unique, where $SrUO_4$ essentially acts as a temperature activated oxygen conduit.

Chapters 4 and 5 expanded this interest in defect formation by studying α-$SrUO_4$ and isostructural $CaUO_4$ in addition to members of the solid solution α-$Sr_xCa_{1-x}UO_4$ aiming to understand the role the A cation size has in inducing oxygen vacancy formation and how this may effect structural behaviour. In particular, the structural response of these oxides when vacancy concentrations are maximised through the use of hydrogen at high temperature. An approximately linear relationship between the number of oxygen vacancies that can form under oxidising conditions at high temperature and the size of the A size cation was observed. This trend was attributed to variable defect-defect interactions modulated by the size of the A site cation. It was remarkably demonstrated that, when a critical number of oxygen vacancies are obtained, rhombohedral α-$SrUO_{4-x}$, α-$Sr_{0.4}Ca_{0.6}UO_{4-x}$ and $CaUO_{4-x}$ can undergo reversible phase transformations upon heating involving the lowering of crystallographic symmetry with the previously disordered oxygen

vacancies becoming ordered resulting in the formation of novel δ phases at high temperature. The transformation is demonstrated to be purely thermodynamically driven where *ab initio* calculations suggest the origin of the transformation lies in a careful balance between the decreasing entropy of ordered vacancies with increasing electronic entropy. At present there seems to be no other known structural systems that undergo such phase transformations. The ramifications of such a novel phase transformation are quite profound, as it suggests materials that contain desirable ordered properties at low temperature but are lost at high temperature, for instance superconductors, may be potentially accessed by carefully balancing different entropic components of the system.

Chapter 6 looked to establish "the missing link" between the orthorhombic $A\mathrm{UO_4}$ oxides in space group *Ibmm* and *Pbcn*. Prior to this investigation many of the phase transformations between structural variants in the $A\mathrm{UO_4}$ oxides were known, albeit with various degrees of precision, except between the orthorhombic $A\mathrm{UO_4}$ oxides in space group *Ibmm* and *Pbcn*. This possibility was addressed using high pressure high temperature synthesis methods to prepare diffraction quality single crystals of two $\mathrm{NiUO_4}$ polymorphs, β (*Ibmm*) and α (*Pbcn*), first reported in the 1960s[3,4], noting that the lack of recent studies led some[5] to question their existence. It was shown, from *ex situ* measurements that the β polymorph is the preferred high pressure phase and it was inferred that the α polymorph would transfer to this irreversibly with increasing temperature and pressure. Surprisingly, it was shown that α-$\mathrm{NiUO_4}$, despite being isostructural with pentavalent uranium containing $\mathrm{CrUO_4}$ and $\mathrm{FeUO_4}$, contained hexavalent rather than pentavalent uranium. This was attributed to the preferred stability of respective $\mathrm{U^{6+}}$ and $\mathrm{Ni^{2+}}$ $5f^0$ and $3d^8$ electron configurations. The requirement of high pressure was argued to be a consequence of the size mismatch between the $\mathrm{Ni^{2+}}$ and $\mathrm{U^{6+}}$ cations, as when compared to isostructural orthorhombic *Ibmm* and *Pbcn* $A\mathrm{UO_4}$ oxides the $\mathrm{Ni^{2+}}$ cation is essentially too small or too large respectively, relative to the $\mathrm{U^{6+}}$ cations to form in these space groups under ambient pressure conditions. The structure of $\mathrm{NiU_3O_{10}}$ was also solved for the first time and the results compared with those previously reported for $\mathrm{NiU_2O_6}$[6,7], making this the most comprehensive study of the Ni-U-O system. Further, based on the initial works of Read *et al.*[5] a comprehensive structural hierarchy for the $A\mathrm{UO_4}$ family of oxides is described which relates structure type with the size of the A site cation.

In Chapter 6, a tilting mechanism was identified in β-$\mathrm{NiUO_4}$ associated with the $\mathrm{NiO_6}$ polyhedra, reminiscent of that occurring in ABX_3 perovskites. Since β-$\mathrm{NiUO_4}$ is isostructural with $\mathrm{MnUO_4}$, $\mathrm{CoUO_4}$, $\mathrm{MgUO_4}$ and related to β-$\mathrm{CdUO_4}$ it was hypothesized, and examined in Chapter 7, that this trend would

be linearly reflected in these oxides and could be related to the initial assignment of the higher symmetry space group of *Cmmm*. It was demonstrated, using a combination of neutron and synchrotron X-ray powder diffraction, single crystal X-ray diffraction and X-ray absorption spectroscopy, that tilting, was most pronounced in β-$NiUO_4$ and least pronounced in β-$CdUO_4$, a consequence of the linear variation in size between the A site cations. It was further shown, with neutron and synchrotron X-ray powder diffraction, that β-$CdUO_4$ is more appropriately assigned to the lower symmetry *Ibmm* space group.

Chapter 8, the penultimate chapter, looked to examine the theorised[8] departure from Badger's rule in uranium materials through *in situ* neutron diffraction studies of uranyl group containing α-$SrUO_4$ and β-$SrUO_4$. It is known that when placed under high pressure, actinides, particularly uranium, can undergo $5f$ electron delocalisation. This was demonstrated to occur in α-$SrUO_4$ and β-$SrUO_4$ when pressured towards 6.15 and 5.7 GPa respectively resulting in an anomalous lengthening of U-O bonds, particularly the uranyl bond. Remarkably this bond lengthening apparently contributes to the pronounced hardness of the α-$SrUO_4$, measurements indicate this has a bulk modulus comparable to diamond and c-BN. However further high pressure measurements are required to establish the precise equation of state, nevertheless such an anomalous bond lengthening process, which is inferred to place *in situ* chemical pressure on the Sr^{2+} cation layers, has not been reported previously. Although it is likely this phenomenon will be present in many other actinide materials, the paucity of published actinide high pressure research has meant very little is known experimentally other than by calculation. This makes this work broadly significant in both actinide and high pressure science as it promotes the possibility that advanced ultrahard materials can be accessed using careful chemical design utilizing uranyl or actinyl groups as structurally reinforcing functional groups.

This dissertation has demonstrated the chemical and structural complexity of the apparently simple AUO_4 family of oxides. Despite the history of these structures transcending the nuclear age, the remarkable structural flexibility and associated properties of this system of structures is only just emerging. Central to the presented dissertation is the employment of systematic approaches of synthesis and experimental design to understand structural-chemical phenomena. This has enabled a near phenomenological picture of the AUO_4 system to be painted which can be used as a predictive means for determining potential structural type, formation and properties for ternary mixed metal uranium oxide systems. A fascinating and remarkable example of this is in the rhombohedral AUO_4 oxides in space group $R\bar{3}m$ which possess the extraordinary ability to access symmetry lowering and vacancy ordering phase transformations with

heating. These present an extremely important new direction in functional material design where thermally induced oxygen defect ordering is desirable. Furthermore if the intrinsic thermodynamic mechanism within these structures can be translated into other materials it may become a means to access properties such as super conductivity at high temperatures. Although this work may only be a fraction of broader actinide science, the significant chemical phenomena uncovered here represents a delectable flavour of the further exotic discoveries that may be found when utilizing $5f$ electron chemistry. Consequently, the continual advancement of actinide research is argued to transpire a plethora of unique and rich discoveries pertinent to both inorganic chemistry and general scientific endeavour.

References

1. Desgranges, L., Baldinozzi, G., Rousseau, G., Niepce, J. C., and Calvarin, G. *Inorganic Chemistry* **48**(16), 7585–7592 (2009).

2. Desgranges, L., Ma, Y., Garcia, P., Baldinozzi, G., Simeone, D., and Fischer, H. E. *Inorganic Chemistry* **56**(1), 321–326 (2017).

3. Hoekstra, H. R. and Marshall, R. H. *Advances in Chemistry Series* (71), 211–218 (1967).

4. Young, A. P. *Science* **153**(3742), 1380–1384 (1966).

5. Read, C. M., Smith, M. D., and zur Loye, H. C. *Solid State Sciences* **37**, 136–143 (2014).

6. Hinatsu, Y. *Journal of Solid State Chemistry* **114**(2), 595–597 (1995).

7. Hinatsu, Y., Doi, Y., and Nakamura, A. *Journal of Nuclear Materials* **385**(1), 49–52 (2009).

8. Osman, H. H., Pertierra, P., Salvado, M. A., Izquierdo-Ruiz, F., and Recio, J. M. *Physical Chemistry Chemical Physics* **18**(27), 18398–18405 (2016).

Appendix A

Least Squares Minimisation R Measurement Factors

The following equations define the quality of a powder diffraction Rietveld refinement [1,2].

The profile:

$$R_p = \frac{\sum |(y_i^{obs} - y_i^{calc})|}{\sum y_i^{obs}} \tag{A.1}$$

The weighted Profile:

$$wR_p = \left[\frac{\sum W_i (y_i^{obs} - y_i^{calc})^2}{\sum W_i (y_i^{obs})^2} \right]^{\frac{1}{2}} \tag{A.2}$$

The Bragg factor:

$$R_{Bragg} = \frac{\sum ||I_k^{obs}| - |I_k^{calc}||}{\sum |I_k^{obs}|} \tag{A.3}$$

The goodness of fit:

$$\chi^2 = \frac{\sum W_i (y_i^{obs} - y_i^{calc})^2}{N - P} = (\frac{R_{wp}}{R_{exp}})^2 \tag{A.4}$$

For the above equations:

y_i^{obs} is the set of observed diffraction intensities collected at each step across the pattern.

y_i^{calc} is the set of calculated intensities corresponding to the observed.

W_i is a weight assigned to each intensity given by $W_i = \frac{n}{\sigma_i^2 I_{ci}}$ where n is the number of detectors contributing to the intensity average and σ_i^2 is the variance at the i^{th} reflection.

N is the total number of observed reflections.

P is the total number of refined parameters.

I_k^{obs} is the observed intensity of the k^{th} Bragg reflection after the refinement cycles.

I_k^{calc} is the calculated intensity of the k^{th} Bragg reflection after the refinement cycles.

References

1. Hamilton, W. C. *Acta Crystallographica* **18**(3), 502–510 (1965).

2. Brunger, A. T. *Nature* **355**, 472 (1992).